Computational studies of interstitial-type oxide ion conductors for applications in solid oxide fuel cells

Weaver, Paul

Award date:
2011

Awarding institution:
University of Bath

Computational Studies of Interstitial-type Oxide Ion Conductors for Applications in Solid Oxide Fuel Cells

Submitted by

Paul Joseph Weaver

for the degree of Doctor of Philosophy of the
University of Bath
Department of Chemistry
July 2011

Signature of author: .....

Dedicated to the Glory of God

Contents

List of Figures

List of Tables

Abstract

Fundamental advances in solid-state ionics are crucial for the development and commercialisation of cleaner energy conversion and storage technologies, such as solid oxide fuel cells (SOFCs). Modern computational techniques play a valuable role in this field by providing insight into the properties of materials on the atomic scale. In this thesis we examine three types of material as potential interstitial-type oxide-ion conductors for application in intermediate-temperature SOFCs. Firstly, we investigate neodymium nickelate, $Nd_2NiO_{4+\delta}$, which is a mixed ionic/electronic conductor with a Ruddlesden–Popper-type structure. We show that interstitial ions are introduced into the structure via Frenkel or oxidation processes. Furthermore, we find an interstitialcy-type conduction mechanism for these ions, as previously found for the $La_2NiO_{4+\delta}$ and $Pr_2NiO_{4+\delta}$ materials. Molecular dynamics simulations reveal a reduction in migration energy for Nd deficient systems, which is consistent with tracer diffusion data. Secondly, we use both atomistic and density functional theory techniques to examine $SrFeO_2$, a recently-discovered material that is isostructural with the 'infinite-layer' cuprates. We find a favourable oxidation energy for the material, in accordance with experiment. The migration of the resulting interstitial oxide ions is predicted to occur in a two-step process very similar to the vacancy-hopping mechanism of the parent perovskite. Lastly, we examine the site selectivity and compensation mechanisms of a wide range of cation dopants in the $La_{9.33}(GeO_4)_6O_2$ apatite material. We find that small, highly charged dopants (e.g., Ti^{4+}) are more favourable on the Ge site, whilst larger dopants with lower charge (e.g., Sr^{2+}) prefer the La site. We also find that subvalent doping is not predicted to reduce the oxide ion content of the material, which is significant for interstitial ion conduction behaviour.

Acknowledgements

There are a number of people whom I would like to thank for the part they have played in helping me complete this work. Firstly, I would like to thank Prof. Saiful Islam for his generous support and input, both directly into the document you see here, and behind the scenes providing opportunities to attend conferences and the trust to allow me to tinker with our group's computational hardware!

Thanks must also go to past and present members of the MSI group: Dr Craig Fisher (ありがとうございます) and Dr Stephen Stokes for their practical help getting up-and-running, and Dr Pooja Panchmatia for lending her expertise with DFT, cake-making and the state of the world in general. Thanks also to Grahame Gardiner for being keen to take on the sysadmin batton (just don't mention `rm -fr /bin` eh?) and to hack away trying to get our computers to do things that they previously couldn't. Jesse Dufton, thanks for all your tough-man stories and I never thought you'd *keep* your monitor upside-down! Dr Chris Eames, thank you for sharing the Lord of the Rings thesis parody, it is totally accurate!

From (slightly) further afield, thanks to Prof. Steve Parker and Prof. Ian Williams for always being available for useful theoretical discussions and to give me a different spin on things. Steve, thanks also for your DL_POLY know-how and `run3dbin` program, without which there would have been much head-scratching! I humbly suggest that Python is awesome, and well worth a look. Thanks also to Tom Shapley of the SCP group for your invaluable pointers on DL_POLY and VMD, and for some `bash` nuggets. Mark Russell thanks for all the work you do keeping the departments machines ticking along, please check in on `kermit2` and the other muppets (no, I don't mean the people working in our office) from time-to-time.

Lastly I offer my heartfelt thanks to my friends and family who have shown an interest in my work and contributed to it with their love and support through the good times and the not-so-good over the last few years. Thanks to my beautiful wife Louise for always lifting me when I felt down — I know this has been as much of a rollercoaster for you as it has for me. I don't know what I'll do now that "I'll do it when I've finished my PhD" is no longer a valid chore-stalling tactic! Thanks to my parents for being totally amazing and for their unerring love for me. Mum, Val, I'm sorry that biology was never my strong point, but *amaryllis* did set me off in a good direction. Dad, Chas, I will always remember the warm green glow of the Amstrad

and how you taught me binary and that computers always do exactly what they're told. You've both been fundamental in making me who I am today. To my Granny, Maureen, thank you for being so kind and generous, and for working so hard to love and support me. I miss Grandad.

To the legendary Dr John Stark, thanks for everything. You are the most awesome man I know — a real "Green & Blacks" bloke. Dzięki za late nights, early mornings, Chopin, Madness, your brilliant ball clock and duck-and-chips. You have the beans.
To Tom Burles, thanks for all the times we drove sideways and your endless energy and encouragement, even in the face of some hard times. You'll go far young man!
To Rupert Swarbrick, thanks for all the hours of brain-stretching fun — you made me push myself. Thanks also to your family for being so hospitable, and to your mum, Wendy, for being such a great (but scary) physics teacher.
To Jenny Norris, thanks for inviting me to South Africa, which was one of the most amazing experiences of my life, and for always being hospitable and always sharing your spiritual side. Make sure Dr Caroline Norris doesn't try to take over the world.
To Emma Hopegood, thanks for scrubbing Tom's nails so hard he ran away, helping to blitz Lou's house and generally being so servant hearted. Make sure you get looked after too sometimes.
To David Cousins, thanks for always being up for a good game of anything (but not so much for almost always being unbeatable). You've just lost The Game.

This document was typeset using LaTeX because I am a perfectionist. Thanks to Christian Feuersänger for his help with the `pgfplots` package. I used Plot-Digitizer by Joseph A. Huwaldt for digitising several printed graphs. Thanks to xkcd.com for their permission to reproduce some of their excellent comics here, and to PhD Comics and Dilbert, who also kept me entertained during my work.

This work was funded by a DTA studentship from the UK Engineering and Physical Sciences Research Council, and I am grateful to the Materials Chemistry Consortium (chaired by Prof. Richard Catlow and Dr Scott Woodley) for access to the HECToR facility, the UK's national high-performance computing service.

List of Publications and Presentations

Publications

2011	P. J. Weaver, M. S. Islam, P. Panchmatia *J. Mater. Chem.* (in preparation). *"Defect, electronic and ion transport properties of $SrFeO_2$: Combined atomistic simulation and DFT studies."*
2011	P. J. Weaver, M. S. Islam, P. Panchmatia *J. Mater. Chem.* (in preparation). *"Atomic-scale insight into oxide-ion migration in Nd_2NiO_4."*
2011	P. J. Weaver, M. S. Islam, P. Panchmatia *Chem. Mater.* (in preparation). *"Dopant incorporation in Ge-apatite oxide-ion conductors."*

Oral Presentations

Jun 2010	E-MRS Conference, Strasbourg *"Atomic-scale Studies of Defects and Ion Transport in Interstitial Ion Conductors"*
May 2010	Chemistry Postgraduate Symposium, University of Bath (Prize Winner) *"Simulation Studies of Oxide Materials for Fuel Cells"*
Jun 2009	Solid State Ionics 17, Toronto *"Atomic-scale Insight into Defects and Ion Transport in Infinite-layered $SrFeO_2$"*

Poster Presentations

Dec 2010	RSC Solid State Chemistry Group Christmas Meeting, University College London *"Atomistic Modelling of Defects and Ion Transport in Layered $SrFeO_2$"*
Jun 2010	E-MRS Conference, Strasbourg *"Modelling of Infinite-Layered $SrFeO_2$ for Clean Energy Applications"*
Dec 2009	RSC Solid State Chemistry Group Christmas Meeting, Open University *"Modelling of Infinite-Layered $SrFeO_2$ for Clean Energy Applications"*
Jun 2009	Solid State Ionics 17, Toronto *"Atomistic Modelling of Novel Metal Oxides for Clean Energy Applications"*
Sep 2009	South West Computational Chemists' group meeting, University of Southampton *"Atomistic Modelling of Novel Metal Oxides for Clean Energy Applications"*

Chapter 1

Introduction

1.1 Sustainable Energy

The generation of clean, sustainable energy is one of the key technological challenges facing humanity today. There is considerable pressure to reduce the usage of fossil fuels because natural resources are limited, energy security is an increasingly important geo-political issue, and, due to concerns about global warming, there is widespread effort to reduce carbon dioxide emissions [1]. A diverse range of alternative energy generation, storage and conversion technologies is being developed to address these challenges, and electrochemical devices, such as solar cells, lithium batteries and fuel cells are predicted to play an important role in the 'energy economy' of the future.

Fuel cells are a class of electrochemical device that convert the chemical energy stored in a fuel directly into electricity, and they offer a number of advantages over traditional heat engines such as the gas turbine or the internal combustion engine. Primarily, fuel cells can be much more efficient than heat engines, converting more of the energy stored in a fuel into a useful form. Furthermore, this conversion produces fewer pollutants (such as carbon monoxide, nitrous oxides, volatile organic compounds, sulphur dioxide and particulate matter, all of which are associated with combustion [2]).

In addition, the physical design of fuel cells is inherently modular and quiet [3, 4], which facilitates their use in a wide variety of situations ranging in scale from portable electronics, through transport and localised stationary electricity generation all the way up to grid-scale generation [5, 6]. Fuel cells are ideal for co-generation (combined heat and power) applications, where waste heat from the cell is used to warm a particular environment. Co-generation is particularly applicable for use in the home environment [7], and prototype systems have already been produced [8].

Another major advantage of some types of fuel cell is their fuel flexibility. The

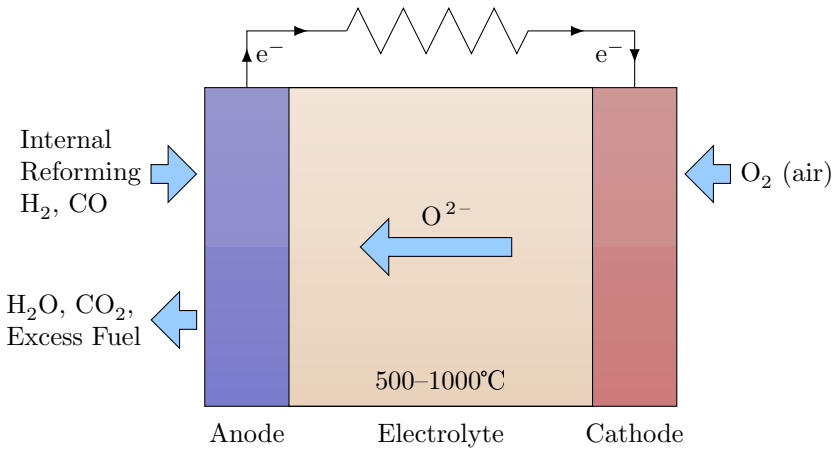

Figure 1.1: Schematic diagram of a typical solid oxide fuel cell. Fuel is oxidised at the anode by oxide ions that have been transported through the electrolyte from the cathode where they were produced by reduction of oxygen from the air.

traditional fuel used in fuel cells is hydrogen, but cells have been developed that can also convert more conventional carbon-containing fuels, such as methanol or alkanes. Hydrogen is an appealing fuel because it produces no carbon dioxide during use, and has a high specific energy. However, moving to an energy economy in which hydrogen is used to store and distribute the energy from clean or renewable energy sources is a difficult process, and the transition would be vastly assisted by devices that can function on both hydrogen and more traditional fuels.

The performance and cost of clean energy devices, and consequently their uptake in real-world applications, are critically dependent on the materials used in their construction. Such materials are at the forefront of materials science, and thus require innovative development to improve their commercial suitability. Experimental and theoretical methods can be used to investigate the fundamental mechanisms that underpin the functionality of these materials, improving existing materials and guiding the design of new ones. This thesis details the use of computational modelling methods to study the solid-state properties of several potential fuel cell materials.

1.2 Fuel Cells

1.2.1 What is a Fuel Cell?

Like traditional electrochemical cells (such as batteries), fuel cells convert chemical potential energy into electrical energy via redox reactions that occur at the surfaces of two electrodes separated by an electrolyte [4]. A battery, however, is a closed system, whereas a fuel cell is supplied with fuel from an external source and can, in theory, keep producing electricity as long as the fuel supply is maintained. Figure 1.1 shows the configuration of a typical solid oxide fuel cell (SOFC).

The central concepts of fuel cell operation are long established; Sir William Grove first published work on his 'gas voltaic battery' in 1839 [9]. He rightly suggested that if it was possible to split water electrochemically into hydrogen and oxygen, then it would be possible to use the reverse process in order to generate electricity. All modern hydrogen fuel cells essentially work in this same way, although there are many differences in implementation.

In fuel cells of the type shown in Figure 1.1, oxygen from the air is reduced at the cathode (Equation 1.1a), and the resulting oxide anions are then transported through the electrolyte and combine with hydrogen at the anode/electrolyte interface (Equation 1.1b). The electrons produced from this second process are driven around an external circuit and can do useful work.

$$\text{Cathode} \qquad \tfrac{1}{2}\mathrm{O_2} + 2\,\mathrm{e^-} \longrightarrow \mathrm{O^{2-}} \tag{1.1a}$$

$$\text{Anode} \qquad \mathrm{H_2} + \mathrm{O^{2-}} \longrightarrow \mathrm{H_2O} + 2\,\mathrm{e^-} \tag{1.1b}$$

$$\text{Overall} \qquad \mathrm{H_2} + \tfrac{1}{2}\mathrm{O_2} \longrightarrow \mathrm{H_2O} \tag{1.1c}$$

The high efficiency of fuel cells stems from this direct electrochemical oxidation of the fuel, because, unlike heat engines, the work-producing process is not subject to the thermodynamic limitation of the Carnot cycle.[a] Fuel cells can attain high electrical efficiencies of about 60–70%, and, if the waste heat generated by the cell is also used, total efficiencies can exceed 90% [4, 11].

In contrast to the oxide-ion-conducting cell depicted in Figure 1.1, it is also possible to construct a cell in which protons are the mobile species. In such cells, hydrogen is oxidised at the anode and the resulting protons are transported through the electrolyte to the cathode, where they reduce oxygen from the air. The main operational difference in this type of cell, aside from the differing material requirements, is that the waste products must be dealt with on the air side, as opposed to the fuel side of the cell. This work is focused on oxide-ion-conducting materials, and so proton conductors will not be discussed further.

1.2.2 Solid Oxide Fuel Cells

Fuel cells can be made from a wide variety of materials, and are generally classified by the type of electrolyte that is used. Grove's early cell used sulphuric acid as the electrolyte and platinum for the electrodes [9]. Platinum is very expensive, however, and although liquid electrolytes are cheap, they can prove difficult to manage in a practical system and put limitations on the physical design of the cell. The corrosive nature of such electrolytes can also be problematic. It is clearly beneficial to implement the idea of a fuel cell using a different system of materials [4, 11].

[a] The maximum theoretical efficiency of any reversible heat engine, as laid out by Carnot [10], is $\eta = 1 - T_C/T_H$, where T_C is the absolute temperature of the cold reservoir and T_H is the absolute temperature of the hot reservoir.

Solid oxide fuel cells (SOFCs) are constructed entirely from ceramic components, which removes the need for precious metal electrodes and means they are less complex to operate and maintain than cells with liquid (or polymeric) electrolytes. Nernst first demonstrated the existence of solid oxide electrolytes with ZrO_2 derivatives in 1899 [12] and, almost a full century after Grove's original discovery, the first ceramic fuel cell was operated by Baur and Preis in 1937 [13]. Ceramic fast oxide ion conductors require very high temperatures to achieve useful levels of ionic conductivity, and this first SOFC operated at around 1000℃.

These high temperatures allow for the *in situ* reforming of hydrocarbon fuels into hydrogen at the anode, making SOFCs fuel-flexible unlike their low-temperature counterparts. Equation 1.2 illustrates the steam reformation process for methane. The carbon monoxide produced by this process may be oxidised in the 'shift equilibrium', presented in Equation 1.3, producing further hydrogen:

$$CH_4 + H_2O \rightleftharpoons CO + 3\,H_2 \tag{1.2}$$

$$CO + H_2O \rightleftharpoons CO_2 + H_2. \tag{1.3}$$

SOFCs are far more tolerant of fuel impurities than other types of fuel cell [4], although even low levels of sulphur (in the parts per million range) can have a significant impact on performance [11]. Their fuel flexibility and tolerance make SOFCs an ideal technology to assist the transition away from a fossil-fuel-based energy economy to one based on hydrogen.

1.2.3 Materials for Solid Oxide Fuel Cells

Despite their operational flexibility, SOFCs place a demanding set of requirements upon their constituent materials. Firstly, the electrolyte must provide a barrier to gas diffusion between the anode and cathode, whilst simultaneously maintaining high levels of ionic conductivity and negligible electronic conductivity. The electrolyte must also be chemically stable under the oxidising and reducing conditions of the anode and cathode respectively. The first generation of SOFCs were based on an yttria-stabilised zirconia (YSZ) electrolyte [11], which is described in more detail in Section 1.5.1.

Both the anode and cathode materials must be porous to allow the diffusion of gases to and from the electrode/electrolyte interface, where the redox reactions actually occur. Both materials must also be stable at the temperatures required for synthesis and over the entire temperature range of cell operation, and they must be stable under their respective harsh redox conditions. Furthermore, both materials must be electronically conductive and have similar thermal expansion coefficients to the rest of the cell to avoid excessive mechanical stress on thermal cycling.

The anode material must catalytically promote the hydrogen oxidation and hydrocarbon reforming reactions, and generally consists of metal particles supported on a porous framework of the electrolyte material [11]. The high-temperature environment is advantageous here, as it allows non-precious metals to be used [14]. The

most typical is nickel because of its chemical activity and low cost compared to other suitable metals such as cobalt, platinum and palladium. The electrolyte material (typically YSZ) is used as the support primarily to match the thermal expansion coefficient of the electrolyte, and keeps the nickel particles well-distributed.

Due to the limited range and prohibitive expense of suitable metals, the most commonly used cathode material is strontium-doped lanthanum manganite ($LaMnO_3$) [11]. $LaMnO_3$ has the perovskite structure, which will be discussed in more detail in Section 1.5.2, and is an electronic conductor due to the mixed oxidation state of manganese (Mn^{3+}/Mn^{4+}), which is promoted by the addition of strontium.

The *interconnect* is a component used to provide an electrical connection between the cells in the fuel cell stack and also to the external circuit. The harsh redox conditions and high temperatures again limit the suitable materials to a small range of oxide systems, and the current material of choice is another perovskite, $LaCrO_3$, which is a p-type conductor and has a very high melting point (> 2400℃) [11]. Conductivity can again be increased by doping with strontium.

1.2.4 Improving Solid Oxide Fuel Cells

The demanding requirements outlined above highlight just how big a challenge it is to improve the SOFC system. Many of the restrictions on the operation of the cell are due, at least in part, to the high operating temperature (800–1000℃), which is primarily a requirement for sufficient oxide ion conductivity in the cell.

Reducing the working temperature of SOFCs to an intermediate level of around 500–700℃ would have benefits for the long-term stability of the cell materials, and would lessen the issues of thermal and chemical compatibility between them [14]. Furthermore, reduced temperatures would allow the use of alternative manufacturing methods and a wider selection of materials (such as stainless steel for the interconnect and supports) [3]. Such improvements would reduce cost and improve performance, which is critical for the commercial success of fuel cell technology in practical applications.

Fundamental materials research is of central importance to these improvements. Understanding of the chemical factors that underpin the structural, defect and conduction properties of existing SOFC materials will guide the improvements of these materials. Furthermore, the discovery of new materials, with potentially superior conduction mechanisms, has the potential for vastly improved performance at lower temperatures. The next section details some of the chemistry that is fundamental to ion conduction in solid ceramics, after which a number of current and potential future SOFC materials are introduced.

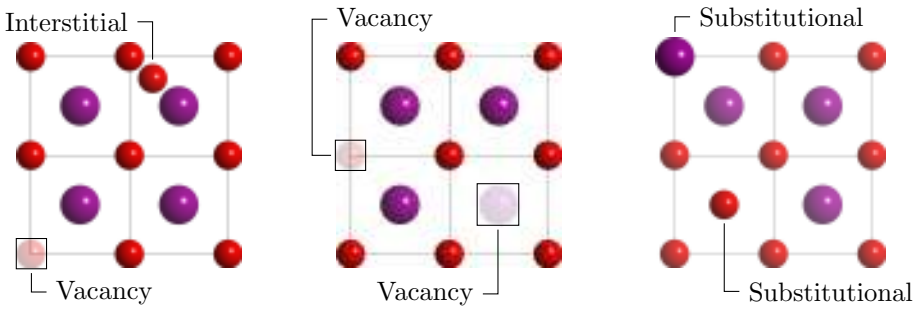

(a) Frenkel **(b)** Schottky **(c)** Anti-site

Figure 1.2: Schematic illustrations of examples three types of intrinsic defects, labelled with their constituent point defects. In this example lattice the large purple spheres represent cations and the small red spheres represent anions of equal and opposite charge.

1.3 Defect Chemistry and Ion Migration

Defects in crystals can have a significant influence on their structure, stability, chemistry and ionic and electronic conductivity. Defects exist intrinsically in all crystals for thermodynamic reasons (discussed in Appendix A), and the defect population increases rapidly with temperature [15]. Schottky, Frenkel and anti-site disorder, illustrated in Figure 1.2, are important examples of intrinsic defect.

Doping, the deliberate introduction of foreign ions into the lattice, may be used to control the properties of a material. As a consequence of doping, additional defects may be introduced into the lattice in order to compensate for the charge of the dopant ion. This provides a mechanism for fine-tuning material properties, for example increasing ionic conductivity by creating larger populations of charge-carrying defects within a material.

Under certain conditions the defects within a crystalline material may be highly mobile. As discussed previously, this ionic conductivity is the fundamental basis for electrochemical devices such as SOFCs. There are a number of mechanisms by which ionic conductivity can occur.

Current-generation SOFC materials based on Y/ZrO_2 employ the vacancy-hopping mechanism, illustrated in Figure 1.3. In the vacancy-hopping mechanism, a lattice oxide ion neighbouring a vacant oxide site hops from its lattice position to the vacant site, resulting in a net motion of oxide ions in one direction and vacancies in the other.

Interstitial-type mechanisms involve the motion of interstitial ions through the lattice, either directly [16, 17] or via exchange with lattice ions [18, 19]. The latter of these two mechanisms, shown in Figure 1.4, is often referred to as an *interstitialcy*-type mechanism. Materials with interstitial conduction mechanisms present

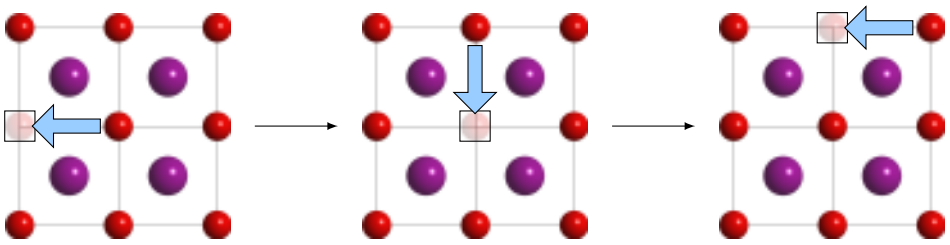

Figure 1.3: Schematic illustration of the vacancy-hopping mechanism for ionic conduction in crystals. Ion migration is achieved by the repeated filling of a vacancy by a neighbouring of the same type, with a net migration of the vacancy in one direction and of the ionic species as a whole in the opposite direction.

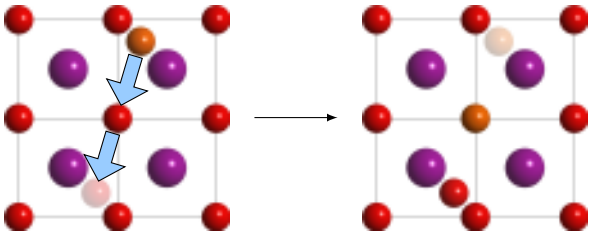

Figure 1.4: Schematic illustration of an interstitial-type mechanism for ionic conduction in crystals. Note the concerted movement of two oxide ions together. The initial interstitial oxide ion is highlighted in orange for clarity.

exciting new opportunities in the field of ion conductors and are being researched extensively as alternate SOFC materials.

1.4 Computational Modelling

Atomic-scale structural features can have a large influence on the properties of materials, so it is important to have a range of tools to investigate materials at this scale. Local structural features (e.g., point defects and conduction pathways) are difficult and expensive to probe experimentally, however, and thus computational simulation techniques are of significant importance in materials research. The principal aims of computational modelling are to complement and assist the interpretation of experimental data (e.g., diffraction and conductivity) and to undertake a predictive role in the development of materials [20]. Such techniques have been used successfully in a wide range of studies, showing good accord with experimental data and correctly predicting a number of material characteristics [21–23].

The field of computational chemistry finds its roots in the early part of the twentieth century, at which time the discipline of quantum physics was being established. Today the field is rather broad, encompassing elements of many diverse disciplines such as physical chemistry and statistical thermodynamics, in addition to quantum physics. The unifying feature of these disciplines is that they seek to encapsulate

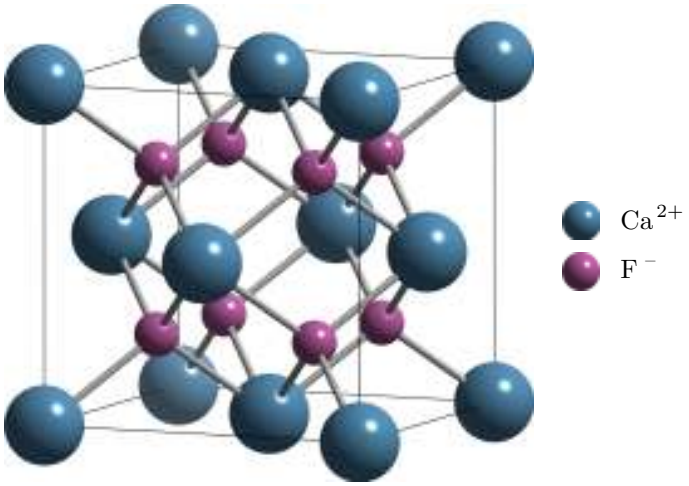

Figure 1.5: Structure of the mineral fluorite, CaF_2, which consists of a face-centred cubic array of cations with anions occupying all of the tetrahedral sites between them.

mathematically the relationships between observable macroscopic parameters and microscopic structure and behaviour.

The mathematics of theoretical chemistry is generally far too complex to solve by hand. The advent of the digital computer in the 1940s kickstarted a revolution in the field, putting numerical solutions within reach for the first time [24, 25]. The ever-increasing power of modern computers provides access to a widening selection of tools to tackle evermore complex problems, whilst reduced hardware costs make such endeavours more accessible to the general materials research community [26]. The basis of the computational methods used in this work are outlined in Chapter 2.

1.5 Current Materials for Solid Oxide Fuel Cells

1.5.1 Fluorite-type Oxides

Several types of material that meet the requirements outlined in Section 1.2.3 have been used or proposed for use in SOFCs. A brief overview is presented below, whilst detailed reviews of these materials can be found elsewhere [3, 11, 23, 27, 28]. The longest established oxide ion conductors are the fluorite-type oxides, which have the structure shown in Figure 1.5 and were first examined by Nernst in 1899 [12]. The general formula of the fluorite structure is AO_2, where A is a large tetravalent cation (e.g., U, Th, Ce). The AO_2 structure can be viewed as a face-centred cubic array of A^{4+} cations with eight oxide anions located in the tetrahedral sites between them, as shown in Figure 1.5.

Zirconium based fluorite oxides have proved to be particularly useful as electrolytes in SOFCs. Because Zr^{4+} is small, however, stoichiometric zirconia only exists with

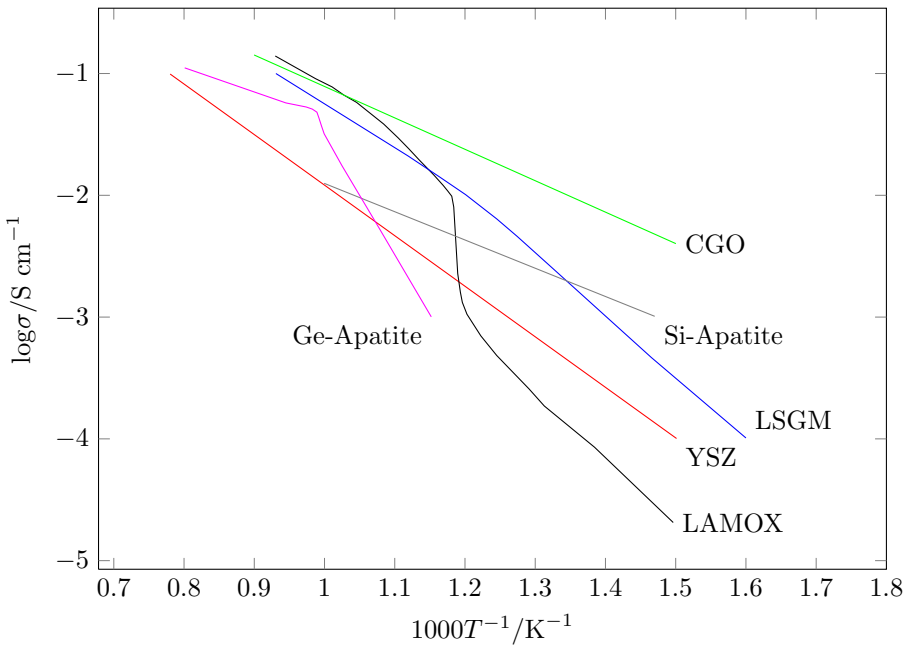

Figure 1.6: Total conductivities from experiment of several well-known oxide-ion conductors as a function of inverse temperature. Original data were collated by Malavasi [23] from a number of sources: YSZ, $(ZrO_2)_{0.92}(Y_2O_3)_{0.08}$ [30]; CGO, $Ce_{0.8}Gd_{0.2}O_{1.9}$ [31]; LSGM, $La_{0.9}Sr_{0.1}Ga_{0.8}Mg_{0.2}O_{2.85}$ [32]; LAMOX, $La_2Mo_2O_9$ [33]; Si-apatite, $La_{10}(SiO_4)_6O_3$, Ge-apatite, $La_{10}(GeO_4)_6O_3$ [34].

the fluorite structure at temperatures in excess of 2300℃ [23]. Partial substitution of zirconium with a larger dopant ion, typically yttrium, is used to stabilise the fluorite structure at ambient temperatures:

$$Y_2O_3 + 2\,Zr_{Zr}^{\times} + O_O^{\times} \longrightarrow 2\,Y_{Zr}' + V_O^{\bullet\bullet} + 2\,ZrO_2. \tag{1.4}$$

Doping with yttria is also beneficial because the oxide ion vacancies it introduces are crucial to the ionic conductivity of the material. This 'yttria stabilised zirconia' (YSZ), with the general formula $Zr_{1-x}Y_xO_{2-\delta}$, has been widely adopted for use in SOFCs and has a good ionic conductivity of around 3×10^{-2} S cm^{-1} at 800℃, when yttrium is present at around 10% ($x = 0.1$) [4]. The levels of total conductivity for various ceramic fuel cell materials with respect to temperature are shown in Figure 1.6. Scandia-doped zirconia has been shown to yield higher conductivities than YSZ (around 1×10^{-1} S cm^{-1} at 800℃) [29], but, because of availability and cost, YSZ has seen more widespread use [11].

It is tempting to think that introducing a greater number of vacancies into the fluorite structure by increased doping will lead to even higher ionic conductivity, but optimum performance is achieved at around the 10% value quoted above. Atomistic modelling [35–37] and experimental techniques [35, 38] have shown that this observed maximum can be attributed to the clustering of the oxide ion vacancies around the dopant ions, which becomes a significant inhibitor to conduction at higher dopant concentrations. How tightly bound together these clusters are also affects the mobility of the oxide ion vacancies, and this *binding energy* has been found to

be influenced just as much by elastic strain in the lattice as by the electrostatic interaction between the oppositely-charged defects [36]. That is, the size mismatch between the dopant ion and the normal lattice ion has a significant influence upon the local structure of the material and the energies involved in migration processes.

Another fluorite-type material that has been the focus of recent development is ceria (CeO_2), which is often doped with gadolinia and is then generally referred cerium–gadolinium oxide (CGO). The conductivity of CGO is considerably higher than that of YSZ, especially at intermediate temperatures (500–700℃), as shown in Figure 1.6. Unfortunately, however, this conductivity is not purely ionic, with a significant proportion the result of n-type electronic conductivity. In addition, ceria is not as stable as YSZ under reducing atmospheres. Despite these difficulties, the overall performance of cells using a ceria electrolyte is not drastically diminished, apart from reducing the overall cell voltage, and cells have been operated successfully at intermediate temperatures. Ceria and zirconia are mutually soluble, giving rise to the possibility of creating materials with a wide range of compositions that may also contain a wide range of dopants. This may provide access to a hybrid material with the superior qualities of both individual materials.

Other fluorite-based materials that may prove useful in SOFCs include δ-Bi_2O_3 and the pyrochlore structure with the general composition $A_2B_2O_7$, both of which are intrinsically anion deficient. δ-Bi_2O_3 exhibits the highest ionic conductivity of any solid, with conductivities in the order of 1 S cm^{-1} at about 730℃ [39], but the material is not stable at room temperature. In most cases the levels of doping required to stabilise the structure at room temperature are high (15–42 mol% [23]), resulting in relatively poor conductivities.

1.5.2 Perovskite-type Oxides

The perovskite structure, shown in Figure 1.7, has a stoichiometry of ABO_3 and consists of a network of corner-sharing BO_6 octahedra with the A cations occupying the 12-coordinate site in the voids between them. The ternary nature of this system immediately opens many more compositional possibilities than for binary systems such as zirconia, as dopant ions may be incorporated onto either the A or B site. This flexibility permits finer control of the properties of the material.

Oxide ion conductivity was first reported in perovskite materials in 1971 [40], and they have subsequently been widely studied for potential application in intermediate temperature SOFCs. Materials based on lanthanum gallate ($LaGaO_3$) doped with strontium and magnesium, of general formula $La_{1-x}Sr_xGa_{1-y}Mg_yO_{3-\delta}$ and often referred to as LSGM, were first reported in 1994 [41, 42]. These materials show significantly higher conductivities than YSZ, even at intermediate temperatures, as shown in Figure 1.6.

The idealised perovskite structure is cubic in symmetry but, depending on the size ratio of the A and B cations and the temperature of the system, the octahedra

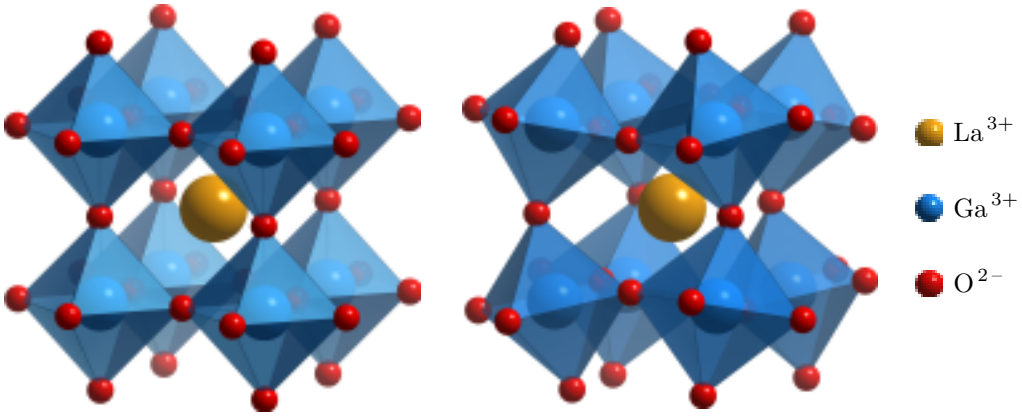

(a) **(b)**

Figure 1.7: The perovskite structure, formula ABO_3, which consists of a network of corner sharing BO_6 octahedra with the A cation located on the 12-coordinate site between them. Part (a) shows the cubic structure, whilst part (b) shows the distorted, orthorhombic structure.

may be tilted, reducing the symmetry of the system as shown in Figure 1.7b. The crystal symmetry has direct implications for oxide ion diffusion. In doped LSGM, for example, the conductivity is found to decrease linearly with the departure from the ideal ratio of ionic radii [29].

Just as in the fluorite-based materials, ionic conduction in perovskite-based materials occurs via a vacancy-hopping-type mechanism. The purpose of doping the material with subvalent ions is again the creation of oxide vacancies to promote this vacancy-hopping:

$$2\,\mathrm{MgO} + 2\,\mathrm{Ga}_{\mathrm{Ga}}^{\times} + \mathrm{O}_{\mathrm{O}}^{\times} \longrightarrow 2\,\mathrm{Mg}_{\mathrm{Ga}}^{\prime} + \mathrm{V}_{\mathrm{O}}^{\bullet\bullet} + \mathrm{Ga}_2\mathrm{O}_3 \tag{1.5}$$

Atomistic simulations [21, 36, 43] predicted that the pathway for oxide ion hops between vacant sites in LSGM would curve away from the B-site cation, as shown in Figure 1.8a. This prediction was subsequently confirmed experimentally by neutron diffraction experiments [44, 45], as shown in Figure 1.8b. The inclusion of a good model for polarisability (see Section 2.4.3) in the atomistic simulation is thought to be critical to modelling the pathway correctly [21].

Several issues have hindered the use of LSGM, such as phase purity, the volatility of gallium at high temperatures and the reactivity of the material with Ni (the typical anode material). Despite these problems, the last of which can been circumvented by the use of a ceria buffer layer between the anode and electrolyte, the LSGM family of materials are the only perovskite-based materials that have thus far proven suitable for use as an SOFC electrolyte [46].

As mentioned in Section 1.2.3, current generation SOFCs use a strontium-doped lanthanum manganite (LSM) perovskite material as the cathode, with the general formula $\mathrm{La}_{1-x}\mathrm{Sr}_x\mathrm{MnO}_3$ ($0.15 \leq x \leq 0.55$) [11, 47]. Lanthanum manganite has

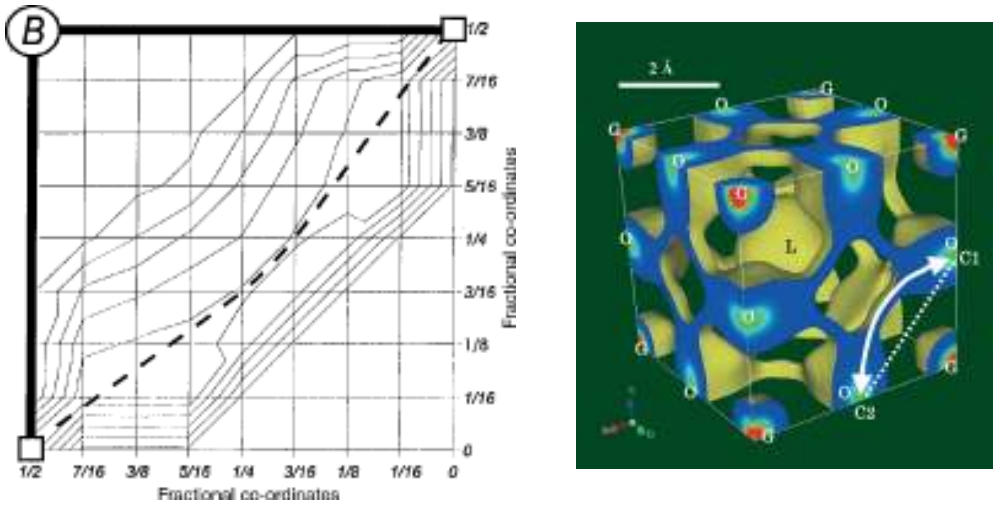

(a) **(b)**

Figure 1.8: The curved migration path for the vacancy-hopping mechanism within the cubic perovskite lattice from both (a) atomistic simulation and (b) neutron diffraction studies. Figure (a), reproduced from [21] shows a contour plot of the potential energy surface for an oxide ion in between two vacant lattice sites (squares) in LaMO$_3$. The heavy dashed line shows the curved minimum energy pathway between the two sites. Figure (b), reproduced from [44], shows the equicontour surface of scattering amplitude from neutron diffraction experiments on $(La_{0.8}Sr_{0.2})(Ga_{0.8}Mg_{0.15}Co_{0.05})O_{2.8}$, in which the curved migration path of the oxide ions is clearly highlighted.

good intrinsic p-type electronic conductivity due to the mixed oxidation state of manganese (Mn^{3+}/Mn^{4+}). Doping with a lower valency cation (like strontium, as above) improves the electronic conductivity of the material by introducing more Mn^{4+} and provides it with a thermal expansion coefficient that better matches YSZ. The material is, however, a very poor oxide ion conductor, meaning that the cathode reactions must take place at the triple phase boundary, where the electrolyte, electrode and gas phase meet.

Improved cathode performance has been attained using doped $LaCoO_3$, which is a mixed ionic–electronic conductor (MIEC) and thus provides improved catalytic activity [14] and a greater surface area for reaction. Doping LSGM with low levels of Co enhances the oxide ion conductivity without introducing electrical conductivity [23, 28]. With such a large range of compositions and structural derivatives, perovskite-based materials are an incredibly important class of compounds for SOFC applications.

1.6 Alternative SOFC Oxide-ion Conductors

As noted, there is considerable interest in developing new SOFC materials, especially for intermediate-temperature operation. This thesis examines three novel materials that accommodate excess oxygen into the lattice and may display interesting and

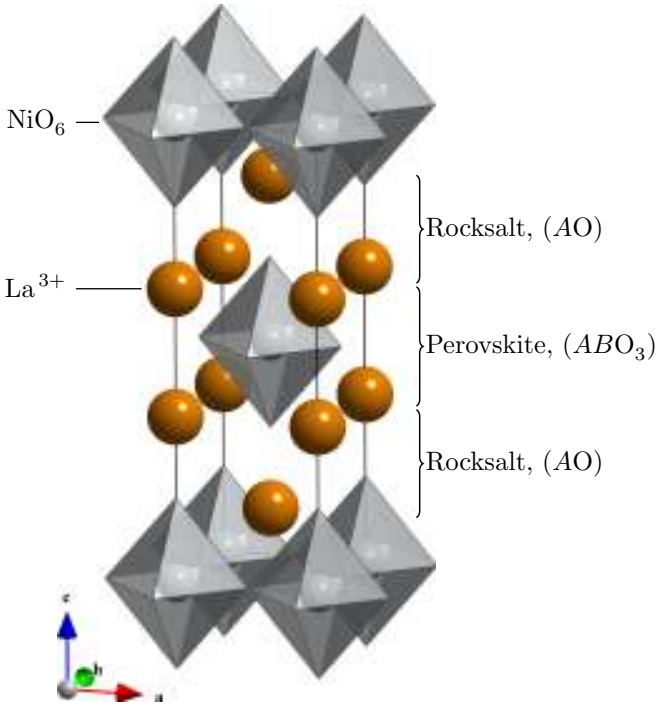

Figure 1.9: Structure of La_2NiO_4, which consists of alternating layers of perovskite- and rocksalt-type material.

useful interstitial migration processes. In the following sections, each material is introduced with a brief summary and an outline of the objectives of our computational studies, which are detailed in later chapters.

1.6.1 Nd_2NiO_4: A Layered Perovskite Derivative

The Ruddlesden–Popper series of compounds, with general formula $AO(ABO_3)_n$, are structurally very closely related to the perovskite materials described in Section 1.5.2. They consist of alternating layers of rocksalt- and perovskite-type material, as shown in Figure 1.9 [48]. The materials were studied intensively because of their structural and electrical similarity to the high-temperature superconducting cuprates [49]. Since the discovery of mixed ionic electronic conductivity in $La_2NiO_{4+\delta}$, however, there has been increased interest in using these materials as SOFC cathode materials [46].

$La_2NiO_{4+\delta}$, $Pr_2NiO_{4+\delta}$ and $Nd_2NiO_{4+\delta}$ are all mixed ionic electronic conductors, and are being investigated for SOFC applications [23]. The oxide ion conduction mechanisms in the lanthanum and praseodymium analogues have been studied in some detail: neutron diffraction data [50] and computational studies [18, 19, 51, 52] both support an interstitialcy-type mechanism. No such computational studies have been performed for the neodymium analogue, however, which accommodates a higher oxygen hyperstoichiometry than its La and Pr counterparts [53]. Further-

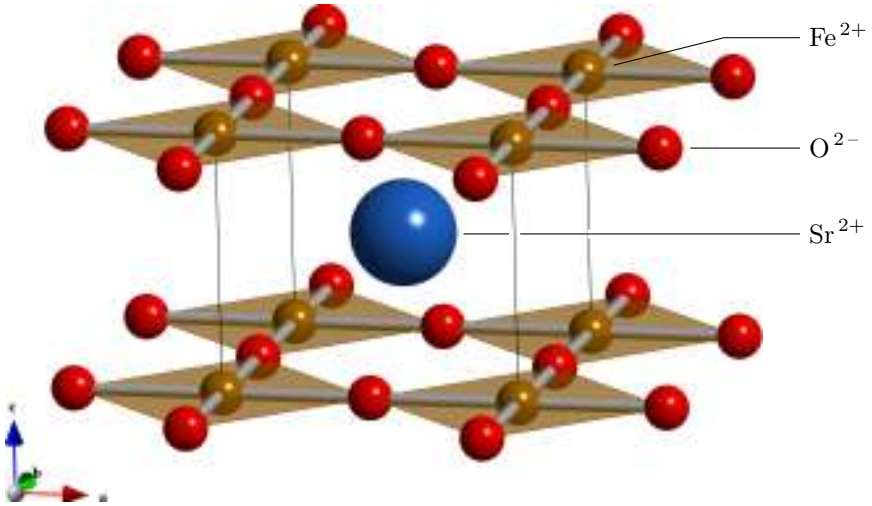

Figure 1.10: Structure of $SrFeO_2$, which consists of 'infinite layers' of corner-sharing square-planar FeO_4 separated by Sr^{2+} ions.

more, a small amount of A-site deficiency in these materials has been shown to increase conductivity [54, 55], which warrants further investigation.

Our study of this material is detailed in Chapter 3. Our aims were to investigate the defect and interstitial migration processes of $Nd_2NiO_{4+\delta}$ and, in addition, to quantify for the first time the effect of A-site deficiency upon diffusion and determine any major differences with cation-stoichiometric compositions.

1.6.2 'Infinite-layered' $SrFeO_2$

$SrFeO_2$ is a recently-discovered material that is also structurally related to the perovskite materials [56]. The material is isostructural with the superconducting 'infinite layer' cuprates, and can be thought of as a perovskite material with a layer of oxide ions removed at $c = 1/2$, as shown in Figure 1.10. The structure is particularly intersting as it contains Fe^{2+} ions in perfectly square-planar coordination.

The $SrFeO_2$ material is formed and undergoes oxidation at relatively low temperatures, which suggests that the oxide ion framework is fairly mobile [57]. The defect behaviour and ionic transport properties of $SrFeO_2$ have not yet been explored. Chapter 4 details our work on the material, the aim of which was to apply both potential-based and density functional simulations to attain, for the first time, detailed information about the intrinsic defect chemistry and possible oxide ion conduction mechanisms of the material.

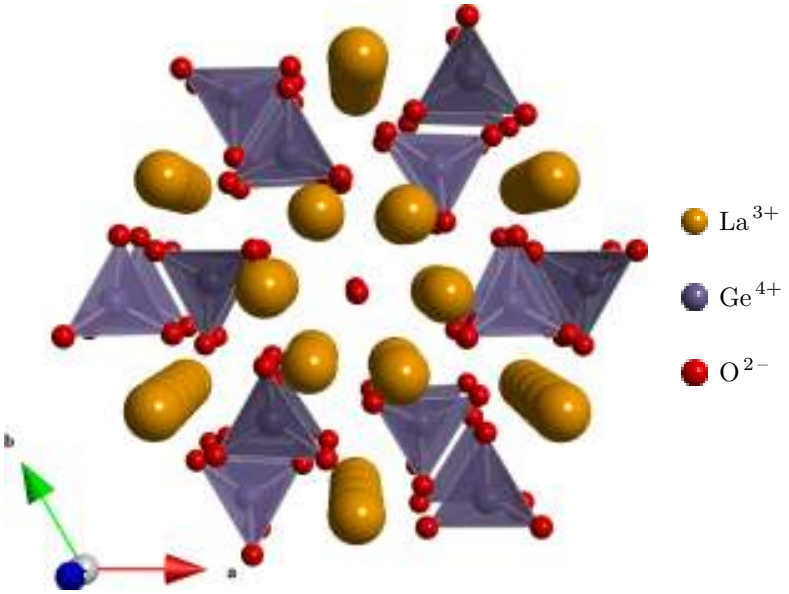

Figure 1.11: The apatite structure viewed down the c axis, which consists of channels of La^{3+} and O^{2-} surrounded by GeO_4 tetrahedra and further La^{3+}.

1.6.3 $La_{9.33}(GeO_4)_6O_2$: An Apatite-structure Material

Apatite materials have a distinctly different structure from the perovskite derivatives discussed so far in this section, as shown in Figure 1.11. The materials have the general formula $M_{10}(XO_4)_6O_{2\pm y}$, where M is a rare-earth or alkaline-earth cation and X is a p-block element such as Si or Ge. The structure is generally hexagonal, and consists of channels of oxide ions and M cations surrounded by XO_4 tetrahedra and further M cations.

Hydroxyapatite biomaterials are naturally found in mammalian bones and tooth enamel [23, 58, 59], and apatite materials have been studied for their applications as bioceramics, waste encapsulation materials and as host structures for rare-earth luminescence properties [14]. Their potential application as SOFC electrolyte materials was first realised by the discovery of fast ion conduction in lanthanide silicates ($Ln_{9.33}(SiO_4)_6O_2$) [60, 61], and subsequently the germanium analogues [62].

The apatite structure is able to accommodate a wider range of dopants on the rare-earth site than most conventional fast ion conductors. The range of available dopants provides a wide array of potential options for improving the properties of the materials towards SOFC applications. In the silicate material, subvalent doping on the Si site with smaller cations, such as Mg^{2+}, has been found to improve conductivity, whilst isovalent doping, particularly with Ti^{4+}, has been found to suppress conductivity considerably [34].

Our understanding of the atomic-level dopant behaviour of Ge-apatite oxide-ion conductors is less complete than for the silicate materials. Understanding the dopant

site selectivity and compensation mechanisms in these complex materials is key to their optimisation for use in SOFCs or ceramic membranes. Our study of this Ge-apatite material is detailed in Chapter 5. The aim of this work was to use atomistic modelling techniques to investigate the site selectivity and compensation mechanisms of a range of D^{+}, D^{2+}, D^{3+} and D^{4+} dopants in the $La_{9.33}(GeO_4)_6O_2$ apatite material.

Chapter 2

Methodology

2.1 Introduction

Computer modelling techniques are now well-established tools in the field of solid-state materials chemistry. Section 1.4 briefly introduced the field of computational chemistry and its applicability to the kinds of research questions that arise in materials chemistry. This chapter focuses on the computational methodology that has been employed in this thesis to tackle such questions, and aims to provide the fundamental details of each of the techniques used. Perhaps more importantly, an understanding of the basic methodology of computational chemistry allows the strengths and limitations of each technique to be appreciated, and the correct emphasis to be placed during the interpretation of results.

The principal techniques used in these studies belong to either the *static lattice* or the *molecular dynamics* family of methods. Static lattice (or energy minimisation) techniques are concerned with finding stable chemical structures, whilst molecular dynamics (MD) is used to simulate the motion of atomic systems. Both of these simulation techniques require a description of the interatomic interactions of the system of interest, which can be provided either in an atomistic (potential-based) manner or derived from the fundamental principles of quantum physics.

These techniques, detailed in the following sections, have been implemented in a variety of well-documented software packages. In this work, static-lattice atomistic calculations were performed using the General Utility Lattice Program (GULP) [63, 64], atomistic molecular dynamics simulations were performed using DL_POLY [65–67] and static-lattice DFT work was carried out using the Vienna Ab-inito Simulation Package (VASP) [68, 69] and CASTEP [70]. Further detail about the programs and performance considerations can be found in Appendix B.

We wish to acknowledge the use of the Chemical Database Service at Daresbury [71].
All figures of static structures were produced using the Visualisation for Electronic

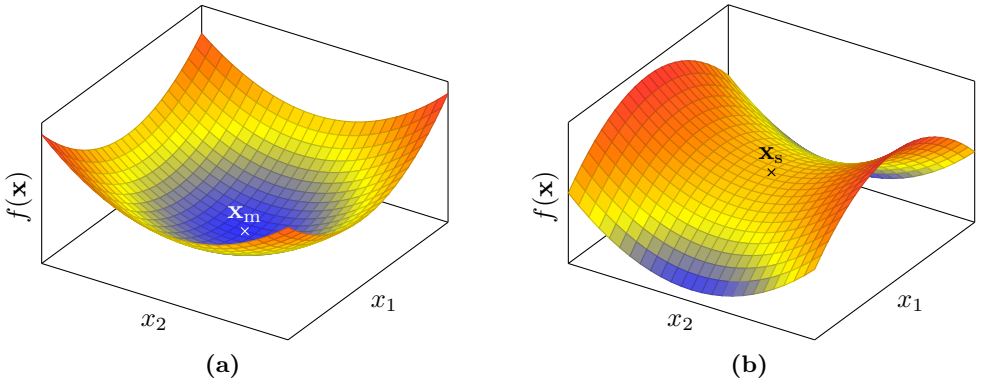

Figure 2.1: Examples of stationary points on a surface. (a) A minimum point $\mathbf{x}_\mathrm{m}$ on a surface with a positive definite Hessian matrix. (b) A saddle point $\mathbf{x}_\mathrm{s}$ on a surface with one negative component in the Hessian matrix.

and STructural Analysis (VESTA) program [72]. Visualisation of MD trajectories was performed using VMD [73]. VMD is developed with NIH support by the Theoretical and Computational Biophysics group at the Beckman Institute, University of Illinois at Urbana-Champaign.

2.2 Energy Minimisation

The potential energy of a chemical system is a function of the coordinates of all N atoms in the system. This function is often referred to as the *potential energy surface*, although the term potential energy *hypersurface* is also used, which alludes more strongly to the multi-dimensional nature of the function. Due to this high dimensionality, visualisation of the entire surface is impracticable. Chemical processes, however, can often be approximated using few key component coordinates and thus can be visualised, which can greatly aid understanding.

The features of the potential energy hypersurface for a particular chemical system provide a great deal of information about that system. Of primary importance are two types of stationary point: the minimum and the saddle point, which represent stable chemical structures and transition states respectively. Examples of both features are shown in Figure 2.1.

A set of three-dimensional Cartesian coordinates can be used to describe the position of each atom, allowing the whole configuration of a system to be described in a vector $\mathbf{x}$ consisting of $3N$ elements. The energy of the system is then some function of these coordinates $U(\mathbf{x})$. The gradient $\mathbf{g}$ of the energy is a vector consisting of the partial

derivatives of the energy function in the direction of each component coordinate:

$$\mathbf{g} = U'(\mathbf{x}) = \begin{bmatrix} \frac{\partial}{\partial x_1} U(\mathbf{x}) \\ \frac{\partial}{\partial x_2} U(\mathbf{x}) \\ \vdots \\ \frac{\partial}{\partial x_{3N}} U(\mathbf{x}) \end{bmatrix}. \tag{2.1}$$

The matrix of second derivatives, which describes the curvature of the surface, is called the *Hessian matrix*, and is defined as

$$H = U''(\mathbf{x}) = \begin{bmatrix} \frac{\partial^2 U}{\partial x_1 \partial x_1} & \frac{\partial^2 U}{\partial x_1 \partial x_2} & \cdots & \frac{\partial^2 U}{\partial x_1 \partial x_{3N}} \\ \frac{\partial^2 U}{\partial x_2 \partial x_1} & \frac{\partial^2 U}{\partial x_2 \partial x_2} & & \frac{\partial^2 U}{\partial x_2 \partial x_{3N}} \\ \vdots & & \ddots & \vdots \\ \frac{\partial^2 U}{\partial x_{3N} \partial x_1} & \frac{\partial^2 U}{\partial x_{3N} \partial x_2} & \cdots & \frac{\partial^2 U}{\partial x_{3N} \partial x_{3N}} \end{bmatrix}. \tag{2.2}$$

Although it is possible to calculate both of these quantities analytically, in practice doing so is not always computationally practical. Atomistic, potential-based techniques (Section 2.4) are generally amenable to such analytical treatment, whilst electronic structure techniques (Sections 2.5 and 2.6) generally require numerical approximation.

At any stationary point, all of the first derivatives of the hypersurface are zero (i.e., the gradient is zero in every direction), and the type of feature is defined by the second derivatives (i.e., the curvature or shape of the surface at that point). At a local minimum, which represents a stable arrangement of the atoms in the system, the second derivative of the energy is positive in all directions[a] and hence any movement away from that point leads to a rise in potential energy. At a saddle point, the second derivative is negative in one direction and positive in all others. The saddle point represents the maximum on the lowest energy path between two stable structures, and is referred to as the transition state. Transitions states are of critical importance in understanding the chemistry of a system because their presence indicates the existence of a viable reaction pathway, and the energy difference between a transition state and its associated reactant species provides the activation barrier to the reaction.

For a given set of atoms there may be many stable arrangements of those atoms (i.e., isomers of an organic compound, or different polymorphs of a crystalline material), each of which corresponds to a different local minimum on the potential energy hypersurface. The *global minimum* is the local minimum of lowest energy for the whole system, and represents the most thermodynamically stable structure.

Because of the complexity of the potential energy function, it is necessary to approximate the local shape of the hypersurface at each step in the minimisation process. The potential energy function $U(\mathbf{x})$ is approximately harmonic (quadratic) at the minimum, and thus its Taylor series can be truncated at the second-derivative term,

[a] More strictly, the Hessian is *positive definite* $\mathbf{x}^T H \mathbf{x} > 0$

about a point $\mathbf{x}_i$:

$$U(\mathbf{x}) = U(\mathbf{x}_i) + (\mathbf{x} - \mathbf{x}_i)U'(\mathbf{x}_i) + (\mathbf{x} - \mathbf{x}_i)^T U''(\mathbf{x}_i)(\mathbf{x} - \mathbf{x}_i)/2!, \tag{2.3}$$

where U' and U'' represent the first and second derivatives of the energy function, which are the gradient vector and Hessian matrix. Thus Equation 2.3 can be rewritten as

$$U(\mathbf{x}) = U(\mathbf{x}_i) + (\mathbf{x} - \mathbf{x}_i)\mathbf{g}_i + \tfrac{1}{2}(\mathbf{x} - \mathbf{x}_i)^T H_i(\mathbf{x} - \mathbf{x}_i).$$

Evidently it is important to be able to find minima on the potential energy surface because of their correspondence to real-world entities. To do this, one of a number of *minimisation algorithms* can be used. These methods all take an initial 'guess' starting structure, and iteratively lower its energy by changing atomic coordinates until a minimum is reached. Different algorithms use different mathematical techniques to achieve this, and each performs differently depending on the relative computational costs of mathematical operations for the system under investigation.

Two types of algorithm will be discussed in the following sections. First-order techniques use information from the first derivative vector in order to achieve optimisation. Second order techniques use additional second-derivative information from the Hessian matrix in order to find a minimum, with the rationale that the extra information will lead to the minimum in fewer iterations.

There are two quantities that will be of use in the discussion of minimisation algorithms. The first is the *error*, which is simply the difference between the current configuration of structural coordinates $\mathbf{x}_i$ and the (unknown) minimum energy configuration $\mathbf{x}_\mathrm{m}$:

$$\mathbf{e}_i = \mathbf{x}_i - \mathbf{x}_\mathrm{m}. \tag{2.4}$$

The second is called the *residual*, which is defined as the error transformed by the Hessian matrix [74]:

$$\mathbf{r}_i = -H\mathbf{e}_i = -U'(\mathbf{x}_i) = -\mathbf{g}_i \tag{2.5}$$

and, more importantly, is a vector pointing in the opposite direction to the gradient. In other words, the residual indicates the direction of steepest descent from point $\mathbf{x}_i$, and describes the forces acting on the system.

2.2.1 Steepest Descent Minimisation

The method of *steepest descent* is the simplest of the first-order minimisation algorithms. From a given configuration $\mathbf{x}_i$ the algorithm generates a point closer to the minimum by moving in the direction of the residual (i.e., directly 'downhill'):

$$\mathbf{x}_{i+1} = \mathbf{x}_i + \alpha_i \mathbf{r}_i. \tag{2.6}$$

What must be determined, however, is *how far* to move in that direction, that is, the size of the scalar α_i must be found.

The size of α_i cannot be determined analytically because the surface has been approximated by the Taylor series shown in Equation 2.3, meaning that the minimum in the search direction is almost certainly not the minimum defined by the harmonic function. Instead a *line search* is used to find the value of α_i that minimises the energy U in the direction of the residual, as illustrated in Figures 2.2a and 2.2b.

By definition, and perhaps intuitively, the gradient of the hypersurface at the minimum of the line search must have no component *in the direction of the line search*. This means that the next step of steepest descent algorithm will be orthogonal to the current search direction (see Figure 2.2c). All these right-angled turns mean that the algorithm can perform rather poorly in some circumstances,[b] taking a rather inefficient route to the minimum. This is because later steps can reintroduce components in the error term that were already minimised out in earlier steps. A better approach would be to use a technique which inherently kept track of where it had already searched.

2.2.2 Conjugate Gradients Minimisation

The *conjugate gradients* minimisation algorithm is part of the *conjugate directions* family of algorithms, and is closely related to the method of steepest descent. The basic premise of the conjugate gradients method is to take a set of orthogonal search directions $\mathbf{d}_0, \mathbf{d}_1, \ldots, \mathbf{d}_n$ and minimise the error in each direction *only once*:

$$\mathbf{x}_{i+1} = \mathbf{x}_i + \alpha_i \mathbf{d}_i. \tag{2.7}$$

After all of the search directions have been minimised, the minimum will have been located. Such a method converges in n steps for a quadratic system of n variables, regardless of the shape of the surface, and the poor performance zig-zagging scenario of the steepest descent method is avoided.

One problem that quickly becomes apparent with the conjugate directions approach, however, is actually finding a set of orthogonal search directions that are of any use. For example, if a set of vectors is chosen that is orthogonal in the Cartesian coordinate space (such as the coordinate axes) then the error must be known in order to compute α_i; that is, it is necessary to have prior knowledge of the answer in order to know how far to move in each search direction!

The solution to this problem is to use a set of search directions that are orthogonal[c]

[b] The best case scenario for all of the algorithms examined here is when the error $\mathbf{e}_i$ is an eigenvector of H, because the point $\mathbf{x}_i$ then lies on an axis of the potential energy surface ellipsoid, and the residual points straight at the minimum, leading to convergence in one step. Actually, if the ellipsoid is quite spherical then convergence is quick regardless of the starting point. In contrast, if the Hessian has a high spectral condition number (meaning the surface forms a narrow trough) the route to the minimum will be very inefficient.

[c] The dot product $\mathbf{a} \cdot \mathbf{b}$ of two vectors $\mathbf{a}$ and $\mathbf{b}$, each with n components, is $\mathbf{a}^T\mathbf{b} = \sum_{i=1}^{n} a_i b_i$. This scalar is related to the angle ϑ between two vectors by $\mathbf{a} \cdot \mathbf{b} = |\mathbf{a}||\mathbf{b}| \cos\vartheta$, so a dot product of zero implies that two vectors are orthogonal.

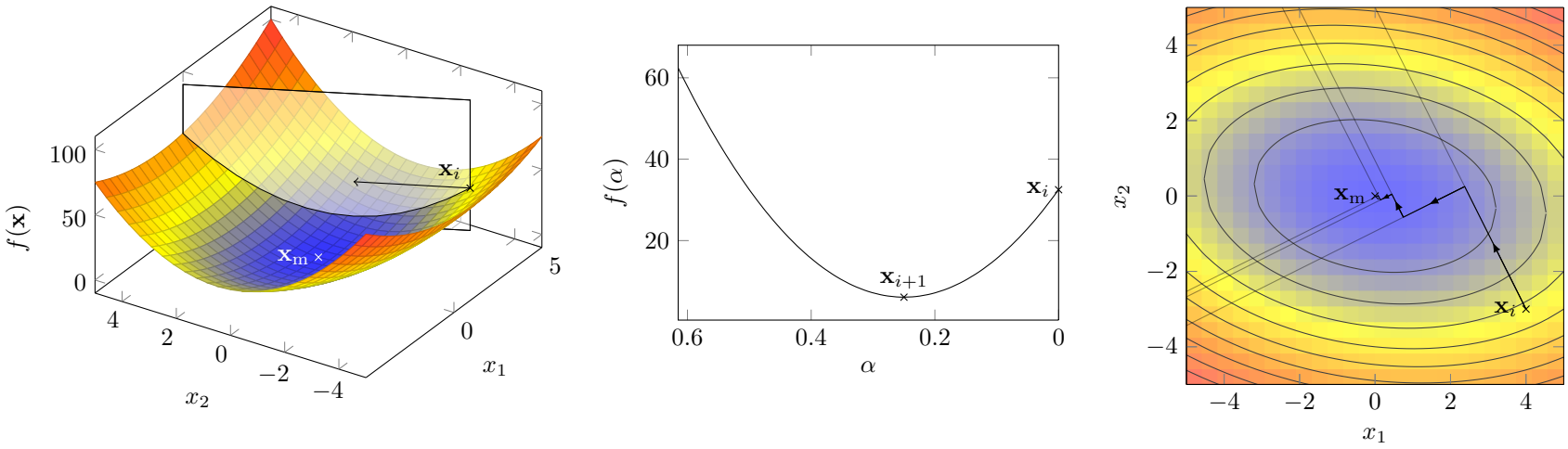

Figure 2.2: Illustration of the steepest descent energy minimisation method. (a) The energy surface along with a vector indicating the direction of steepest descent from the current configuration $\mathbf{x}_i$ in the xy plane (the direction in which the line search will take place). (b) The intersecting plane from part (a), which contains the energy function in the direction of steepest descent and is minimised by a line search, generating a new configuration. (c) The xy plane, and the positions of corresponding iterations of the steepest descent algorithm towards the minimum.

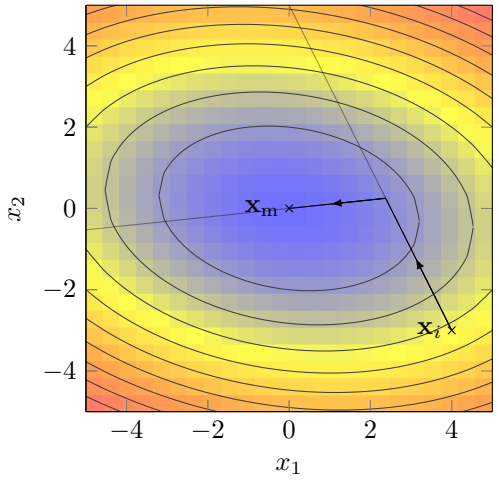

Figure 2.3: Illustration of the conjugate gradients energy minimisation method. Note that the first step is identical to that from the steepest descent method, illustrated in Figure 2.2

in the space defined by the Hessian matrix. Two vectors that have this property are said to be H-orthogonal.[d]

At any given point $\mathbf{x}_{i+1}$ that has been arrived at by a search in a given direction $\mathbf{d}_i$ from point $\mathbf{x}_i$ (as per Equation 2.7), it is possible to find a new, H-orthogonal search vector $\mathbf{d}_{i+1}$ using just the gradients of both points $\mathbf{g}_i$ and $\mathbf{g}_{i+1}$ and the old search vector $\mathbf{d}_i$:

$$\mathbf{d}_{i+1} = -\mathbf{g}_{i+1} + \beta_{i+1}\mathbf{d}_i, \tag{2.8}$$

where

$$\beta_{i+1} = \frac{\mathbf{g}_{i+1} \cdot \mathbf{g}_{i+1}}{\mathbf{g}_i \cdot \mathbf{g}_i}. \tag{2.9}$$

The simplicity of the conjugate gradients algorithm[e] is achieved because information from the previous directions is carried forward into each new search direction. This in turn means that at every step the algorithm finds the best solution within the bounds it has been permitted to explore [74]. Because no previous gradient information exists when choosing an initial search direction, the first step of the conjugate gradients algorithm is exactly the same as that of the steepest descent method, and at each iteration α_i is determined using the same line search technique. An illustration of the resulting search is shown in Figure 2.3.

[d] The idea of H-orthogonal vectors can best be visualised by imagining an elliptical potential well and stretching it until it becomes circular. Any two orthogonal vectors in the circular space are H-orthogonal in the original, unstretched space. Recall that the steepest descent method is more efficient for surfaces that are near-circular in real space.

[e] Whilst the outcome of the conjugate gradients methodology is this simple algorithm, the derivation of the method, and the reasons why it works well, are reasonably complicated. A full and clear explanation has been written by Shewchuk [74].

2.2.3 Newton–Raphson Minimisation

The *Newton–Raphson* method is another widely used iterative approach to finding minima. Unlike the steepest descent and conjugate gradients techniques it is a second-order technique, using both first- and second-derivative information to generate each configuration closer to the minimum. Each new point $\mathbf{x}_{i+1}$ is generated by taking the current point $\mathbf{x}_i$ and subtracting the gradient at that point $\mathbf{g}_i$ transformed by the inverse of the Hessian matrix H_i^{-1}:

$$\mathbf{x}_{i+1} = \mathbf{x}_i - H_i^{-1}\mathbf{g}_i. \tag{2.10}$$

This methodology can be derived quite simply from the Taylor series used to approximate the potential energy surface at a point $\mathbf{x}_i$, outlined in in Equation 2.3:

$$U(\mathbf{x}) = U(\mathbf{x}_i) + (\mathbf{x} - \mathbf{x}_i)\mathbf{g}_i(\mathbf{x}_i) + {}^1\!/_2(\mathbf{x} - \mathbf{x}_i)^T H_i(\mathbf{x}_i)(\mathbf{x} - \mathbf{x}_i).$$

The first derivative of this equation is

$$U'(\mathbf{x}) = \mathbf{g}_i + (\mathbf{x} - \mathbf{x}_i)H_i, \tag{2.11}$$

At the minimum ($\mathbf{x} = \mathbf{x}_\mathrm{m}$) the gradient is zero in all directions so Equation 2.11 can be set to zero, and is then simply rearranged into:

$$\mathbf{x}_\mathrm{m} = \mathbf{x}_i - H_i^{-1}\mathbf{g}_i. \tag{2.12}$$

Thus, if the potential energy surface is truly harmonic, the Newton–Raphson method will find the minimum in just one step *regardless of the number of variables*. This unfortunately is not the case with real systems and hence the process must still be repeated iteratively, as in Equation 2.10.

The harmonic approximation can be very close to the real shape of the potential energy surface, in which case the convergence of this method is still very rapid. At points further from the minimum, however, the Taylor series will not approximate the surface as well, and convergence will be poorer, perhaps considerably so. Thus, as with all minimisation algorithms, it is important to choose a good starting structure for optimisation.

The calculation and inversion of the Hessian matrix are computationally expensive processes and thus, despite the rapid convergence, the Newton–Raphson method is generally only suited to atomistic, potential based calculations due to their simplicity. Even in such models, inverting the Hessian at every optimisation step is time consuming. To improve the performance of the algorithm, it is possible to take advantage of the fact that the Hessian does not change very much between each iteration. GULP employs the Broyden–Fletcher–Goldfarb–Shanno [75] update scheme to update the inverted Hessian matrix between each optimisation step. The full Hessian is then only recalculated and inverted under certain conditions: when the energy of the system has fallen more than a certain amount, if there is a large discrepancy between the directions of the search vector and the gradient vector, if a minimum cannot be found along the search direction, or if a certain number of iterations have been performed without calculating the Hessian [64].

2.2.4 Transition States

The discussion about minimisation has so far focused on locating minima on the potential energy surface. Transition states, however, are also incredibly important structures in terms of the information they can provide about the chemistry of a system, because their presence indicates a reaction pathway between two minima, and their energy with respect to a particular minimum is the energy barrier to the reaction. Transition states (first-order saddle points) are stationary points at which the Hessian has exactly one negative eigenvalue[f] and thus it is useful to have a minimisation algorithm that can find a stationary point with this property.

Simple Constrained Minimisation

The simplest way to find a first-order saddle point is if the gradient at the starting configuration has a component of zero in the direction of negative curvature (i.e., the starting point already lies on the 'spine' of the saddle surface). In such a case, when every other component is minimised in the normal way, the system will remain unchanged in the direction of negative curvature. This method is particularly suitable for the high-symmetry environment in crystal structures, where transition states are likely to be confined to a small number of possible geometries. For an example of how this methodology can be used see Section E.2.

Alternatively, points on the minimum energy path between two minima (the path on which the transition state lies, and is itself a maximum) can be found by displacing an ion or ions of interest and removing one or more degrees of freedom from the minimisation. For example, one can displace a migrating ion between two stable sites, and constrain its position such that it can only relax orthogonal to the migration direction, and not along the path back to its stable site. Thus this can be used to obtain a migration energy profile for an ion and structures very close to the transition state.

The Nudged Elastic Band Technique

The minimum energy path between optimised 'product' and 'reactant' species can also be achieved using the *nudged elastic band* (NEB) technique [76–78]. This method simultaneously minimises several points on the potential energy surface that are linked by a spring force (mimicking an elastic band). The method performs better than the manually constrained minimisation detailed above, and requires less intervention on behalf of the user.

To perform a nudged elastic band calculation, a set of starting structures (*replicas*) are generated at discrete steps directly between the minimised product and reactant

[f] or, equivalently, are structures with exactly one imaginary vibrational frequency.

species by linear interpolation. The points are then connected with an harmonic spring force, which constrains their movement on the surface, ensuring continuity of the path. All the forces, including those due to the connecting springs, are then minimised for each point, resulting in the 'band' resting along the minimum energy path.

The term 'nudging' refers to the force projection used to stop the spring forces interfering with the convergence of the band to the minimum energy path, and to stop the force from the atoms in the system affecting the distribution of points along the band. Only the component of the spring force parallel to the band, and that of the component of the atomic force perpendicular to the band are used in the minimisation of each point.

Rational Function Optimisation

The rational function optimisation method [79] is based on the Newton–Raphson minimisation algorithm, but takes the form of the Hessian into account so that it can move towards points with the desired properties. It is possible to determine if the current point on the potential energy surface has a curvature consistent with the type of stationary point required by examining the eigenvalues of the Hessian matrix (see Section C.2). If the Hessian has an incorrect form at any step of the rational function optimisation process, then it is altered accordingly along with the search direction to move the search towards a transition state [64].

2.3 Molecular Dynamics

The minimisation techniques outlined in the previous sections are often referred to as *static lattice* simulations, because no atomic motions have been taken into account explicitly. Although much valuable information can be gained from such calculations, it is often advantageous to include the effects of thermal energy in a simulation. This is because most properties of chemical systems are affected to some degree by temperature, and most experiments and applications are not undertaken at temperatures near absolute zero. In contrast to the term "static lattice", simulations that incorporate atomic motions are referred to as *molecular dynamics* (MD) simulations, and can generate such information as thermal expansion coefficients, diffusion coefficients and time-averaged structures. The basis of these MD techniques is outlined in the following sections. Detailed information can be found elsewhere [80, 81].

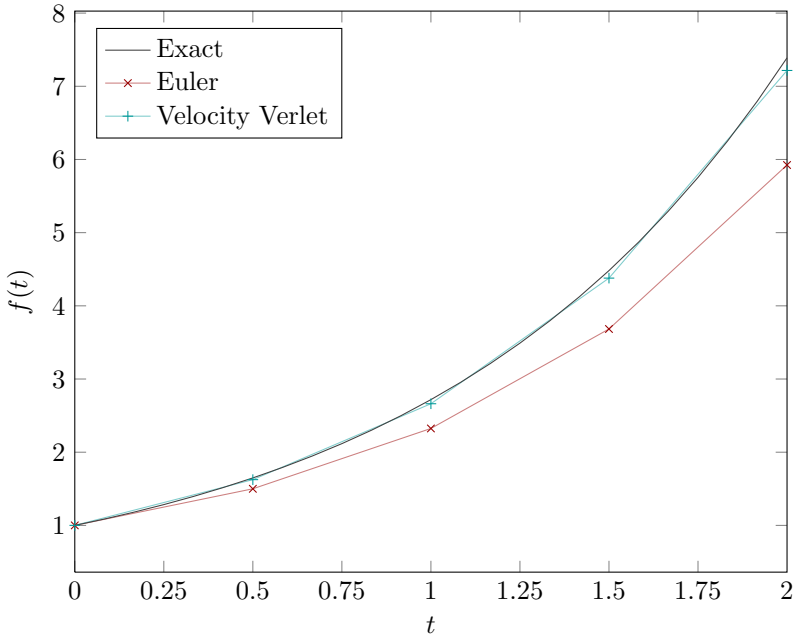

Figure 2.4: Comparison of finite difference integrations of $f(t) = e^t$ generated using the Euler method and the velocity Verlet method with $\Delta t = 0.5$.

2.3.1 Integrating Newton's Equations of Motion

Calculating dynamic properties requires a method of calculating the movement of the atoms (or ions) in a system; that is, it is necessary to integrate Newton's equations of motion for the entire system. This, however, is a coupled many-body problem, and as such cannot be solved analytically. Thus, an iterative numerical *finite difference* method is employed.

In finite difference methods, the current state of the system is used to generate a new state at a very small but non-zero time Δt into the future. It is possible to implement this idea quite simply by taking the current positions $\mathbf{r}(t)$ and velocities $\mathbf{v}(t)$ of the atoms and generating the new positions using

$$\mathbf{r}(t + \Delta t) = \mathbf{r}(t) + \mathbf{v}(t)\Delta t. \tag{2.13}$$

The velocities of the atoms can then be updated in a similar fashion by calculating the acceleration acting upon them:

$$\mathbf{v}(t + \Delta t) = \mathbf{v}(t) + \mathbf{a}(t)\Delta t. \tag{2.14}$$

This is known as Euler integration. Although intuitive, Euler integration very quickly leads to large deviations from the ideal atom trajectories (see Figure 2.4).

Euler integration suffers because it is only a first-order method (i.e., because Equations 2.13 and 2.14 include terms no higher in order than the first derivative). The inclusion of higher-order terms in the integration vastly reduces the error of the

simulation. Such a scheme was devised by Verlet [82], variants of which are widely used in molecular dynamics simulations.

Before detailing the Verlet algorithm, some terms must be defined. The current simulation time t_n is defined as an integer multiple of the *timestep* Δt:

$$t_n = n\Delta t. \tag{2.15}$$

The current atomic positions $\mathbf{r}_n$ are a function of the simulation time

$$\mathbf{r}_n = \mathbf{r}(t_n), \tag{2.16}$$

as are the velocities, accelerations and rates of change of acceleration (jerks), which are $\mathbf{v}_n$, $\mathbf{a}_n$ and $\mathbf{b}_n$ respectively. It should be noted that velocity, acceleration and jerk are the first-, second- and third-derivatives respectively of position with respect to time:

$$\mathbf{v}_n = \dot{\mathbf{r}}_n, \tag{2.17a}$$
$$\mathbf{a}_n = \dot{\mathbf{v}}_n = \ddot{\mathbf{r}}_n, \tag{2.17b}$$
$$\mathbf{b}_n = \dot{\mathbf{a}}_n = \ddot{\mathbf{v}}_n = \dddot{\mathbf{r}}_n; \tag{2.17c}$$

and that, according to Newton's second law, the acceleration of each individual atom is proportional to the force $\mathbf{f}_n$ acting on that atom:

$$\mathbf{a}_n = \mathbf{f}_n/m = \nabla \mathscr{V}_n/m, \tag{2.18}$$

where m is the mass of the atom, $\mathscr{V}$ is the potential of the system and ∇ is the vector differential operator.

The Verlet algorithm can be derived by approximating the trajectory of the atoms as a Taylor series truncated at the third-order term. The general Taylor series approximating a function $f(x)$ around a point p is

$$f(x) = f(p) + \frac{f'(p)}{1!}(x-p) + \frac{f''(p)}{2!}(x-p)^2 + \frac{f'''(p)}{3!}(x-p)^3 + \dots. \tag{2.19}$$

Substituting $f = \mathbf{r}$, $x = t_{n+1}$ and $p = t_n$ into this expression results in an algorithm that will generate the positions of the atoms iteratively:

$$\mathbf{r}_{n+1} = \mathbf{r}_n + \mathbf{v}_n\Delta t + \tfrac{1}{2}\mathbf{a}_n\Delta t^2 + \tfrac{1}{6}\mathbf{b}_n\Delta t^3 \tag{2.20}$$

The third-order nature of this expression provides good accuracy, but $\mathbf{b}_n$ is very hard to compute. Verlet used a neat trick to include the $\mathbf{b}_n$ term implicitly in the trajectory calculation by using information already known.

Derived in the same manner as Equation 2.20, the Taylor series Δt *back* in time is

$$\mathbf{r}_{n-1} = \mathbf{r}_n - \mathbf{v}_n\Delta t + \tfrac{1}{2}\mathbf{a}_n\Delta t^2 - \tfrac{1}{6}\mathbf{b}_n\Delta t^3, \tag{2.21}$$

and the sum of Equations 2.20 and 2.21 yields the Verlet algorithm:

$$\mathbf{r}_{n+1} = 2\mathbf{r}_n - \mathbf{r}_{n-1} + \mathbf{a}_n\Delta t^2 \tag{2.22}$$

The Verlet algorithm not only eliminates the need to calculate the troublesome third derivative term, but also eliminates the velocities. As consequence of this, however, the configuration of atoms from the previous timestep $\mathbf{r}_{n-1}$ must be stored in addition to the current atomic postions. The presence and equal weighting of the $\mathbf{r}_{n+1}$ and $\mathbf{r}_{n-1}$ terms in the Verlet algorithm means that the algorithm is "properly centred", that is, reversible in time [25, 80]. Time-reversibility is an important property of Newton's equations of motion, and simulations that are not time-reversible may exhibit instabilities over long periods of time [83]. Verlet integration is also area-preserving, which is a necessary property if energy is to be conserved during the simulation [25]. The superiority of trajectories generated by the Verlet algorithm compared to those generated using Euler integration is illustrated in Figure 2.4.

Although explicit calculation of the velocity is not necessary to generate atomic trajectories, velocity is still an important quantity to compute. For example, computing the kinetic energy $\mathscr{T}$ is necessary when calculating the total energy of the system $\mathscr{H} = \mathscr{T} + \mathscr{V}$, and scaling of the velocities of the system is used to maintain a desired temperature (see Section 2.3.2). The velocities can be recovered from the Verlet trajectory using

$$\mathbf{v}_n = (\mathbf{r}_{n+1} - \mathbf{r}_{n-1})/2\Delta t, \tag{2.23}$$

but this introduces numerical imprecision and is awkward to implement.

These deficiencies are avoided in a widely-used variant of the Verlet algorithm called the *velocity Verlet* algorithm [84], which is used in this work. As the name suggests, in the velocity Verlet algorithm, the velocities at each timestep are explicitly calculated and are used to generate the next configuration in conjunction with the accelerations:

$$\mathbf{r}_{n+1} = \mathbf{r}_n + \mathbf{v}_n\Delta t + \tfrac{1}{2}\mathbf{a}\Delta t^2, \tag{2.24}$$

$$\mathbf{v}_{n+1} = \mathbf{v}_n + \tfrac{1}{2}\left(\mathbf{a}_n + \mathbf{a}_{n+1}\right)\Delta t. \tag{2.25}$$

It can be shown that the velocity Verlet system of equations is equivalent to the standard Verlet algorithm detailed in Equations 2.22 and 2.23 (see Appendix C.1), thus the two algorithms generate identical atomic trajectories and share identical properties. The only differences between the two algorithms are the storage requirements and implementation.

2.3.2 Controlling Temperature and Pressure

By definition, dynamic simulations change over time, generating a collection of related configurations of atoms. The complete collection of such configurations (states) is referred to in statistical thermodynamics as an *ensemble*. In the type of simulation described above, the states that are generated have the same number of atoms N, simulation cell volume V and total energy E. This collection of states is called the *microcanonical* (or NVE) ensemble. Within the NVE ensemble, the distribution between potential and kinetic energy can vary, but the total energy remains the

same. That is, the Hamiltonian $\mathscr{H}$ for the system, which describes the motion of the atoms, is

$$\mathscr{H} = \mathscr{T} + \mathscr{V}, \tag{2.26}$$

where $\mathscr{T}$ is the kinetic component and $\mathscr{V}$ is the potential component.

Unfortunately, the conditions of the NVE ensemble do not correspond to those of most experiments and applications. More relevant in such situations are the properties of the system as a function of temperature T and possibly pressure P, which correspond to either the *canonical* (or NVT) ensemble or the isobaric-isothermal (or NPT) ensemble. Thus, in order to link the dynamic simulation and empirical data, a method of controlling the temperature and possibly pressure of the system under simulation is vitally important.

Furthermore, control of the system temperature via a mathematical *thermostat* (or pressure via a *barostat*) provides a means to model the dynamic response of a system to changes in temperature and pressure, and allows the study of non-equilibrium systems (in which the total energy is necessarily changing) [85]. More mundanely, such control of equilibrium simulations also provides a mechanism to compensate for the slow accumulation over time of numerical errors in properties such as the total energy [85, 86].

For the purposes of this discussion, the term 'temperature' is a measure of the instantaneous kinetic energy of the system [87], which is directly related to the atomic velocities [86]:

$$T \propto \sum_{i=1}^{N} \tfrac{1}{2} m_i v_i^2. \tag{2.27}$$

Berendsen et al. [85] defined a simple thermostat in which the simulation cell is weakly coupled[g] to a hypothetical external heat bath with a fixed temperature T_0. This is physically equivalent to frequent collisions of the simulated atoms with light particles that form an ideal gas at T_0, and is implemented by scaling the velocity of all the particles in the system by a scaling factor λ. The value of λ is determined such that the rate of change of temperature is proportional to the difference in temperature between the simulation cell and the external bath:

$$\frac{dT(t)}{dt} = \frac{1}{\tau}\left(T_0 - T(t)\right). \tag{2.28}$$

This produces an exponential decay of the system temperature towards the desired temperature over time. The empirical parameter τ, known as the *rise time*, allows the user to control the speed of this decay [88].

At small values of τ the simulation cell and the bath are tightly coupled together, so the fluctuations in the system temperature will be unrealistically small. As $\tau \to \infty$ the effect of the Berendsen thermostat is removed and the simulation is effectively

[g] A *coupling constant* describes the strength of an interaction of two systems. If the coupling constant is much smaller than one, the systems are said to be weakly (or loosely) coupled.

sampling the original *NVE* ensemble. A value of $\tau \approx 0.1$ ps is used for condensed-phase systems [86].

Whilst the Berendsen thermostat is relatively easy to implement and efficiently relaxes the system to the target temperature, it has two major drawbacks. Firstly, the equations are not reversible in time, which is important for the reasons discussed in Section 2.3.1. Secondly, because of the way it affects the atomic motions, it technically does not generate solutions that belong to the canonical ensemble, although the approximation is roughly correct for systems containing many atoms [85].

Nosé [89] used a different approach to control the temperature of the system, which was subsequently refined by Hoover [87] and is now known as the Nosé–Hoover thermostat. Just as in the Berendsen thermostat, the Nosé–Hoover thermostat couples the system to an external heat reservoir. In the Nosé–Hoover thermostat, however, the effect of the heat bath is included as an integral part of the system by including an additional degree of freedom in the Hamiltonian. Thus, the functions defining atomic motion are directly affected. The Nosé–Hoover thermostat produces smooth, deterministic, time-reversible trajectories that belong to the canonical ensemble.

Both the Berendsen and Nosé–Hoover thermostats are readily altered to affect cell volume based on pressure, and as such can be used as barostats.

2.3.3 Data Analysis

Calculating the properties of materials from MD simulations requires careful analysis of the ion trajectories, and calculated values are necessarily derived by averaging a large number of configurations. It is possible to extract information about average structure and the rate of ion migration from MD trajectory data.

The Radial Distribution Function

The *radial distribution function* (RDF) is a useful way of describing the structure of a dynamic system. It is defined as the probability of finding two atoms at a separation r relative to the probability of finding two atoms at that separation in a homogeneous gas of the same density [80]. The RDF quantifies the amount and range of ordering in a material, and can also be generated using experimental diffraction techniques, making it a valuable comparative tool.

The radial distribution function $g(r)$ can be defined as

$$g(r) = \frac{V}{N^2} \left\langle \sum_{i=1}^{N-1} \sum_{j>i}^{N} \delta(r - r_{ij}) \right\rangle, \tag{2.29}$$

where the angle brackets denote the mean value over all configurations, r_{ij} is the distance between atoms i and j, N is the total number of atoms, and δ is a function

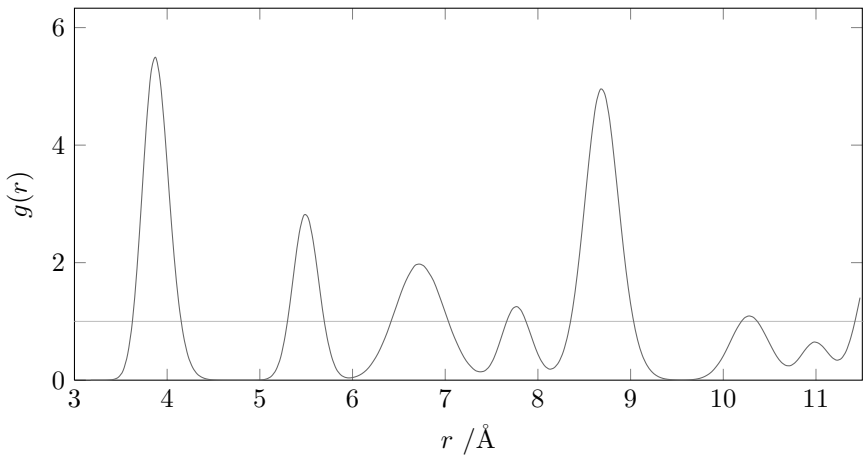

Figure 2.5: Example of a radial distribution function between cations in a crystalline material. Note the presence of well-defined peaks at large ion separations.

that is non-zero only for small input values. Thus, pairs of atoms are only 'counted' when their separation is close to the desired value of r. Lastly, V is the volume of a spherical shell of inner radius r and thickness Δr, given by

$$V \approx 4\pi r^2 \Delta r, \tag{2.30}$$

which accounts for the increasing numbers of atoms in shells of greater radius in an ideal gas.

Practically, the RDF can be generated during a molecular dynamics simulation by compiling a histogram, over discrete intervals of r ('bins'), of the number of pairs of atoms with interatomic separations between r and $r + \Delta r$. At each timestep, the number of pairs of atoms that fall in each of these intervals, which correspond to individual spherical shells as described above, is added on to the existing distribution. At the end of the simulation, the value for each interval of r is then divided by the number of timesteps and scaled according to the volume of the spherical shell.

For crystalline materials, the RDF consists of an infinite series of sharp peaks because the material is ordered infinitely in space. An example of an RDF from a crystalline material is shown in Figure 2.5. The separations and heights of these peaks are characteristic of the crystal structure [81]. The RDF of liquids and gases tends to one (i.e., the same as an ideal gas) at greater separations, with liquids still exhibiting some short-range order. The migrating species in a fast ion conductor is also expected to show short-range ordering and long range disorder.

Generating Time-averaged Densities

For systems in which ion migration occurs, it is very useful to be able to view the trajectory data in such a way that the pathways of ion migration become apparent.

One way to achieve this is to generate a time-averaged atomic density of the simulation cell from ion trajectories. In this approach, the cell is divided into a number of three-dimensional boxes. The positions of the atoms at each timestep are all superimposed and then the number of atoms in each box is counted and the final dataset normalised. This technique produces comparable results to the experimental neutron diffraction maximum entropy method data shown in Figure 1.8b. We have produced a script, which is described in Appendix G.1, to perform this data analysis.

Mean Square Displacement

The *mean square displacement* (MSD) is a measure of how far the atoms in a simulation have moved from their initial locations. As such, examining the MSD with respect to time provides valuable information about the predicted ion transport properties of a material. The MSD is calculated simply by examining the square of the displacement of each atom from its original position at time t, and calculating the mean over all the atoms examined:

$$\mathrm{MSD}(t) = \frac{1}{N}\sum_{i=1}^{N} |\mathbf{r}_i(t) - \mathbf{r}_i(0)|^2, \tag{2.31}$$

where N is the total number of atoms of interest, and $\mathbf{r}_i(0)$ and $\mathbf{r}_i(t)$ are the initial and current positions of atom i respectively. In practice, whilst generating a dataset of MSD versus time, $\mathbf{r}_i(0)$ is often periodically reset as a further averaging step.

The gradient of the MSD plot is directly related to the self-diffusion D^* coefficient for the species of interest via the Einstein relation:

$$\mathrm{MSD}(t) = 2dD^*t, \tag{2.32}$$

where d is the dimensionality of the system. For three-dimensional systems, this means that

$$D^* = \frac{1}{6}\lim_{t\to\infty}\frac{d}{dt}\mathrm{MSD}(t). \tag{2.33}$$

The self-diffusion coefficient can be related to the ionic conductivity σ of a material via the Nernst–Einstein relation:

$$\sigma = \frac{DCq^2}{H_R T k_B}, \tag{2.34}$$

where C is the number of charge carriers per unit volume, q is the carrier charge and k_B is the Boltzmann constant. H_R is the Haven ratio of the material, which is defined as the ratio of the self-diffusion coefficient to a diffusion coefficient based on the ionic conductivity [90], and takes a value of 0.65 for ZrO_2 [91], which is used in this work.

The activation energy barrier for ion migration can also be extracted from a set of MSD data at different temperatures using an Arrhenius ($\ln D$ vs T^{-1}) plot. The Arrhenius equation is

$$k = A\mathrm{e}^{-E_\mathrm{a}/RT}, \tag{2.35}$$

which can be rearranged to the form

$$\ln k = \frac{-E_\mathrm{a}}{RT} + \ln A. \tag{2.36}$$

Letting $y = \ln k \equiv \ln D$ and $x = T^{-1}$,

$$y = \frac{-E_\mathrm{a}}{R}x + \ln A, \tag{2.37}$$

thus the gradient of the Arrhenius plot is proportional to the activation energy and the intercept is equivalent to the pre-exponential factor A of Equation 2.35.

2.4 Atomistic Techniques

The discussions of energy minimisation and molecular dynamics presented above presuppose the existence of mathematically defined atomic interactions that dictate the energy of the system. The remainder of this methodology chapter will focus on the description of these interatomic interactions and the calculation of the energy of the system, which is intimately related.

Two broad approaches to the definition of interatomic interactions exist: *Atomistic* techniques, discussed in this section, employ simple equations based on empirical observations of interatomic interactions, whilst *ab initio* techniques, discussed in Sections 2.5 and 2.6, are based on the fundamental principles of quantum mechanics and are thus more complex.

The choice of technique to employ is determined by the information required from the simulation. The atomistic approach can treat large numbers (tens of thousands) of atoms, and thus is generally used for modelling the relaxation around defects, whose influence can extend tens of ångströms into the lattice. It is also suitable for the large simulation cells and long simulation times required to achieve good statistical data in molecular dynamics simulations. *Ab initio* techniques can provide a much more detailed picture of the chemistry of a material, but are vastly more computationally expensive, and thus are suited to smaller systems. It is important to note that all techniques have advantages and limitations, and all techniques require some degree of approximation in their implementation.

2.4.1 Interatomic Potentials

Atomistic (or *potential-based*) models are constructed from a set of empirically-derived equations that describe the energetics of atomic interactions. These *inter-*

atomic potentials take different forms depending on the type of interaction they are representing, and are parameterised, which allows their precise nature to change based on chemical factors such as atomic radius or strength of bonding.

For crystalline materials, interatomic potentials can be used to calculate the lattice energy of the system. The most general expression for the lattice energy U_{L} is a series expansion of terms pertaining to increasingly large groups of atomic interactions:

$$U_{\mathrm{L}} = \sum_{i=1}^{N}\sum_{j>i}^{N} V_{ij}(r_{ij}) + \sum_{i=1}^{N}\sum_{j>i}^{N}\sum_{k>j}^{N} V_{ijk}(r_{ijk}) + \ldots, \tag{2.38}$$

where N is the total number of ions in the system. Higher order terms have increasingly smaller contributions to the overall energy, and thus are generally not considered. In 1920, Born [92] produced a model based on Equation 2.38 that contained *only* the pairwise term, which he then sub-divided into a term for long-range Coulombic interactions and a term for short-range electron cloud interactions:

$$U_{\mathrm{L}} = \sum_{i=1}^{N}\sum_{j>i}^{N} \frac{q_i q_j}{4\pi\epsilon_0 r_{ij}} + \sum_{i=1}^{N}\sum_{j>i}^{N} \phi_{ij}(r_{ij}). \tag{2.39}$$

A number of different expressions exist for the short-range term ϕ_{ij}, and which of these is most suitable for a particular application depends on the type of bonding interactions that the model is attempting to reproduce.[h] The Buckingham potential [95], which is used in this work, has proved successful in modelling a large and diverse range of polar solids [21, 23]. It provides a simple model of short-range interaction that includes a term for repulsion between electron clouds (Pauli repulsion) and a term expressing dipole–dipole (van der Waals) interactions, and takes the form

$$\phi_{ij}(r_{ij}) = A\exp\left(\frac{-r_{ij}}{\rho_{ij}}\right) - \frac{C_{ij}}{r_{ij}^6}, \tag{2.40}$$

where A, ρ and C are the empirically determined parameters of the model. The electron cloud repulsion is parameterised by A and ρ, where A is representative of the strength of the repulsion, and ρ defines its decay over distance. The C parameter of the second term simply describes the strength of the Van der Waals interactions, and the term is negative because of the attractive nature of the interactions. Figure 2.6 provides a graphical illustration of how the energy for a pair of ions changes with separation when modelled using the Coulomb term from Equation 2.39 and the Buckingham potential.

Ewald Summation

The Coulomb term in the Born model (the first term in Equation 2.39) is problematic to compute for an infinite array of ions because even though the energy of each

[h] For example, the Leonard–Jones potential [93] is used for describing the interactions of neutral atoms, whilst the Morse potential better describes covalently bonded species [94].

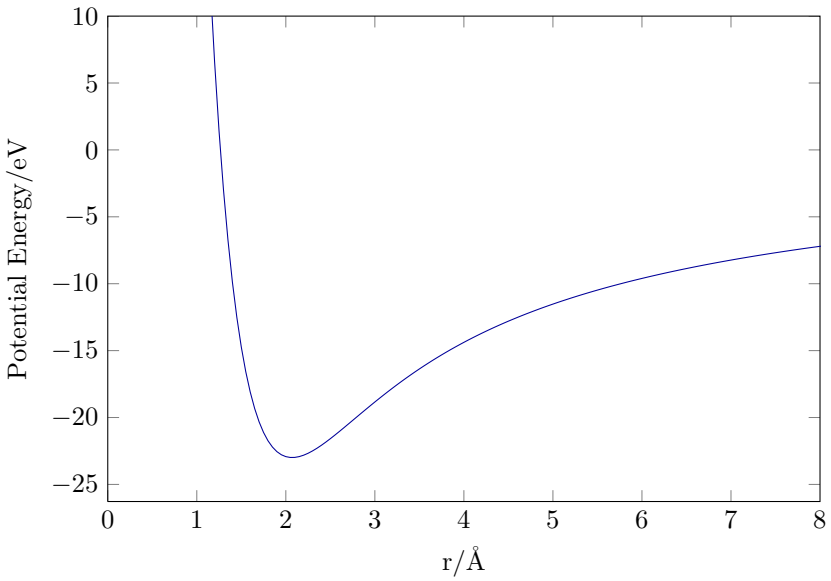

Figure 2.6: Energy as a function of interatomic separation r for the interaction $La^{3+}\cdots O^{2-}$, as defined by the Born model shown in Equation 2.39 and the Buckingham potential from Equation 2.40.

interaction becomes smaller at greater distances like the function r^{-1}, the number of interactions increases at greater distances like $4\pi r^2$, the surface area of a sphere of radius r. This makes the Coulomb term series only *conditionally convergent*[i] and therefore the Coulomb energy ill-defined.

This problem was overcome by Ewald in 1921 [96] by transforming the Coulomb series into the sum of two convergent series using the temporary addition of Gaussian screening charges, as shown in Figure 2.7. The sum of the screened ionic charges can easily be calculated in real space because the potential between them falls off rapidly with distance. The screening charges themselves, because they form a smooth periodic function, can be represented by a rapidly converging Fourier series in reciprocal space.

It is important to note that the use of the Ewald method for calculating the Coulombic term means that it is only possible to perform calculations on cells that are charge neutral and have a dipole moment of zero.

2.4.2 Fitting a Potential to Experimental Data

The parameters for a potential model need to be derived somehow. This can be done either by using *ab initio* calculations [97, 98] or by using experimental data.

[i] A conditionally convergent series does converge to a finite limit, but taking the modulus of each term leads to a divergent series (i.e., the sub-series of either just the positive terms or just the negative terms in the parent series is divergent). Moreover, the limit of a conditionally convergent series is dependent upon the order in which the terms are considered.

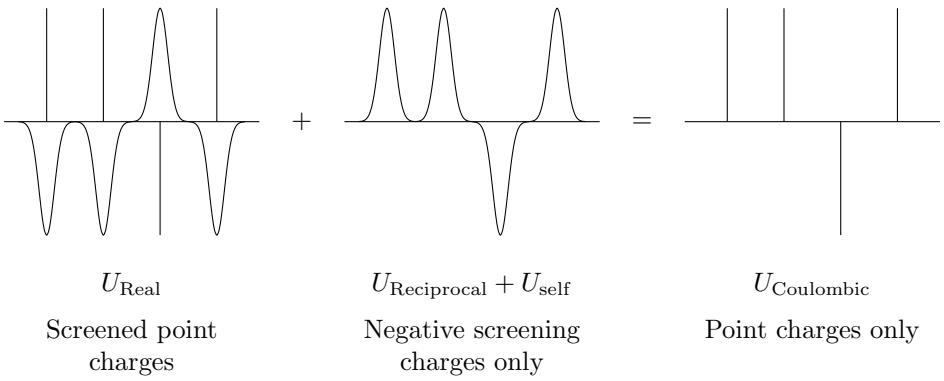

Figure 2.7: Schematic diagram of the series used in the Ewald summation. The total Coulombic contribution to the lattice energy $U_{\text{Coulombic}}$ is calculated from two sums: the U_{Real} sum contains point and diffuse screening charges and is performed in real space; and the $U_{\text{Reciprocal}}$ sum contains terms that counteract the screening charges and is performed in reciprocal space. In these figures the horizontal axis represents spatial distribution and the vertical represents charge.

Fitting is the process by which the potential parameters for an atomistic model are varied to produce a better fit to a set of data. The data could simply be the crystal structure of the material, but it is also desirable to use other physical properties such as elastic constants and phonon frequencies as additional constraints. This additional data has the advantage that it provides second-derivative information about the potential energy surface.

Obviously it is necessary to judge how well the data generated by a given set of potentials fits the data set that is provided. This is measured by calculating the *sum of squares*

$$F = \sum_{n=1}^{N} w_n (f_{n,\text{calc}} - f_{n,\text{obs}})^2, \tag{2.41}$$

where N is the number of observable parameters that we are fitting to, f_n is the value of the observable parameter from both calculation and real observation, and w_n is a weighting factor to adjust for both the magnitude of each piece of data and its reliability. Ideally the sum of squares should be zero (i.e., the simulation exactly reproduces all the experimental observations), but this will not be the case apart from in the most trivial of situations.

In practice, the fitting process involves the minimisation of the sum of squares, and this is achieved in GULP using the Newton–Raphson minimisation algorithm [64]. In normal fitting, the structure and other experimental data remain constant, and the fitting algorithm minimises the force acting upon the atoms. However, in order to determine better structural parameters and the positions of the ion shells (see Section 2.4.3), a modified scheme referred to as *relax fitting* is used. In relax fitting the model is relaxed at each iteration of the process before the sum of squares is assessed and the parameters adjusted accordingly.

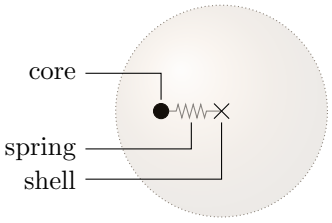

Figure 2.8: The shell model approach of Dick and Overhauser, used for modelling the polarisability of an ion. A shell of charge Y is connected to a core of charge $q_{\text{ion}} - Y$ via an harmonic spring of force constant k.

2.4.3 The Shell Model of Polarisability

It is important that a representation of polarisability is included in the atomistic model. Polarisability not only affects the relaxation of the lattice during the energy minimisation process, but is also fundamental in the calculation of other properties, such as the static and high-frequency dielectric constants, the refractive index and phonon data. The addition of point defects polarises other ions in the lattice, therefore it is very important to include polarisation in the model when examining defect chemistry.

The simplest representation of polarisability is the point polarisable ion model, which relates the dipole μ induced by an electric field E using the polarisability α:

$$\mu = \alpha E. \tag{2.42}$$

Unfortunately this model performs poorly in calculations, because it does not include coupling between the ion's polarisability and the short-range interactions discussed in Section 2.4.1. The *shell model* of Dick and Overhauser [99], illustrated in Figure 2.8, has proven much more successful in modelling polarisation in ionic solids, because it includes this coupling. It is a simple mechanical model in which polarisable atoms are represented as a massless shell of charge Y connected to a massive core of charge $X = q_{\text{ion}} - Y$ by an harmonic spring of force constant k. A dipole is generated by the displacement of the shell relative to the core. In a simulation that includes the shell model, Coulombic interactions between the core and shell are ignored, and the short-range interactions are applied only to the shell of each ion.

The polarisability of an ion is related to the shell charge Y and spring constant k:

$$\alpha = \frac{1}{4\pi\varepsilon_0}\left(\frac{Y^2}{k}\right). \tag{2.43}$$

where ε_0 is the permittivity of free space. Evidently there are no unique values of Y and k that satisfy this relation for a given polarisability, and thus Y and k are treated as parameters of the potential model. The polarisability of an ion is also related to the C parameter of the Buckingham potential via the Slater–Kirkwood formula [100, 101], which must also be taken into consideration when adjusting the potential model.

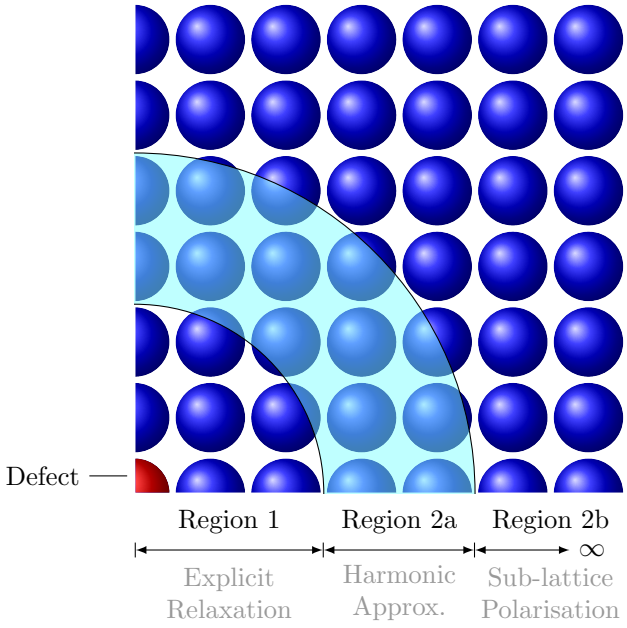

Figure 2.9: The Mott-Littleton two-region approach to defect modelling. Ions close to the defect are modelled explicitly, whilst a more approximate response is modelled at greater separation.

2.4.4 Modelling Defects: The Mott-Littleton Approach

As discussed in Section 1.3 and Appendix A, real crystals are not perfect arrays of ions. Because defects are important in processes such as catalysis, electronic and ionic conductivity, and ion exchange, it is important to be able to model them accurately.

Introducing a defect reduces the symmetry of the system, which can no longer be modelled as an infinite array of identical unit cells. The approach most generally used in these circumstances is the Mott-Littleton [102] 'two region' strategy, shown in Figure 2.9, whereby the crystal is divided into two spherical regions centred around the defect(s).

The inner region (region 1), which feasibly can consist of anything up to 2000 ions, is relaxed explicitly according to the atomistic model outlined above. The outer region (region 2b), where the forces are weaker, extends to infinity and is treated using quasi-continuum methods. The Mott-Littleton approximation assumes that the response of region 2b is a dielectric response to the charge of the defect. Region 2a is used as a buffer between regions 1 and 2b. It contains explicit ions that are relaxed according to forces from either the defect(s) only (the default approximation) or all the atoms in region 1.

When performing energy minimisation using the Mott-Littleton approach it is very important that the region sizes used are at least as big as the cutoff radius for the

Buckingham potential, and that increasing the region size causes no appreciable change in the final energy obtained.

It should be noted that using the Mott-Littleton approach effectively examines the energies of point defects at infinite dilution. If it is desirable to examine high concentrations of defects then it is possible to do so using a supercell. This method is simply an extension of the methodology used for the bulk structure calculations.

2.4.5 Calculating Defect Concentration

The concentration of intrinsic defects in crystals increases dramatically with increasing temperature (see Appendix A). Because of its bearing on material properties, such as oxide ion conduction, it is instructive to estimate this concentration. In-depth discussion of these solid-state chemistry issues can be found elsewhere [103, 104].

The Gibbs free energy of defect formation is the sum of an enthalpic term, computed using the methods discussed previously, and an entropic term:

$$\Delta G = \Delta H - T\Delta S. \tag{2.44}$$

The Boltzmann equation states that

$$\Delta S = k \ln W, \tag{2.45}$$

where k is the Boltzmann constant and W is the number of ways of arranging the point defects in the crystal. To distribute n defects over N permissible sites, W is given by

$$W = \frac{N!}{(N-n)!n!}. \tag{2.46}$$

For multiple point defects on different sites, values of W can be multiplied together. For example, Schottky defects in NaCl require a set of cation vacancies and a set of anion vacancies of the same size, so

$$W_{\text{total}} = W_{\text{c}} W_{\text{a}}, \tag{2.47}$$

and using this in conjunction with Sterling's approximation[j] gives the results

$$\Delta S = 2k \left\{ N \ln N - (N-n) \ln(N-n) - n \ln n \right\}, \tag{2.48}$$

$$\Delta G = n\Delta H - 2kT \left\{ N \ln N - (N-n) \ln(N-n) - n \ln n \right\}. \tag{2.49}$$

The defect concentration will minimise the Gibbs free energy of the system. Thus, we can find an expression for the defect concentration by differentiating Equation 2.49, and setting it equal to zero, which yields

$$n = (N-n) \exp\left(\frac{-\Delta H}{2kT} \right). \tag{2.50}$$

[j] $\ln N! \approx N \ln N - N$

Finally, because $N \gg n$, we have $(N - n) \approx N$, allowing the fraction of defects can be approximated by

$$\frac{n}{N} \approx \exp\left(\frac{-\Delta H}{2kT}\right). \tag{2.51}$$

2.5 Calculation of Electronic Structure: Hartree–Fock Theory

Ab initio, or "from first principles", calculations aim to derive the properties of chemical systems using the basic laws of quantum mechanics without using any empirical data. Ground-state energy, band structure, vibrational spectra and magnetic and optical properties can all be determined readily, via calculation of the electronic structure.

Because *ab initio* techniques treat electrons explicitly, they are ideal for modelling dynamic systems such as those involving the making and breaking of bonds, and those that have complex magnetic properties, where empirical, atomistic methods would fall short. The problem, however, is that these electronic structure calculations are far more computationally expensive than atomistic techniques. This is because of the complex interdependencies (correlation) of the motions of the electrons. Such *many-body* problems become intractable for large numbers of atoms (encountered during, for example, point defect simulations, as discussed above).

Due to the nature of the problem under investigation, it is usually impossible to find analytical solutions to these many-body quantum mechanical problems. Hence such problems must be solved using numerical techniques to provide a close approximation to the real solution. In addition, problems are simplified by applying a number of approximations so that solutions can be generated in a reasonable time on the appropriate computational hardware.

One such framework of approximations is *density functional theory* (DFT), which will be discussed in detail in Section 2.6. This framework builds upon substantial work in the field of quantum mechanics, which will briefly be described in order to provide the relevant context for the later discussion. Work from references [26, 81, 105, 106] has been used substantially throughout these sections.

2.5.1 The Time-Independent Schrödinger Wave Equation

Starting from the known basic physical behaviour of matter waves, such as the de Broglie relations and classical plane-waves, it is possible to produce an equation expressing the behaviour of a system of wave-particles located in an external field. Erwin Schrödinger first did this in 1926 [107], and a good explanation can be found in reference [108].

The time-independent Schrödinger equation for a single particle (e.g., an electron) located in an external field (e.g., that due to the charge from an atomic nucleus) is

$$\mathscr{H}\Psi = E\Psi, \tag{2.52}$$

where $\mathscr{H}$ is called the Hamiltonian operator, E represents the energy of the particle and Ψ is the wavefunction, which describes the particle's motion and contains all the information that it is possible to know about the quantum system.

The Schrödinger equation is an example of a partial differential eigenvalue equation. In this type of equation an operator acts on a function (the eigenfunction) and returns the function multiplied by a scalar (the eigenvalue).[k] In the Schrödinger equation Ψ is the eigenfunction, $\mathscr{H}$ is the operator and E is the resultant eigenvalue.

The Hamiltonian operator for calculating the energy of an electronic system is

$$\mathscr{H} = -\frac{1}{2}\nabla^2 + \mathscr{V}, \tag{2.53}$$

where the first term, sometimes labelled $\mathscr{T}$, is the *kinetic energy* part of the Hamiltonian operator, and $\mathscr{V}$ is the *potential energy* part, which encompasses the behaviour of an external field in which the electron is moving (e.g., that due to the nuclei). ∇^2 is known as the Laplacian operator, and is defined as

$$\nabla^2 = \frac{\partial^2}{\partial x^2} + \frac{\partial^2}{\partial y^2} + \frac{\partial^2}{\partial z^2}. \tag{2.54}$$

For a single nucleus, $\mathscr{V}$ is simply

$$\mathscr{V}_{\mathrm{Ne}} = \frac{Z}{|\mathbf{R} - \mathbf{r}|}, \tag{2.55}$$

which is the classical Coulomb relation where Z is the nuclear charge in atomic units, and $\mathbf{R}$ and $\mathbf{r}$ represent points in space where the nucleus and electron are located respectively. This makes the denominator of the above expression the nucleus–electron separation. The interaction of a single electron with M nuclei can be obtained simply by adding up M terms of the form above with differing values of $\mathbf{R}_i$.

The Schrödinger equation can only be used in the time-independent form, shown in Equation 2.52, if the external field does not change with time. This is a valid assumption for chemical systems because nuclear and electronic motion are decoupled from each other according to the Born–Oppenheimer approximation [109]. That is, any change in the position of the nuclei will have a nearly instantaneous effect upon the electronic wavefunction because the masses of the nuclei are vastly greater than the mass of an electron.

[k] A good example of this type of equation is $\frac{\mathrm{d}}{\mathrm{d}x}(y) = ry$, where r is a constant. An eigenfunction of this equation is $y = e^{rx}$, and r is the corresponding eigenvalue.

2.5.2 Properties of Solutions to the Schrödinger Equation

The wavefunctions that are generated as solutions to the Schrödinger equation have to obey certain constraints. The Born interpretation of the wavefunction states that the wavefunction Ψ at a point $\mathbf{r}$, multiplied by its complex conjugate Ψ^*, is the probability of finding the particle at that point. Since the particle in question must be somewhere, integrating this probability expression over all space (indicated by $d\tau$) must equal 1:

$$\int \Psi^* \Psi \, \mathrm{d}\tau = 1. \tag{2.56}$$

Wavefunctions with this property are said to have been *normalised*. Different solutions to the Schrödinger equation are also usually required to be orthogonal:

$$\int \Psi_m^* \Psi_n \, \mathrm{d}\tau = 0 \quad (m \neq n). \tag{2.57}$$

As an example of orthogonality, consider the product of an s orbital and a p orbital on a single atom, which does not yield an electron density. Wavefunctions that adhere to both the normality and orthogonality constraints are said to be *orthonormal*.

The energy of the system (or, more strictly, the expectated value of the Hamiltonian) can be found by calculating

$$E = \frac{\int \Psi^* \mathscr{H} \Psi \, \mathrm{d}\tau}{\int \Psi^* \Psi \, \mathrm{d}\tau}, \tag{2.58}$$

which is simply obtained by pre-multiplying both sides of the Schrödinger equation (2.52) by the complex conjugate of the wavefunction and integrating over all space. Note that if the wavefunction is normalised then the denominator of this expression will be 1. Properties other than the energy of the electronic system, such as momentum, may be found by using operators other than the Hamiltonian operator.

2.5.3 Polyelectronic and Polynuclear Systems: The Hartree Approximation

The total wavefunction Ψ that describes all the electronic motions in a polyelectronic system can be constructed from single-electron wavefunctions ϕ. However, because the electrons interact with each other Coulombically, the wavefunction of each electron is dependent upon the wavefunctions of all the other electrons; their motions are said to be *correlated*. These complex interrelations create a *many-body* problem, which cannot be solved exactly. This means that the wavefunction must be approximated numerically. One consequence of this is that the wavefunction may be expressed in more than one functional form (see Section 2.5.6), and no form is necessarily more valid or useful than another.

In 1928, Hartree proposed that the problem of solving the Schrödinger equation for a many-particle system could be tackled by considering the electrons as moving in a total field due to the nuclei plus a *static* field created by all the other electrons

in the system [110]. He added an operator to the Hamiltonian that accounts for the electron–electron interaction $\mathscr{V}_{ee}$, in addition to the operators for each single electron's kinetic energy $\mathscr{T}$ and interaction with all the nuclei $\mathscr{V}_{\mathrm{Ne}}$:

$$\begin{aligned}\mathscr{H}(\mathbf{R},\mathbf{r}) &= \mathscr{T}(\mathbf{r}) + \mathscr{V}_{\mathrm{Ne}}(\mathbf{R},\mathbf{r}) + \mathscr{V}_{\mathrm{ee}}(\mathbf{r}) \\ &= \sum_{i=1}^{N} \hat{h}_{\mathrm{core}}(i) + \sum_{i=1}^{N}\sum_{j>i}^{N} \hat{v}_{\mathrm{ee}}(i,j),\end{aligned} \tag{2.59}$$

where N is the number of electrons in the system, and $\mathbf{R}$ and $\mathbf{r}$ represent the sets of *all* the nuclear and electronic coordinates respectively. The first two terms $\mathscr{T}$ and $\mathscr{V}_{\mathrm{Ne}}$ depend only on each electron i individually, and can be combined into a term called the *core Hamiltonian*:

$$\hat{h}_{\mathrm{core}}(i) = -\frac{1}{2}\nabla^2_{\mathbf{r}_i} + \hat{v}_{\mathrm{Ne}}(\mathbf{R},\mathbf{r}_i), \tag{2.60}$$

which can be summed over all the electrons as in Equation 2.59. The two-electron term that was added by Hartree corresponds to the Coulomb electron–electron interaction:

$$\hat{v}_{\mathrm{ee}}(i,j) = \frac{1}{|\mathbf{r}_i - \mathbf{r}_j|}. \tag{2.61}$$

The component of the energy of a polyelectronic system that arises from the single-electron terms of the Hamiltonian can be found by substituting the core Hamiltonian into Equation 2.58, giving

$$E_{\mathrm{single}} = \int \Psi^*(\mathbf{r}) \left(\sum_{i=1}^{N} \hat{h}_{\mathrm{core}}(i) \right) \Psi(\mathbf{r})\, \mathrm{d}\mathbf{r}, \tag{2.62}$$

assuming the total wavefunction is normalised. A similar substitution can be made with the $\hat{v}_{\mathrm{ee}}$ part of the full Hamiltonian to find the energy arising from the two-electron terms. These integrals are important, because they provide the basis for actually calculating the energy of the system from the single-electron wavefunctions.

Slater originally suggested the total wavefunction be constructed as the product of N single-electron wavefunctions ϕ [111]:

$$\Psi(\mathbf{r}) = \prod_{i=1}^{N} \phi_i(\mathbf{r}_i), \tag{2.63}$$

which is known as the *Hartree product*. Substituting the Hartree product for $\Psi(\mathbf{r})$ in Equation 2.62 yields a sum of N multiple-integrals which each involve all N of the single-electron wavefunctions. However, because the single-electron wavefunctions are orthonormal, many terms readily cancel, reducing E_{single} to the sum of N terms of the form

$$E_{ii} = \int \phi_i^*(\mathbf{r}_i) \hat{h}_{\mathrm{core}}(i) \phi_i(\mathbf{r}_i)\, \mathrm{d}\mathbf{r}_i. \tag{2.64}$$

This means that the energy contribution from the core Hamiltonian of each electron depends only on the wavefunction of that electron.

Similar steps can be performed to determine the contribution to the total energy of the system from the two-electron terms of the full Hamiltonian (Equation 2.59). This produces terms depending only on the single-electron wavefunctions of the two electrons involved:

$$J_{ij} = \int \phi_i^*(\mathbf{r}_i)\phi_j^*(\mathbf{r}_j)\hat{v}_{\text{ee}}\phi_i(\mathbf{r}_i)\phi_j(\mathbf{r}_j)\,\mathrm{d}\mathbf{r}_i\mathrm{d}\mathbf{r}_j. \tag{2.65}$$

Each J_{ij} is referred to as a *Coulomb integral*, and these integrals play an important part in density functional theory.

The way in which the system of one-electron wavefunctions has been set up in this section is referred to as the *Hartree Approximation*, and the corresponding energy produced is called the *Hartree Energy*. Note that it does not account for the effects of electron spin, which limits its applicability.

2.5.4 Electron Spin and Slater Determinants

Electron spin complicates the behaviour of polyelectronic systems. The quantum number m_s is used to describe the two states of an electron's quantised spin angular momentum, and can take values of $+1/2$ and $-1/2$. These values are commonly referred to as 'up spin' and 'down spin' respectively.

To incorporate electron spin into solutions to the Schrödinger equation, each single-electron wavefunction is written as the product of a spatial function $\phi(\mathbf{r})$ and one of two spin functions $\alpha(m_s)$ or $\beta(m_s)$. Single-electron wavefunctions of this form are called *spin orbitals*, and are given the symbol $\chi(i)$, where i represents a set of spatial and spin coordinates $\mathbf{x}_i$ of electron i.

Electrons are indistinguishable, thus swapping all the coordinates (including spin) of a pair of electrons should not change the observed electron density. Mathematically, this means that the wavefunction must either remain completely unchanged or only change sign if such a swap occurs. It turns out that for particles with $m_s = \pm 1/2$, like electrons, the wavefunction is required to change sign. This is called the *antisymmetry* principle, and is also known as the Pauli exclusion principle. The well-known consequence of the Pauli exclusion principle is that no two electrons in a system may have the same set of quantum numbers, because if they did, swapping them would not lead to a change in sign of the wavefunction.

The Hartree product discussed previously does not produce a total wavefunction that adheres to the antisymmetry principle. Therefore, for calculations involving spin, the total wavefunction is defined by the linear combination of Hartree products as encapsulated in the *Slater determinant* [112]. The Slater determinant is defined as

$$\Psi = \frac{1}{\sqrt{N!}}\begin{vmatrix} \chi_1(1) & \chi_2(1) & \cdots & \chi_N(1) \\ \chi_1(2) & \chi_2(2) & \cdots & \chi_N(2) \\ \vdots & \vdots & \ddots & \vdots \\ \chi_1(N) & \chi_2(N) & \cdots & \chi_N(N) \end{vmatrix}, \tag{2.66}$$

where the coefficient $1/\sqrt{N!}$ ensures the wavefunction is normalised. Using a determinant is convenient because it necessarily evaluates to zero if any two rows or columns are the same (i.e., if any electron wavefunctions or quantum numbers are the same). Furthermore, swapping any two rows or columns of a determinant leads to a change in sign.

2.5.5 The Hartree–Fock Approximation: the Origins of the Exchange Energy

Expressions for the one- and two-electron contributions to the total energy were outlined previously in Section 2.5.3. Using a Slater determinant to describe the total wavefunction adds some complexity to the derivation of these expressions, and leads to important new contributions to the total energy called the *exchange integrals*.

The complexity arises because of extra terms that appear when expanding the energy expression of Equation 2.62 and the equivalent two-electron expression using a Slater determinant description of the wavefunction. For the single-electron integrals these terms all cancel due to the orthonormality of the wavefunctions, leaving the single-electron integral unchanged:

$$E_{ii} = \int \chi_i^*(i)\hat{h}_{\text{core}}(i)\chi_i(i)\,\mathrm{d}\mathbf{x}_i. \tag{2.67}$$

The two-electron expression, however, is significantly affected by the use of the Slater determinant, yielding cross-multiplication terms that do not cancel. Two classes of term arise. The first are Coulomb integrals that are of a very similar form to those in Equation 2.65:

$$J_{ij} = \iint \chi_i^*(i)\chi_j^*(j)\hat{v}_{\text{ee}}(i,j)\chi_i(i)\chi_j(j)\,\mathrm{d}\mathbf{x}_i\mathrm{d}\mathbf{x}_j. \tag{2.68}$$

The second class of integrals have the form

$$K_{ij} = -\iint \chi_i^*(i)\chi_j^*(j)\hat{v}_{\text{ee}}(i,j)\chi_i(j)\chi_j(i)\,\mathrm{d}\mathbf{x}_i\mathrm{d}\mathbf{x}_j, \tag{2.69}$$

and are called *exchange integrals*. It is worth noting here that in the exchange integral χ_i^* and χ_i are associated with *different* electrons.

Unlike the Coulomb integral, the exchange integral does not have a classical equivalent, and represents a stabilisation of the system due to making the wavefunction antisymmetric. It can be thought of as a manifestation of the Pauli principle, whereby it will be less likely to find an electron near other electrons of the same spin, and the Coulomb energy for pairs of like-spin electrons is reduced due to their increased separation. This effect is known as *Fermi correlation*, *exchange correlation*, or the *exchange interaction*, and the associated reduction in electron density around an

electron of a given spin is called the *exchange hole*, because of its positive nature. It is important to note that Fermi correlation is not a consequence of the charge of the electrons (it is equally applicable to uncharged Fermions), and that it only applies to electrons of like spin.

Representing the wavefunction with a Slater determinant and calculating the energy as shown above is known as the *Hartree–Fock* (HF) or *self-consistent field* (SCF) approximation [113, 114]. It should be noted at this point the the Hartree energy can be obtained from this system simply by discarding all of the exchange terms.

2.5.6 The Hartree–Fock Method

Whilst it is of critical importance to be able to calculate the energy of a chemical system from its wavefunction(s), it is equally important to be able to generate such wavefunctions in the first place. Hartree and Fock [113, 114] devised a means for achieving this within the framework of the Hartree–Fock approximation.

The *variation theorem* (or *variational principle*) states that the ground-state energy calculated from an *approximation* to the true wavefunction will always be greater than the true ground-state energy (i.e., $E_{\mathrm{HF}} > E_0$). Moreover, a good approximation to the ground-state wavefunction will have a lower energy than a bad one, and hence the best approximation attainable will be found at an energy minimum.

A set of initial single-electron molecular orbitals (the 'trial wavefunction') must be generated before the system can be energy-minimised. These orbitals could be constructed from a linear combination of the atomic orbitals, as is taught traditionally in the field of chemistry. However, the atomic orbitals are themselves solutions to the Schrödinger equation for single atoms, and it is much more efficient to describe any wavefunction as a linear combination of more suitable mathematical functions. These functions are called *basis functions*, and a linear combination of such functions is simply

$$\chi_i = \sum_{v=1}^{K} c_{vi}\phi_v, \tag{2.70}$$

where ϕ_v are the basis functions and the coefficients c_{vi} define the contributions of each basis function to the single-electron wavefunction χ_i, and thus fully describe the orbital.

The set of basis functions, called the *basis set*, is chosen depending on the simulation. The size of the basis set is important. At least K basis functions are required to generate K molecular orbitals. Adding extra functions to the basis set facilitates the generation of a better (lower energy) wavefunction, but increases the required computation. There comes a point when increasing the size of the basis set ceases to improve the quality of the wavefunctions, at which point the *Hartree–Fock limit* is said to have been reached. Of particular relevance to calculations of the solid state are the plane wave basis sets, discussed in Section 2.6.4.

In the Hartree–Fock method, each initial wavefunction is energy-minimised in the average field of the all the other electrons. However, because altering the wavefunction of an electron necessarily affects all the other electrons' wavefunctions, the energy minimisation must be repeated until no further change in the wavefunctions occurs. At this point the system is said to be self-consistent, and hence the Hartree–Fock method is also known as the self-consistent field (SCF) method.

Because the Hartree–Fock approximation treats each electron in a fixed average field of the other electrons, it does not account at all for the *instantaneous* Coulomb interaction between two electrons. That is, if an electron is at one particular instant located at $\mathbf{r}$, the likelihood of finding another electron at, or close to, $\mathbf{r}$ at that instant should be greatly reduced due to their Coulomb repulsion. Thus Hartree–Fock predicts the electrons spend more time close to each other than they do in reality, which results in an increase of the Coulomb energy of the system. Neglecting this correlation can produce incorrect results for other properties such as bonding and charge distribution. The difference between the true energy of the system and the Hartree–Fock energy is often referred to as the *correlation energy*, $E_{\text{cor}} = E_0 - E_{\text{HF}}$.

2.6 Calculation of Electronic Structure: Density Functional Theory

The previous section outlined the Hartree–Fock approach to generating approximate solutions to the Schrödinger equation, which can then be used to obtain properties of atomic systems. Each solution Ψ was an N-electron wavefunction constructed from a set of N single-electron wavefunctions χ_i. Density functional theory (DFT) is built on the same quantum-mechanical basis, but directly calculates the overall electron density distribution ρ and corresponding electronic energy of the system, without calculating the wavefunction.

The electron density is

$$\rho(\mathbf{r}) = |\Psi(\mathbf{r}_1, s_1; \ldots; \mathbf{r}_N, s_N)|^2, \tag{2.71}$$

where $\mathbf{r}_i$ and s_i are the position and spin respectively of electron i. The main advantage of this approach is that it dramatically reduces the dimensionality of the problem under consideration, from the $4N$ degrees of freedom of the electrons' spin-orbitals $(\mathbf{r}_1, s_1; \ldots; \mathbf{r}_N, s_N)$ to just the three spatial coordinates $\mathbf{r}$. This speeds up the generation of a solution.

The key mathematical building block of density functional theory is the *functional*. A functional maps a function that exists in a vector space to a scalar, and is denoted by square brackets. For example, a common type of functional, here denoted by Q, is the integral functional:

$$Q[f] = \int f(\mathbf{r})\, \mathrm{d}\mathbf{r}, \tag{2.72}$$

where f is dependent on other well-defined functions (which, for the purposes of this work, will be single-electron basis functions).

The first attempts to describe an atomic system in this way were made by Thomas [115] and Fermi [116] in 1927, very shortly after the derivation of the Schrödinger equation. This initial work made a number of approximations, including the omission of exchange and correlation effects, which made it too inaccurate for practical use. In 1930, Dirac added a local approximation for exchange [117], which is still in use in modern DFT techniques, but a suitably accurate framework for calculating the electron density directly only really emerged in the 1960s with the developments of Hohenberg and Kohn.

2.6.1 The Hohenberg–Kohn Theorems

There are two key theorems that underpin the entirety of modern density functional theory, and both of these were originally formalised and proven by Hohenberg and Kohn in 1964 [118].[l] The first is that the external potential[m] $\mathscr{V}_{\text{ext}}$ is a *unique* functional of the electron density ρ. A corollary of this is that, because $\mathscr{V}_{\text{ext}}$ is part of the Hamiltonian, the full many-particle ground state wavefunction Ψ is also a unique functional of ρ. In other words all the ground-state and excited-state properties of an atomic system are *uniquely* determined by the electron density.

The second theorem defines an energy functional that produces an energy given an electron density:

$$\begin{aligned} E[\rho] &= \int \mathscr{V}_{\text{ext}}(\mathbf{r})\rho(\mathbf{r})\,\mathrm{d}\mathbf{r} + F[\rho] \\ &= \quad E_{\text{Ne}}[\rho] \quad + F[\rho], \end{aligned} \tag{2.73}$$

and, crucially, shows that this functional produces the lowest energy for a given system when provided with the true ground-state electron density. This is another application of the variational principal (see Section 2.5.6), and its application within DFT is merely an extension of how it was applied within the Hartree–Fock methodology: an energy minimisation is performed when trying to find the best approximation to the electron density.

The $F[\rho]$ term in Equation 2.73 is called the *Hohenberg–Kohn functional* and is composed of a kinetic energy term $T[\rho]$ and a term for the energy of interelectronic interactions $E_{\text{ee}}[\rho]$. Its contribution to the total energy is the same as that produced by the kinetic and full electron–electron parts of the Hamiltonian:

$$F[\rho] = T[\rho] + E_{\text{ee}}[\rho] = \int \Psi^*(\mathscr{T} + \mathscr{V}_{\text{ee}})\Psi\,\mathrm{d}\tau. \tag{2.74}$$

[l] The Hohenberg–Kohn theorems were later simplified and generalised by Levy [119].

[m] Within this work, $\mathscr{V}_{\text{ext}}$ is due to the electric field of the nuclei. Therefore if $\mathscr{V}_{\text{ext}}$ is known, the number, type and position of all the nuclei are known.

The electron–electron interaction energy functional $E_{\text{ee}}[\rho]$ includes a classical contribution $J[\rho]$ as well as a non-classical contribution $E_{\text{ncl}}[\rho]$:

$$E_{\text{ee}}[\rho] = J[\rho] + E_{\text{ncl}}[\rho]. \tag{2.75}$$

The classical contribution is of the same form as the Coulomb integral of Hartree–Fock theory

$$J[\rho] = \frac{1}{2}\iint \frac{\rho(\mathbf{r})\rho(\mathbf{r}')}{|\mathbf{r}-\mathbf{r}'|}\mathrm{d}\mathbf{r}\mathrm{d}\mathbf{r}', \tag{2.76}$$

and simply follows from Equation 2.68 in the previous section. The non-classical contribution $E_{\text{ncl}}[\rho]$ contains contributions from exchange and correlation.

It should be noted that $J[\rho]$ is the only contribution to $F[\rho]$ that is known explicitly at this point; $T[\rho]$ and $E_{\text{ncl}}[\rho]$ remain undefined, although it is useful to have separated out their contributions conceptually. One significant advantage of the Hohenberg–Kohn framework over the Hartree–Fock or Thomas–Fermi models is that, if all the functionals are known explicitly, the exact solution to the Schrödinger equation could be found. Whilst this is not possible in practice, it is important that no approximations have been made at this stage.

2.6.2 The Kohn–Sham Equations

Whilst the Hohenberg–Kohn theorems provide a rigorous foundation for the development of density functional methods, they provide no means of actually finding a solution in themselves. The pivotal work in this respect was performed by Kohn and Sham in 1965 [120].

In the previous section, the energy functional that Hohenberg and Kohn provided was split into contributions from the nuclear–electronic interaction (the external potential), the kinetic energy, the classical Coulomb interaction and a non-classical portion that contains contributions from exchange and correlation:

$$E[\rho] = E_{\text{Ne}}[\rho] + T[\rho] + J[\rho] + E_{\text{ncl}}[\rho]. \tag{2.77}$$

Of these, only the nuclear-electronic interaction $E_{\text{Ne}}[\rho]$ and the classical Coulomb interaction $J[\rho]$ were defined explicitly within the Hohenberg–Kohn paper, whilst the forms of the other functionals were left undefined.

There is a complicated relationship between the kinetic energy, which is dependent on electron velocities, and the electron density, which provides only the spatial distribution of the electrons. That is, the kinetic energy is inherently *non-local*. The Thomas–Fermi–Dirac model [115–117] failed to perform well due largely to their representation of kinetic energy entirely as an explicit functional of ρ. Kohn and Sham take a very different approach, and calculate as much of the kinetic energy as possible in an exact manner, but then deal with the remainder approximately.

To do this, they suggest that a reference system of *non-interacting* electrons is used. The reference system is defined such that it has the same electron density as the real solution, and is described by the Hamiltonian

$$\mathscr{H}_{\mathrm{Ref}} = \sum_{i=1}^{N} \left[-\frac{1}{2}\nabla_i^2 + V_{\mathrm{Ref}}(\mathbf{r}_i) \right], \tag{2.78}$$

where V_{Ref} is called the *reference potential*. It is the choice of V_{Ref} that ensures the ground state density for $\mathscr{H}_{\mathrm{Ref}}$ is equal to the true electron density. An important consequence of the densities being equal is that the ground-state energy of this non-interacting system will be *the same as* the ground-state energy of the real interacting system. This comes out of the Hohenberg–Kohn theorems and will be exploited later.

Because the Hamiltonian of the reference system $\mathscr{H}_{\mathrm{Ref}}$ contains no electron–electron interaction terms, the solution to the reference system can be represented exactly by a Slater determinant composed of single-electron functions φ_i. These single-electron functions are named Kohn–Sham orbitals. It may seem counterproductive at this point to have reintroduced wavefunctions into the methodology, since the whole aim of using the electron density directly was to reduce the dimensionality of the system, but, because the reference system consists of non-interacting electrons, each single-particle solution can be found independently:

$$\left[-\frac{1}{2}\nabla_i^2 + V_{\mathrm{Ref}}(\mathbf{r}_i) \right] \varphi_i = \epsilon_i \varphi_i. \tag{2.79}$$

The kinetic energy of this non-interacting system is given *exactly* by

$$T_{\mathrm{Ref}} = -\frac{1}{2} \sum_{i=1}^{N} \int \varphi_i^* \nabla^2 \varphi_i \mathrm{d}\tau. \tag{2.80}$$

This can then be incorporated into the expression for the energy of the real system of fully interacting electrons, which is now defined as

$$E_{\mathrm{KS}}[\rho] = E_{\mathrm{Ne}}[\rho] + T_{\mathrm{Ref}}[\rho] + J[\rho] + E_{\mathrm{xc}}[\rho], \tag{2.81}$$

where the new quantity $E_{\mathrm{xc}}[\rho]$ is called the *exchange-correlation functional*, and not only contains the exchange and correlation energies, but also the remainder of the true kinetic energy (which is also due to correlation effects between the electrons). All the unknown elements of the system have now been grouped into the exchange-correlation functional $E_{\mathrm{xc}}[\rho]$, which is defined as

$$\begin{aligned} E_{\mathrm{xc}}[\rho] &\equiv (T[\rho] - T_{\mathrm{Ref}}[\rho]) + (E_{\mathrm{ee}}[\rho] - J[\rho]) \\ &= \quad T_{\mathrm{Corr}}[\rho] \quad + \quad E_{\mathrm{ncl}}[\rho]. \end{aligned} \tag{2.82}$$

The remaining problem is finding a reference potential V_{Ref} that produces a non-interacting system of electrons with the same electron density as the real system. For both the reference system and the interacting system, $E[\tilde{\rho}] \geq E_0$ for any trial density

$\tilde{\rho}$, where E_0 is the true ground-state energy. Furthermore, $E[\tilde{\rho}]$ is only equal to E_0 when the trial density $\tilde{\rho}$ is the true electron density ρ. Thus, when supplied with the true electron density, the energy of both the reference system and interacting system must be at a minimum, meaning that the functional derivatives $E_{V_{\text{Ref}}}[\tilde{\rho}]$ and $E_{KS}[\tilde{\rho}]$ can be equated, yielding an expression for the reference potential in terms of the interacting system:

$$V_{\text{Ref}}(\mathbf{r}) = V_{\text{ext}}(\mathbf{r}) + \int \frac{\rho(\mathbf{r}')}{|\mathbf{r} - \mathbf{r}'|}\,\mathrm{d}\mathbf{r}' + V_{\text{xc}}(\mathbf{r}), \tag{2.83}$$

where $V_{\text{xc}}(\mathbf{r})$ is the exchange–correlation potential determined by the functional derivative

$$V_{\text{xc}}(\mathbf{r}) = \frac{\delta E_{\text{xc}}}{\delta \rho(\mathbf{r})}. \tag{2.84}$$

Finally, this system can be solved self-consistently by generating an initial set of Kohn–Sham orbitals, which are then used to calculate a reference potential (Equation 2.83), which is subsequently used to minimise the energy of the Kohn–Sham orbitals within the reference system (Equation 2.79), and so on until the system has reached convergence.

2.6.3 Approximate Exchange–Correlation Functionals

All the uncertainty within the framework of Kohn–Sham DFT has been grouped together in the exchange–correlation functional. The accuracy of the whole technique thus depends upon finding a good approximation for this quantity. A wide variety of approaches to this problem have been taken, and there is still debate [121] as to whether the best approximation is achieved semi-empirically (for example, using a functional such as B3LYP) or purely theoretically (this work). Most functional approximations are currently based on the *local density approximation*, of which the *generalised gradient approximation* is an extension.

The Local Density Approximation

The local density approximation (LDA) is based on the uniform (or homogeneous) electron gas model [118]. In this model the electron density is uniform over all space and E_{xc} is known accurately for all densities of electron gas that are of use in computational chemistry. The LDA may be generically written as

$$E_{\text{xc}}^{\text{LDA}}[\rho] = \int \rho(\mathbf{r})\varepsilon_{\text{xc}}[\rho]\,\mathrm{d}\mathbf{r} \tag{2.85}$$

where $\varepsilon_{\text{xc}}[\rho]$ is the exchange–correlation energy density (i.e., the energy per particle of the homogeneous electron gas of density ρ).

The major assumption made in the local density approximation is that at a point $\mathbf{r}$ in the electron distribution of the system of interest, the value of the exchange–correlation functional E_{xc} will be the same as that for the homogeneous electron gas of the same density. That is, in the LDA the exchange–correlation functional is *local*, depending only on the density at $\mathbf{r}$ (i.e., $E_{\mathrm{xc}}[\rho(\mathbf{r})]$), rather than *non-local*, where it would depend on both the local density and the density elsewhere (i.e, $E_{\mathrm{xc}}[\rho(\mathbf{r}), \rho(\mathbf{r}')]$). This means that the LDA should function poorly for chemical systems because of their variation in density.

Kohn and Sham applied the LDA to limiting cases in their original paper [120], but initially thought it to be too approximate for any practical use. Subsequent calculations describing molecules using the LDA, however, produced surprisingly good results.

The $\varepsilon_{\mathrm{xc}}$ term can be broken up into exchange and correlation terms individually, of which correlation is smaller but more complicated to compute. The exchange part ε_{x} takes the original form proposed by Dirac [117] (see the introduction to Section 2.6). In current LDA functionals, the correlation part ε_{c} is fit to data from Ceperley and Alder [122], who performed high-precision quantum Monte Carlo calculations of the homogeneous electron gas at different densities. Two such fits, with different functional forms, are proposed by Perdew and Zunger [123] and Vosko et al. [124].

The local density approximation hinges on the assumption that the exchange–correlation potential depends only on the local value of ρ. However, because correlation is inherently non-local, this assumption can lead to a number of errors, especially when the density is rapidly changing in space [26]. Particularly, binding energies are overestimated, which can lead to shorter bond lengths and reduced system volumes; the band-gap in semiconductors is often smaller than the measured value; and groundstate electronic structure can be predicted incorrectly (for example, the LDA fails to reproduce the groundstate structure of iron correctly) [26, 81, 105].

The LDA does generally achieve good equilibrium geometries, harmonic vibrational frequencies and charge moments, however, and hence has seen widespread use. The technique is successful not so much because the electron gas model is good, but because the approximation obeys most of the constraints of a real system.

Generalised Gradient Approximations

To improve upon the local density approximation, it is obviously necessary to include some mechanism to account for the inhomogeneity of chemical systems. The simplest way to achieve this is to incorporate the gradient of density into the expression for the exchange–correlation functional, yielding the generalised gradient approximation (GGA):

$$E_{\mathrm{xc}}^{\mathrm{GGA}}[\rho] = \int \rho(\mathbf{r})\varepsilon_{xc}(\rho, |\nabla\rho|)d\mathbf{r}. \tag{2.86}$$

Practically, the generalised gradient approximation is achieved by applying a correction to the LDA exchange–correlation functional that is dependent only on the (reduced) density gradient. For the correction to the exchange part, Becke [125] proposed a function with a single empirical parameter which is fitted to experimental data for the rare gas atoms. This form is used in the exchange–correlation functional of Perdew and Wang (PW91) [126], trialled in this work, but has been modified to remove the dependence on the empirical parameter.

An alternative approach to correcting the exchange functional is to use a rational function in which all the coefficients are determined computationally. Such an approach is used by Perdew, Burke and Ernzerhof in the so-called PBE functional [127], which was used in this work.

The correlation functionals have even more complicated forms than the exchange parts. Furthermore, they begin to stray away from direct relation to a physical basis. It should be noted that whilst GGA functionals attempt to account for a changing density, they are still local in the sense that they depend only on the properties of the density at $\mathbf{r}$. GGA functionals tend to perform better than LDA functionals for the transition metal series, but improvements are not consistent, with some calculations leading to poorer results. For example, like the LDA, the GGA still generally gives an underestimation of bandgap energies.

LDA+U (GGA+U): The Hubbard Coefficient

Strongly correlated systems of electrons, such as those involving atoms with partially filled d and f shells, are particularly sensitive to the chosen description of correlation. When applying the LDA to transition metal compounds, partially filled d bands with metallic electronic structure and itinerant d electrons are obtained. This is in stark contrast to the experimental observations of late-transition-metal oxides and rare-earth compounds, which have localised d and f electrons and well separated occupied and unoccupied d electron bands [128].

In the LDA+U (or GGA+U) technique [129, 130], the exchange correlation functional is altered to account for this strong on-site correlation of the d and f electrons. The s and p electrons are treated with the normal LDA, whilst the d and f electrons are separated out and their Coulomb interaction is treated in a mean-field, Hartree–Fock-type way instead. The strength of this correction is controlled by the parameter U (sometimes referred to as the *Hubbard coefficient*), which is the resulting energy gap between the occupied and unoccupied bands.

The exchange J can be dealt with in a similar manner and only the effective value of U, given by $U_{\text{eff}} = U - J$, appears in the LDA+U formulation. The value of U can be calculated in an *ab initio* manner, and thus this technique is not technically semi-empirical. However, the value of U_{eff} is often tuned to the bandgap of a material in a semi-empirical manner in the literature.

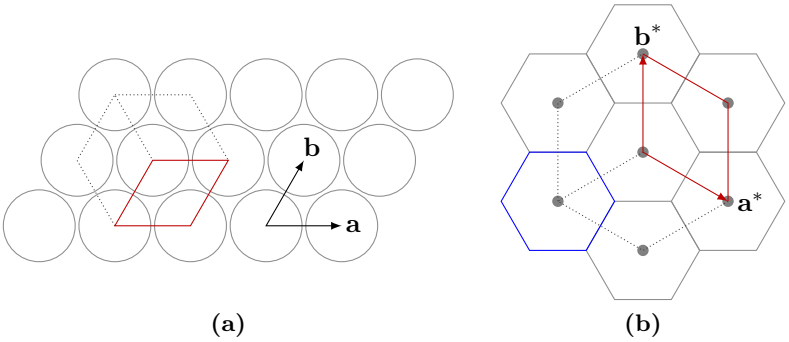

Figure 2.10: Illustration of the relationship between real space and reciprocal space using a two-dimensional hexagonal lattice. Figure (a) shows the real-space lattice of atoms (grey circles), overlaid with the unit cell (in red) and lattice vectors **a** and **b**. Figure (b) shows the corresponding reciprocal lattice points (grey dots), the reciprocal unit cell and unit cell vectors $\mathbf{a}^*$ and $\mathbf{b}^*$ (in red) and the first Brillouin zone (in blue).

2.6.4 Using DFT with Periodic Boundary Conditions

The Reciprocal Lattice

The reciprocal lattice is a representation of the crystal lattice defined in reciprocal space, which is also referred to as **k**-space and is generated from the real-space lattice by a Fourier transform. The relationship between the real-space lattice vectors (**a**, **b** and **c**) and the **k**-space lattice vectors ($\mathbf{a}^*$, $\mathbf{b}^*$ and $\mathbf{c}^*$) is

$$\mathbf{a}^* = 2\pi\frac{\mathbf{b}\times\mathbf{c}}{\mathbf{a}\cdot\mathbf{b}\times\mathbf{c}}; \quad \mathbf{b}^* = 2\pi\frac{\mathbf{c}\times\mathbf{a}}{\mathbf{b}\cdot\mathbf{c}\times\mathbf{a}}; \quad \mathbf{c}^* = 2\pi\frac{\mathbf{a}\times\mathbf{b}}{\mathbf{c}\cdot\mathbf{a}\times\mathbf{b}}; \tag{2.87}$$

and is illustrated in Figure 2.10.

The infinite reciprocal lattice can be constructed from primitive cells in exactly the same way as the real-space lattice. In reciprocal space, this primitive cell is called the *first Brillouin Zone*, and is of central importance to the description of periodic systems because the wavefunction can be completely described within this volume.

Bloch's Theorem and Plane-wave Basis Sets

An infinite solid presents two problems in the solution of Schrödinger's equation. Firstly, the wavefunctions of an infinite number of electrons must be determined. Secondly, the wavefunction for each of these electrons spreads across the entire lattice, meaning that the basis set needed to describe it is also infinite [131]. These problems are overcome by utilising the periodicity of the crystal.

Bloch's theorem states that the wavefunction of an electron i in a periodic potential may be written as the product of a wave-like term and a term that has the same

periodicity as the unit cell:

$$\psi_i(\mathbf{r}) = e^{i\mathbf{k}\cdot\mathbf{r}} f_i(\mathbf{r}), \tag{2.88}$$

where $\mathbf{k}$ is the wave vector, which lies within the first Brillouin zone and determines the direction and frequency of the wave-like term.

The cell-periodic part of the wavefunction can be constructed from a basis set of discrete plane waves $e^{i\mathbf{G}\cdot\mathbf{r}}$, whose wave vectors $\mathbf{G}$ are the set of all possible reciprocal lattice vectors (translations to identical lattice points):

$$f_i(\mathbf{r}) = \sum_{\mathbf{G}} c_{i,\mathbf{G}} e^{i\mathbf{G}\cdot\mathbf{r}}. \tag{2.89}$$

The wavefunction of each electron can then be written as the sum of plane waves

$$\psi_i(\mathbf{r}) = \sum_{\mathbf{G}} c_{i,\mathbf{k}+\mathbf{G}} e^{i(\mathbf{k}+\mathbf{G})\cdot\mathbf{r}}, \tag{2.90}$$

where the coefficients $c_{i,\mathbf{k}+\mathbf{G}}$ define the solution.

The set of reciprocal lattice vectors, and hence the size of the basis set, can be limited because plane waves with higher $|\mathbf{G}|$ will have a correspondingly higher kinetic energy and will contribute less to the wavefunction. Above some limit, the 'cutoff' energy, their effect will be negligible. Likewise, if the wavefunction ψ is assumed to be a continuous function of $\mathbf{k}$, then ψ will not vary much with small variations in $\mathbf{k}$, and the system can be sampled discretely at a finite number of $\mathbf{k}$-points, eliminating the need to consider an infinite number of electrons [131, 132].

The selection of $\mathbf{k}$-points is crucial for integrating across the first Brillouin zone and obtaining a good representation of the band-structure and density-of-states of the material. The selection scheme of Monkhorst and Pack [133] uses an evenly spaced grid of $\mathbf{k}$-points, chosen such that many of the points are related by symmetry. This further reduces the number of $\mathbf{k}$-points that must be considered, because the wavefunction (or density) needs only to be calculated at each unique $\mathbf{k}$-point, and can then be related to the others by symmetry. An example of a Monkhorst–Pack grid for a hexagonal reciprocal-space lattice is shown in Figure 2.11. The *irreducible Brillouin zone*, which contains all the unique $\mathbf{k}$-points, is highlighted.

Pseudopotentials

The potential, and thus the electron wavefunctions, vary rapidly near the nuclei. Representing this fine spatial detail would require a very large number of plane waves, making calculations extremely slow. The core electrons, however, tend to remain relatively unaffected by changes in the atomic environment, and thus can be regarded as essentially fixed. Therefore the core states can be removed from the system and the core potential replaced by a much smoother *pseudopotential*, whose wavefunction ψ_{pseudo} is the same as the all-electron valence wavefunction ψ_V outside a certain cut-off radius r_c (see Figure 2.12). This removes the rapid oscillation of the

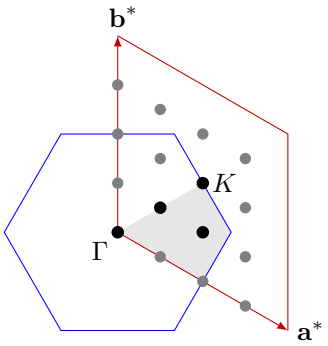

Figure 2.11: Example of a Monkhorst–Pack **k**-point grid for a hexagonal reciprocal-space lattice. The irreducible Brillouin zone is filled in grey, and irreducible **k**-points are shown in black. The Γ and K points are named because of their particularly high symmetry.

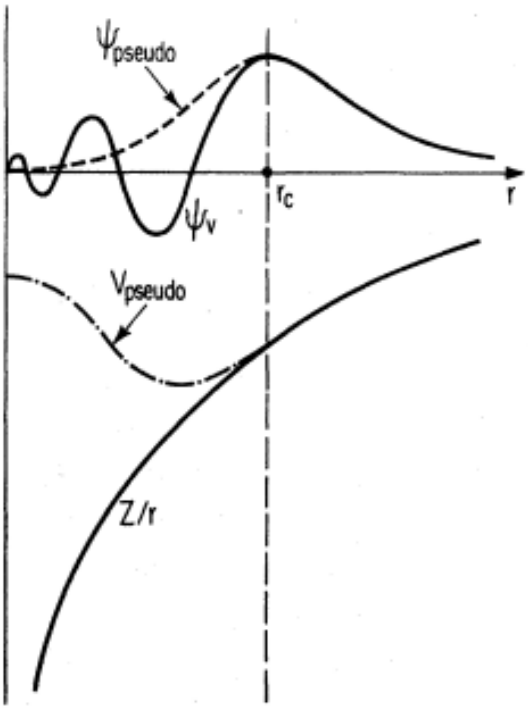

Figure 2.12: Schematic illustration of a pseudopotential V_{pseudo} used to produce a smooth pseudowavefunction ψ_{pseudo}, which can be represented using a smaller basis set. Reproduced from [131].

valence orbitals near the nucleus and expedites the generation of a solution, with the obvious caveat that the generated wavefunction is only representative of the valence region.

Pseudopotentials are not unique, and the form of the pseudopotential can be chosen to simplify computation. Although they can be defined empirically, the most accurate and transferable pseudopotentials are generated using *ab inito* calculations. The 'softness' of a pseudopotential is a measure of both its smoothness and how large the cutoff radius is. Smoother pseudopotentials require fewer basis functions, but large cut-off radii provide a poorer description of the atom and make the pseudopotential less transferable.

Pseudopotentials that produce orthonormal pseudowavefunctions are referred to as 'norm-conserving'. Norm-conserving pseudopotentials are more accurate and transferable, and simplify the application of the pseudopotential concept, because the solutions automatically reproduce the valence properties of the atom.

Ultrasoft pseudopotentials achieve both a higher level of smoothness and larger cut-off radii by redefining the pseudopotential problem in terms of a very smooth pseudopotential, which is *not* norm-conserving and has a large cut-off radius, and an auxiliary function around each ion core, which represents the rapidly varying core density. Detailed information regarding pseudopotential methods can be found elsewhere [26, 134].

The *projector augmented wave* (PAW) method [135], used in this work, is similar to the ultrasoft pseudopotentials in that it uses localised auxiliary functions. The important distinction is that the PAW approach treats the full all-electron wavefunction. Using the PAW method, all the integrals are composed of smooth functions that extend in space, plus localised contributions that are evaluated by radial integration over 'muffin-tin' spheres. The term 'projector' refers to mathematical operations that are used in the transformation of the smooth pseudowavefunction back to the real wavefunction.

Chapter 3

Defect and Oxide-ion Transport Properties of Nd_2NiO_4-based Materials

3.1 Background

3.1.1 Ruddlesden–Popper-structured Nickelates

The Ruddlesden–Popper series of oxide compounds have the general formula $AO(ABO_3)_n$ and consist of layers of perovskite-type material separated by single layers of material with the rocksalt structure [48]. The A cation is generally an alkaline earth or rare earth metal and the B cation is generally a transition metal [49]. The value of n corresponds to the thickness of the perovskite-type layer, and the first-order structure ($n = 1$), which is often referred to as the K_2NiF_4 structure, is illustrated in Figure 3.1. The first-order structure is the focus of this study and contains nine-coordinate A cations, compared to the twelve ion coordination in the perovskite structure.

The first-order Ruddlesden–Popper phases Ln_2NiO_4 (Ln = La, Pr, Nd) and various derivatives were initially studied intensively because of the similarity of their structural and electronic properties to the high-temperature superconducting cuprate $La_{1-x}Sr_xCuO_4$ [49]. Since the discovery of mixed ionic/electronic conductivity in $La_2NiO_{4+\delta}$, however, there has been increased interest in using these materials as cathode materials for solid oxide fuel cells (SOFCs) [46] and in other electrochemical devices. In general, the materials also exhibit suitable thermal expansion coefficients for SOFC applications and have good electrocatalytic activity towards oxygen reduction [136].

In the ideal case, the lattice parameters of the constituent rocksalt and perovskite

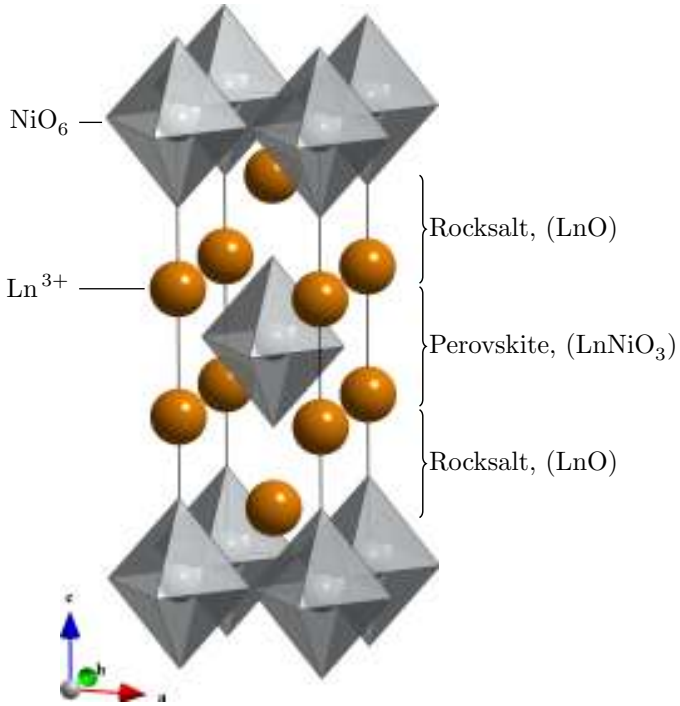

Figure 3.1: Ideal high-temperature structure of Ln_2NiO_4 (Ln = La, Pr, Nd), which has the tetragonal $I4/mmm$ space group and consists of alternating layers of perovskite- and rocksalt-type structures.

materials exactly match, producing the structure shown in Figure 3.1. In most cases, however, the mismatch between the lattice parameters gives rise to a strain between the layers in Ln_2NiO_4 that is minimised by the expansion of the rocksalt layer and a possible contraction of the perovskite layer through tilting of the NiO_6 octahedra [137]. The resulting large free volume in the rocksalt layer can easily accommodate excess oxygen, which reduces the strain and stabilises the structure [49, 54, 55], and hence all the Ln_2NiO_4 materials can be oxidised. The charge of the excess oxide ions is compensated by the oxidation of some of the Ni^{2+} ions to Ni^{3+}, which reduces the charge separation between the rocksalt and perovskite layers [49, 137], further stabilising the oxygen excess material. The mixed oxidation state of the nickel gives rise to the electronic conductivity of the material [136]. As a result of these factors, the phase behaviour of the material is complicated, and will be discussed separately in the next section.

The excess oxygen in $Ln_2NiO_{4+\delta}$ resides on a tetragonally-coordinated interstitial site, ideally located at (0, 1/2, 1/4), as shown in Figure 3.2 [136–139]. Due to the aforementioned structural complexities, however, the actual position of the oxide ion is particular to the material under investigation. For example, using neutron diffraction techniques Toyosumi et al. [140] find cavities in $Nd_2NiO_{4+\delta}$ at the equivalent of (0, 1/2, 0.194), within which excess oxygen may be accommodated. Atomistic simulations of the La and Pr analogues exhibit a similar range of positions for the interstitial oxide ions [19, 137, 141]. Detailed single crystal neutron diffraction

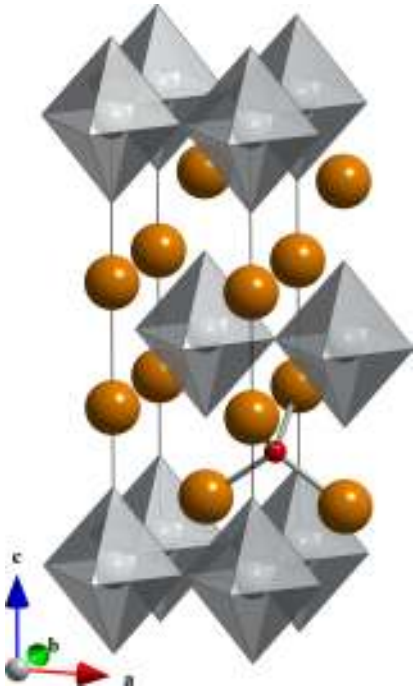

Figure 3.2: Favoured position for the interstitial oxide ion within the perfect Ln_2NiO_4 lattice. The site, located at (0, 1/2, 1/4) is tetrahedrally coordinated to four Ln^{3+} ions (shown) and to four O^{2-} ions.

studies have shown that, in the vicinity of interstitial oxide ion defects, the NiO_6 octahedra tilt away from the defect site, increasing the volume of the site [136, 142]. This tilting has also been observed in atomistic simulations of similar materials, and the flexibility of the octahedral framework is cited as a key feature facilitating oxide ion migration [143].

Oxide ion migration in Ln_2NiO_4 has been shown experimentally to occur in the La_2NiO_4 [136, 144, 145], Pr_2NiO_4 [50, 54, 136] and Nd_2NiO_4 materials [55, 136, 146]. The migration occurs in the rocksalt layer [147], which has been attributed to the low density of oxygen in that plane [54, 55]. Neutron diffraction maximum entropy method studies by Yashima et al. [50] clearly show (Figure 3.3a) the connected nature of the oxide-ion density in the rocksalt plane, and show that the migration involves ions from both the lattice (O2) and interstitial sites (O3). Molecular dynamics (MD) simulations of the La [18, 51, 52, 137] and Pr [19] analogues have produced similar results (Figure 3.3b), and have shown that migration occurs via an interstitialcy-type mechanism. The anisotropic nature of oxide ion conductivity in the materials is mirrored in their electronic conductivity, which is also found to be higher in the *ab* plane [148].

The interstitialcy conduction mechanism, discussed in detail in Section 3.2.4, involves the concerted movement of two oxide ions: the interstitial oxide ion and a lattice oxide ion from the apical site of a neighbouring NiO_6 octahedron. The interstitial ion displaces the lattice ion, which moves onto a neighbouring interstitial site

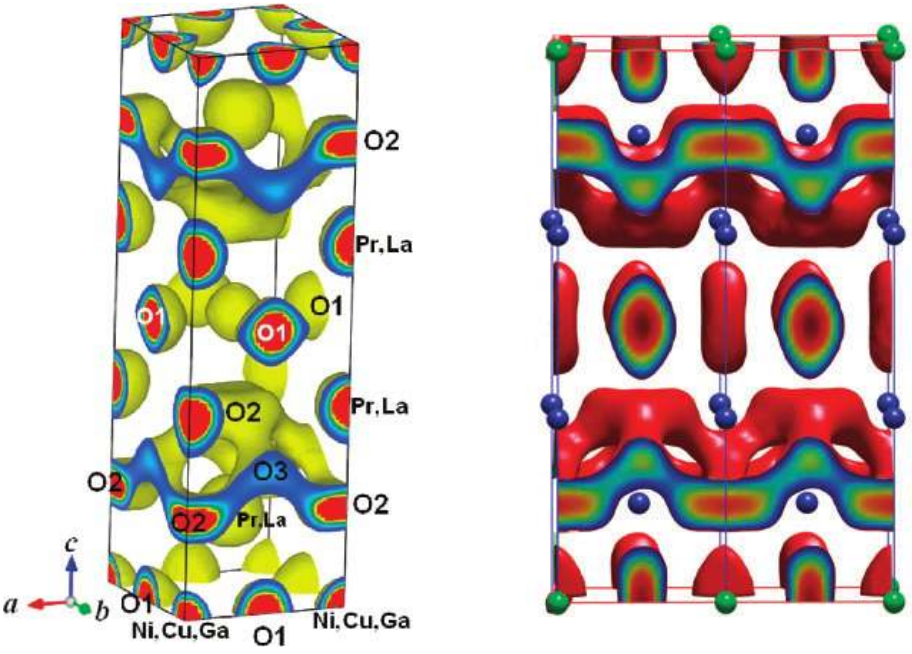

(a) Experimental **(b)** Simulated

Figure 3.3: Oxygen density in $Pr_2NiO_{4+\delta}$ showing evidence of an interstitialcy oxide ion conduction mechanism. (a) Experimental neutron diffraction data sampled at 1015.6℃, reproduced from [50]. (b) Comparable data from a molecular dynamics simulation run at 1100 K, reproduced from [19].

resulting in a net motion of oxide ions. The structural factors that affect this mechanism, and thus affect the conductivity of the materials, are of central importance to the development of intermediate temperature SOFCs.

Figure 3.4 shows experimental oxide-ion diffusion data for four layered nickelate phases [136]. Immediately apparent is the much higher level of diffusion in the nickelates in comparison to the oxide-ion-conducting perovskites LSFN and LSFC, which is due to the lower activation energies in the layered nickelate materials. The Pr-based materials show significantly higher levels of oxide-ion conductivity than the La and Nd analogues, especially at lower temperatures. A small amount of A-site (Nd) deficiency has been found to increase the conductivity of the materials.

Activation energies for oxide-ion diffusion in several Ln_2NiO_4-based materials are listed in Table 3.1. In general these energies are low (< 1 eV) and increase as the size of the lanthanide ion decreases There is good agreement between experimental and calculated values. Of particular note is the reduction in activation energy upon A-site deficiency ($Nd_{1.95}NiO_{4+\delta}$) or substitution, which indicates the potential for better cell performance at lower temperatures.

The maximum oxygen content also varies according to the rare-earth cation. Nd-based materials retain higher levels of interstitial oxide ion defects than the La-based materials [146], with maximum mean reported values of $\delta = 0.13$, 0.21 and 0.22 for

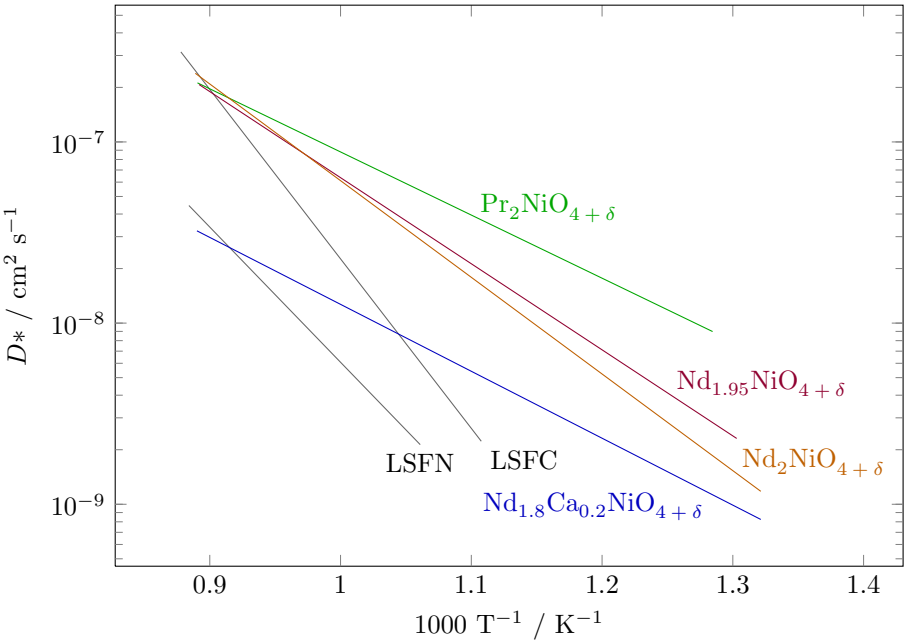

Figure 3.4: Experimental oxide-ion tracer diffusion coefficients of four nickelate phases versus $10^3/T$. The nickelate materials show considerably better performance at low temperature than conventional perovskite-type conductors such as (La/Sr)(Fe/Ni)$O_{3-\delta}$ (LSFN) and (La/Sr)(Co/Fe)$O_{3-\delta}$ (LSCF), included for comparison. Original data from [136].

Table 3.1: Activation energies for oxide ion diffusion in Ln_2NiO_4 (Ln = La, Pr, Nd) from the literature.

Material	Study Type	E_a for D^* /eV	Temp. Range /°C	Ref.
$La_2NiO_{4+\delta}$	Expt.	0.85	640–842	[145]
$La_2NiO_{4+\delta}$	Expt.	0.88	460–900	[147]
$La_2NiO_{4+\delta}$	Stat. Latt.	0.88	-	[137]
$La_2NiO_{4+\delta}$	MD	0.51	527–827	[18]
$La_{1.9}Sr_{0.1}NiO_{4+\delta}$	Expt.	0.57	640–799	[145]
$La_2Ni_{1-x}Co_xO_{4+\delta}$	Expt.	0.6	450–785	[149]
$Pr_2NiO_{4+\delta}$	Expt.	1.0	700–950	[150]
$Pr_2NiO_{4+\delta}$	MD	0.49–0.64	527–1227	[19]
$Nd_2NiO_{4+\delta}$	Expt.	1.06	480–780	[136]
$Nd_{1.95}NiO_{4+\delta}$	Expt.	0.94	480–780	[136]

La, Pr and Nd respectively [136]. Fuel cells with Nd-based electrodes have been assessed at intermediate temperatures (600–800℃) and have shown good performance when compared to current-generation perovskite-based materials [53, 146]

3.1.2 Phase Behaviour of Nd_2NiO_4

The structure of $Nd_2NiO_{4+\delta}$ was first reported to be of the K_2NiF_4 type in the 1960s [151, 152]. However, because the strain induced by the misfit between the rocksalt and perovskite layers can be alleviated by the inclusion of excess oxygen in the structure and/or by a rotating of the octahedra in the perovskite layer, the phase behaviour of $Nd_2NiO_{4+\delta}$ is complicated and several distinct phases have since been discovered [140, 153–158]. The oxygen stoichiometry of the material does not vary continuously, with phase separations occurring as a function of both oxygen stoichiometry and temperature [49].

The stoichiometric material ($\delta = 0$) exists in the tetragonal $P4_2/ncm$ spacegroup below 130 K (Figure 3.5c), at which temperature it undergoes a phase transition. Above 130 K the material occupies the orthorhombic $Bmab$ spacegroup (Figure 3.5b). Both of these phases are characterised by tilting of the octahedra in the perovskite layer with respect to the idealised tetragonal $I4/mmm$ material, which is shown in Figure 3.5a. In the low temperature tetragonal structure, the NiO_6 octahedra are tilted around both the a and b axes, whilst in the orthorhombic structure the octahedra tilt only around the a axis. These strain-relieving distortions are more pronounced in the Nd material, compared to both the La and Pr analogues, due to the smaller ionic radius of Nd^{3+} [136].

The ideal tetragonal $I4/mmm$ phase (Figure 3.5a), in which all the NiO_6 octahedra are aligned with the cell axes, is found not to exist if the material is completely stoichiometric; The extrapolated high-temperature transition to the $I4/mmm$ phase occurs at 1896 K, which is above the melting point of the material [156]. This phase can be stabilised, however, by the incorporation of excess oxygen. Nishijima et al. [157] report an $I4/mmm$ phase with an oxygen content of $Nd_2NiO_{4.11}$ via synthesis under oxygen, and a similar phases have since been reported by Tamura[a] [153] and Rodríguez-Carvajal et al. [156]. These latter two phases are formed above temperatures of 846 and 790 K respectively. The conditions of intermediate-to-high temperature and oxidising atmosphere are exactly those that are present at the SOFC cathode, making the study of the $I4/mmm$ phase relevant to clean energy research.

[a]The Tamura paper reports the material to be stoichiometric ($\delta = 0$), but similar synthesis conditions have subsequently been shown to lead to oxygen excess materials.

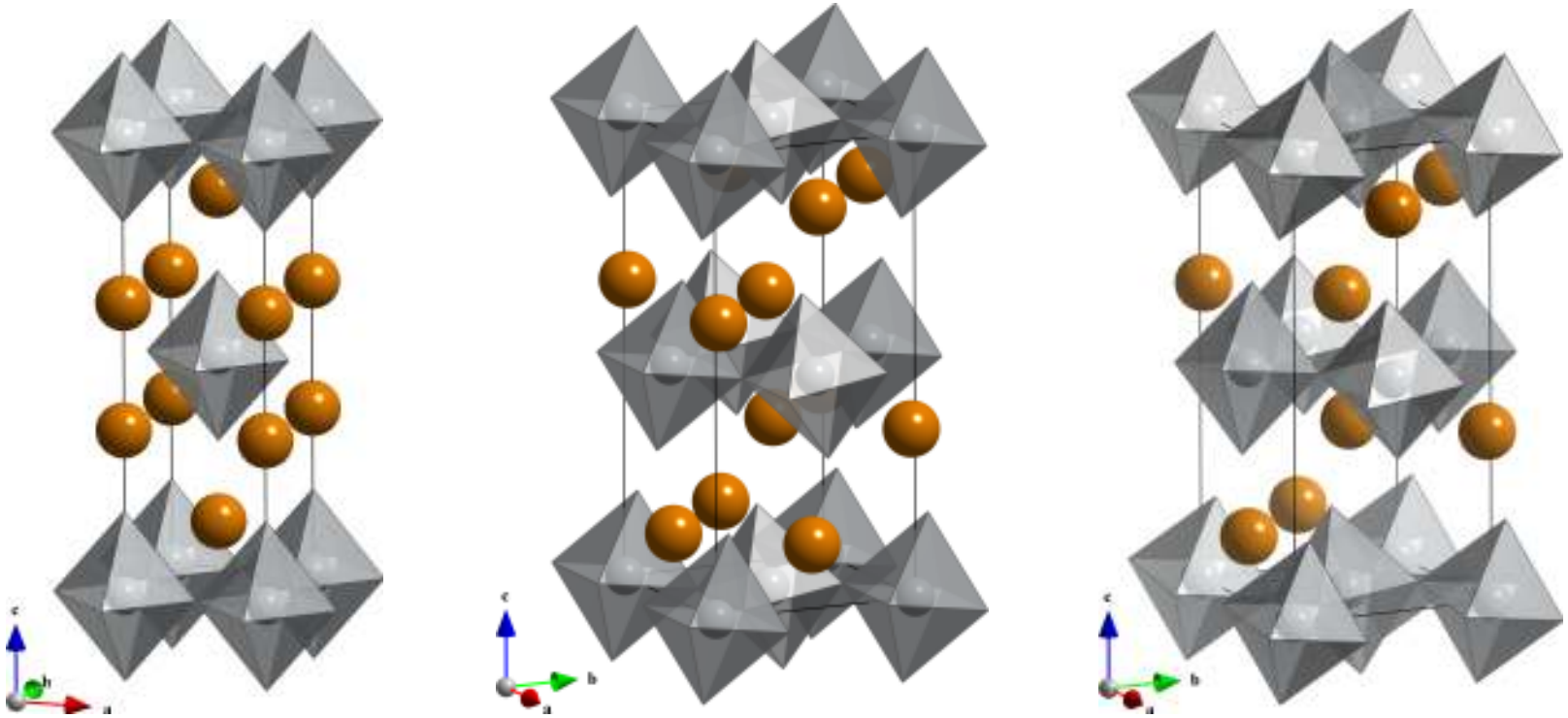

(a) $I4/mmm$; Predicted $T >$ MP **(b)** $Bmab$; 130 K $< T <$ MP **(c)** $P4_2/ncm$; $T <$ 130 K

Figure 3.5: Experimentally determined crystal structures of stoichiometric Nd_2NiO_4 shown in order of increasing temperature. The idealised high-temperature tetragonal $I4/mmm$ phase is shown in part (a), and is only stable above the melting point (MP) of the material. The orthorhombic $Bmab$ phase shown in (b) exists above 130 K and exhibits rotation of the BO_6 octahedra around the a axis only, whilst (c) shows the tetragonal $P4_2/ncm$ phase that exists below 130 K, in which the BO_6 octahedra are rotated around both their a and b axes. Nd cations are shown in orange, whilst NiO_6 octahedra are shown in grey.

3.1.3 Oxide-ion Transport and Project Objectives

In order to improve the $Ln_2NiO_{4+\delta}$ materials with respect to their application as SOFC cathode materials, it is vital to understand what atomic-scale features affect their macroscopic properties. Doping with Sr on the rare-earth (A) site in $La_2NiO_{4+\delta}$ has, for instance, been shown to stabilise the material by reducing the strain between the rocksalt and perovskite layers [49]. However, the factors affecting the ion transport properties, which are central to SOFC operation, are complex. Doping on the A site and Ni site, and A-site deficiency have all been shown to affect the oxide ion conductivity of the layered nickelate materials.

Most impure or non-stoichiometric phases of $Ln_2NiO_{4+\delta}$ are reported to have lower oxide ion conductivity than the pure nickelates [136]. For example, the doping of $La_2NiO_{4+\delta}$ with Sr^{2+} on the rare-earth site, which stabilises the material, also leads to a reduction in oxide-ion mobility [145]. The same effect is observed upon doping the Nd analogue with Ca^{2+} [136]. Despite lower diffusion, Skinner et al. [145] find that the activation barrier for diffusion in the Sr-doped material is actually lower than for the stoichiometric, indicating that the substitution has a direct effect on the migration mechanism. Doping with Ga^{3+} on the Ni site and, in some cases, A-site deficiency have been shown to improve the diffusivity of the materials [54, 55, 136].

Kawahara et al. [55] examined the effects of doping the Nd analogue with Cu and Ga on the Ni site, and the effects of subsequent Nd deficiency in the materials. The excess oxygen content of the materials was found to increase upon doping with Ga^{3+}, compensating for the charge of the $Ga^{\bullet}_{Ni}$ defects, and a concomitant rise in the oxygen permeation was observed. The neodymium deficient materials, with the general formula $Nd_{2-\alpha}(Ni_{0.75}Cu_{0.25})_{0.95}Ga_{0.05}O_4$, showed a further increase in oxygen permeation rate, with a maximum value obtained when $\alpha = 0.1$. Similar findings have been published by Ishihara et al. for the Pr analogue [54], and Figure 3.4 shows the diffusion coefficients of a Ni-stoichiometric, Nd deficient material are also higher than the pure phase.

Regarding the structural factors that affect these changes in ion transport, Boehm et al. [136], citing Fisher [159], state that oxide ion diffusion "is enhanced when, in the direct environment of a mobile ion, an ion is substituted by another one having a smaller oxidation state but with almost the same ionic radius." In such a case, the Coulombic attraction between the lattice ion and migrating species is reduced, whilst at the same time as little strain as possible is imposed upon the surrounding lattice. Boehm et al. [136] designate the radius of a Ln^{3+} vacancy to be the same as that of the vacant ion, and thus infer that Ln deficiency is even more favourable than substitution. Kawahara et al. [55] suggest that the extra free volume in the rocksalt layer created by the neodymium vacancies allows the migrating oxide ions to move more easily through the material. These propositions are difficult, if not impossible, to verify experimentally, and hence these issues are ideal candidates for examination using simulation techniques.

The aim of this study was to create, for the first time, an atomistic model of Nd_2NiO_4

Table 3.2: Buckingham potential and shell model parameters used for modelling Nd_2NiO_4.

Ion,[a] M	A /eV	ρ /Å	C /eV Å^6	Y /|e|	k /eV A^{-2}	Ref.
Nd^{3+}	1995.20	0.3430	22.59	-	-	[162]
Ni^{2+}	905.40	0.3145	0.0	-	-	[137]
O^{2-}	9547.96	0.2072	32.0	-2.04	6.30	[137]

[a] Note the Buckingham parameters apply to the interaction $M\cdots O^{2-}$, whilst the shell model parameters apply just to the ion M itself.

in order to investigate the defect and ion transport properties of both stoichiometric and Nd-deficient compostions. Static-lattice and molecular dynamics techniques were used to examine the mechanism and energetics of oxide ion migration in the material. These results were then compared with those available for the La and Pr analogues. Furthermore the techniques were used, also for the first time, to investigate the affects of A-site (Nd) deficiency upon ion migration within the material. The results obtained were used to comment upon the experimental findings presented in the literature.

3.2 Results and Discussion

3.2.1 Structural Modelling

Our first step towards simulating Nd_2NiO_4 was to derive an effective interatomic potential model from experimental data. We tested a number of the available stoichiometric crystal structures [153–157] using a variety of interatomic potentials from previous studies of related oxides [36, 137, 160–163]. Complete lists of the structures and potentials are located in the supplementary material in Appendix D.

Each structure was energy-minimised with a comprehensive number of combinations of Nd···O, Ni···O and O···O potentials. Because of its applicability to SOFC operating conditions and the general behaviour of the atomistic models, the high-temperature tetragonal $I4/mmm$ phase reported by Nishijima et al. [157] was chosen for the modelling work.

Despite being devoid of excess oxygen, the $I4/mmm$ structure was found to be stable with acceptable errors in the structural parameters when modelled using a number of sets of interatomic potentials. Table 3.2 lists the potentials used throughout the rest of this work. It should be noted that the Ni···O and O···O potentials were previously used to model the La and Pr analogues of the material [18, 19, 137] and that no refinement of the potential parameters was successful. A comparison of the experimental and calculated $I4/mmm$ structures is shown in Table 3.3.

Table 3.3: Comparison of the experimental $I4/mmm$ structure of $Nd_2NiO_{4.11}$ and that calculated using the atomistic model described in Table 3.2.

Parameter		Expt.	Calc.	Δ	Deviation /%
a, b	/Å	3.854	3.779	-0.075	-1.94
c	/Å	12.214	12.557	0.343	2.80
Vol.	/Å^3	181.42	179.33	-2.08	-1.15
Nd−$O_{(1)}$	/Å	2.567	2.557	-0.010	-0.39
Nd−$O_{(2)}$	/Å	2.152	2.302	0.150	6.97
Ni−$O_{(1)}$	/Å	1.927	1.890	-0.037	-1.92
Ni−$O_{(2)}$	/Å	2.230	2.254	0.024	1.08

Due to the oxygen excess of the synthesised $I4/mmm$ material, and the very high temperature of the predicted phase transition to the stoichiometric $I4/mmm$ phase, the stability of various sizes of supercells of the $I4/mmm$ structure was assessed. Supercells that were larger than one unit cell in either the a or b directions were found to be unstable, which suggests that the stability of the single cell was due to restricted degrees of freedom. The introduction of a small proportion of excess oxygen, around the same percentage as reported experimentally, was found to stabilise the supercells. For example, four additional oxide ions were introduced into a $4 \times 4 \times 1$ supercell, resulting in an oxygen excess of $\delta = 0.13$, or 3.1%. It was necessary to compensate for the charge of these excess oxide ions either by increasing the charge on all the nickel sites by a small amount or by introducing explicit Ni^{3+} ions, rather than by using a background charge. These findings are in very good agreement with the experimental phase behaviour of the material, discussed in Section 3.1.2. The inclusion of excess oxygen did not significantly affect the lattice parameters of the simulated material.

Molecular dynamics simulations, detailed in Section 3.2.4, were carried out primarily to assess the ion transport properties of the $Nd_2NiO_{4.11}$ material. Nevertheless, the lattice parameters determined during these simulations, shown in Figure 3.6, are noted here. These lattice parameters are projected to be 3.855 and 12.216 Å for a/b and c respectively at 298 K, both of which are very close to the experimental parameters of 3.854 and 12.214 Å respectively, and further support the interatomic potentials employed.

3.2.2 Intrinsic Defect Chemistry

The defect chemistry of La_2NiO_4 has previously been examined in detail using the same atomistic methodology as implemented in this study [137, 141]. The behaviour and properties of Nd_2NiO_4 have been less rigorously examined, however, and thus we performed a series of defect calculations to determine the energetics of intrinsic defect formation.

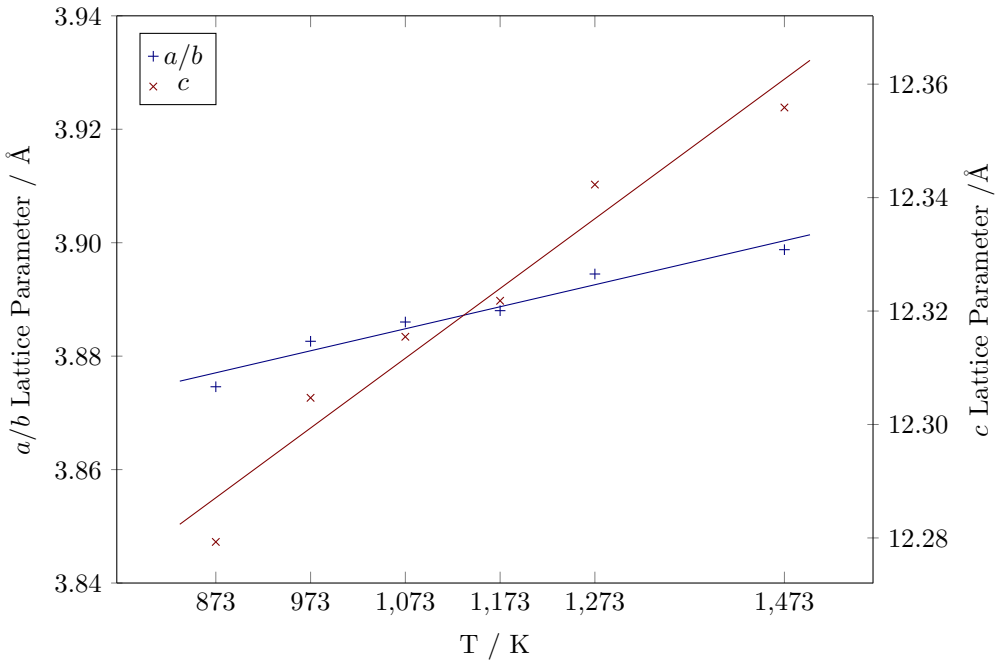

Figure 3.6: Unit cell lattice parameters of $Nd_2NiO_{4.11}$ determined from MD simulations at various temperatures. The thermal expansion coefficients were calculated to be $3.88 \cdot 10^{-5}$ and $1.23 \cdot 10^{-4}$ K^{-1} in the a/b and c directions respectively.

We first examined the formation of full- and partial-Schottky disorder, Frenkel disorder and cation anti-site defects within the Nd_2NiO_4 lattice. These processes are described below:

$$\text{Full Schottky:} \quad 2\,Nd_{Nd}^{\times} + Ni_{Ni}^{\times} + 4\,O_O^{\times} \longrightarrow 2\,V_{Nd}^{'''} + V_{Ni}^{''} + 4\,V_O^{\cdot\cdot} + Nd_2NiO_4 \tag{3.1}$$

$$Nd_2O_3\ \text{Schottky:} \quad 2\,Nd_{Nd}^{\times} + 3\,O_O^{\times} \longrightarrow 2\,V_{Nd}^{'''} + 3\,V_O^{\cdot\cdot} + Nd_2O_3 \tag{3.2}$$

$$\text{NiO Schottky:} \quad Ni_{Ni}^{\times} + O_O^{\times} \longrightarrow V_{Ni}^{''} + V_O^{\cdot\cdot} + NiO \tag{3.3}$$

$$\text{Nd Frenkel:} \quad Nd_{Nd}^{\times} \longrightarrow V_{Nd}^{'''} + Nd_i^{\cdot\cdot\cdot} \tag{3.4}$$

$$\text{Ni Frenkel:} \quad Ni_{Ni}^{\times} \longrightarrow V_{Ni}^{''} + Ni_i^{\cdot\cdot} \tag{3.5}$$

$$\text{O Frenkel:} \quad O_O^{\times} \longrightarrow V_O^{\cdot\cdot} + O_i^{''} \tag{3.6}$$

$$\text{Nd/Ni anti-site:} \quad Nd_{Nd}^{\times} + Ni_{Ni}^{\times} \longrightarrow Nd_{Ni}^{\cdot} + Ni_{Nd}^{'} \tag{3.7}$$

In order to examine the energetics of these formation processes, we calculated the energies of each of their constituent point defects, and lattice energies as required. No excess oxygen was incorporated into the bulk structure. The energies of the individual point defects are listed in Table 3.4.

Considering their importance, interstitial ions were considered on four sites, shown in Figure 3.7a, with Wykoff positions 2b, 4d, 8f, and 8g as listed in Table 3.4b, along with their associated energies. The 2b site is located in the dense perovskite layer

Table 3.4: Energies of isolated point defects within the perfect $I4/mmm$ Nd_2NiO_4 lattice.

(a) Isolated vacancies and substitutional defects.

Type of Defect	Symbol	Energy /eV
Nd^{3+} Vacancy	V'''_{Nd}	43.42
Ni^{2+} Vacancy	V''_{Ni}	29.66
O^{2-}(1) Vacancy	$V^{\cdot\cdot}_{O(1)}$	17.17
O^{2-}(2) Vacancy	$V^{\cdot\cdot}_{O(2)}$	16.17
Nd on Ni	$Nd^{\cdot}_{Ni}$	-10.01
Ni on Nd	Ni'_{Nd}	17.26
Ni^{3+} on Ni^{2+}	$Ni^{\cdot}_{Ni}$	-36.40

(b) Interstitial defects at four possible interstitial sites.

Wykoff Position	Coordinates		Defect Energy /eV $Nd_i^{\cdot\cdot\cdot}$	$Ni_i^{\cdot\cdot}$	O_i''
2b	(0,0,1/2)		-19.80	-14.55	-5.56
4d	(0,1/2,1/4)	(1/2,0,1/4)	-32.31	-20.14	-15.07
8f	(1/4,1/4,1/4)	(3/4,3/4,1/4)			
	(3/4,1/4,1/4)	(1/4,3/4,1/4)	-29.30	-18.48	-12.91
8g	(0,1/2,z)	(1/2,0,z)			
	(0,1/2,$-z$)	(1/2,0,$-z$)	-34.64	-20.15	-16.73

and is found to be highly unfavourable, whilst the remaining sites are located in the rocksalt layer. The 4d site is tetrahedrally coordinated to four apical oxide ions and four Nd ions, whilst the 8g site is closely-related by reduced symmetry in the c direction. The 8f site sits between two 4d sites.

We find the oxide interstitial to be most favourable at the 8g site. This is consistent with x-ray and neutron diffraction data [50, 140] and previous computational studies of the La and Pr analogues [19, 137, 139, 141]. A portion of the relaxation of the surrounding lattice around the interstitial oxide ion is shown in Figure 3.7b. The neighbouring Nd ions have been drawn towards the interstitial position by only 0.04 Å, whilst the nearest oxide ions have been displaced away by 0.69 Å. The distortion of the oxide ions is larger than that of ∼0.5 Å observed in La_2NiO_4 [138], indicating that the oxygen sublattice in the Nd analogue is more flexible. The nearest-neighbour octahedra are distorted and tilt approximately 14° from alignment with the c axis. It can be seen that similar distortions occur to a lesser extent at greater distances into the lattice (for example, in the perovskite layer below that directly neighbouring the interstitial ion, as shown).

The formation energies of the intrinsic defects described in Equations 3.1–3.7 are listed in Table 3.5. From these results it can be seen that Schottky, cation Frenkel and cation anti-site disorder are found to be high in energy and are unlikely to be

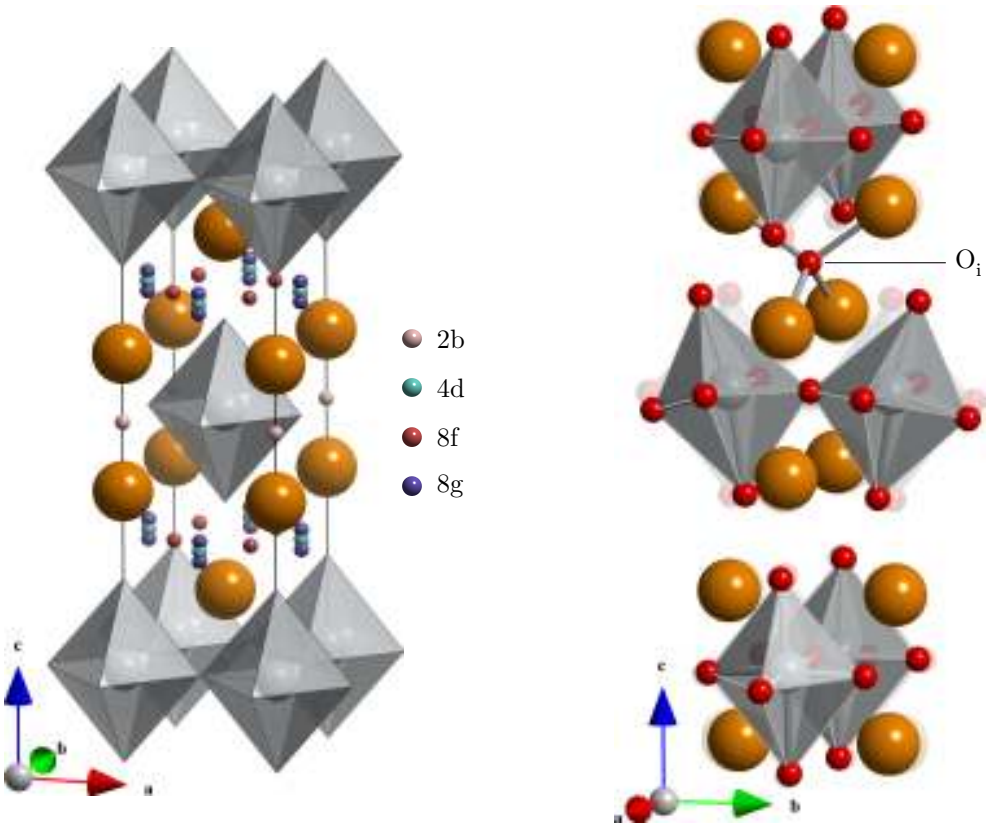

(a) **(b)**

Figure 3.7: Interstitial ions in the high-temperature tetragonal $I4/mmm$ lattice of Nd_2NiO_4. (a) Possible interstitial sites labelled according to their Wykoff position. (b) The local relaxation of the lattice around an interstitial oxide ion inserted at the most favourable position. The unrelaxed structure is included faintly for reference.

Table 3.5: Formation energies for intrinsic defects in Nd_2NiO_4.

Defect	Equation	Total Formation Energy /eV	Formation Energy /eV defect^{-1}
Full Schottky[a]	3.1	14.54	2.08
Nd_2O_3 partial Schottky[b]	3.2	8.49	1.70
NiO partial Schottky[b]	3.3	5.49	2.75
Nd Frenkel	3.4	8.78	4.39
Ni Frenkel	3.5	9.52	4.76
O Frenkel	3.6	0.44	0.22
Nd/Ni Anti-site	3.7	7.25	3.63

[a] A lattice energy of -170.63 eV was calculated for for Nd_2NiO_4.

[b] The lattice energies used for Nd_2O_3 and NiO were found to be -129.84 and -41.34 eV respectively, and were calculated using structures from [164] and [165].

present in the lattice at any significant concentration. Oxide ion Frenkel disorder is, however, considerably more favourable, indicating that Nd_2NiO_4 is expected to exhibit a considerable amount of oxide ion disorder at SOFC operating temperatures (approximately 1.9×10^{-1} Frenkel defects per formula unit at 873 K calculated using Equation 2.51). This disorder is conducive to oxide ion migration.

The energetic ordering of the intrinsic defects is the same as that calculated by Minervini et al. for La_2NiO_4 [137], with the exception of the of cation Frenkel energies, which is consistent with the similarity of the two materials. The comparatively low energy of Nd_2O_3 partial Schottky disorder suggests that a small degree of Nd non-stoichiometry is possible at elevated temperatures, although high levels are unlikely to form without being introduced synthetically.

3.2.3 Redox Chemistry

As outlined previously, Nd_2NiO_4 readily accommodates excess oxygen within the rocksalt layer of the lattice [136, 146]. The introduction of this excess oxygen is accompanied by the oxidation of Ni^{2+} to Ni^{3+} [49], and these electron holes give rise to the electronic conductivity of the material [136, 148].

Oxidation proceeds via

$$\tfrac{1}{2}O_2 \rightleftharpoons O_i'' + 2\,h^{\cdot}, \tag{3.8}$$

where, in our atomistic calculations, the hole species $h^{\cdot}$ is modelled explicitly as a small polaron on the nickel site. Minimisations in which the hole was located on an oxide ion site failed to converge. The overall energy for the oxidation process is found[b] to be -3.15 eV defect^{-1}, which is in good accord with the experimental finding that the material readily accommodates excess oxygen.

[b] The individual defect energy for $Ni_{Ni}^{\cdot}$ is calculated to be -36.50 eV; The third ionisation energy

Whilst care must be taken when considering the absolute value of the calculated oxidation energy (see Appendix C.4), it is instructive to compare our value with other experimental and theoretical results. DiCarlo et al. find a favourable oxidation energy for $La_2NiO_{4.03}$ of -108 kJ mol^{-1} = −1.12 eV [167] using calorimetry, whilst Bhavaraju et al. [168] find oxidation of the neodymium analogue $Nd_2NiO_{4+\delta}$, $0.04 \leq \delta \leq 0.08$ to be about twice as exothermic at -204 kJ mol^{-1} = −2.11 eV using electrochemical methods. Atomistic computational studies of La_2NiO_4 have produced oxidation energies of between -2.21 eV $defect^{-1}$ [137] and -1.52 eV $defect^{-1}$ [141], which are consistent with experiment.

Our calculated energy for the oxidation of Nd_2NiO_4 is about twice that produced by Read et al. [141], which is consistent with the difference between the experimental oxidation energies of the La and Nd materials. The exothermic nature of the oxidation reaction in Nd_2NiO_4 is in agreement with the thermochemical data and is important for conduction behaviour.

3.2.4 Oxide Ion Migration

The migration of interstitial oxide ions within the Nd_2NiO_4 lattice is of central importance in the application of this material as a SOFC cathode. The atomistic simulations presented in the following section attempt to expand upon the existing work concerning interstitial oxide ion migration in the Ln_2NiO_4 materials, not only by considering the Nd analogue, but also by considering, for the first time, the affect of A-site (Nd) deficiency on oxide ion conduction.

We performed both static-lattice and MD calculations to probe oxide ion migration in $Nd_2NiO_{4+\delta}$. The static-lattice calculations included nudged elastic band (NEB) calculations of migrating ions within supercells of $Nd_{2-x}NiO_{4.09}$ ($x = 0, 0.03$), giving direct access to migration energies. The MD simulations were performed on large supercells of $Nd_{2-x}NiO_{4.11}$ ($x = 0, 0.1$) at a range of temperatures between 873 and 1473 K. Full details of these simulations are given in Appendices D.3.1 and D.3.2.

Nd Stoichiometric: $Nd_2NiO_{4.11}$

Firstly, our MD simulations confirm that the interstitialcy mechanism, illustrated in Figure 3.8, is predicted to be the dominant ionic conduction mechanism in the $Nd_2NiO_{4+\delta}$ material. Figure 3.9 shows the time-averaged density of oxide ions during one of these simulations, which is directly comparable to the results of Yashima et al. [50] and Parfitt et al. [19] presented previously. Direct visualisation of the computed ion trajectories reveals that the motion of the oxide ions is strongly correlated; that is, several neighbouring oxide ions all change positions in a concerted

of nickel is 35.19 eV [166]; The energy for $\frac{1}{2}O_2 \longrightarrow O^{2-}$ is taken to be 9.86 eV, which includes terms for the dissociation of O_2 (5.1652 eV [139, 166]) and the first and second electron affinities of oxygen (-1.47 and 8.75 eV respectively [139])

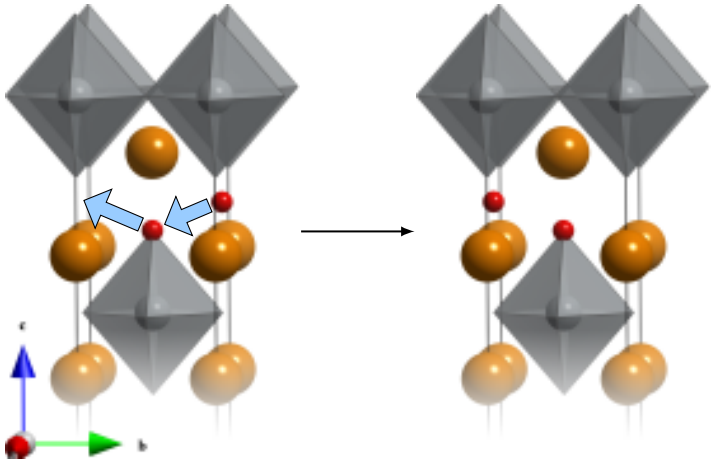

Figure 3.8: Schematic illustration of the interstitialcy mechanism for oxide ion conduction in $Ln_2NiO_{4+\delta}$. The mechanism involves the simultaneous movement of both highlighted oxide ions (shown in red).

manner. Examples of these motions are shown in Figure 3.10. Videos of selected ion trajectories are included in the electronic supplementary material, the contents of which is summarised in Appendix H.

Using the NEB technique, energy profiles (Figure 3.11) were calculated for the migration of interstitial oxygen via the interstitialcy mechanism and directly between two nearest-neighbour interstitial sites. The direct path is found to be high in energy, with an activation energy of 2.65 eV, whilst the interstitialcy mechanism is found to be considerably more favourable, with an activation energy of 0.44 eV. This result is in concordance with the data from the MD simulations.

Structural information can be obtained from the MD simulations using the pairwise radial distribution function (RDF), which provides an insight into the degree of long-range ordering in the crystal lattice. The Ni···Ni and Nd···Nd RDFs, shown in Figures 3.12 and 3.13, illustrate the long-range crystallinity of the cation lattice; Ni/Nd ions are present in the lattice at well-defined intervals even at large separations.

The RDF between Nd and the equatorial oxide ions (O1) also shows well ordered peaks, suggesting that the O1 ions stay located on their lattice sites throughout the simulation (see Figure 3.14). The oxide ions which are initially at the apical and interstitial sites (O2 and O3 respectively) generate very similar RDFs, meaning that the ions have exchanged sites and become essentially indistinguishable during the simulation. Furthermore, the peaks are very broad and the function stays near a value of one at ion separations greater than around 6 Å, suggesting that there is considerably greater disorder in the O2/O3 sublattice than in either the cation or equatorial oxide ion sublattices throughout the simulation. This is consistent with the migration of the O2 and O3 species.

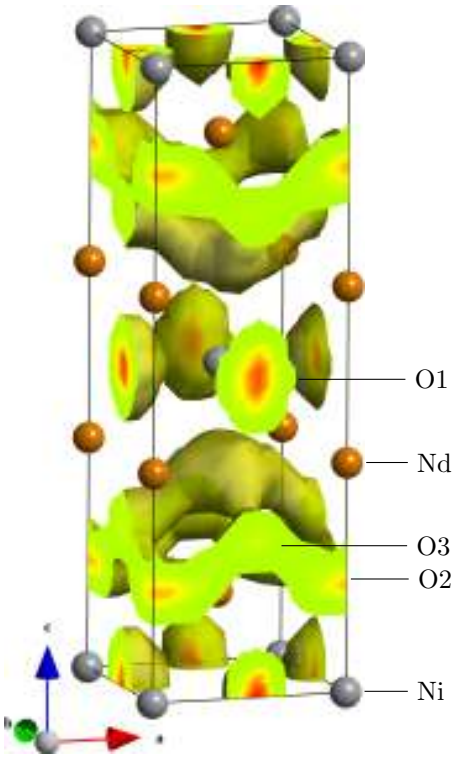

Figure 3.9: Projection onto a single unit cell of time-averaged density data constructed from the trajectories of all the oxide ions in a MD simulation of $Nd_2NiO_{4.11}$ at 1073 K. These data compare directly with those previously determined for Pr_2NiO_4 [19, 50], and clearly show the connected nature of the density due to the O2 and O3 ions.

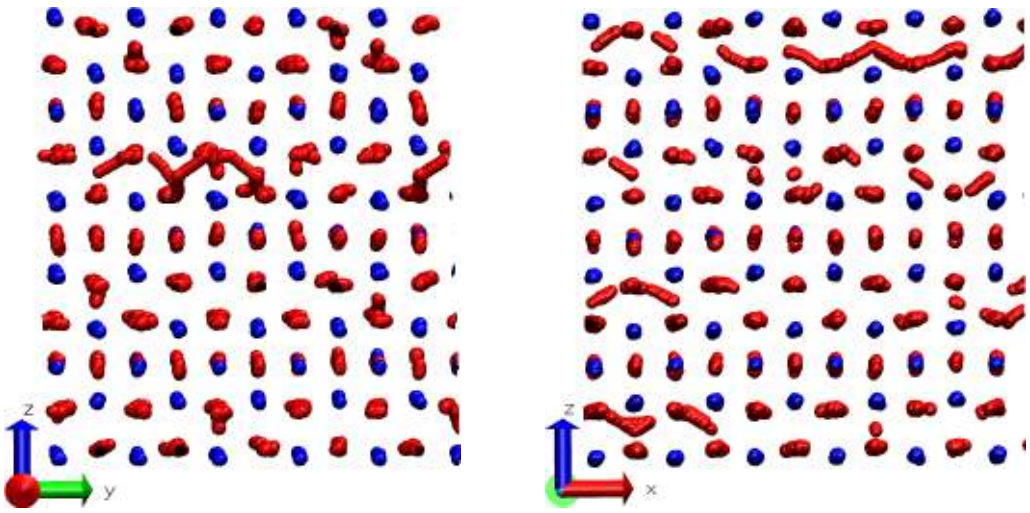

(a) **(b)**

Figure 3.10: Composites of snapshots from the ion trajectories generated by the Nd_2NiO_4 MD simulation. (a) view down the a axis; (b) view down the b axis. Both images display blocks of 100 frames superimposed, which clearly show multiple neighbouring ion hops occurring simultaneously. Cations are shown in blue, oxide ions are shown in red.

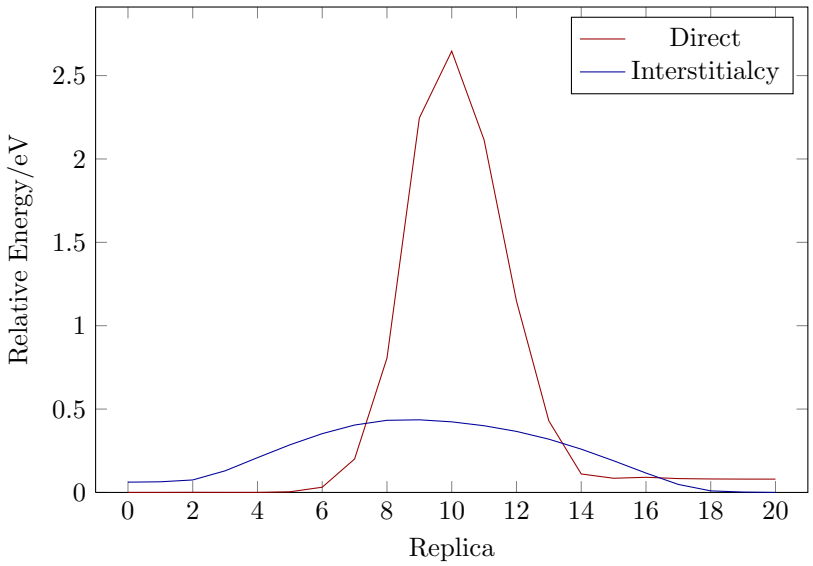

Figure 3.11: Migration profiles for interstitial oxide migration in a $4 \times 4 \times 1$ supercell of $Nd_2NiO_{4+\delta}$ calculated using the nudged elastic band methodology. Paths were calculated directly between interstitial sites and via an interstitialcy-type mechanism involving the apical lattice oxide ion.

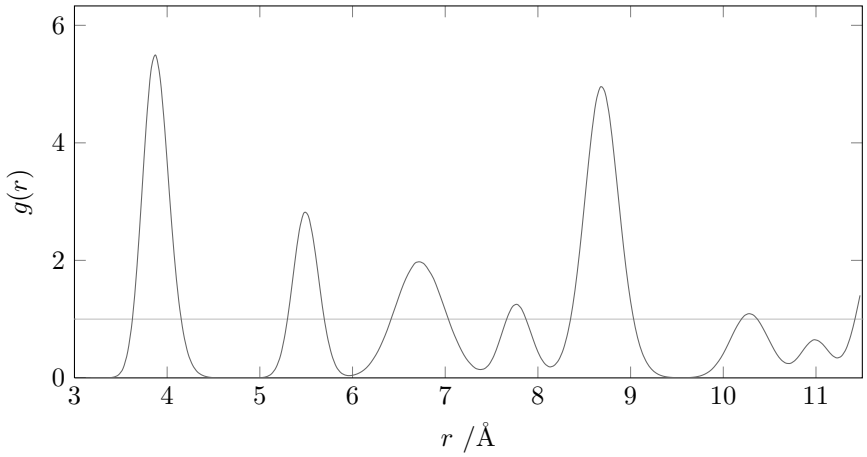

Figure 3.12: Ni···Ni radial distribution function of Nd_2NiO_4 at 1073 K.

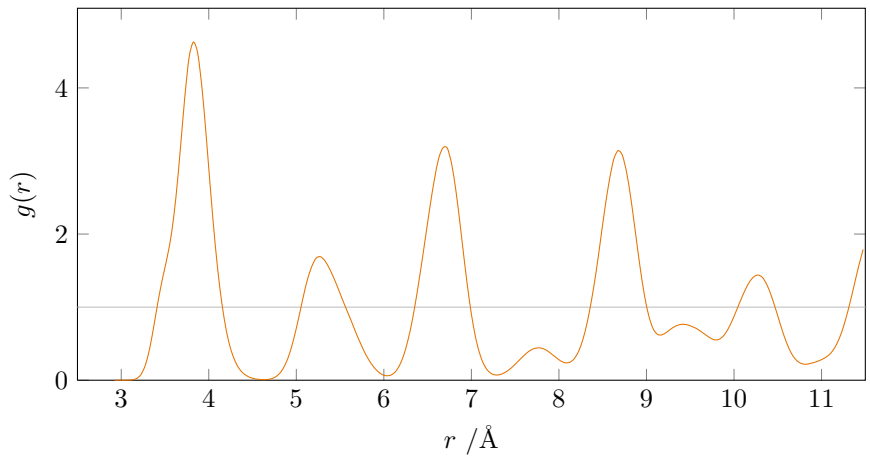

Figure 3.13: Nd···Nd radial distribution function of Nd_2NiO_4 at 1073 K.

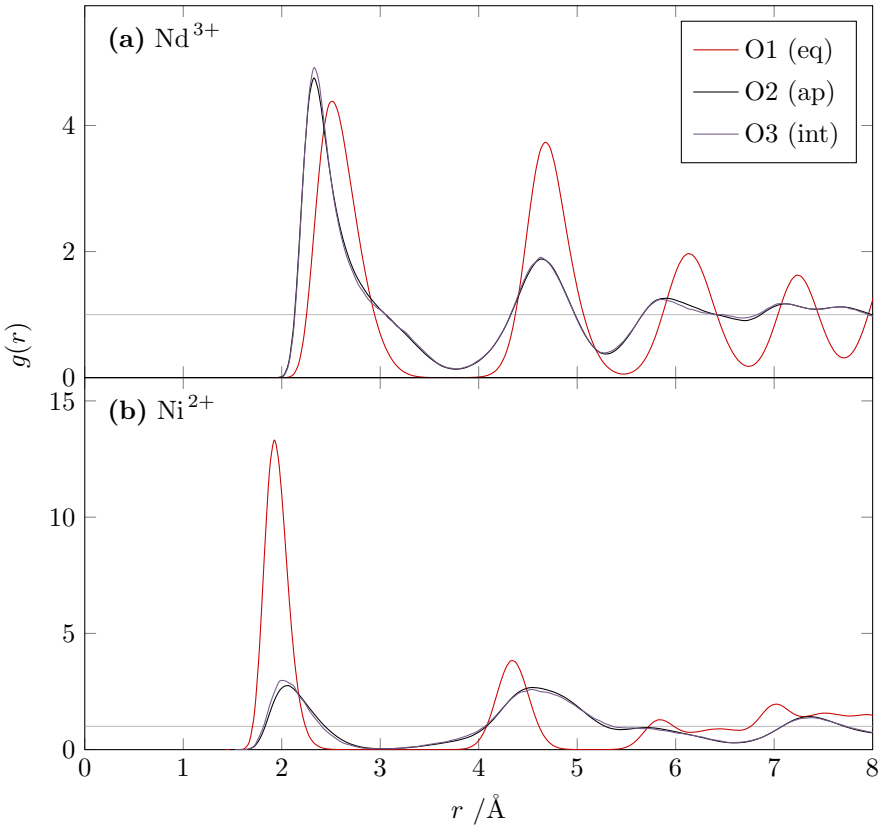

Figure 3.14: Cation–oxide-ion radial distribution functions of Nd_2NiO_4 at 1073 K. (a) Nd···O; (b) Ni···O; O1 ions are equatorial, whilst O2 and O3 are initially apical and interstitial respectively.

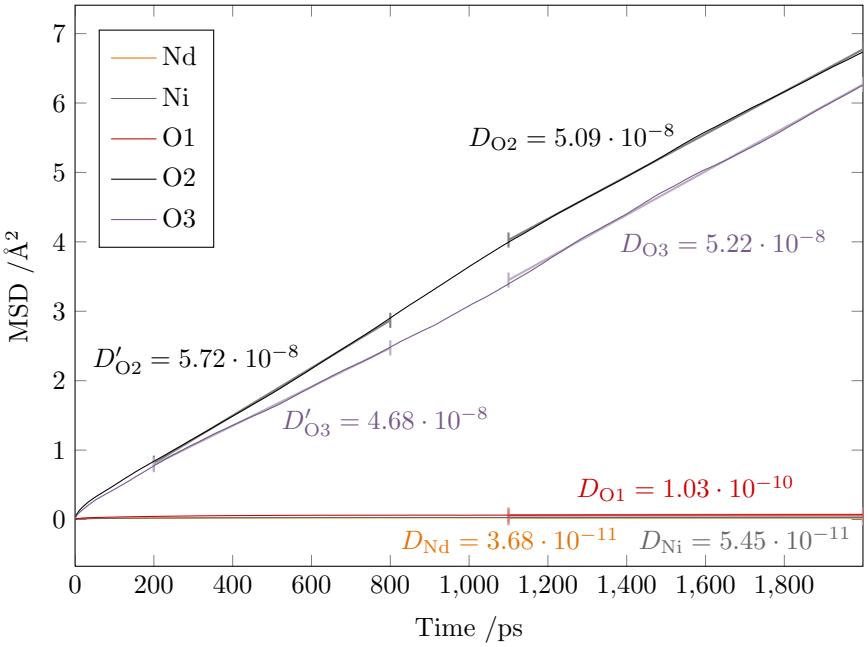

Figure 3.15: Mean square displacement of each ion species in $Nd_2NiO_{4.11}$ from a large time-scale MD simulation at 1173 K. Diffusion coefficients for each species, in unit of $cm^2\ s^{-1}$, are shown next to the lines of best fit from which they were measured.

The diffusion coefficient D is extracted from the ion trajectories using the time-dependent mean square displacement (MSD), which is shown in Figure 3.15 for each type of ion in the simulation cell. These data clearly show that the rate of diffusion of the O2 and O3 species is several orders of magnitude greater than either the cation or equatorial (O1) oxide ion species. The values are comparable to the experimental tracer diffusion coefficient of $6.46 \cdot 10^{-8}$ cm s^{-1} obtained for the La-based material at 1038 K by Skinner and Kilner [145].

Weighted mean O2/O3 MSD data was used to generate average oxide ion diffusion coefficients at a variety of temperatures (Figure D.2). A plot of $\ln D$ versus $1/T$ (Figure 3.4) shows that the calculated activation energy for oxide ion diffusion is 0.74 eV. This compares well to previous results for similar materials, which are listed in Table 3.1. In particular, the value is larger than those obtained for the La and Pr analogues using similar methodology. The trend in activation energy for $Ln_2NiO_{4+\delta}$ (Nd > Pr > La) is possibly related to the size of the A cation (Nd < Pr < La). The trend in the experimentally observed diffusion coefficients is less clear, which suggests that other factors are also important in the diffusion process.

As discussed previously, oxide-ion diffusion through the Ln_2NiO_4 materials is highly anisotropic, with larger diffusion coefficients observed in the *ab* plane [144]. Minervini et al. [137] calculate that the activation energy in the *c* direction[c] is over three times larger than in the *ab* plane (3.15 eV cf. 0.88 eV respectively). Experimentally, diffusion coefficients are found to be between one and two orders of magnitude dif-

[c]When the axes are labelled according to the scheme used in this work

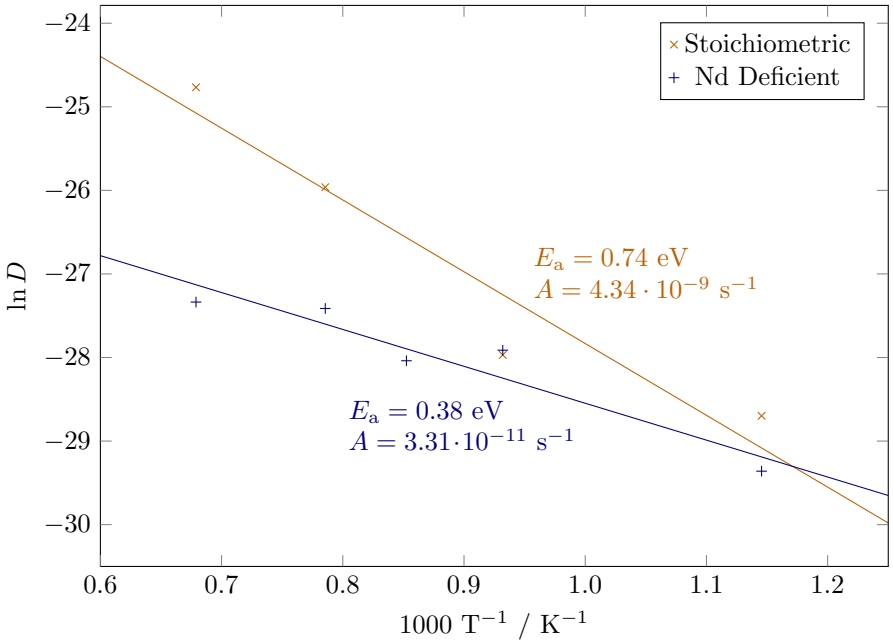

Figure 3.16: Arrhenius ($\ln D$ vs $1/T$) plot comparing stoichiometric and A-site deficient neodymium nickelate materials. For the cation stoichiometric compound data points at 973 and 1173 K have been omitted, for the Nd deficient system, just the 973 K data point has been omitted.

ferent between the two regimes [136]. We find that the diffusion coefficients from our simulations of $Nd_2NiO_{4.11}$ are around seven times higher in the *ab* plane than in the *c* direction (see Figure D.3), which is in accord with these experimental findings.

Neodymium Deficient: $Nd_{1.90}NiO_{4.11}$

As outlined in Section 3.1.3, there has been some debate concerning exactly how certain structural factors affect oxide ion mobility on the atomic scale in the $Ln_2NiO_{4+\delta}$ materials. A-site deficiency has been found in some cases to increase oxide ion migration, which has been attributed to a greater free volume in the rocksalt layer [54, 55], or to a weaker interaction between the mobile species and the lattice [136]. A full atomic-scale investigation of this phenomenon is, however, still lacking.

The natural starting point for an investigation of Nd deficiency is the interaction of the neodymium vacancy with an oxide ion interstitial. Defect calculations reveal that an oxide ion interstitial directly neighbouring a Nd vacancy relaxes onto the nearby apical (O2) site, displacing the apical oxide ion into an adjacent interstitial position. The relaxed defect cluster, with the displaced apical ion, is found to be around 0.7 eV higher in energy than the sum of the isolated defects. The instability of the O_i'' defect directly adjacent to the V_{Nd}''' defect is probably due to the mutual repulsion of the species, which share the same effective charge. Therefore, the arguments presented in the literature [54, 55, 136] do not seem to account for the effective charge of the

Nd vacancy.

We performed NEB migration profile calculations in an attempt to assess the impact of V'''_{Nd} on the oxide-ion migration energy. In these calculations the migrating ions moved between sites in the vicinity of those directly neighbouring the Nd vacancy, including migrations occurring in an adjacent rocksalt layer. None of these calculations showed a significant decrease in the activation energy for interstitialcy migration.

MD simulations of Nd-deficient supercells were also performed. On the whole, the data from these simulations looks very similar to that generated for the stoichiometric material (see Appendix D.3.3). MSD data from simulations at a range of temperatures were again used to plot $\ln D$ versus $1/T$, which is shown in Figure 3.16 alongside the data for the Nd-stoichiometric system.

It is apparent from Figure 3.16 that, in the simulated temperature range, the diffusion coefficients D_O for the Nd-deficient material are lower than those for the Nd-stoichiometric. Perhaps more importantly, the activation energy for the migration process is also found to be lower in the Nd-deficient material, with a value of 0.38 eV. Our results are consistent with those in the literature: reduced diffusivity and activation energy were observed in tracer diffusion studies of the Sr-substituted La-based material $La_{1.9}Sr_{0.1}NiO_{4+\delta}$ [145], and the faster diffusion observed for $Nd_{1.95}NiO_{4+\delta}$ [136] are generally observed at lower temperatures than those employed in our MD study. These results clearly show that Nd-deficiency affects the oxide-ion migration in the nickelate material in a complex manner and warrants further investigation.

3.3 Chapter Summary

We have successfully produced and tested an atomistic potential model to investigate the defect chemistry and ion transport properties of the Nd_2NiO_4 system. In particular we find that the calculated energetics of intrinsic defect formation are very similar to those calculated for the La_2NiO_4 material and that the incorporation of interstitial oxygen via oxidation is very favourable, in accordance with calorimetry and electrochemical experiments.

Oxide ion migration is found to occur via an interstitialcy-type mechanism, involving the concerted movement of both interstitial and apical lattice oxide ions. This is the same mechanism found previously by MD simulations and neutron diffraction MEM studies of other nickelate materials. The activation energy for oxide ion migration in $Nd_2NiO_{4.11}$ is predicted to be 0.74 eV from our MD simulations. This value is reduced considerably if the material is slightly Nd deficient, with an activation energy of 0.38 eV predicted for $Nd_{1.90}NiO_{4.11}$. Our simulations suggest that the reduction in activation energy is not achieved through increased free volume or decreased Coulombic interaction, but by more complex structure–property relationships.

Chapter 4

Defect, Electronic and Ion Transport Properties of Infinite-layered $SrFeO_2$

4.1 Background

4.1.1 Infinite-layered $SrFeO_2$

Members of the family of Sr−Fe−O ternary oxides have been found to exhibit high oxide-ion and electronic conductivities at intermediate temperatures [169–173], and are thus potential candidates for application in next-generation solid oxide fuel cells (SOFCs). Materials can be formed with a range of compositions, and the corresponding structures vary from the simple perovskite type to more complex systems with perovskite-like features.

For the $SrFeO_{3-\delta}$ series of oxides, the lowest achieveable level oxygen content was historically considered to be embodied in the brownmillerite-structured $SrFeO_{2.5}$ [174]. The brownmillerite material contains intrinsic, ordered oxide-ion vacancies, which give rise to the ionic conducivity of the material [170, 173, 174]. New materials may exhbibit alternate conduction mechanisms which have particular application at lower temperatures [174], and much effort has been directed towards reducing the oxygen content of the $SrFeO_{3-\delta}$ system using a variety of approaches [56].

In 2007, Tsujimoto et al. [56] reported the first synthesis of the new compound $SrFeO_2$, shown in Figure 4.1. The compound is isostructural with the 'infinite-layer' cupric oxides ($ACuO_2$, where A = Sr, Ca), and is formed by reduction of the perovskite-structured $SrFeO_{3-x}$ ($x = 0.125$) using a binary metal hydride (CaH_2) at the relatively low temperature of 553 K. This synthesis route avoids the thermodynamic limitations of high temperature reactions, producing $SrFeO_2$ in a kinetically

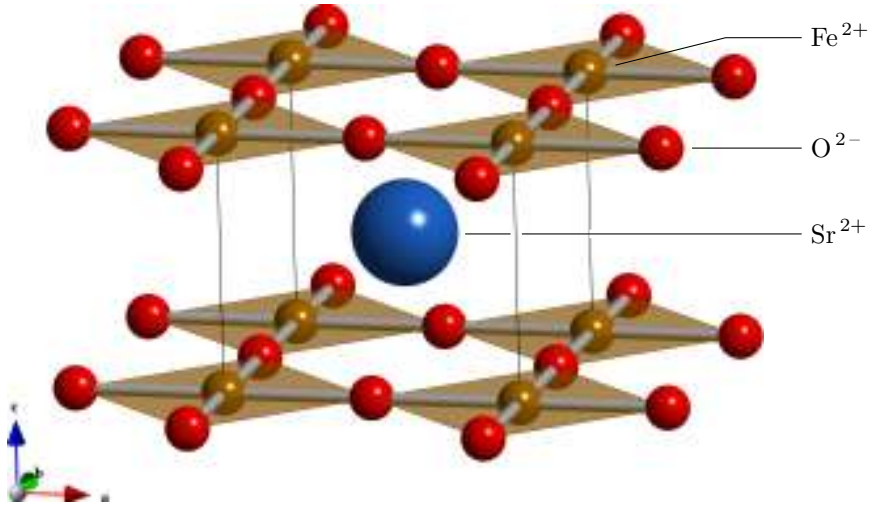

Figure 4.1: Experimentally determined structure of $SrFeO_2$, space group $P4/mmm$ (no. 123), with lattice parameters $a, b = 3.991(1)$ Å and $c = 3.474(1)$ Å. Sr lies at (1/2, 1/2, 1/2), Fe at (0, 0, 0) and O at (1/2, 0, 0) [56].

controlled manner [57]. The reduction leads to unusual square-planar coordination of oxide ions around Fe^{2+} via the brownmillerite-type intermediate, $SrFeO_{2.5}$.

The two-step formation process of $SrFeO_2$ is illustrated in Figure 4.2. Whilst the parent perovskite $SrFeO_{3-x}$ phase and the layered $SrFeO_2$ phase are structurally very similar, the formation reaction involves a considerable reorganisation of the oxide-ion sublattice, because the intermediate brownmillerite phase is composed of alternating layers of FeO_6 octahedra and FeO_4 tetrahedra. The formation of the layered $SrFeO_2$ material from the brownmillerite involves the rearrangement of these tetrahedra into square planar units, as well as the removal of further oxide ions from the system, which demonstrates that the oxide ions remaining in the lattice are still potentially highly mobile [57]. Furthermore, the material is found to be easily oxidised at temperatures as low as 400 K [56].

Despite the metastable nature of $SrFeO_2$, the compound is found to be remarkably stable with respect to temperature. Furthermore, the formation of a full range of solid solutions with the Ca analogue, forming $Sr_{1-x}Ca_xFeO_2$, illustrates that the formation of $SrFeO_2$ is more than just a fortunate structural curiosity. This robustness permits the tuning of material properties for industrial applications [179, 180].

4.1.2 Electronic Structure of $SrFeO_2$

The perfectly square coordination of environment of Fe^{2+} in $SrFeO_2$ is very unusual. Tsujimoto et al. [56] find that the Fe^{2+} ion to be in the high-spin state, and such high-spin d^6 ions generally have an electronic configuration of $(d_{xz}, d_{yz})^3(d_{xy})^1(d_{z^2})^1$

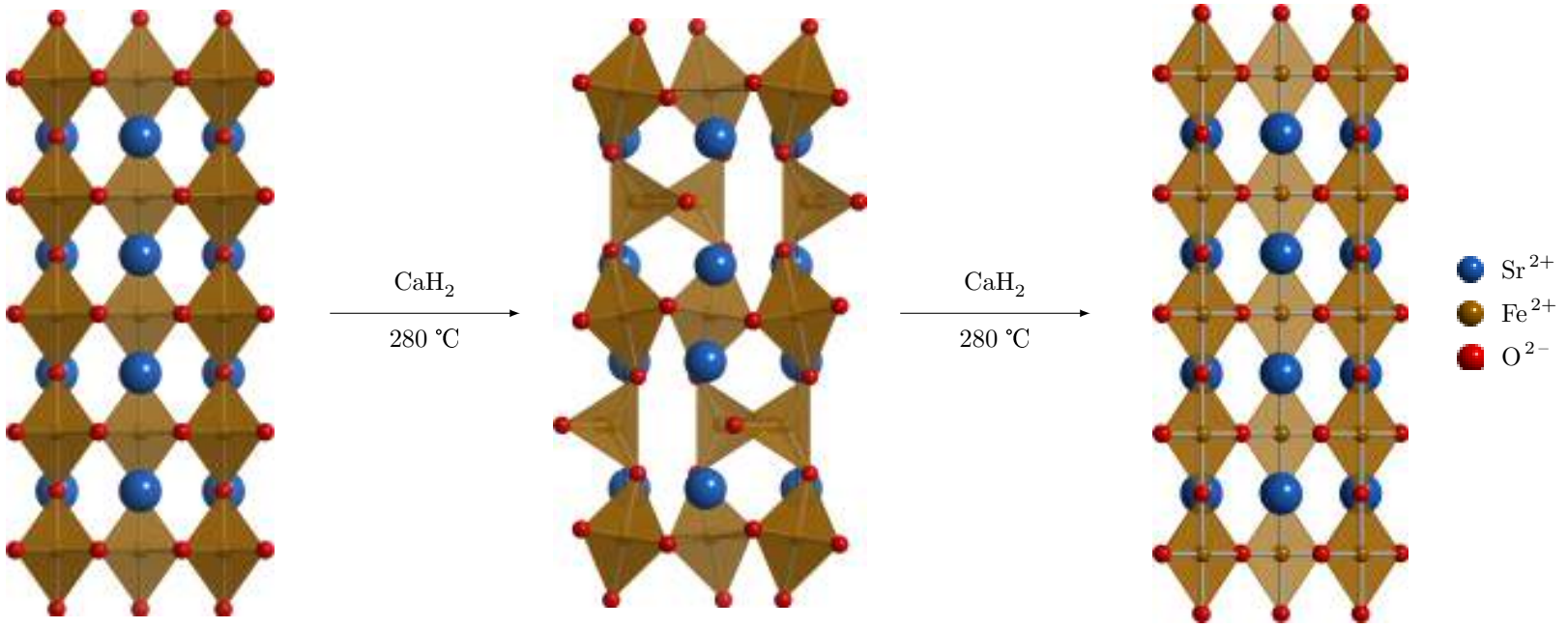

(a) $SrFeO_3$ **(b)** $SrFeO_{2.5}$ **(c)** $SrFeO_2$

Figure 4.2: Structural transformation of (a) the perovskite-structured $SrFeO_3$ into (c) the infinite-layer-structured $SrFeO_2$, which occurs via (b) a brownmillerite-type intermediate, $SrFeO_{2.5}$, in a topochemical manner involving rearrangement of the oxygen around the iron site. Note how alternate layers of octahedra in $SrFeO_3$ are transformed into tetrahedra, which then rearrange to form square planar units in the final product. The structure of $SrFeO_3$ is taken from Takeda et al. [175] and the structure of $SrFeO_{2.5}$ was supplied by Craig Fisher [176].

$(d_{x^2-y^2})^1$ in a square planar environment. This electronic configuration should, however, lead to a Jahn–Teller distortion to remove the degeneracy of the d_{xz} and d_{yz} orbitals and consequently lower the overall energy of the system, but this is not observed experimentally for the $SrFeO_2$ material.

Recent electronic structure calculations have provided fundamental insights into the behaviour of the material [181–183]. Firstly, Xiang et al. [181] find that the minority ('down') spin electron occupies the d_{z^2} orbital, rather than the degenerate d_{xz} or d_{yz} orbitals. This solves the degeneracy issue and removes the need for a Jahn–Teller distortion to stabilise the system.

Pruneda et al. [182] provided the first satisfactory explanation for the occurance of the doubly occupied d_{z^2} orbital. The authors rule out a number of possible independent-electron causes, including reduced Coulomb repulsion of the d_{z^2} orbitals, and in-plane bonding effects, such as π-donor interactions. Their conclusion is that a perfectly symmetrical environment around the Fe^{2+} ion allows for the $3d_{z^2}$ orbital to hybridise with the formally empty $4s$ orbital. The density of states (DOS) calculated by Pruneda et al. for $SrFeO_2$ is shown in Section 4.2.1, Figure 4.3a.

Although the structure of $SrFeO_2$ appears to be highly two-dimensional in nature, the spins on the Fe ions within the structure are found to be aligned antiferromagnetically [56] with high coupling constants between the FeO planes [182]. This yields a high Néel temperature for the material, which is comparable to materials with extended three-dimensional bonding [56].

4.1.3 Project Outline

As is often found with new materials, information about the defect and oxide-ion transport properties of $SrFeO_2$ is currently limited. The suitable mixed ionic–electronic conduction properties of other members of the Sr−Fe−O ternary oxide family and the ease with which $SrFeO_2$ is oxidised suggest that the material might possess useful, and potentially novel, oxide-ion transport characteristics. Such features make $SrFeO_2$ and ideal candidate for computational modelling studies.

In this work we use a combination of classical and DFT-based electronic structure techniques to examine the defect properties of the $SrFeO_2$ material. Atomistic simulations are used to calculate the formation energy of intrinsic defects and the solution energy of a range of mono-, di- and tri-valent dopants. In addition, we use static-lattice and molecular dynamics (MD) techniques to explore the mechanisms and energetics of oxide-ion migration within the material. Our DFT calculations are used to examine the oxidation of the material, and provide a crucial benchmark for the atomistic work.

Table 4.1: Buckingham potential and shell model parameters used for modelling $SrFeO_2$.

Ion[a] M	A /eV	ρ /Å	C /eV·Å^6	Y_M /|e|	k_M /eV·A^{-2}
Sr^{2+}	4814.85	0.3001	39.83	1.33	21.53
Fe^{2+}	1204.61	0.3000	0.0	2.00	10.92
O^{2-}	22764.3	0.149	10.0	-2.239	42.00
Fe^{3+}	1102.4	0.3299	0.0	4.97	304.7

[a] Note: the Buckingham parameters apply to the interaction $M\cdots O^{2-}$, whilst the shell model parameters apply only to the ion M itself.

Table 4.2: Comparison of the experimental structure of $SrFeO_2$ and that calculated using the atomistic model.

Parameter		Expt.	Calc.	Δ	Deviation /%
a, b	/Å	3.991	3.991	0.000	0.00
c	/Å	3.474	3.474	0.000	0.00
Vol.	/Å^3	53.33	53.33	-0.003	-0.01
Sr−O	/Å	2.646	2.646	0.000	0.00
Fe−O	/Å	1.996	1.995	-0.000	-0.00

4.2 Results and Discussion

4.2.1 Structural Modelling

It is essential to produce and validate effective computational models of the $SrFeO_2$ system before investigating the defect chemistry and ion migration processes of the material. For this work we produced both an atomistic (potential-based) model and a plane-wave DFT model of the system. The quality of the models was primarily assessed on the accuracy with which they reproduced the experimental crystal structure. Due to the novelty of the $SrFeO_2$ material, only a limited amount of experimental data is available in the literature; second-derivative data such as dielectric or elastic constants or phonon data were not available.

In order to construct an atomistic model for $SrFeO_2$, we tested a comprehensive array of combinations of Buckingham potentials from the literature [36, 43, 160, 173, 184–186]. A full list of the tested potentials is included in Table E.1. We found that none of these sets of potentials produced a stable system, and refinement of the parameters did not improve the model sufficiently (see Appendix E.1). Therefore we manually adjusted the potential paramters in a systematic fashion and refined our new potentials. The final set of potential parameters that were used for all subsequent atomistic calculations is listed in Table 4.1. A comparison of the experimental and calculated structures is shown in Table 4.2, and indicates an excellent reproduction of the observed structure of $SrFeO_2$.

Table 4.3: Comparison of the experimental structure of $SrFeO_2$ and that calculated using the DFT model.

Parameter		Expt.	Calc.	Δ	Deviation /%
a, b	/Å	3.991	4.041	0.050	1.26
c	/Å	3.474	3.499	0.025	0.73
Vol.	/Å^3	55.33	57.15	1.82	3.29
Sr−O	/Å	2.646	2.673	0.027	1.02
Fe−O	/Å	1.996	2.021	0.025	1.23

Our electronic structure calculations were performed primarily with VASP, using the projector augmented wave (PAW) pseudo-potential and a kinetic energy cut-off of 500 eV for the plane-wave basis set. The generalised gradient approximation (GGA) of Perdew and Wang (PW91) [126] was used as the parameterisation of the exchange–correlation functional. The atomic limit version of the on-site correlation correction (GGA+U) approach was used [128, 130], with a Ueff value of 4.0 eV. An initial magnetic moment was applied to the Fe ions in order to align their spins at the start of the calculation. We find antiferromagnetic ordering of the Fe spins to be the most favourable, which is in accordance with previous experimental [56] and theoretical results [182].

In order to investigate the insertion of a single oxide ion interstitial into the $SrFeO_2$ lattice, our main DFT calculations were run on a $4 \times 4 \times 4$ (256 atom) supercell of the material. A comparison of the experimental and calculated structures, shown in Table 4.3, indicates our model reproduces the experimental structure well, with all lattice parameters and bond distances within 1.3 % of the experimental values.

The density of states (DOS) data from our supercell DFT model is shown in Figure 4.3b. The data for the bulk structure correspond very well to that of Pruneda et al. [182], indicating that our electronic structure model is behaving in a satisfactory manner. The occupied down-spin d_{z^2} state and the hybridisation (coincident peaks) of the d_{z^2} and $4s$ states can be seen.

We note that, in comparison to the data of Pruneda et al., our calculated DOS for the bulk structure shows an overall movement of peaks towards the Fermi energy, suggesting that the calculations differ in their effective values of U. The reversal in energy of the minority spin d_{xy} and d_{xz}, d_{yz} orbitals between the two data sets is probably due to a difference in the parameterisation of the GGA functional used. Discussion of Figure 4.3c can be found in Section 4.2.3.

4.2.2 Intrinsic Atomic Defects

We undertook defect calculations, using the potential-based model, to investigate posisble intrinsic defects within the $SrFeO_2$ material. Firstly, we considered the formation of Frenkel disorder, full- and partial-Schottky disorder and cation anti-

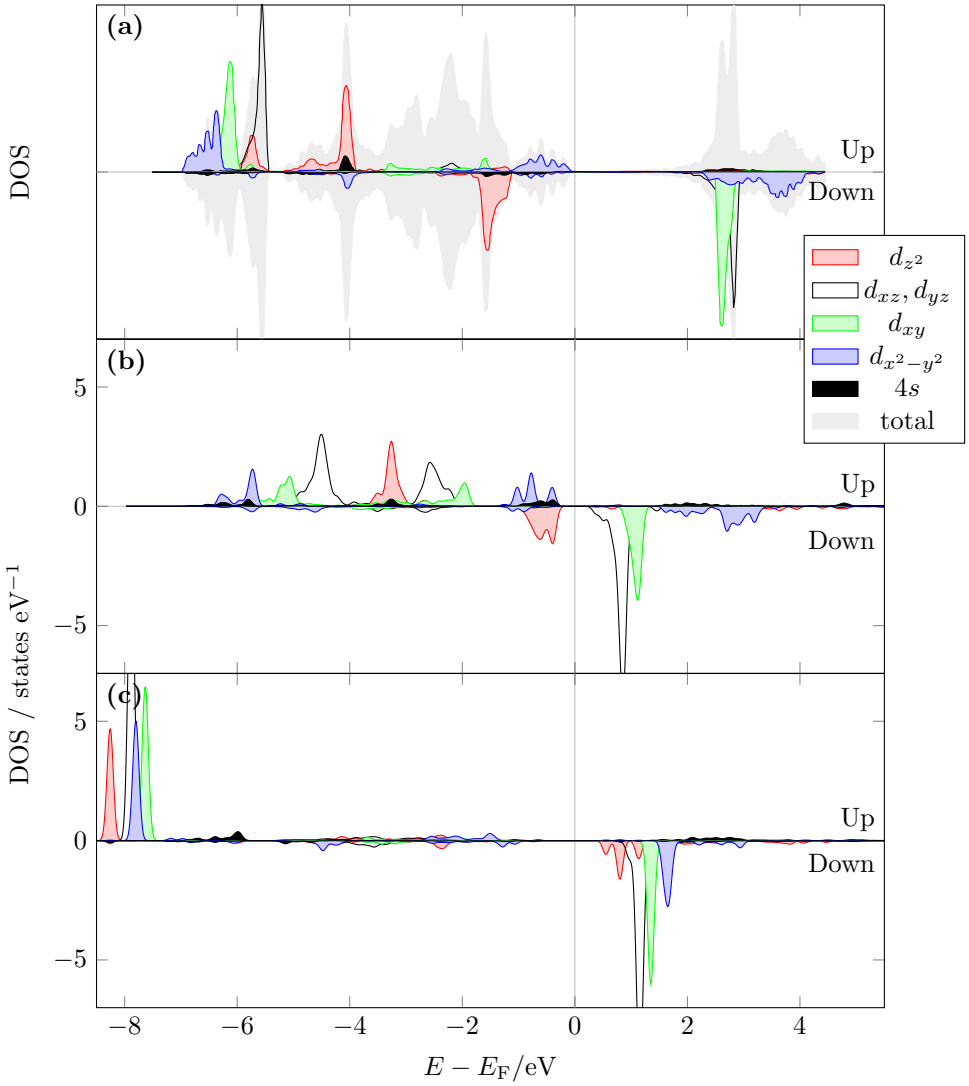

Figure 4.3: Comparison density of states (DOS) data for a single Fe^{2+} ion in DFT calculations of $SrFeO_2$. (a) Data from the 16-atom cell of Pruneda et al. [182], clearly showing occupied down-spin d_{z^2} states below the Fermi at about -1.5 eV and the hybridisation (coincident peaks) of the d_{z^2} and $4s$ states at about -4 eV; (b) Data from the $4 \times 4 \times 4$ supercell used in this study, which correspond well to that of Pruneda et al.; (c) Data from an Fe^{2+} ion directly neighbouring an interstitial oxide ion inserted into the $4 \times 4 \times 4$ supercell used in this study. Upon oxidation of the Fe ion, the down-spin d_{z^2} becomes unoccupied, and the up-spin states move further into the occupied band and become more localised (ionic).

Table 4.4: Energies of isolated point defects within the perfect $SrFeO_2$ lattice.

(a) Vacancies and substitutional defects.

Type of Defect	Symbol	Defect Energy /eV
Sr^{2+} Vacancy	V''_{Sr}	21.64
Fe^{2+} Vacancy	V''_{Fe}	25.87
O^{2-} Vacancy	$V^{\cdot\cdot}_{O}$	20.65
Sr on Fe	$Sr^{\times}_{Fe}$	8.48
Fe on Sr	$Fe^{\times}_{Sr}$	-4.22
Fe^{3+} on Fe^{2+}	$F^{\cdot}_{Fe}$	-23.56

(b) Three possible interstitial sites.

		Defect Energy /eV		
Wyckoff Position	Coordinates	$S^{\cdot\cdot}_{i}$	$F^{\cdot\cdot}_{i}$	O''_{i}
1b	(0, 0, 1/2)	-7.16	-12.21	-16.23
2e	(1/2, 0, 1/2) (0, 1/2, 1/2)	-4.23	-12.73	-13.44
1c	(1/2, 1/2, 0)	-1.28	-16.35	-2.64

site disorder. The equations for these processes are listed below:

Full Schottky: $$Sr^{\times}_{Sr} + Fe^{\times}_{Fe} + 2\,O^{\times}_{O} \longrightarrow V''_{Sr} + V''_{Fe} + 2\,V^{\cdot\cdot}_{O} + SrFeO_2 \quad (4.1)$$

SrO Schottky: $$Sr^{\times}_{Sr} + O^{\times}_{O} \longrightarrow V''_{Sr} + V^{\cdot\cdot}_{O} \quad (4.2)$$

FeO Schottky: $$Fe^{\times}_{Fe} + O^{\times}_{O} \longrightarrow V''_{Fe} + V^{\cdot\cdot}_{O} \quad (4.3)$$

Sr Frenkel: $$Sr^{\times}_{Sr} \longrightarrow V''_{Sr} + S^{\cdot\cdot}_{i} \quad (4.4)$$

Fe Frenkel: $$Fe^{\times}_{Fe} \longrightarrow V''_{Fe} + Fe^{\cdot\cdot}_{i} \quad (4.5)$$

O Frenkel: $$O^{\times}_{O} \longrightarrow V^{\cdot\cdot}_{O} + O''_{i} \quad (4.6)$$

Sr/Fe anti-site: $$Sr^{\times}_{Sr} + Fe^{\times}_{Fe} \longrightarrow Fe^{\times}_{Sr} + Sr^{\times}_{Fe} \quad (4.7)$$

In order to examine the energetics of these formation processes, we calculated the energies of each of their constituent point defects, and lattice energies as required. Defect energies were calculated using the Mott–Littleton two region approach, with radii of 13 and 25 Å for regions 1 and 2a respectively. The energies of the individual point defects are shown in Table 4.4. Interstitials were considered on three sites, shown in Figure 4.4, with Wyckoff positions 1b, 1c and 2e as listed in Table 4.4b.

The interstitial oxide ion is found to be most favourable on the 1b site, which is the same site that it occupies in the parent perovskite $SrFeO_3$ structure. This prediction is supported by our DFT calculations, which also find this site to be most favourable. The relaxation of the lattice around the interstitial defect is shown in Figure 4.5. The distortion of the lattice oxide ions away from the inserted interstitial oxide ion is apparent, as well as the relaxation of the strontium ions towards the defect. This

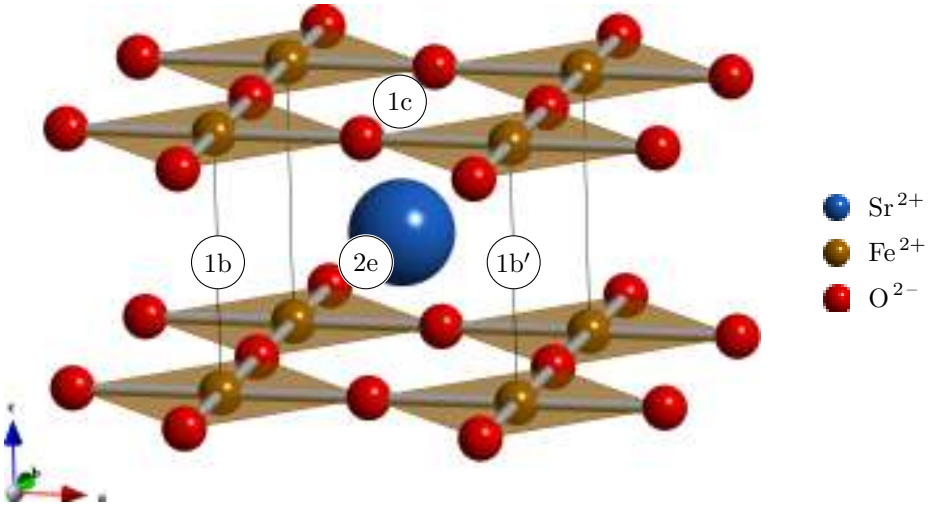

Figure 4.4: Positions of three possible sites for interstitial ions within the $SrFeO_2$ lattice, labelled using their Wyckoff labels.

relaxation is similar in both the DFT model and the atomistic model, implying that the atomistic approximation is performing well for these types of defects.

The formation energies of the intrinsic defect listed in Equations 4.1–4.7 are shown in Table 4.5. The anti-site and oxide Frenkel defects exhibit the lowest energy, but it is noted that all the formation energies are high with respect to other fast ion conductors. As a result, the concentration of intrinsic atomic defects of these types is predicted to be very low. For example, the energy of the oxide ion Frenkel corresponds defect concentration of around 1.6×10^{-16} defects per formula unit.

4.2.3 Redox Chemistry

An understanding of the redox behaviour of $SrFeO_2$ is critical for understanding the conditions in which various conductivity regimes may be exploited. We modelled the oxidation process in $SrFeO_2$ using both atomistic and DFT techniques.

As in the Nd_2NiO_4 system, oxidation proceeds in the following manner:

$$\tfrac{1}{2}O_2 \rightleftharpoons O_i'' + 2\,h^{\bullet}, \tag{4.8}$$

where, in the atomisitic calculations, the hole species $h^{\bullet}$ is modelled explicitly as a small polaron, on either the iron site ($Fe^{2+} \longrightarrow Fe^{3+}$) or the lattice oxygen site ($O^{2-} \longrightarrow O^{-}$). Within the electronic structure calculations, however, no such assumption is made as the additional electrons from inserted oxygen atom are incorporated into a new ground state electron density.

Our atomistic simulation predicts that the hole resides on the iron. This prediction is confirmed by our electronic structure calculations, which shows a change in

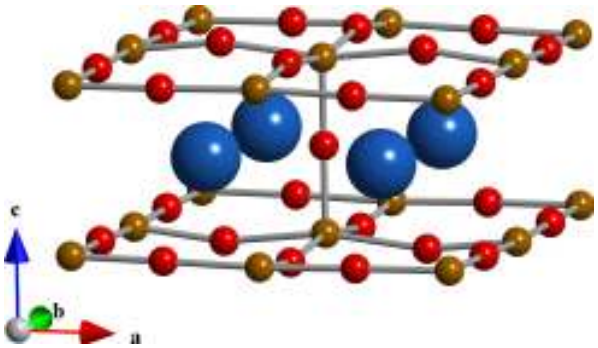

(a)

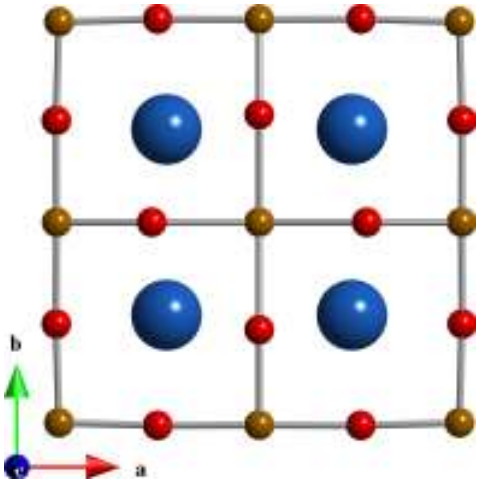

(b)

Figure 4.5: Local relaxation around an interstitial oxide ion inserted at the 1b position within the $SrFeO_2$ lattice viewing (a) in three dimensions and (b) down the *c* axis. The distortion of the lattice oxide ions away from the inserted interstitial is aparent, as well as the relaxation of the strontium ions towards the defect.

Table 4.5: Formation energies for intrinsic defects in $SrFeO_2$.

Defect	Equation	Total Formation Energy /eV	Formation Energy /eV defect^{-1}
Full Schottky[a]	4.1	14.25	3.56
SrO partial Schottky[b]	4.2	7.70	3.85
FeO partial Schottky[b]	4.3	5.12	2.56
Sr Frenkel	4.4	14.48	7.24
Fe Frenkel	4.5	9.52	4.76
O Frenkel	4.6	4.41	2.21
Sr/Fe Anti-site	4.7	4.26	2.13

[a] A lattice energy of -74.56 eV was calculated for for $SrFeO_2$.

[b] The lattice energies used for SrO and FeO were -34.59 and -41.40 eV respectively, and were calculated using structures from [187] and [188].

magnetic moment consistent with an increase in oxidation state for the two Fe ions neighbouring the inserted interstitial oxide ion. The DOS (Figure 4.3c) shows that the down-spin d_{z^2} orbital is above the Fermi level (i.e., unoccupied) in the Fe^{3+} ion. The up-spin d electrons obey Hund's rule, and move deeper into the occupied band. The narrower DOS peaks for the oxidised Fe ions indicate that bonding has become much more localised (ionic) than for the bulk structure.

We find that oxidation of $SrFeO_2$ with oxide ion interstitial formation is highly favourable (exothermic), which is in accordance with the original experimental findings [56]. An oxidation energy of -0.84 eV per electronic defect was calculated using the DFT model. This value is similar to experimental enthalpies of oxidation of $SrFeO_{2.5}$ to $SrFeO_3$, which range from -0.83 to -1.43 eV [189]. The insertion of interstitial oxide ions into the $SrFeO_2$ lattice may be important for the oxide ion transport properties of the material, especially given the low predicted concentration of intrisic Schottky- and Frenkel-type defects.

4.2.4 Oxide Ion Migration

Oxide ion migration within the $SrFeO_2$ lattice is of critical importance to the potential application of the material in electrochemical devices. When first considering possible oxide ion migration mechanisms it is tempting to propose a linear pathway in the [1 0 0] direction, directly between two interstitial sites and between the FeO layers. Atomistic calculations using a $4 \times 4 \times 4$ supercell of the material rule out this possibility, however, as placing the interstitial oxide ion at the 2e site (Figure 4.4) produces imaginary vibrational frequencies, indicating that this configuration is unstable.

All of the possible mechanisms of oxide ion migration other than the direct linear pathway include migration of the lattice oxide ions in addition to the interstitial. Ion hops can occur in an isolated fashion, which is directly equivalent to the vacancy hops in an oxygen deficient perovksite, or in a concerted interstitialcy-type mechanism similar to that found in the Ruddlesden–Popper-type phases.

To test the possible migration mechanisms involving lattice oxide ions, we performed nudged elastic band (NEB) calculations on a $4 \times 4 \times 4$ supercell of $SrFeO_2$. Single hops of lattice ions in the centre of the cell were tested both in isolation (Figure 4.6) and neighbouring an existing interstitial oxide ion (Figure 4.7). The barriers to all of these single-ion hops were found to be large (at least 1 eV). Further calculations also suggest the vacancies resulting from these lattice ion hops may be mobile in the FeO plane (see Appendix E.2).

The energy barriers for concerted oxide ion migration (Figure 4.8) were found to be very high in energy, and structures near the maximum were found to be unstable. Therefore, the prediction from our static lattice calculations is that the oxide ion conductivity of $SrFeO_2$ is low and proceeds in a stepwise manner.

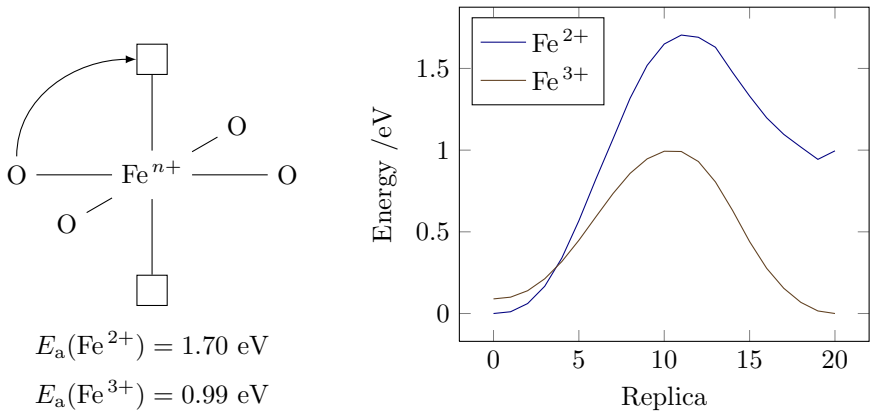

(a) **(b)**

Figure 4.6: (a) Schematic illustration of a single oxide ion migration pathway between an occupied lattice site and a vacant interstitial site; (b) migration energy profiles for oxide ions moving along this pathway neighbouring both Fe^{2+} and Fe^{3+}.

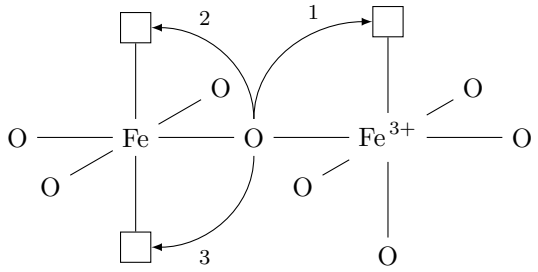

$E_{a1} = 1.01$ eV; $E_{a2} = 1.36$ eV; $E_{a3} = 1.95$ eV

(a)

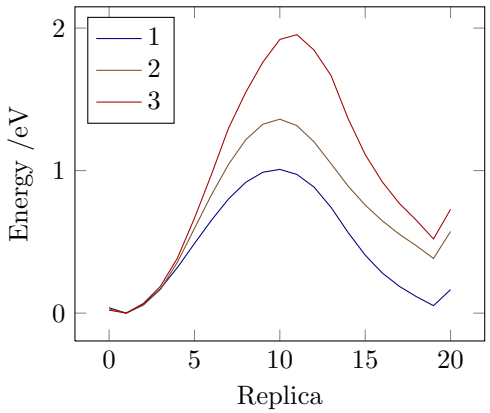

(b)

Figure 4.7: (a) Schematic illustration of single oxide ion migration pathways to a vacant interstitial site from an occupied lattice site adjacent to an existing interstitial; (b) migration energy profiles for oxide ions moving along these pathways.

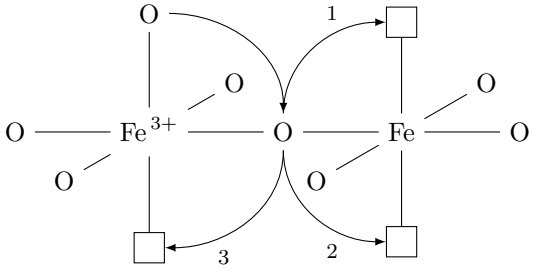

(a)

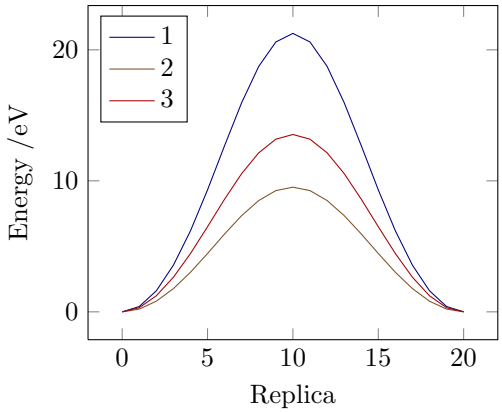

(b)

Figure 4.8: (a) Schematic illustation of possible cooperative migration mechanisms in which an existing intersitial ion displaces a lattice ion (unnumberred arrow) onto an adjacent interstitial site in a concerted manner; (b) migration energy profiles for oxide ions moving along these pathways.

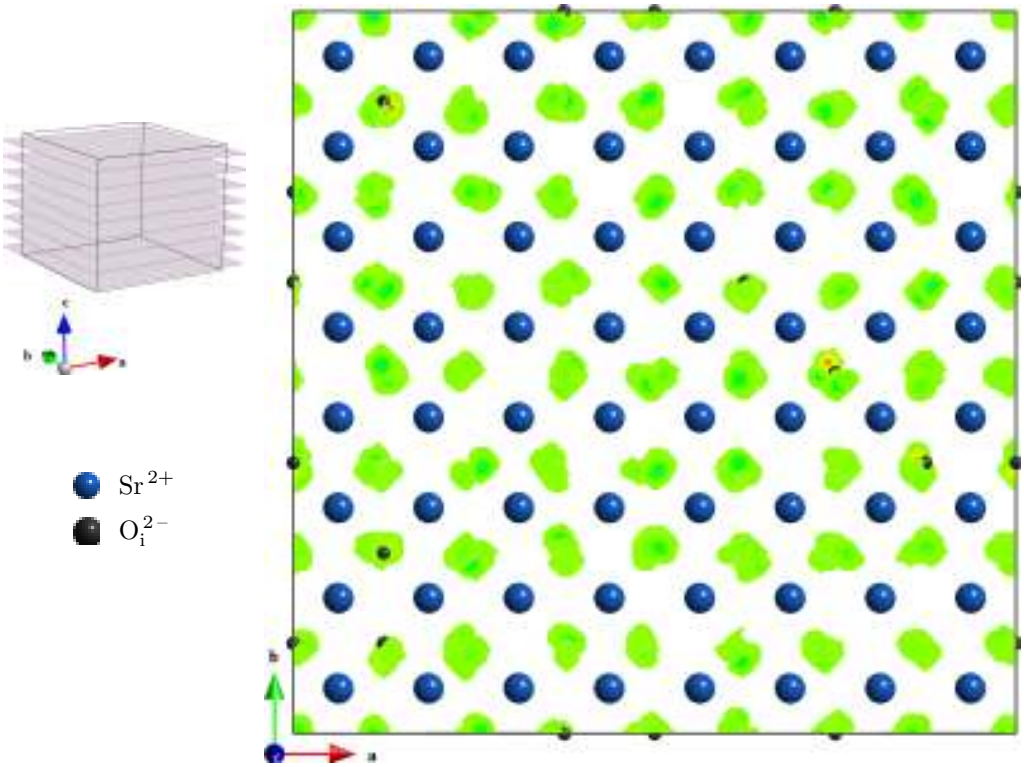

Figure 4.9: Composite image of sections, through each Sr-containing plane, of the oxygen time-averaged density data from MD simulations of an $8 \times 8 \times 8$ supercell of $SrFeO_{2.06}$. The 3D unit cell illustrates which planes compose the image.

Further insight into the migration properties of $SrFeO_{2.06}$ was obtained from MD simulations, outlined in Appendix E.2. Firstly, the results of these simulations support the prediction that there is no direct oxide ion migration in the [1 0 0] direction between the interstitial sites, as illustrated by Figure 4.9. Instead, oxide ions appear to move along all the pathways predicted by our static-lattice calculations (Figures 4.10 and 4.11).

In agreement with the high migration energies obtain using our NEB calculations, our MD simulations predict that the oxide ion diffusivity is low. MSD data, shown in Figure 4.12, provides a mean diffusion coefficient of around 2.3×10^{-9} cm^2 s^{-1} for the oxide species, which equates to a conductivity of around 4.2×10^{-4} S cm^{-1}. Despite slow diffusion, however, the oxide ion sublattice shows a considerable amount of disorder during the simulation, to the point where the RDFs of the original lattice and interstitial ions with respect to Fe have become essentially indistinguishable (Figure 4.13).

Decomposing the oxide ion MSD data into x, y and z components (Figure 4.14) reveals that the MD simulation predict highly isotropic diffusion, a result which contrasts with our static lattice calculations. Structural analysis of the simulation cell reveals that the square-planar units have undergone a distortion to become more tetrahedron-like at the high simulation temperatures employed, although the

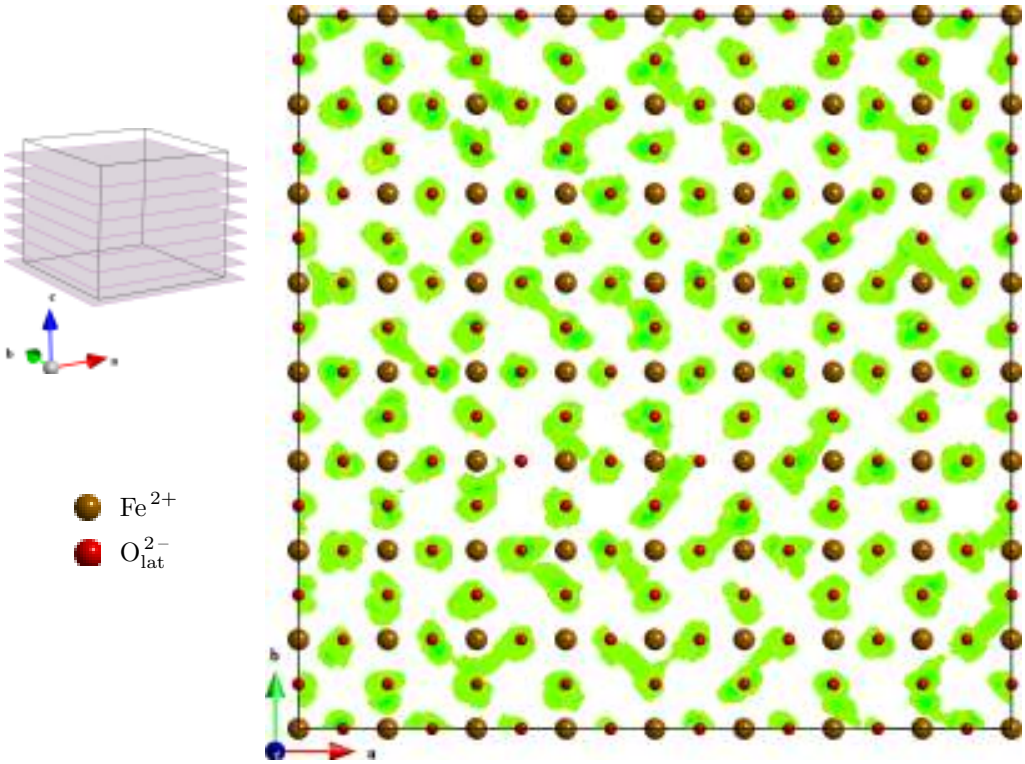

Figure 4.10: Composite image of sections, through each Fe- and O-containing plane, of the oxygen time-averaged density data from MD simulations of an $8 \times 8 \times 8$ supercell of $SrFeO_{2.06}$, viewing down the c axis. The 3D unit cell illustrates which planes compose the image.

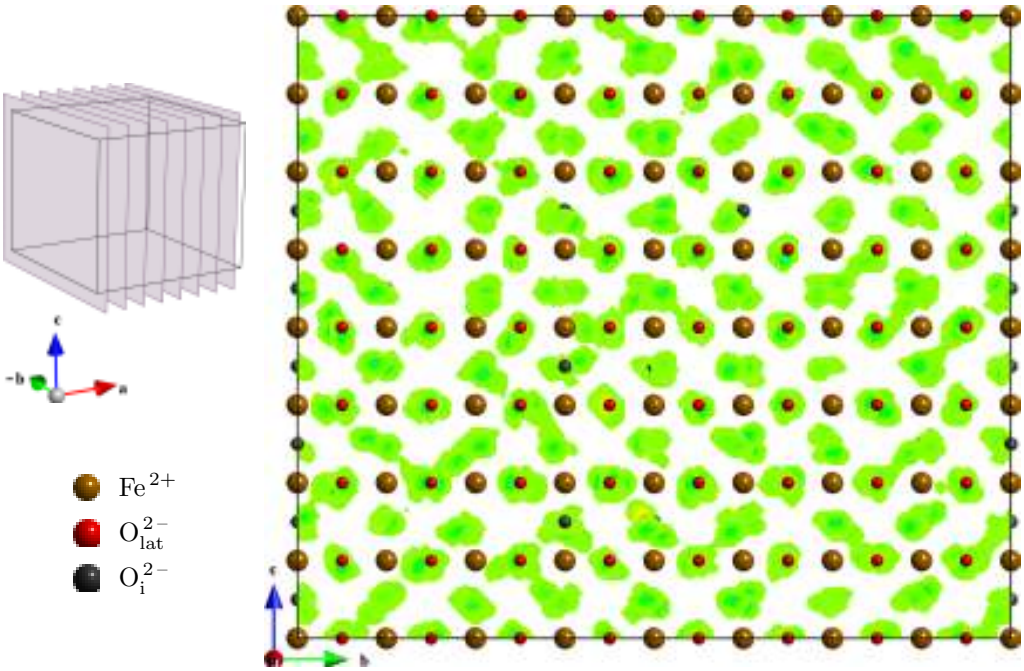

Figure 4.11: Composite image of sections, through each Fe- and O-containing plane, of the oxygen time-averaged density data from MD simulations of an $8 \times 8 \times 8$ supercell of $SrFeO_{2.06}$, viewing down the a axis. The 3D unit cell illustrates which planes compose the image.

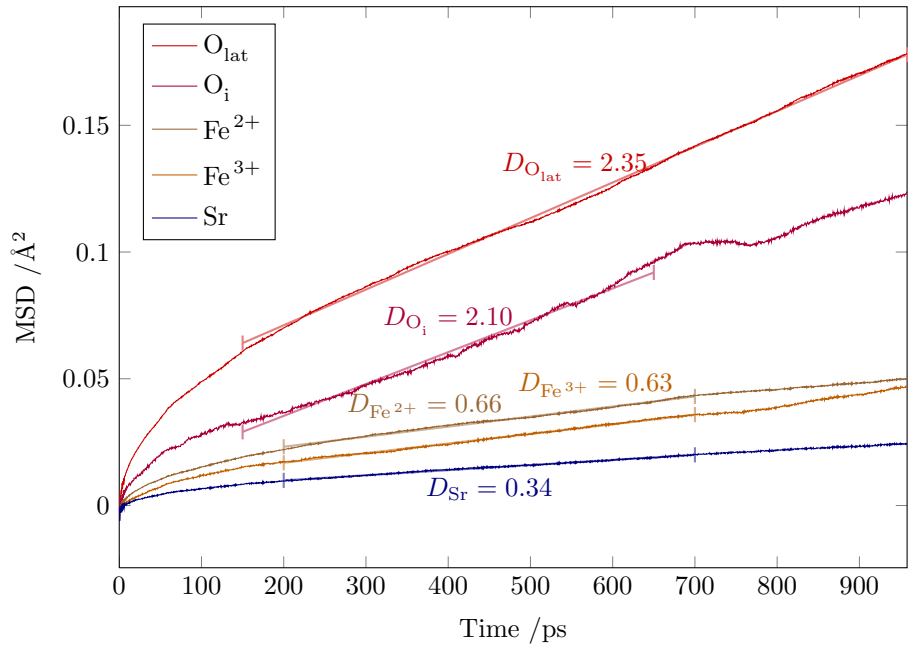

Figure 4.12: Mean square displacement (MSD) data for each ion-type in $SrFeO_{2.06}$ at 1073 K. Least squares regression lines have been calculated between the points indicated by the vertical check marks, and their corresponding self-diffusion coefficients (in units of 10^{-9} cm^2 s^{-1}) are included.

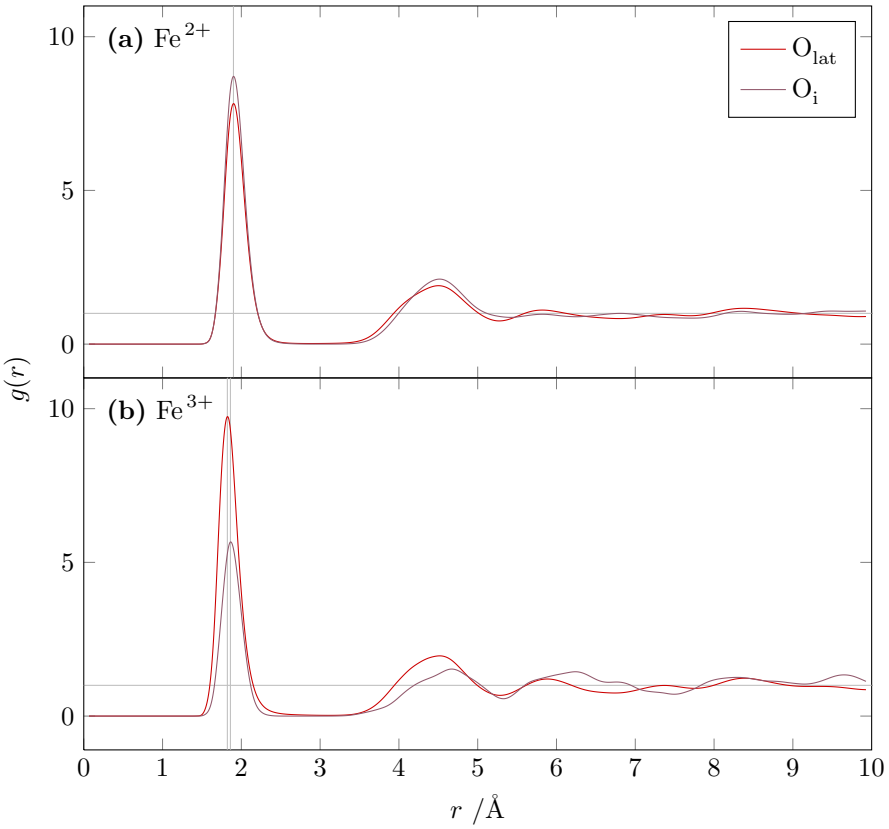

Figure 4.13: Plot of the radial distribution function between iron and oxide ions $SrFeO_2$ at 1073 K. The horizontal line indicates $g(r) = 1$, the probability of finding an ion at distance r in a unform distribution. Vertical lines are added as a guide to the eye for peak centres.

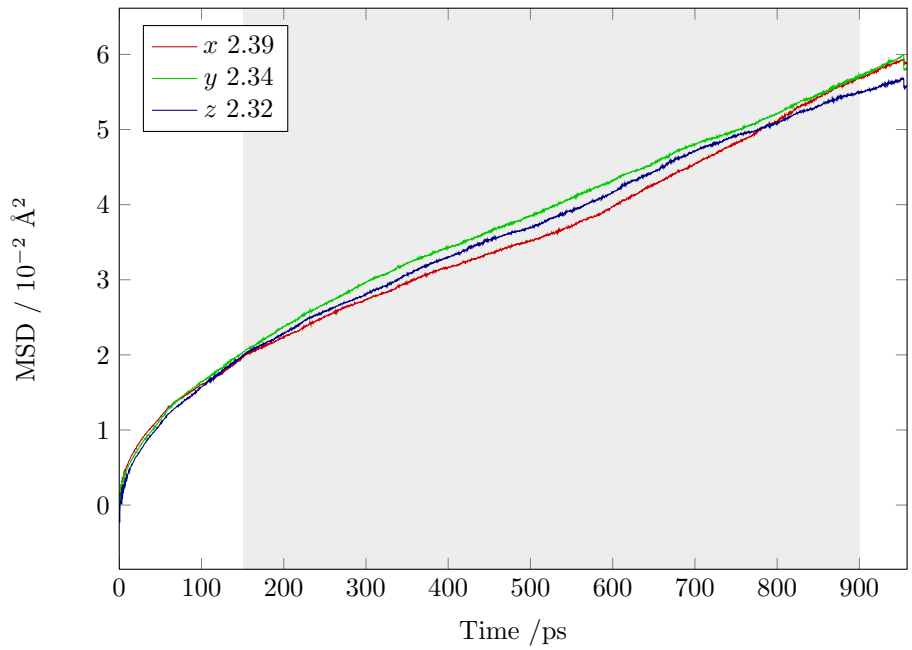

Figure 4.14: MSD data for oxide ions in $SrFeO_2$ at 1073 K separated into x, y and z components. Linear regression analysis was performed for the time-span highlighted in grey, yielding the diffusion coefficients (in units of 10^{-9} cm^2 s^{-1}) included in the key.

cell retains its tetragonal proportions. The Fe···O RDFs (Figure 4.13) shows single, well-defined peaks for the nearest neighbour Fe···O, suggesting a more isotropic Fe environment. It is noted that the coordinational and structural flexibility of cation species, such as Fe, is believed to be a crucial feature in fast interstitial oxide-ion conductors [190–192].

4.2.5 Cation Dopants

The importance of introducing small amounts of a 'foreign' ion into the perfect crystal lattice to create defects and thus influence the physical properties of a material has been discussed previously (Section 1.5.1 and Appendix A). In this study, we considered the following dopant reactions (or 'solution' processes):

$$(\mathrm{D}^{1+}) \qquad \tfrac{1}{2}\mathrm{D_2O} + \mathrm{M_M^\times} + \tfrac{1}{2}\mathrm{O_O^\times} \longrightarrow \mathrm{D_M'} + \tfrac{1}{2}\mathrm{V_O^{\bullet\bullet}} + \mathrm{MO}, \tag{4.9}$$

$$(\mathrm{D}^{2+}) \qquad \mathrm{DO} + \mathrm{M_M^\times} \longrightarrow \mathrm{D_M^\times} + \mathrm{MO}, \tag{4.10}$$

$$(\mathrm{D}^{3+}) \qquad \tfrac{1}{2}\mathrm{D_2O_3} + \mathrm{M_M^\times} \longrightarrow \mathrm{D_M^\bullet} + \tfrac{1}{2}\mathrm{O_i''} + \mathrm{MO}; \tag{4.11}$$

where D represents a dopant ion, and M represents either the Sr^{2+} or the Fe^{2+} lattice ion.

To calculate the defect energies of the isolated dopant ions within the lattice, we used Buckingham potential and shell-model parameters for the dopant ion from a number of sources [36, 160, 161, 193–195]. The full list of parameters pertaining to

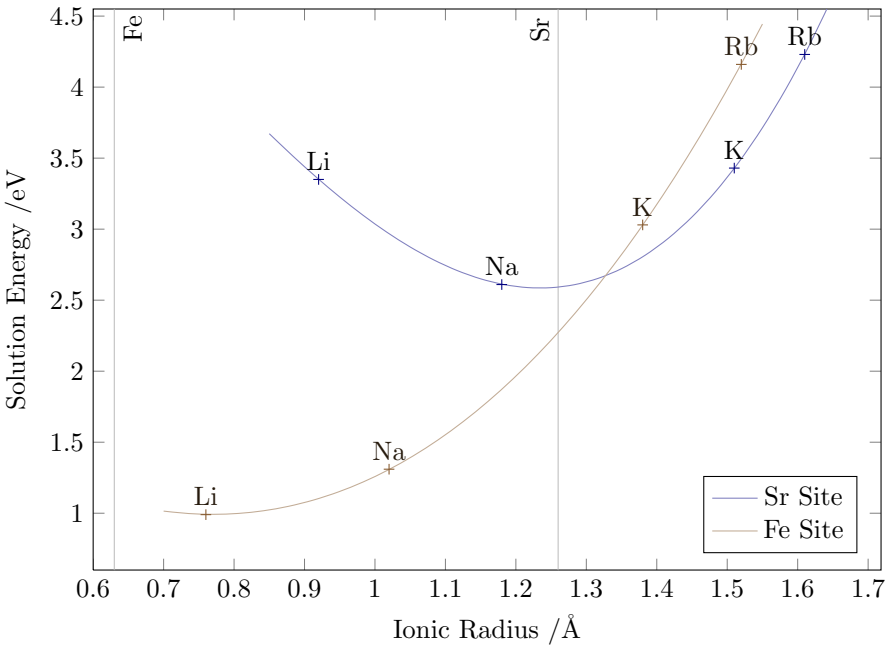

Figure 4.15: Solution energies of selected monovalent dopants (alkali metals) on both the strontium and iron sites in $SrFeO_2$. Note that polynomial lines of best fit have been added purely as a guide to the eye. The ionic radii of Sr^{2+} and Fe^{2+} are also indicated.

the dopant ions is reproduced in the appendix (Table E.2). In order to calculate the energies of these solution reactions, the appropriate defect and lattice energies must be combined. For example, the energy of the monovalent doping process in Equation 4.9 would be calculated using

$$E_{\text{soln}}(\text{D}^{+}) = E(\text{D}'_{\text{M}}) + {}^{1}/_{2}E(\text{V}^{\bullet\bullet}_{\text{O}}) + U_{\text{latt}}(\text{MO}) - U_{\text{latt}}(\text{D}_2\text{O}). \tag{4.12}$$

The structures of the corresponding oxides were taken from a variety of sources [165, 187, 188, 196–211] in order to calculate the lattice energies required to determine the solution energies for mono-, di- and trivalent cation dopants, which are are plotted against the dopant's ionic radii in Figures 4.15, 4.16 and 4.17 respectively.

The isovalent dopants Co, Mn, Ni and Mg were found to be the most favourable species for incorporation into the $SrFeO_2$ lattice overall, and are predicted to occupy the Fe site. Li on the Fe site is found to be the most favourable monovalent dopant, whilst La, Gd and Y on the Sr site are found to be the most favourable trivalent dopants. Thus, it may be feasible to introduce excess oxgyen into the $SrFeO_2$ lattice using La, Gd or Y dopants, which warrants further investigation experimentally. Although the energies of Ca are similar on both the Sr and Fe sites, it is noted that experimentally Ca is found to occupy only the Sr site [179, 180].

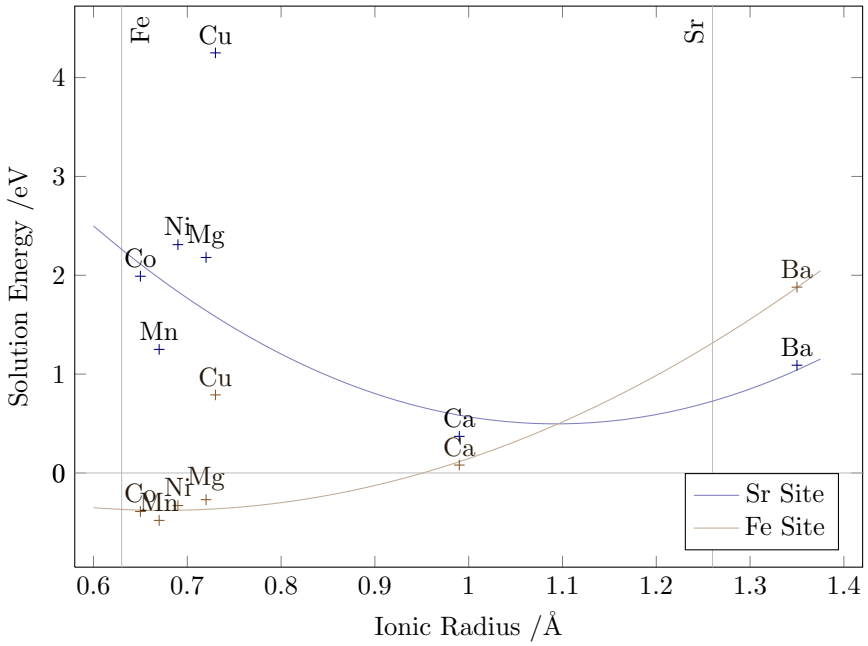

Figure 4.16: Solution energies of selected divalent dopants (alkaline-earth metals and first row transition metals) on both the strontium and iron sites in $SrFeO_2$. Note that polynomial lines of best fit have been added purely as a guide to the eye.

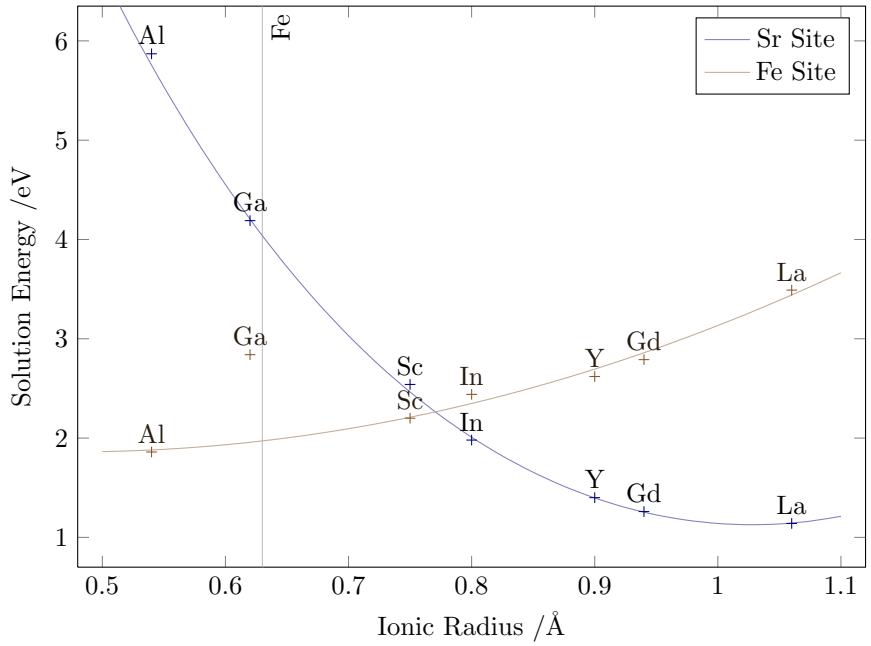

Figure 4.17: Solution energies of selected trivalent dopants on both the strontium and iron sites in $SrFeO_2$. Note that polynomial lines of best fit have been added purely as a guide to the eye.

4.3 Chapter Summary

We have developed effective atomistic and DFT models that accurately reproduce the observed structure of the new layered material $SrFeO_2$. We note that although modelling this material is not a trivial task, our atomistic model is stable and our calculated electronic structure accords well with that calculated by Pruneda et al. [182]. The atomistic calculations predict that the formation of intrinsic atomic defects is relatively unfavourable, although the preferred mode would be of the O Frenkel type.

Both our atomistic and DFT models predict the position of interstitial oxide ions to be between the Fe atoms of the FeO layers, which is the position occupied in the parent $SrFeO_3$ perovskite structure. Oxidation is predicted to involve the formation of holes on the Fe site in addition to the insertion of interstitial oxide ions. The oxidation energy of -0.84 eV per electronic defect predicted using our detailed DFT model is highly favourable, which is consistent with the low-temperature oxygen uptake of the material found experimentally [56]. It may also be possible to introduce excess oxygen into $SrFeO_2$ via doping with La, Gd or Y on the Sr site, which warrants further experimental investigation.

The migration of oxide ions in the lattice was found to occur via a step-wise mechanism comparable to the vacancy-hopping mechanism found in the perovskite-type materials, rather than by a direct interstitial or interstitialcy mechanism. NEB calculations predict that the activation barrier to migration is high, however, which is supported by low diffusion coefficients obtained using MD simulations.

Chapter 5

Dopant Chemistry of the $La_{9.33}(GeO_4)_6O_2$ Apatite Material

5.1 Background

5.1.1 Apatite-structured Oxide-ion Conductors

The apatite-type oxides are an intriguing class of material that have shown high levels of oxide ion conductivity and are being researched extensively as candidate SOFC electrolytes. Fast oxide ion conductivity was first discovered in the silicate-based apatites $Ln_{9.33}(SiO_4)_6O_2$ (where Ln is typically a large lanthanide ion) in the mid-1990s [60, 61], and a large number of experimental and computational studies have subsequently been undertaken to elucidate the structure–property relationships in the materials, reviews of which may be found elsewhere [23, 34].

The general formula of the apatite oxides is $M_{10}(XO_4)_6O_{2\pm y}$, where M is a rare-earth or alkaline earth metal and X is a *p*-block element such as Si or Ge. These oxides share the same structure as the well-known apatite minerals and the hydroxy-apatite biomaterials that compose mammalian bones and tooth enamel [34, 58, 59]. The structure, shown in Figure 5.1, consists of isolated XO_4 tetrahedra arranged to form two distinct types of channel that run parallel to the *c* axis. One channel type contains staggered triangles of lanthanum ions (La1) surrounding a central row of oxide (O5) ions. The other channel type contains just single rows of lanthanum ions (La2).

A number of rare-earth apatite systems have been synthesised. The highest oxide ion conductivities are observed for the Si- and Ge-based systems with the larger rare-earth cations, particularly lanthanum [60, 61, 212]. These conductivities are

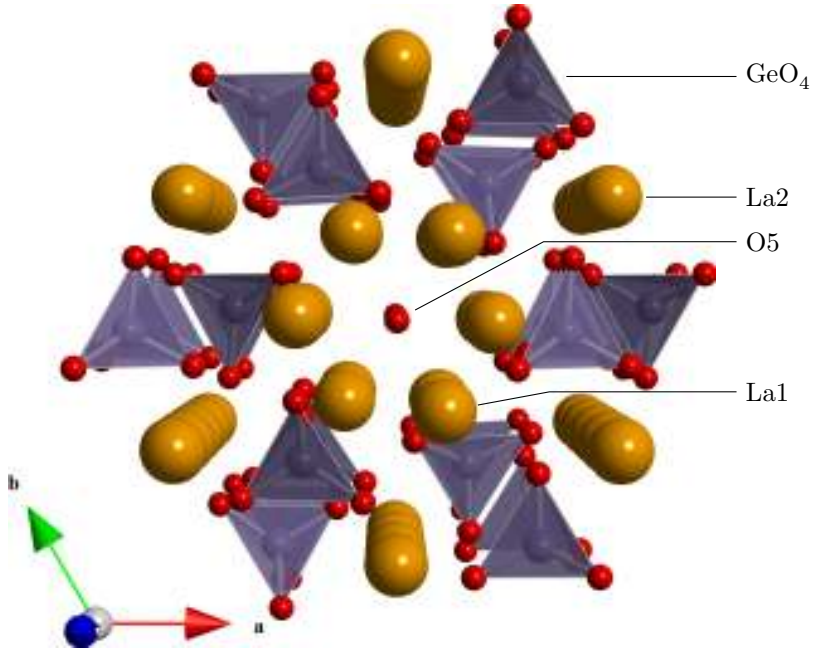

Figure 5.1: Structure of lanthanum germanium apatite, $La_{9.33}(GeO_4)_6O_2$.

comparable to other electrolytes being considered for SOFC applications, as was shown in Figure 1.6.

5.1.2 Interstitial Oxide Ions and Ionic Conductivity

The principal defects responsible for the high ionic conductivity of the apatite materials are interstitial oxide ions. The cation and oxygen stoichiometries of these materials can be varied considerably, and have a significant effect upon the ionic conductivity. The completely stoichiometric materials $La_8M_2(SiO_4)_6O_2$, where M is an alkaline earth, show very low levels of conductivity, whilst materials with vacancies on the rare-earth site, such as $La_{9.33}(SiO_4)_6O_2$, show improved conductivity. Using both atomistic modelling and neutron powder diffraction, this improvement has been attributed to the presence of interstitial oxide ions through Frenkel disorder, the formation of which is promoted by the presence of the cation vacancies [16, 213, 214].

For both Si- and Ge-based apatites, the highest oxide ion conductivities are observed for oxygen excess materials such as $La_9M(SiO_4)_6O_{2.5}$ or $La_{9.33+x}(SiO_4)_6O_{2+1.5x}$, due to the presence of larger numbers of the interstitial charge-carriers. For example, at 500℃ the conductivity of the latter material increases from 1.1×10^{-4} S cm^{-1} for $x = 0$ to 1.3×10^{-3} S cm^{-1} for $x = 0.34$ [213]. The germanate material is reported to tolerate higher oxygen overstoichiometries than the silicate [23], with the important implication of higher possible conductivities for these materials.

The favoured interstitial site in the silicate material $La_{9.33}(SiO_4)_6O_2$ is at the periph-

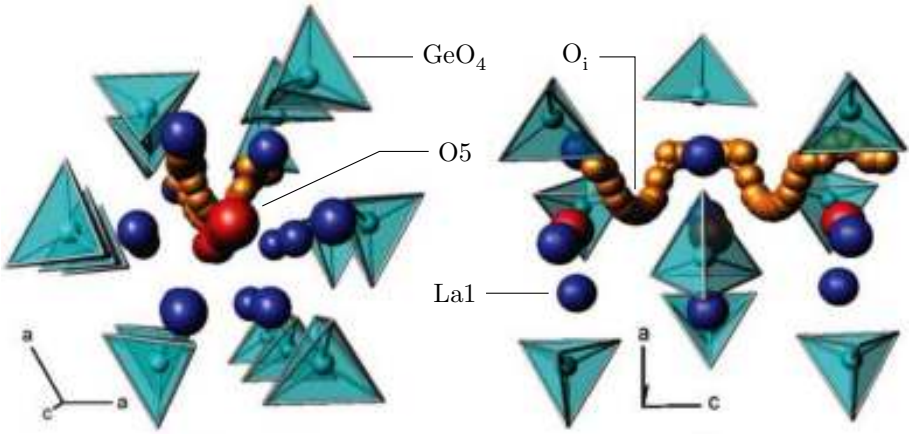

Figure 5.2: The "sinusoidal-like" interstitial oxide ion migration pathway predicted using a static-lattice atomistic model of $La_{9.33}(SiO_4)_6O_2$ [16], reproduced from [34].

ery of the La1/O5 channel. This position was first predicted by atomistic modelling of the material [16], and has subsequently been supported by ^{29}Si NMR, Raman spectroscopy, and x-ray and neutron diffraction [215–218]. In the germanium analogue, more recent atomistic modelling has identified two equally favourable interstitial sites: one at the channel periphery, as in the Si-based material, and one directly in between two GeO_4 tetrahedra, forming a Ge_2O_9 unit [219]. Because of lattice relaxation, however, these sites are effectively identical. The presence of interstitial oxide ions within the channel walls of the germanate system is consistent with neutron diffraction studies [220, 221].

The above static-lattice models have also been used to predict the oxide ion migration pathways in both materials [16, 219]. For the Si-based material, a "sinusoidal-like" pathway is found, in which the oxide interstitial meanders down the La1/O5 channel as shown in Figure 5.2. In contrast, oxide ion migration in the Ge analogue is predicted to occur via the "fan-like" mechanism shown in Figure 5.3, in which the migrating ion is passed between GeO_4 units well away from the La1/O5 channel.

An activation energy of 0.56 eV was calculated for the "sinusoidal-like" (silicate) pathway, whilst a value of 0.79 eV was calculated for the "fan-like" (germanate) pathway respectively. These values compare well with experiment, which provides values of between 0.65 and 0.74 eV for the silicate material, and 0.94 eV for the germanate [213, 219, 222]. The higher activation energies of the germanate system are commensurate with smaller observed conductivities at lower temperatures (< 600°C) compared to the silicate system. However, the germanate materials exhibit better conductivity than the silicates at higher temperatures (see Figure 1.6).

The flexibility of the silicate/germanate substructure is of critical importance to the oxide ion conduction mechanisms of the apatite materials. In the calculated mechanisms, shown in Figures 5.2 and 5.3, the progress of the migrating oxide ion is greatly facilitated by the cooperative distortion of the tetrahedral units. This

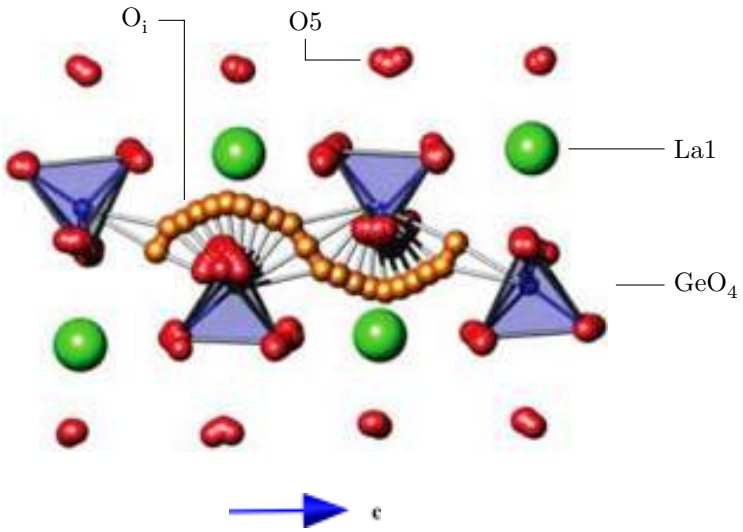

Figure 5.3: The "fan-like" interstitial oxide ion migration pathway predicted using a static-lattice atomistic model of $La_{9.33}(GeO_4)_6O_2$, reproduced from [219].

has been supported experimentally by high values for the thermal displacement parameters of the oxygen ions in the silicate groups [213].

5.1.3 Cation Doping and Project Objectives

The apatite structure is able to accommodate a wider variety of dopant species than most conventional fast oxide-ion conductors (such as YSZ or LSGM) in terms of both dopant size and charge state. Doping can significantly affect the oxide ion mobility within the materials, either directly or as a consequence of changes in stability or oxygen stoichiometry. In general, the conductivity of the silicate systems is more sensitive to the nature of the dopant than that of the germanates, which may be indicative of a range of conduction pathways in the germanates [34].

A range of experimental and theoretical doping studies have confirmed that larger dopant cations (such as Ca, Sr) are more favourable on the La site, whilst smaller dopant cations (such as Al, Ti) are more favourable on the Si/Ge site [34, 193]. Dopants with intermediate ionic radii (such as Mg, Mn, Ni, Cu, Co) are found to display 'ambi-site' behaviour, in which the dopant may be incorporated at either site. Furthermore, the charge of some transition metal dopants (such as Co) is determined by the site on which the dopant is present [34, 223].

The oxygen stoichiometry of the system, and hence its ionic conductivity, is easily altered by doping. As discussed in the previous section, the substitution of La with an alkaline-earth metal M, forming $La_{10-z}M_z((Si/Ge)O_4)_6O_{3-0.5z}$, reduces the amount of excess (interstitial) oxygen, and this reduction in the number of charge carriers leads to a reduction in conductivity.

At low-to-intermediate temperatures, germanate materials with high oxygen content have reduced, triclinic symmetry, which leads to more strongly bound oxygen and hence reduced conductivities [23, 34, 220, 221, 224]. The hexagonal structure can be stabilised at lower temperatures by site-selective doping on the La1 site with Y [225]. Conversely, doping on the Ge site (e.g., Co, Al, Ga) tends to result in triclinic cells.

Doping with subvalent cations onto the La2 site in the silicate materials has been found to reduce ionic conductivity, particularly with smaller cations (e.g., Mg^{2+}) [34]. This effect has been attributed to a reduction in coordination number of the La2 site from nine to six upon substitution with the smaller dopant, which is associated with the encroachment of an oxide ion of the silicate group into the oxide ion channel [226]. The germanate materials show less of a reduction in conductivity when doping on the La site, which is consistent with the differing conduction mechanisms of the two materials.

Subvalent doping on the Si site has, in contrast, been found to improve conduction [23, 34]. This has again been attributed to local relaxation factors, which widen the oxide ion channel and rotate the silicate group. Furthermore, it has been suggested that the ability of dopants such as Mg to increase their coordination sphere facilitates the structural changes required during migration [226].

Isovalent doping on the Si/Ge site, particularly with Ti, tends to reduce the conductivity of the apatite materials substantially [23, 227, 228]. It has been proposed that this is due to the 'trapping' of migrating oxide ions by Ti increasing its coordination sphere [34, 227–229]. Again, the observed reduction in conductivity is smaller for the germanates than for the silicates.

Despite this wealth of knowledge, particularly for the silicate systems, our understanding of the atomic-level dopant behaviour of Ge-apatite oxide-ion conductors is still incomplete. There is limited information on cation doping processes at the local structural level, particularly the role of dopants on the Ge site. There are also important questions relating to the dopant site selectivity and compensation mechanisms in these complex materials, the understanding of which is key to their optimisation for use in SOFCs or ceramic membranes.

In this work, well-established static-lattice atomistic modelling techniques are used, for the first time, to investigate the site selectivity and incorporation mechanisms of a range of D^{+}, D^{2+}, D^{3+} and D^{4+} dopants in the $La_{9.33}(GeO_4)_6O_2$ apatite material. Furthermore, local relaxation data may provide insight into dopant–interstitial association, which has a direct influence on oxide ion migration.

Table 5.1: Buckingham potential and shell model parameters used for modelling the germanium apatite $La_{9.33}(GeO_4)_6O_2$.

Ion[a] M	A /eV	ρ /Å	C /eV Å^6	Y /|e|	k /eV A^{-2}	Ref.
La^{3+}	4579.24	0.30438	0.0	-	-	[16]
Ge^{4+}	1497.3996	0.325646	16.0	-	-	[219]
O^{2-}	22764.30	0.14900	24.99	-2.89	74.920	[16, 231][b]

[a] Note the Buckingham parameters apply to the interaction $M\cdots O^{2-}$, whilst the shell model parameters apply just to the ion M itself.

[b] The C parameter has been modified for this work.

5.2 Results and Discussion

5.2.1 Structural Modelling

The starting point of our study is the modelling of the crystal structure and a comparison with experimental data. The structural data for the $La_{9.33}(GeO_4)_6O_2$ material modelled in this study was originally from Berastegui et al. [230], and was previously used in the atomistic modelling work of Kendrick et al. [219]. In order to achieve the required stoichiometry, two La2 vacancies are introduced into a $1 \times 1 \times 3$ $P1$ supercell of the perfect apatite structure.

The Buckingham potentials used for this study are listed in Table 5.1, along with references to their original sources. These potentials are the same as those used by Kendrick et al. with the exception of the O···O potential, in which the C parameter has been adjusted slightly to improve the stability of the cell. A comparison of the calculated and experimental structures is presented in Table 5.2.

Good agreement is shown between the simulated and experimental structures, despite the complex, non-stoichiometric nature of the Ge-apatite material. The differences in unit cell parameters are small, and nearly all are below 1.5%. The differences in bond lengths are all found to be less than 0.1 Å. This degree of agreement provides support for the validity of the potential model. It should be emphasised that modelling of the complex apatite structure to such levels of accuracy is a non-trivial task. The optimised structure has been used for all subsequent defect calculations.

5.2.2 Dopant Chemistry

As discussed in Section 5.1.3, the range of dopant ions that may be incorporated into the apatite structure is large and the affect of dopant ions on the behaviour of the materials can be significant and complex. Atomistic simulation methods can address key doping issues and yield quantitative estimates of the relative energies of different mechanisms of dopant incorporation (or "solution"). Although calculations

Table 5.2: Comparison of the experimental structure of the $La_{9.33}(GeO_4)_6O_2$ germanium apatite and that calculated using the atomistic model described in Table 5.1.

Parameter		Expt.	Calc.	Δ	Deviation /%
a	/Å	9.9117	10.0080	0.0963	0.97
b	/Å	9.9117	10.0506	0.1389	1.40
c	/Å	21.8499	21.3215	-0.5284	-2.42
α	/°	90.0	89.9352	-0.0648	-0.07
β	/°	90.0	90.1073	0.1073	0.12
γ	/°	120.0	120.1393	0.1393	0.12
Vol.	/Å^3	1858.99	1854.72	-4.27	-0.23
La−$O_{(5)}$	/Å	2.356	2.367(23)	0.011	0.47
Ge−$O_{(1)}$	/Å	1.645	1.720(29)	0.075	4.56
Ge−$O_{(2)}$	/Å	1.652	1.744(22)	0.092	5.56
Ge−$O_{(3)}$	/Å	1.662	1.744(19)	0.092	5.56
Ge−$O_{(4)}$	/Å	1.665	1.743(19)	0.078	4.68

are performed at infinite dilution they can provide a useful guide to the likely site selectivity, solubility and compensation mechanisms of different dopants.

In this study a number of defect processes were investigated. We examined mono-, di-, tri- and tetra-valent dopants on both the La and Ge sites of $La_{9.33}(GeO_4)_6O_2$ and, where charge compensation is required, we considered both constant oxygen and constant cation stoichiometry, which reflect experimentally employed doping strategies [232]. Appendix F contains additional information to supplement the results presented below: The energies of individual point defects are listed in Table F.1; the dopant potentials, defect energies and solution energies are listed in Table F.3.

Monovalent Dopants, D^+

The defect processes for the incorporation of monovalent dopants on both the La site and the Ge site are detailed in Equations 5.1 to 5.4 below. Throughout the following sections, where appropriate, the constant cation stoichiometry (compensating oxide defect) equations for each site are listed first, whilst the constant oxygen stoichiometry equations (compensating La defect) follow.

La site:

$$\tfrac{1}{2}D_2O + La_{La}^{\times} + O_O^{\times} \longrightarrow D_{La}'' + \tfrac{1}{2}La_2O_3 + V_O^{\bullet\bullet} \quad (5.1)$$

$$\tfrac{1}{2}D_2O + La_{La}^{\times} \longrightarrow D_{La}'' + \tfrac{1}{6}La_2O_3 + \tfrac{2}{3}La_i^{\bullet\bullet\bullet} \quad (5.2)$$

Ge site:

$$\tfrac{1}{2}D_2O + Ge_{Ge}^{\times} + \tfrac{3}{2}O_O^{\times} \longrightarrow D_{Ge}''' + GeO_2 + \tfrac{3}{2}V_O^{\bullet\bullet} \quad (5.3)$$

$$\tfrac{1}{2}D_2O + \tfrac{1}{2}La_2O_3 + Ge_{Ge}^{\times} \longrightarrow D_{Ge}''' + La_i^{\bullet\bullet\bullet} + GeO_2 \quad (5.4)$$

Monovalent doping on both the La site and the Ge site is found to be more favourable

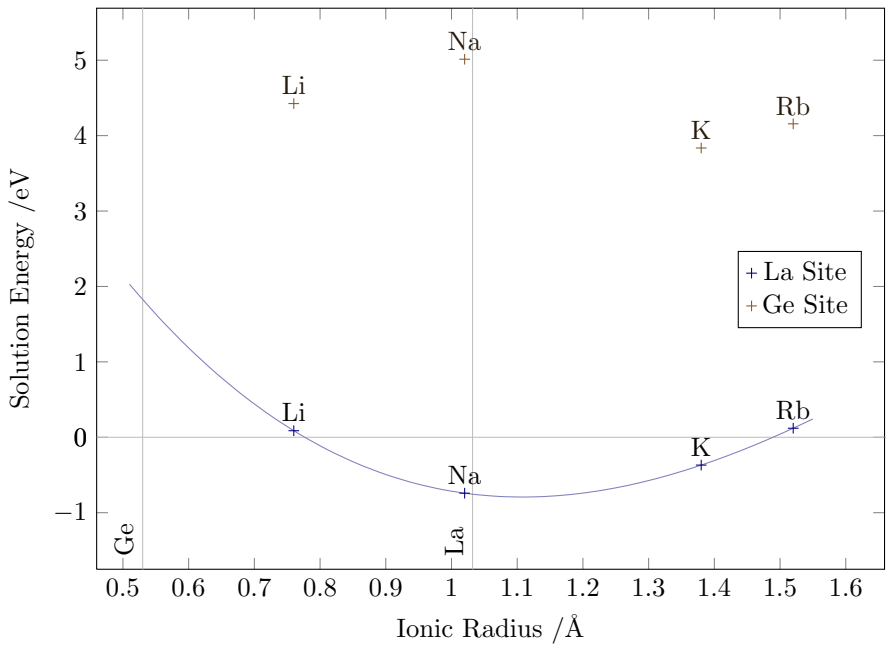

Figure 5.4: Monovalent dopant solution energies for both the La and Ge sites in $La_{9.33}(GeO_4)_6O_2$. The favoured compensation mechanisms shown in Equations 5.2 and 5.4 were used for the La and Ge sites respectively. Note that the polynomial line of best fit has been added purely as a guide to the eye.

when constant oxygen stoichiometry is maintained (i.e., the formation of La interstitials is preferable). For the La site, the process in Equation 5.2 is lower in energy by 2.18 eV, whilst for the Ge site the process in Equation 5.4 is lower by 3.00 eV.

The trends in solution energy versus the ionic radius of the dopant for these processes are plotted in Figure 5.4. Throughout this section, ionic radii are taken from Shannon [233]; the six-coordinate radius is used for all dopants due to incomplete four-coordinate data for the range of dopants tested. The six-coordinate ionic radii for La^{3+} and Ge^{4+} are 1.032 Å and 0.53 Å respectively, and are highlighted in each of the following plots.

The monovalent cations are found to be more favourable on the La site, which is consistent with their large ionic radii (cf. Ge^{4+}). Furthermore, on the La site, as is generally observed in doping studies, the solution energy of the dopant ion is at a minimum when the mistmatch between the ionic radius of the dopant ion and that of the host site ion is at a minimum. Although Na is the most favourable dopant, these simulations predict that Li, Na, K and Rb can all be incorporated onto the La site.

Divalent Dopants, D^{2+}

The defect processes for the solution of divalent dopants onto the La and Ge sites are shown in Equations 5.5 to 5.8 below:

La site:
$$DO + La_{La}^{\times} + \tfrac{1}{2}O_O^{\times} \longrightarrow D'_{La} + \tfrac{1}{2}La_2O_3 + \tfrac{1}{2}V_O^{\cdot\cdot} \quad (5.5)$$
$$DO + La_{La}^{\times} \longrightarrow D'_{La} + \tfrac{1}{3}La_2O_3 + \tfrac{1}{3}La_i^{\cdot\cdot\cdot} \quad (5.6)$$

Ge site:
$$DO + G_{Ge}^{\times} + O_O^{\times} \longrightarrow D''_{Ge} + GeO_2 + V_O^{\cdot\cdot} \quad (5.7)$$
$$DO + \tfrac{1}{3}La_2O_3 + Ge_{Ge}^{\times} \longrightarrow D''_{Ge} + La_i^{\cdot\cdot\cdot} + GeO_2 \quad (5.8)$$

Charge compensation of divalent dopants on both sites is again predicted to occur via a change in cation stoichiometry, although to a lesser extent than for the monovalent dopants. For the La site, the process in Equation 5.6 is lower in energy by 0.99 eV, whilst for the Ge site the process in Equation 5.8 is lower by 2.04 eV.

A plot of solution energy versus ionic radius of the divalent dopant is shown in Figure 5.5. The alkaline-earth metals (Ca, Sr, Ba) and Cd are found to be the most favourable dopants and display a much greater affinity for the La site than the Ge site in accordance with the experimental observations reported previously [34]. In contrast, the smaller dopant ions, with radii intermediate between those of La and Ge, are closer in energy between the two sites. Although these dopants, such as Mg, Co, Fe, Ni and Mn, are still predicted to be more stable on the La site, the occurrence of ambi-site behaviour is highly likely, given the trends observed both theoretically [193] experimentally [34] for the silicate.

Trivalent Dopants, D^{3+}

The defect processes for the solution of trivalent dopants onto the La and Ge sites are shown in Equations 5.9 to 5.11 below. Note that the dopants are isovalent with La^{3+}, and therefore do not require charge compensation on the La site.

La site:
$$\tfrac{1}{2}D_2O_3 + La_{La}^{\times} \longrightarrow D_{La}^{\times} + \tfrac{1}{2}La_2O_3 \quad (5.9)$$

Ge site:
$$\tfrac{1}{2}D_2O_3 + Ge_{Ge}^{\times} + \tfrac{1}{2}O_O^{\times} \longrightarrow D'_{Ge} + GeO_2 + \tfrac{1}{2}V_O^{\cdot\cdot} \quad (5.10)$$
$$\tfrac{1}{2}D_2O_3 + \tfrac{1}{6}La_2O_3 + Ge_{Ge}^{\times} \longrightarrow D'_{Ge} + La_i^{\cdot\cdot\cdot} + GeO_2 \quad (5.11)$$

Trivalent doping on the Ge site was found to be 0.98 eV more favourable when constant oxygen stoichiometry was maintained (Equation 5.11). A plot of solution energy versus ionic radius of the trivalent dopant is shown in Figure 5.6. Nd, Gd and Y are all predicted to be favourable on the La site, which is in accord with both the general series of rare-earth-based apatite materials [60, 61], and the stabilisation of hexagonal symmetry in Ge-apatite by Y, discussed earlier [225].

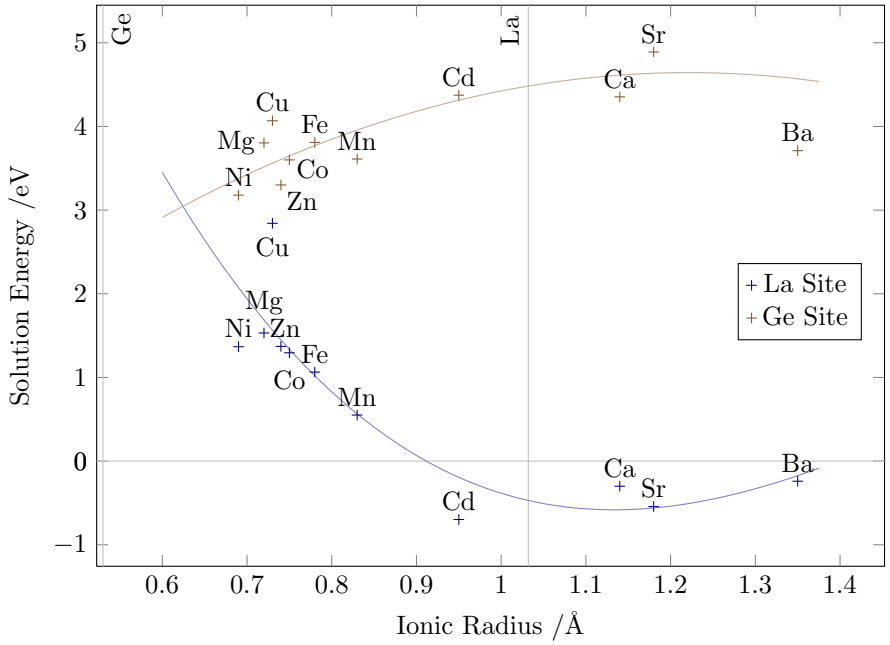

Figure 5.5: Divalent dopant solution energies for both the la and Ge sites in $La_{9.33}(GeO_4)_6O_2$. The favoured compensation mechanisms shown in Equations 5.6 and 5.8 were used for the La and Ge sites respectively. Note that polynomial lines of best fit have been added purely as a guide to the eye.

In contrast, Al, Co, Ga and Fe are more favourable on the Ge site. However, for all but Co the difference in energy between the sites is small enough to suggest that ambi-site behaviour is possible. It should be noted that although Co^{3+} is predicted to be much more favourable on the Ge site, the situation is reversed for Co^{2+}, as found in the previous section. This finding is in agreement with that of Tolchard et al. for the silicate materials [223], in which the charge of the Co dopant is determined by the host site.

Tetravalent Dopants, D^{4+}

The defect processes for the solution of tetravalent dopants on the La and Ge sites are shown in Equations 5.12 to 5.14 below. Note that the dopants are isovalent with Ge, and therefore do not require compensation on the Ge site.

La site:
$$DO_2 + La_{La}^{\times} \longrightarrow D_{La}^{\bullet} + \tfrac{1}{2}La_2O_3 + \tfrac{1}{2}O_i'' \tag{5.12}$$
$$DO_2 + \tfrac{4}{3}La_{La}^{\times} \longrightarrow D_{La}^{\bullet} + \tfrac{2}{3}La_2O_3 + \tfrac{1}{3}V_{La}''' \tag{5.13}$$

Ge site:
$$DO_2 + Ge_{Ge}^{\times} \longrightarrow D_{Ge}^{\times} + GeO_2 \tag{5.14}$$

In contrast to dopants with lower valence, tetravalent doping on the La site was found to be 0.30 eV more favourable when constant cation stoichiometry was main-

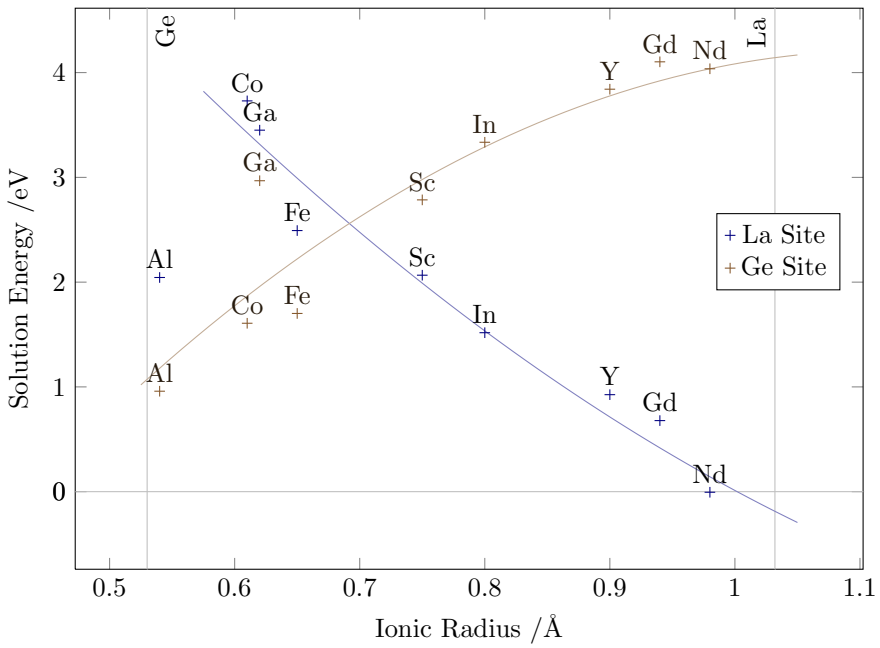

Figure 5.6: Trivalent dopant solution energies for both the lanthanum and germanium sites in $La_{9.33}(GeO_4)_6O_2$. The favoured compensation mechanism shown in Equation 5.11 was used for the Ge site. Note that polynomial lines of best fit have been added purely as a guide to the eye.

tained (i.e., charge compensation with oxide interstitials was favourable, as in Equation 5.12).

A plot of solution energy versus dopant ionic radius is shown in Figure 5.7. There appears to be limited correlation of energy with ion size for the La site dopants. A large range of energies is observed for the Ge site, with the large dopants such as Ce being particularly unfavourable. Thus, Ce is predicted to be incorporated on the La site. In contrast, Ti, which has been discussed at length in Section 5.1.3 is found to be very low in energy on the Ge site. Mn and Sn both display very similar energies on either site, and are therefore predicted to be ambi-site dopants.

General Dopant Trends

Several overarching trends are apparent from the results of our dopant incorporation calculations. Firstly, $La_{9.33}(GeO_4)_6O_2$ exhibits a preference for compensation of aliovalent dopants with interstitial defects (either additional La in the case of subvalent doping, or interstitial oxide ions in the case of tetravalent doping). That is, the material is predicted to be intolerant of vacancy defects. A significant consequence of this is that subvalent doping is predicted not to reduce the oxide ion content of the material.

The second major trend across all dopant species is that dopants of higher charge

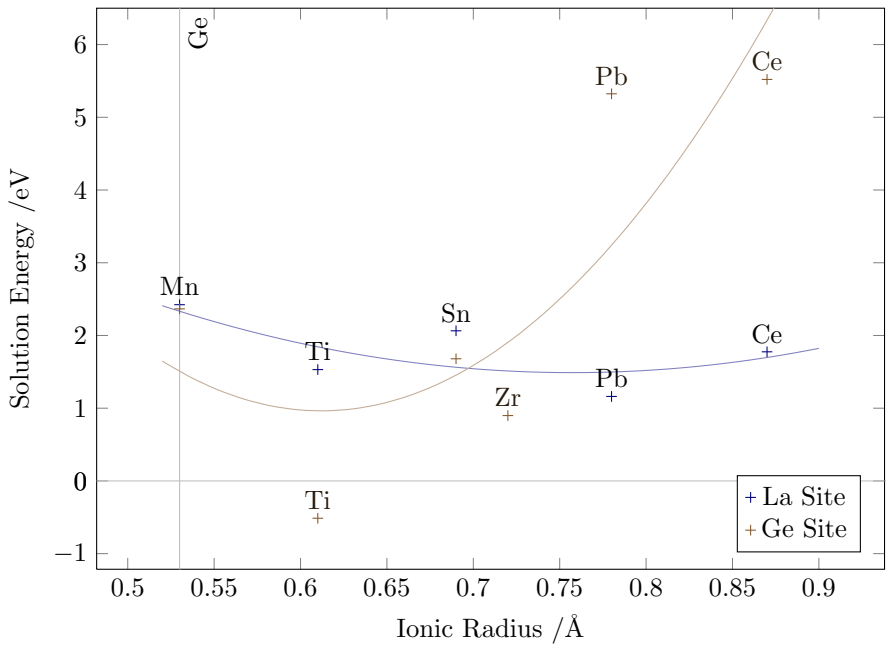

Figure 5.7: Tetravalent dopant solution energies for both the lanthanum and germanium sites in $La_{9.33}(GeO_4)_6O_2$. The favoured compensation mechanism shown in Equation 5.12 was used for the La site. Note that polynomial lines of best fit have been added purely as a guide to the eye.

are increasingly stable on the Ge^{4+} site, particularly when the ionic radius is small. Conversely, dopants with a higher charge become less stable on the La^{3+} site, particularly when the ionic radius is small. Thus, small, highly charged dopants (such as Al^{3+}, Co^{3+}, Fe^{3+} and Ti^{4+}) are favourable on the Ge site, whilst larger dopants with lower charge (such as Na^{+}, K^{+}, Ca^{2+}, Sr^{2+}, Cd^{2+} and Nd^{3+}) are preferable on the La site. Finally, as has been found experimentally, there are a substantial number of dopants that are predicted to be soluble on either the La or Ge site (particularly Co and Mn, but also many of the smaller divalent dopants).

5.3 Chapter Summary

Our computer simulations have provided new insight into the dopant behaviour of the $La_{9.33}(GeO_4)_6O_2$ apatite material, producing quantitative data regarding the site selectivity and charge compensation mechanisms of a wide range of cation dopants.

Consistent with the Si-based apatite materials and with experiment, the results indicate that a broad range of dopants may be substituted for La in the material. In contrast, a more select range of tri- and tetravalent cations with smaller ionic radii are found to be soluble on the Ge site. In all cases, compensation for the dopant ions is achieved through interstitial rather than vacancy mechanisms, which indicates that oxygen hyperstoichiometry is likely to remain unchanged upon subvalent

doping.

The breadth of possible doping regimes in these novel materials provides new opportunities to design and optimise the conduction properties for SOFC electrolytes. Understanding of the relationship between macroscopic properties and local structure is fundamental to unlocking this potential. Further computational study of local phenomena, such as dopant–interstitial-oxide association, is required to advance this understanding.

Chapter 6

Conclusions and Future Work

6.1 General Remarks

This thesis has presented computational modelling studies of three oxide material systems with potential applications as interstitial oxide-ion conductors in solid oxide fuel cells (SOFCs). By examining their atomic-scale properties, we have attempted to provide valuable insight into the defect chemistry and oxide-ion transport properties of these materials. Such insight is valuable in developing advanced materials for fuel cells and other clean-energy applications. It is appropriate to conclude with a review of our findings and discussion of potential extensions to each study.

6.2 Defect and Ion Transport Properties of Nd_2NiO_4-based Materials

The Nd_2NiO_4-based materials are found to be broadly similar to the closely-related La_2NiO_4 and Pr_2NiO_4 materials. The formation of interstitial oxide ions via Frenkel disorder or oxidation is favourable, and the interstitials reside in the rock-salt plane of the Ruddlesden–Popper-type structure. The migration of these interstitial oxide ions proceeds via an interstitialcy-type mechanism involving the apical lattice oxide ions, with a low activation barrier of between 0.44 and 0.74 eV.

Our novel work on Nd deficiency in the material reveals a complex relationship between the local atomic structure and the oxide ion migration properties. We find, in accordance with experimental diffusion measurements, that Nd deficiency results in a reduction in the activation energy, but also a reduction in the diffusion coefficient at high temperatures. This behaviour warrants further investigation, which could include (a) studying individual migration pathways with more complex configurations of ions or (b) investigating the effect of oxide ion and/or Nd concentration on

the migration energy.

In addition, DFT studies would help elucidate the electronic structure of Ni of Ln_2NiO_4 (where Ln = La, Nd, Pr), particularly upon oxidation. The possible delocalisation of bonding in the Ni^{2+}/Ni^{3+} sublattice has important implications for the electronic conductivity of the materials. Electronic structure calculations may also provide further detail concerning Ln deficiency in the materials.

6.3 Defect, Electronic and Ion Transport Properties of Infinite-layered $SrFeO_2$

We modelled the new infinite-layered $SrFeO_2$ material using both atomistic and DFT techniques, which was a challenging task. Both techniques predict that interstitial oxide ions are favoured directly between two Fe ions, the same site occupied in the parent $SrFeO_3$ perovskite structure. Our atomistic calculations predict that the material will be intolerant of intrinsic Schottky and Frenkel disorder. Our detailed electronic structure calculations predict that oxidation is highly favourable and occurs via the formation of interstitial oxide ions and holes on the neighbouring Fe sites.

The migration of interstitial oxide ions within the $SrFeO_2$ lattice was found to occur via a step-wise mechanism comparable to the vacancy-hopping mechanism found in the perovskite-type materials, rather than by a direct interstitial or interstitialcy mechanism. We calculate a high energy barrier to this migration, however, which is supported by low diffusion coefficients from our MD simulations.

Future investigation of the phase transition between $SrFeO_2$ and the $SrFeO_{2.5}$ brownmillerite phase using MD simulations may clarify the local mechanisms via which structural rearrangement occurs. Such mechanisms could be important in the design and optimisation of future SOFC materials. MD simulations of $Sr_{1-x}Ca_xFeO_2$ solid solutions may help elucidate the structural factors underpinning the differences of the $SrFeO_2$ and $CaFeO_2$ materials. Electronic structure calculations could be used to probe the energetics of water incorporation in the $SrFeO_2$ material, and explore the possibility of proton migration.

6.4 Dopant Chemistry of the $La_{9.33}(GeO_4)_6O_2$ Apatite Material

Our dopant studies of the $La_{9.33}(GeO_4)_6O_2$ apatite material produced quantitative data regarding the solubility, site selectivity and charge compensation mechanisms of a range of dopants. We find that a large range of dopants may be substituted for La in the material, whilst a more select range of tri- and tetravalent cations with

smaller ionic radii are soluble on the Ge site. The local structure data from these simulations suggests a complex relationship between the dopant ion and migrating interstitial oxide-ion, in terms of binding between the two species.

To extend this work, further atomistic calculations on supercells could be conducted to investigate the effects of dopant concentration and cluster configuration on oxide–dopant binding energy and the ion conduction mechanism. DFT calculations could provide valuable information about the changes in electronic structure upon oxide ion insertion, Ti-doping and the trapping or blocking of migrating ions.

References

[1] McDowall, W. and Eames, M. *Energy Policy* **34**, 1236–1250 (2006).

[2] MacLean, H. L. and Lave, L. B. *Prog. Energy Combust. Sci.* **29**(1), 1–69 (2003).

[3] Steele, B. H. C. and Heinzel, A. *Nature* **414**, 345–352 (2001).

[4] Winter, M. and Brodd, R. J. *Chem. Rev.* **104**, 4245–4269 (2004).

[5] Wang, Y., Chen, K. S., Mishler, J., Cho, S. C., and Adroher, X. C. *Appl. Energy* **88**, 981–1007 (2011).

[6] Skinner, S. J. *Internat. J. Inorg. Mat.* **3**, 113–121 (2001).

[7] Sansawatt, T., Whiteford, J. R. G., and Harrison, G. P. In *UPEC: 2009 44th International Universities Power Engineering Conference*, 26–30 (IEEE, 345 E 47$^{\text{th}}$ St, New York, NY 10017 USA, 2009).

[8] Ceramic Fuel Cells (Europe) Limited. *Preliminary Specifications for the Net-Gen pre-commercial demonstration micro-CHP unit*, Regus House, Herons Way, Chester Business Park, Chester, CH4 9QR, UK.

[9] Grove, W. R. *Philos. Mag.* **14**, 127–130 (1839).

[10] Carnot, S., Carnot, H., and Kelvin, W. T. *Reflections on the motive power of heat and on machines fitted to develop this power.* J. Wiley, (1890).

[11] Minh, N. Q. *J. Am. Ceram. Soc.* **76**, 563–588 (1993).

[12] Nernst, W. *Z. Elektrochem.* **6**, 41–43 (1899).

[13] Baur, E. and Preis, H. *Z. Elektrochem.* **43**, 727–732 (1937).

[14] Orera, A. and Slater, P. R. *Chem. Mater.* **22**(3), 675–690 (2010).

[15] Catlow, C. R. A. In *Solid State Chemistry: Techniques.* Clarendon Press, Oxford, (1987).

[16] Tolchard, J. R., Islam, M. S., and Slater, P. R. *J. Mater. Chem.* **13**, 1956–1961 (2003).

[17] Kendrick, E., Kendrick, J., Knight, K. S., Islam, M. S., and Slater, P. R. *Nature Mater.* **6**, 871–875 (2007).

[18] Chroneos, A., Parfitt, D. C., Kilner, J. A., and Grimes, R. W. *J. Mater. Chem.* **20**, 266–270 (2010).

[19] Parfitt, D. C., Chroneos, A., Kilner, J. A., and Grimes, R. W. *Phys. Chem. Chem. Phys.* **12**, 6834–6836 (2010).

[20] Islam, M. S. and Slater, P. R. *MRS Bull.* **34**(12), 935–941 (2009).

[21] Islam, M. S. *J. Mater. Chem.* **10**, 1027–1038 (2000).

[22] Catlow, C. R. A., Guo, Z. X., Miskufova, M., Shevlin, S. A., Smith, A. G. H., Sokol, A. A., Walsh, A., Wilson, D. J., and Woodley, S. M. *Phil. Trans. R. Soc. Lond. A* **368**(1923), 3379–3456 (2010).

[23] Malavasi, L., Fisher, C. A. J., and Islam, M. S. *Chem. Soc. Rev.* **39**, 4370–4387 (2010).

[24] Cramer, C. J. *Essentials of Computational Chemistry.* John Wiley and Sons Ltd, The Atrium, Southern Gate, Chichester, West Sussex, PO19 8SQ, England, second edition, (2004).

[25] Frenkel, D. and Smit, B. *Understanding Molecular Simulation.* Elsevier, (2002).

[26] Martin, R. M. *Electronic Structure: Basic Theory and Practical Methods.* Cambridge University Press, (2004).

[27] Haile, S. M. *Materials Today* **6**, 24–29 (2003).

[28] Skinner, S. J. and Kilner, J. A. *Materials Today* **6**, 30–37 (2003).

[29] Boivin, J. C. and Mairesse, G. *Chem. Mater.* **10**, 2870–2888 (1998).

[30] Kwon, O. H. and Choi, G. M. *Solid State Ionics* **177**, 3057 (2006).

[31] Pérex-Coll, D. and Mather, G. C. *Solid State Ionics* **181**, 20 (2010).

[32] Huang, K., Tichy, R. S., and Goodenough, J. B. *J. Am. Ceram. Soc.* **81**, 2565 (1998).

[33] Tealdi, C., Chiodeli, G., Malavasi, L., and Flor, G. *J. Mater. Chem.* **14**, 3553 (2004).

[34] Kendrick, E., Islam, M. S., and Slater, P. R. *J. Mater. Chem.* **17**, 3104–3111 (2007).

[35] Butler, V., Catlow, C. R. A., Fender, B. E. F., and Harding, J. H. *Solid State Ionics* **8**, 109–113 (1983).

[36] Khan, M. S. and Islam, M. S. *J. Phys. Chem. B* **102**, 3099–3104 (1998).

[37] Minervini, L., Zacate, M. O., and Grimes, R. W. *Solid State Ionics* **116**, 339–349 (1999).

[38] Kilner, J. A. *Solid State Ionics* **129**, 13–23 (2000).

[39] Takahashi, T., Iwahara, H., and Nagai, Y. *Appl. Electrochem.* **2**, 97 (1972).

[40] Takahashi, T. and Iwahara, H. *Energy Convers.* **11**, 105 (1971).

[41] Ishihara, T., Matsuda, H., and Takita, Y. *J. Am. Chem. Soc.* **116**, 3801–3803 (1994).

[42] Feng, M. and Goodenough, J. B. *Eur. J. Solid State Inorg. Chem.* **T31**, 663 (1994).

[43] Davies, R. A., Islam, M. S., and Gale, J. D. *Solid State Ionics* **126**, 323–335 (1999).

[44] Yashima, M., Nomura, K., Kageyama, H., Miyazaki, Y., Chitose, N., and Adachi, K. *Chem. Phys. Lett.* **380**, 391–396 (2003).

[45] Yashima, M. and Tsuji, T. *J. Appl. Cryst.* **40**, 1166–1168 (2007).

[46] Skinner, S. J. *Solid State Sci.* **5**(3), 419–426 (2003).

[47] Jiang, S. P. *J. Mater. Sci.* **43**, 6799–6833 (2008).

[48] Popper, P. and Ruddlesded, S. N. *Brit. Ceram. Soc. T.* **62**(5), 443–449 (1963).

[49] Greenblatt, M. *Cur. Op. Solid State Mater. Sci.* **2**(2), 174–183 (1997).

[50] Yashima, M., Enoki, M., Wakita, T., Ali, R., Matsushita, Y., Izumi, F., and Ishihara, T. *J. Am. Chem. Soc.* **130**, 2762–2763 (2008).

[51] Cleave, A. R., Kilner, J. A., Skinner, S. J., Murphy, S. T., and Grimes, R. W. *Solid State Ionics* **179**(21-26), 823–826 SEP 15 (2008).

[52] Naumovich, E. N. and Kharton, V. V. *J. Mol. Struct.* **946**, 57–64 (2010).

[53] Chauveau, F., Mougin, J., Bassat, J.-M., Mauvy, F., and Gernier, J. C. *J. Power Sources* **195**, 744–749 (2010).

[54] Ishihara, T., Sirikanda, N., Nakashima, K., Miyoshi, S., and Matsumoto, H. *J. Electrochem. Soc.* **157**(1), B141–B146 (2010).

[55] Kawahara, A. and Ishihara, T. *Electrochem. and Solid State Lett.* **13**(7), B76–B78 (2010).

[56] Tsujimoto, Y., Tassel, C., Hayashi, N., Watanabe, T., Kageyama, H., Toshimura, K., Takano, M., Ceretti, M., Ritter, C., and Paulus, W. *Nature* **450**, 1062–1066 (2007).

[57] Hayward, M. A. and Rosseinsky, M. J. *Nature* **450**, 960–961 (2007).

[58] de Leeuw, N. H., Bowe, J. R., and Rabone, J. A. L. *Faraday Discuss.* **134**, 195–214 (2007).

[59] de Leeuw, N. H. *J. Mater. Chem.* **20**, 5376–5389 (2010).

[60] Nakayama, S., Aono, H., and Sadaoka, Y. *Chem. Lett.* **24**(6), 431–432 (1995).

[61] Nakayama, S., Kagayama, T., Aono, H., and Sadaoka, Y. *J. Mater. Chem.* **5**, 1801–1805 (1995).

[62] Arikawa, H., Nishiguchi, H., Ishihara, T., and Takita, Y. *Solid State Ionics* **136–137**, 31–37 (2000).

[63] Gale, J. D. *J. Chem. Soc., Faraday Trans.* **93**, 629–637 (1997).

[64] Gale, J. D. *General Utility Lattice Program Manual*, 3.1 edition.

[65] Smith, W. and Forester, T. R. *J. Mol. Graphics* **14**(3), 136–141 (1996).

[66] Smith, W., Yong, C. W., and Rodger, P. M. *Mol. Simul.* **28**(5), 385–471 (2002).

[67] Smith, W., Forester, T. R., and Todorov, I. T. *The DL_POLY_2.0 User Manual.* Daresbury Laboratory, United Kingdom, 2.19 edition, (2010).

[68] Kresse, G. and Hafner, J. *Phys. Rev. B* **49**, 14251 (1994).

[69] Kresse, G. and Furthmüller, J. *Comput. Mater. Sci.* **6**, 15 (1996).

[70] Clark, S. J., Segall, M. D., Pickard, C. J., Hasnip, P. J., Probert, M. J., Refson, K., and Payne, M. C. *Z. Kristallographie* **220**(5–6), 567–570 (2005).

[71] Fletcher, D. A., McMeeking, R. F., and Parkin, D. *J. Chem. Inf. Comput. Sci.* **36**, 746–749 (1996).

[72] Momma, K. and Izumi, F. *J. Appl. Cryst.* **41**, 653–658 (2008).

[73] Humphrey, W., Dalke, A., and Schulten, K. *J. Mol. Graphics* **14**, 33–38 (1996).

[74] Shewchuk, J. R. *An Introduction to the Conjugate Gradient Method Without the Agonizing Pain.* Technical report, School of Computer Science, Carnegie Mellon University, , Pittsburgh, PA 15213, August (1994).

[75] Shanno, D. F. *Mathematics of Computation* **24**(111), 647–656 (1970).

[76] Mills, G., Jónsson, H., and Schenter, G. K. *Surf. Sci.* **324**, 305–337 (1995).

[77] Henkelman, G. and Jónsson, H. *J. Chem. Phys.* **113**(22), 9978–9985 (2000).

[78] Henkelman, G., Uberuaga, B. P., and Jónsson, H. *J. Chem. Phys.* **113**(22), 9901–9904 (2000).

[79] Banerjee, A., Adams, N., Simons, J., and Shepard, R. *J. Phys. Chem.* **89**(1), 52–57 (1985).

[80] Allen, M. P. and Tildesley, D. J. *Computer Simulation of Liquids.* Oxford University Press, Great Clarendon Street, Oxford, OX2 6DP, (1989).

[81] Leach, A. R. *Molecular Modelling, Principals and Applications.* Pearson, Prentice Hall, 2nd edition, (2001).

[82] Verlet, L. *Phys. Rev.* **159**(1), 98–103 (1967).

[83] Tuckerman, M., Berne, B. J., and Martyna, G. J. *J. Chem. Phys.* **97**(3), 1990–2001 (1992).

[84] Swope, W. C., Andersen, H. C., Berens, P. H., and Wilson, K. R. *J. Chem. Phys.* **76**(1), 637–649 (1982).

[85] Berendsen, H. J. C., Postma, J. P. M., and van Gunsteren, W. F. *J. Chem. Phys.* **81**(8), 3684–3690 (1984).

[86] Rühle, V. *Berendsen and Nosé-Hoover thermostats.* Technical report, Max Planck Institute for Polymer Research, Ackermannweg 10, D-55128 Mainz, (2007).

[87] Hoover, W. G. *Phys. Rev. A* **31**(3), 1695–1697 (1985).

[88] Buehler, M. J. *Atomistic modeling of materials failure.* Springer–Verlag, New York Inc., (2008).

[89] Nosé, S. *J. Chem. Phys.* **81**(1), 511–519 (1984).

[90] Murch, G. E. *Solid State Ionics* **7**, 177–198 (1982).

[91] Simpson, L. A. and Carter, R. E. *J. Am. Ceram. Soc.* **49**, 139 (1966).

[92] Born, M. *Z. Physik* **1**, 45–48 (1920).

[93] Leonard-Jones, J. E. *Proc. R. Soc. Lond. A* **106**(738), 463–477 (1924).

[94] Morse, P. M. *Phys. Rev.* **34**, 57–64 (1929).

[95] Buckingham, R. A. *Proc. R. Soc. Lond. A* **168**(933), 264–283 (1938).

[96] Ewald, R. P. *Ann. Phys.* **64**, 253–287 (1921).

[97] Gale, J. D., Catlow, C. R. A., and Mackrodt, W. C. *Modelling Simul. Mater. Sci. Eng.* **1**, 73–81 (1992).

[98] Gale, J. D. *Philos. Mag. B* **73**(1), 3–19 January (1996).

[99] Dick, B. G. and Overhauser, A. W. *Phys. Rev.* **112**, 90–103 (1958).

[100] Slater, J. C. and Kirkwood, J. G. *Phys. Rev.* **37**, 682 (1931).

[101] Pyper, N. C. *Phil. Trans. R. Soc. Lond. A* **320**, 107–158 (1986).

[102] Mott, N. F. and Littleton, M. T. *Trans. Faraday Soc.* **34**, 485 (1938).

[103] Smart, L. E. and Moore, E. A. *Solid State Chemistry, An Introduction.* Taylor & Francis, 3rd edition, (2005).

[104] Kingery, W. D., Bowen, H. K., and Uhlmann, D. R. *Introduction to Ceramics.* Wiley series on the science and technology of materials. Wiley-Interscience, second edition, (1976).

[105] Koch, W. and Holthausen, M. C. *A Chemist's Guide to Density Functional Theory.* Wiley-VCH, second edition, (2000).

[106] Kohanoff, J. *Electronic Structure Calculations for Solids and Molecules: Theory and Computational Methods*. Cambridge University Press, first edition, (2006).

[107] Schrödinger, E. *Phys. Rev.* **28**(6), 1049–1070 (1926).

[108] Rae, A. I. M. *Quantum Mechanics*. Taylor & Francis, 5$^{\text{th}}$ edition, (2008).

[109] Born, M. and Oppenheimer, R. *Ann. Physik* **84**, 457 (1927).

[110] Hartree, D. R. *Proc. Camb. Phil. Soc.* **24**, 89–110 (1928).

[111] Slater, J. C. *Phys. Rev.* **32**, 339–348 (1928).

[112] Slater, J. C. *Phys. Rev.* **34**, 1293–1322 (1929).

[113] Fock, V. *Z. Phys.* **61**, 126–148 (1930).

[114] Hartree, D. R. and Hartree, W. *Proc. R. Soc. Lond. A* **150**(869), 9–33 (1935).

[115] Thomas, L. H. *Proc. Camb. Phil. Soc.* **23**, 542 (1927).

[116] Fermi, E. *Rend. Accad. Lincei* **6**, 602 (1927).

[117] Dirac, P. A. M. *Proc. Camb. Phil. Soc.* **26**, 376 (1930).

[118] Hohenberg, P. and Kohn, W. *Phys. Rev.* **136**(3B), B864–B871 Nov (1964).

[119] Levy, M. *Proc. Natl. Acad. Sci. U.S.A.* **76**, 6062–6065 (1979).

[120] Kohn, W. and Sham, L. J. *Phys. Rev.* **140**(4A), A1133–A1138 Nov (1965).

[121] Jones, R. O. volume 31 of *NIC Series*, 45–70. John von Neumann Institute for Computing, Jülich (2006).

[122] Ceperley, D. M. and Alder, B. J. *Phys. Rev. Lett.* **45**(7), 566–569 Aug (1980).

[123] Perdew, J. P. and Zunger, A. *Phys. Rev. B* **23**(10), 5048–5079 May (1981).

[124] Vosko, S. J., Wilk, L., and Nusair, M. *Can. J. Phys.* **58**, 1200 (1980).

[125] Becke, A. D. *Phys. Rev. A* **38**(6), 3098–3100 (1988).

[126] Perdew, J. P. and Wang, Y. *Phys. Rev. B* **45**, 13244 (1992).

[127] Perdew, J. P., Burke, K., and Ernzerhof, M. *Phys. Rev. Lett.* **77**, 3865–3868 (1996).

[128] Anisimov, V. I., Aryasetiawan, F., and Lichtenstein, A. I. *J. Phys. Cond. Mat.* **9**, 767–808 (1997).

[129] Hubbard, J. *Proc. R. Soc. Lond.* **285**, 542–560 (1965).

[130] Anisimov, V. I., Zaanen, J., and Anderson, O. K. *Phys. Rev. B* **44**, 943 (1991).

[131] Payne, M. C., Teter, M. P., Allan, D. C., Arias, T. A., and Joannopoulos, J. D. *Rev. Mod. Phys.* **64**(4), 1045–1097 (1992).

[132] Rutter, M. J. *Bloch's Theorem: Some Notes.* Technical report, University of Cambridge, (2005).

[133] Monkhorst, H. J. and Pack, J. D. *Phys. Rev. B* **13**, 5188–5192 (1976).

[134] Singh, D. J. and Nordström, L. *Planewaves, Pseudopotentials and the LAPW Methoding.* Springer, 233 Spring Street, New York, NY 10013, USA, second edition, (2006).

[135] Blöchl, P. E. *Phys. Rev. B* **50**(24), 17953–17979 (1994).

[136] Boehm, E., Bassat, J.-M., Dordor, P., Mauvy, F., Grenier, J.-C., and Stevens, P. *Solid State Ionics* **176**, 2717–2725 (2005).

[137] Minervini, L., Grimes, R. W., Kilner, J. A., and Sickafus, K. E. *J. Mater. Chem.* **10**, 2349–2354 (2000).

[138] Jorgensen, J. D., Dabrowski, B., Pei, S., Richards, D. R., and Hinks, D. G. *Phys. Rev. B* **40**, 2187–2199 (1989).

[139] D'Arco, S. and Islam, M. S. *Phys. Rev. B* **55**, 3141 (1997).

[140] Toyosumi, Y., Ishikawa, H., and Ishikawa, K. *J. Alloys Compd.* **408–412**, 1200–1204 (2006).

[141] Read, M., Islam, M. S., King, F., and Hancock, F. *J. Phys. Chem. B* **103**, 1558–1562 (1999).

[142] Paulus, W., Cousson, A., Heger, G., Revcolevschi, A., Dhalenne, G., and Hosoya, S. *Physica B: Cond. Matt.* **234–236**, 20–22 (1997).

[143] Kushima, A., Parfitt, D. C., Chroneos, A., and Yildiz, B. *Phys. Chem. Chem. Phys.* **13**, 2242–2249 (2011).

[144] Sayers, R., De Souza, R. A., Kilner, J. A., and Skinner, S. J. *Solid State Ionics* **181**, 386–391 (2010).

[145] Skinner, S. J. and Kilner, J. A. *Solid State Ionics* **135**, 709 (2000).

[146] Wan, J., Goodenough, J. B., and Zhu, J. H. *Solid State Ionics* **178**, 281–286 (2007).

[147] Bassat, J.-M., Odier, P., Villesuzanne, A., Marin, C., and Pouchard, M. *Solid State Ionics* **167**, 341 (2004).

[148] Bassat, J.-M., Odier, P., and Loup, J. P. *J. Solid State Chem.* **110**, 124–135 (1994).

[149] Kilner, J. A. and Shaw, C. K. M. *Solid State Ionics* **154–155**, 523–527 (2002).

[150] Kovalevsky, A. V., Kharton, V. V., Yaremchenko, A. A., Pivak, Y. V., Naumovich, E. N., and Frade, J. R. *J. Europ. Ceram. Soc.* **27**(13–15), 4269–4272 (2007).

[151] Foëx, M. *Bull. Soc. Chim. Fr.* , 109 (1961).

[152] Bernard, W. and Marc, D. *C. R. Acad. Sci.* **C267**(22), 1482 (1968).

[153] Tamura, S. *J. Phys. Soc. Japan* **33**, 574 (1972).

[154] Lehmann, U. and Mueller-Buschbaum, H. *Z. Naturforsch., Part B* (35), 389–390 (1980).

[155] Saez-Puche, R., Fernandez, F., Rodríguez-Carvajal, J., and Martinez, J. L. *Solid State Commun.* **72**(3), 273–277 (1989).

[156] Rodríguez-Carvajal, J., Fernandez-Diaz, M. T., Martinez, J. L., Fernandez, F., and Saez-Puche, R. *Europhys. Lett.* **11**, 261–268 (1990).

[157] Nishijima, M., Takeda, Y., Inanishi, N., Yakamoto, O., and Kanno, R. *Phase Transition* **38**, 127–220 (1992).

[158] Watanabe, K., Asakawa, H., Fujinawa, G., Ishikawa, K., and Nakamura, T. *X-sen Bunseki no Shinpo* **29**, 137–152 (1998). Data from ICSD.

[159] Fisher, C. A. J. *Electrical conductivity of brownmillerite-structured oxide ceramicsPhysic.* PhD thesis, University of Oxford, Faculty of Physical Sciences, (1996).

[160] Lewis, G. V. and Catlow, C. R. A. *J. Phys. C: Solid State Phys.* **18**, 1149 (1985).

[161] Freeman, G. M. and Catlow, C. R. A. *J. Solid State Chem.* **85**, 65 (1990).

[162] Grimes, R. W. and Chen, S. P. *J. Phys. Chem. Solids* **61**(8), 1263–1268 (2000).

[163] Bush, T. S., Gale, J. D., Catlow, C. R. A., and Battle, P. D. *J. Mater. Chem.* **4**, 831–837 (1994).

[164] Faucher, M., Pannetier, J., Charreire, Y., and Caro, P. *Acta Cryst. B* **38**, 344–346 (1982). Nd2O3 Structure.

[165] Slack, G. A. *J. Appl. Phys.* **31**, 1571–1582 (1960).

[166] Lide, D., editor. *Handbook of Chemistry and Physics.* CRC Press, 86$^{\text{th}}$ edition, (2005).

[167] DiCarlo, J., Mehta, A., Banschick, D., and Navrotsky, A. *J. Solid State Chem.* **103**(1), 186–192 (1993).

[168] Bhavaraju, S., DiCarlo, J. F., Scarfe, D. P., Yazdi, I., and Jacobson, A. J. *Chem. Mater.* **6**(11), 2172–2176 (1994).

[169] Ma, B., Balachandran, U., Park, J.-H., and Segre, C. U. *J. Electrochem. Soc.* **143**(5), 1736–1744 (1996).

[170] Ma, B., Victory, N. I., and Balachandran, U. *J. Am. Ceram. Soc.* **85**(11), 2641–2645 (2002).

[171] Shao, Z. and Haile, S. M. *Nature* **431**, 170–173 (2004).

[172] Shao, Z. and Haile, S. M. *Nature* **435**, 795–798 (2005).

[173] Fisher, C. A. J. and Islam, M. S. *J. Mater. Chem.* **15**, 3200–3207 (2005).

[174] Inoue, S., Kawai, M., Ichikawa, N., Kageyama, H., Paulus, W., and Schimakawa, Y. *Nature Chem.* **2**, 213–217 (2010).

[175] Takeda, T., Kanno, R., Kawamoto, Y., Takano, M., Kawasaki, S., Kamiyama, T., and Izumi, F. *Solid State Sciences* **2**, 673–687 (2000).

[176] Fisher, C. A. J. Crystal structure as used in [173] from direct communication with the author. The crystal structures as published in the ICSD [177, 178] contain some Fe and O sites with half occupancy., May (2010).

[177] Greaves, C., Jacobson, A. J., Tofield, B. C., and Fender, B. E. F. *Acta Cryst. B* **31**, 641–646 (1975).

[178] Hodges, J. P., Short, S., Jorgensen, J. D., Xiong, X., Dabrowski, B., Mini, S. M., and Kimball, C. W. *J. Solid State Chem.* **151**, 190–209 (2000).

[179] Tassel, C., Watanabe, T., Tsujimoto, Y., Hayashi, N., Kitada, A., Sumida, Y., Yamamoto, T., Kageyama, H., Takano, M., and Yoshimura, K. *J. Am. Chem. Soc.* **130**, 3764–3765 (2008).

[180] Tassel, C., Pruneda, J. M., Hayashi, N., Watanabe, T., Kitada, A., Tsujimoto, Y., Kageyama, H., Yoshimura, K., Takano, M., Nishi, M., Ohoyama, K., Mizumaki, M., Kawamura, N., Íñiguez, J., and Canadell, E. *J. Am. Chem. Soc.* **131**(1), 221–229 (2009).

[181] Xiang, H. J. and Wei, S.-H. *Phys. Rev. Lett.* **100**, 167207 (2008).

[182] Pruneda, J. M., Íñiguez, J., Canadell, E., Kageyama, H., and Takano, M. *Phys. Rev. B* **78**, 115101 (2008).

[183] Wu, H.-P., Deng, K.-M., Tan, W.-S., Xiao, C.-Y., Hu, F.-L., and Li, Q.-X. *Chi. Phys. B* **18**(11), 5008–5014 (2009).

[184] Islam, M. S., Driscoll, D. J., Fisher, C. A. J., and Slater, P. R. *Chem. Mater.* **17**, 5085–5092 (2005).

[185] Snedden, A., Lightfoot, P., Dinges, T., and Islam, M. S. *J. Solid State Chem.* **177**(10), 3660–3665 (2004).

[186] Olson, C., Nelson, J., and Islam, M. S. *J. Phys. Chem. B* **110**(20), 9995–10001 (2006).

[187] Rutt, O. J., Williams, G. R., and Clarke, S. J. *Chem. Commun.* , 2869–2871 (2006).

[188] Fjellvag, H., Gronvold, F., Stolen, S., and Hauback, B. C. *J. Solid State Chem.* **124**, 52–57 (1996).

[189] Bakken, E., Stølen, S., Norby, T., Glenne, R., and Budd, M. *Solid State Ionics* **167**, 367–377 (2004).

[190] Paulus, W., Schober, H., Eibl, S., Johnson, M., Berthier, T., Hernandez, O., Ceretti, M., Plazanet, M., Conder, K., and Lamberti, C. *J. Am. Chem. Soc.* **130**, 16080–16085 (2008).

[191] Kageyama, H., Watanabe, T., Tsujimoto, Y., Kitada, A., Sumida, Y., Kanamori, K., Yoshimura, K., Hayashi, N., Muranaka, S., Takano, M., Ceretti, M., Paulus, W., Ritter, C., and André, G. *Angw. Chemie* **47**, 5740–5745 (2008).

[192] Tealdi, C., Mustarelli, P., and Islam, M. S. *Adv. Funct. Mater.* **20**, 3874–3880 (2010).

[193] Tolchard, J. R., Slater, P. R., and Islam, M. S. *Adv. Funct. Mater.* **17**, 2564–2571 (2007).

[194] Read, M., Islam, M. S., Watson, G., King, F., and Hancock, F. *J. Mater. Chem.* **10**(10), 2298–2305 (2000).

[195] Fisher, C. A. J., Islam, M. S., and Brook, R. J. *J. Solid State Chem.* **128**, 137 (1997).

[196] Farley, T. W. D., Hayes, W., Hull, S., Hutchings, M. T., and Vrtis, M. *J. Phys. Cond. Mat.* **3**, 4761–4781 (1991).

[197] Zintl, E., Harder, A., and Dauth, B. *Z. Elektrochem.* **40**, 588–593 (1934).

[198] Touzain, P., Brisse, F., and Caillet, M. *Canadian J. Chem.* **48**, 3358–3361 (1970).

[199] Touzain, P. and Caillet, M. *Revue de Chimie Minerale* **8**, 277–286 (1971).

[200] Zhao, J.-Z., Lu, L.-Y., Chen, X.-R., and Bai, Y.-L. *Physica B: Cond. Matt.* **387**, 245–249 (2007).

[201] Shen, C. H., Liu, R. S., Lin, J. G., and Huang, C. Y. *Mater. Res. Bull.* **36**, 1139–1148 (2001).

[202] Liu, L.-G. and Bassett, W. A. *J. Geophys. Research* **77**, 4934–4937 (1972).

[203] Sasaki, S., Fujino, K., and Takeuchi, Y. *Proc. Japan Acad.* **55**, 43–48 (1979).

[204] Yamada, H., Soejima, Y., Zheng, X. G., and Kawaminami, M. *Trans. Mater. Research Soc. Japan* **25**, 1199–1202 (2000).

[205] Pillet, S., Souhassou, M., Lecomte, C., Schwarz, K., Blaha, P., Rerat, M., Lichanot, A., and Roversi, P. *Acta Cryst. A* (57), 290–303 (2001).

[206] Bartos, A., Lieb, K. P., Uhrmacher, M., and Wiarda, D. *Acta Cryst. B* **49**, 165–169 (1993).

[207] Marezio, M. and Remeika, J. P. *J. Chem. Phys.* **46**, 1862–1865 (1967).

[208] Santos, C., Strecker, K., Suzuki, P. A., Kycia, S., Silva, O. M. M., and Silva, C. R. M. *Mater. Res. Bull.* **40**, 1094–1103 (2005).

[209] Marezio, M. *Acta Cryst.* **20**, 723–728 (1966).

[210] Hirosaki, N., Ogata, S., and Kocer, C. *J. Alloys Compd.* **351**, 31–34 (2003).

[211] Heiba, Z. K., Arda, L., and Hascicek, Y. S. *J. Appl. Cryst.* **38**, 306–310 (2005).

[212] Nakayama, S., Higuchi, Y., Kondo, Y., and Sakamoto, M. *Solid State Ionics* **170**(3–4), 219–223 (2004).

[213] Sansom, J. E. H., Richings, D., and Slater, P. R. *Solid State Ionics* **139**(3–4), 205–210 (2001).

[214] Islam, M. S., Tolchard, J. R., and Slater, P. R. *Chem. Commun.* , 1486–1487 (2003).

[215] Sansom, J. E. H., Tolchard, J. R., Islam, M. S., Apperley, D. C., and Slater, P. R. *J. Mater. Chem.* **16**, 1410–1413 (2006).

[216] Orera, A., Kendrick, E., Apperley, D. C., Orera, V. M., and Slater, P. R. *Dalton Trans.* (39), 5296–5301 (2008).

[217] León-Reina, L., Losilla, E. R., Martínez-Lara, M., Bruque, S., and Aranda, M. A. G. *J. Mater. Chem.* **14**, 1142–1149 (2004).

[218] León-Reina, L., Losilla, E. R., Martínez-Lara, M., Bruque, S., Llobet, A., Sheptyakov, D. V., and Aranda, M. A. G. *J. Mater. Chem.* **15**, 2489–2498 (2005).

[219] Kendrick, E., Islam, M. S., and Slater, P. R. *Chem. Commun.* , 715–717 (2008).

[220] Pramana, S. S., Klooster, W. T., and White, T. J. *Acta Cryst. B* **63**, 597–602 (2007).

[221] Kendrick, E., Orera, A., and Slater, P. R. *J. Mater. Chem.* **19**, 7955–7958 (2009).

[222] Tao, S. and Irvine, J. T. S. *Mater. Res. Bull.* **36**(7–8), 1245–1258 (2001).

[223] Tolchard, J. R., Sansom, J. E. H., Islam, M. S., and Slater, P. R. *Dalton Trans.* , 1273–1280 (2005).

[224] Baikie, T., Mercier, P. H. J., Elcombe, M. M., Y., K. J., Le Page, Y., Mitchell, L. D., White, T. J., and Whitfield, P. S. *Acta Cryst. B* **63**, 251–256 (2007).

[225] Kendrick, E. and Slater, P. R. *Mater. Res. Bull.* **43**, 2509–2513 (2008).

[226] Kendrick, E., Sansom, J. E. H., Tolchard, J. R., Islam, M. S., and Slater, P. R. *Faraday Discuss.* **134**, 181–194 (2007).

[227] Sansom, J. E. H., Sermon, P. A., and Slater, P. R. *Solid State Ionics* **176**, 1765–1768 (2005).

[228] Orera, A., Baikie, T., Panchmatia, P. M., White, T. J., Hanna, J. V., Smith, M. E., Islam, M. S., Kendrick, E., and Slater, P. R. *Fuel Cells* **11**(1), 10–16 (2011).

[229] Sansom, J. E. H. and Slater, P. R. *Solid State Ionics* **2004**(1–2), 23–27 (2004).

[230] Berastegui, P., Hull, S., García García, F. J., and Grins, J. *J. Solid State Chem.* **168**(1), 294–305 (2002).

[231] Gale, J. D. and Henson, N. J. *J. Chem. Soc., Faraday Trans.* **90**, 3175–3179 (1994).

[232] Panchmatia, P. M., Orera, A., Kendrick, E., Hanna, J. V., Smith, M. E., Slater, P. R., and Islam, M. S. *J. Mater. Chem.* **20**, 2766–2772 (2010).

[233] Shannon, R. D. *Acta Cryst.* **A 32**, 751 (1976).

[234] Kröger, F. A. and Vink, H. J. In *Solid State Phyics,* Seitz, F. and Turnbull, D., editors, volume 3, 307. Academnic Press, 525 B Street, Suite 1900, San Diego, CA 92101-4495, USA (1956).

[235] Kröger, F. A. *The Chemistry of Imperfect Crystals*. North-Holland: Amsterdam, 2nd edition, (1974).

[236] Gardiner, G. R. and Islam, M. S. *Chem. Mater.* **22**(3), 1242–1248 (2010).

[237] Weller, M. T. *Inorganic Materials Chemistry*. Oxford University Press, Great Clarendon Street, Oxford, OX2 6DP, (1994).

[238] Williams, G. *Linear Algebra with Applications*. Jones and Bartlett, Barb House, Barb Mews, London, W6 7PA, fourth edition, (2001).

[239] Press, W. H., Teukolsky, S. A., Vetterling, W. T., and Flannery, B. P. *Numerical Recipes: The Art of Scientific Computing*. Cambridge University Press, third edition, (2007).

[240] Harding, J. H. and Pyper, N. C. *Philos. Mag. Lett.* **71**(2), 113–121 (1995).

[241] Tealdi, C., Malavasi, L., Fisher, C. A. J., and Islam, M. S. *J. Phys. Chem. B* **110**, 5396–5402 (2006).

[242] Busker, G., Chroneos, A., Grimes, R. W., and Chen, I.-W. *J. Am. Ceram. Soc.* **82**(6), 1553–59 (1999).

[243] Cherry, M., Islam, M. S., and Catlow, C. R. A. *J. Solid State Chem.* **118**, 125–132 (1995).

[244] Jorgensen, J. D. *J. Appl. Phys.* **49**, 5473–5478 (1978).

[245] Abrahams, S. C. and Bernstein, J. L. *Acta Cryst. B* **25**, 1233–1236 (1969).

[246] Walmsley, H. P. *Proc. Phys. Soc. Lond.* **40**, 7–13 (1928).

[247] Shirane, G., Pickart, S. J., Nathans, R., and Ishikawa, Y. *J. Phys. Chem. Solids* **10**, 35–43 (1959).

[248] Abrahams, S. C. and Bernstein, J. L. *J. Chem. Phys.* **55**, 3206–3211 (1971).

[249] Baur, W. H. *Acta Cryst. B* **32**, 2200–2204 (1976).

[250] Howard, C. J., Hill, R. J., and Reichert, B. E. *Acta Cryst. B* **44**, 116–120 (1988).

[251] Baur, W. H. and Khan, A. A. *Acta Cryst. B* **27**, 2133–2139 (1971).

[252] Harada, H., Sasa, Y., and Uda, M. *J. Appl. Cryst.* **14**, 141–142 (1981).

[253] Taylor, D. *Trans. J. British Ceram. Soc.* **83**, 32–37 (1984).

[254] OriginLab Corporation, One Roundhouse Plaza, Suite 303, Northampton, MA 01060. *Online Help for Origin 7*, (2001).

Appendix A

Defect Chemistry and Ion Migration

The fundamental importance of defects and ion migration were outlined in Chapter 1. Below, we present more detailed information on the thermodynamics of defect formation and introduce further terminology, including Kröger–Vink notation.

A.1 Point Defects

Defects exist within all crystalline materials, and the chemistry of these defects is fundamentally important to the ionic conduction processes that underpin solid oxide fuel cell operation. A *point defect* is a structural deviation from the perfect periodicity of the crystal that is localised around one particular point in space (i.e., it does not extend significantly in any direction[a]).

There are three basic types of point defect that can be formed within a crystal lattice: *vacancies*, *interstitials* and *substitutionals*. A vacancy is simply the absence of an atom from its normal lattice site, whilst an interstitial defect is the presense of *any* atom on a site not normally occupied. Lastly, a substitutional is the replacement of an atom with *any* different atom (e.g., a dopant) at a normal lattice site.

Introducing a point defect into a crystal disrupts the normal charge distribution of the lattice, which has structural and energetic consequences. The difference in charge between the defect and the same site in the perfect lattice, referred to as the 'effective' charge of the defect, is of critical importance when considering the defect chemistry of a material. The influence of the effective charge of a defect extends

[a]Examples of *extended defects* include edge dislocations, stacking faults and grain boundaries. Whilst these defects do influence the physical properties of materials, their investigation is beyond the scope of this work.

several Ångström into the lattice, and the local relaxation of the defective lattice in this region is important to the properties of the material.

A.2 Kröger–Vink notation

Conceptualising chemical process involving point defects can be quite difficult using the normal tools of chemical notation, particularly because effective charges must be distinguished from real charges, and the location of atoms within the lattice is important. To address these issues, Kröger and Vink suggested a chemical notation in the early 1950s which neatly encapsulates any instance of the point defects described in the previous section [234, 235].

In Kröger–Vink notation, the main symbol a point defect is given is used to denote whether it is a vacancy (using V) or is a particular atom (using the normal atom label). The symbol is then given a subscript that is used to describe the location of the defect. So, for example, a vacancy on a manganese site would be written as V_{Mn}, a fluorine substitutional on an oxygen site as F_O, and an oxygen interstitial as O_i.

Three different symbols are then available to denote the effective charge of a defect: neutral defects are labelled with a cross $\times$, defects with an effective positive charge are labelled with one or more dots $\cdot$, and those with an effective negative charge are labelled with one or more prime symbols $'$. So, the three examples above would look like V''_{Mn}, $F^{\cdot}_{O}$ and O''_i if manganese was in its +2 oxidation state and fluorine and oxygen took their usual charges.

A.3 Origins of Defects in Crystals

A.3.1 Intrinsic Defects

There are a number of mechanisms by which defects are introduced into real crystals. Due to thermodynamic considerations, all crystals will be defective to some degree intrinsically, and the defect population increases rapidly with temperature [15]. These *intrinsic defects* are composed of two or more point defects that together maintain the charge neutrality of the system. The *Frenkel* defect, the *Schottky* defect and the *anti-site* defect, illustrated in Figure A.1, are three prominent types of intrinsic defect that will be considered in this work.

Frenkel defects are composed of a vacancy–interstitial pair, as shown in Figure A.1a. Effectively, an ion has been displaced from its normal site to another, empty location within the lattice. In Kröger–Vink notation, the formation of an oxide Frenkel defect

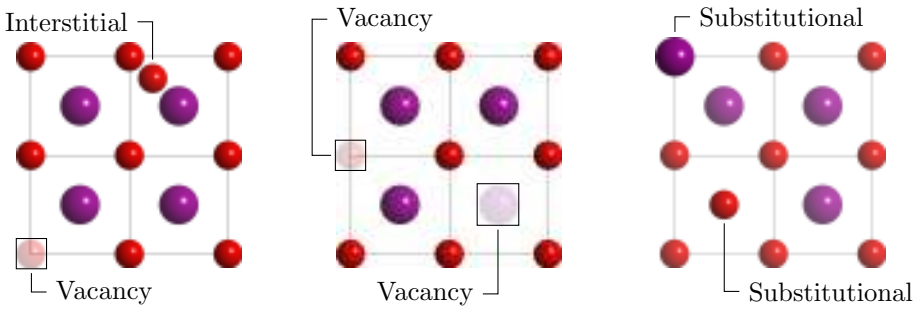

(a) Frenkel **(b)** Schottky **(c)** Anti-site

Figure A.1: Schematic illustrations of examples three types of intrinsic defects, labelled with their constituent point defects. In this example lattice the large purple spheres represent cations and the small red spheres represent anions of equal and opposite charge.

can be written as

$$\mathrm{O}_{\mathrm{O}}^{\times} \longrightarrow \mathrm{V}_{\mathrm{O}}^{\bullet\bullet} + \mathrm{O}_{\mathrm{i}}^{\prime\prime}. \tag{A.1}$$

The formation enthalpy of a Frenkel defect is simply the enthalpy of the above reaction the process above (i.e., the sum of the constituent defect energies). This type of disorder can be an important source of interstitial oxide ions in fast oxide ion conductors.

A Schottky defect consists of a set of vacancies that remove a whole formula unit of ions from the crystal (see Figure A.1b). For example, a Schottky defect in the $LaGaO_3$ perovskite material can be written as

$$\mathrm{La}_{\mathrm{La}}^{\times} + \mathrm{Ga}_{\mathrm{Ga}}^{\times} + 3\,\mathrm{O}_{\mathrm{O}}^{\times} \longrightarrow \mathrm{V}_{\mathrm{La}}^{\prime\prime\prime} + \mathrm{V}_{\mathrm{Ga}}^{\prime\prime\prime} + 3\,\mathrm{V}_{\mathrm{O}}^{\bullet\bullet} + \mathrm{LaGaO}_3. \tag{A.2}$$

In addition to the energies of the individual point defects, the calculation of the Schottky formation energy requires a lattice energy term, as exemplified by the final term in Equation A.2.

Finally, the anti-site defect consists of a pair of substitutional defects that swap the positions of two ions within a lattice; for example, in the $LiFePO_4$ olivine lithium-battery material [236]:

$$\mathrm{Li}_{\mathrm{Li}}^{\times} + \mathrm{Fe}_{\mathrm{Fe}}^{\times} \longrightarrow \mathrm{Fe}_{\mathrm{Li}}^{\prime} + \mathrm{Li}_{\mathrm{Fe}}^{\bullet}. \tag{A.3}$$

Intrinsic defects occur naturally in all crystals because the energetic cost of moving ions away from where they are lowest in energy is balanced by the entropic gain in introducing some disorder into the system. The formation enthalpy of an intrinsic defect is necessarily positive,[b] and can be assumed to increase linearly with the number of defects formed because the concentration of defects is very low. The change in entropy for the formation of an intrinsic defect will also be positive, therefore *lowering* the Gibbs free energy, because introducing the defect into the system will

[b] If this were not the case, the crystal structure would not represent the most stable arrangement of the constituent ions.

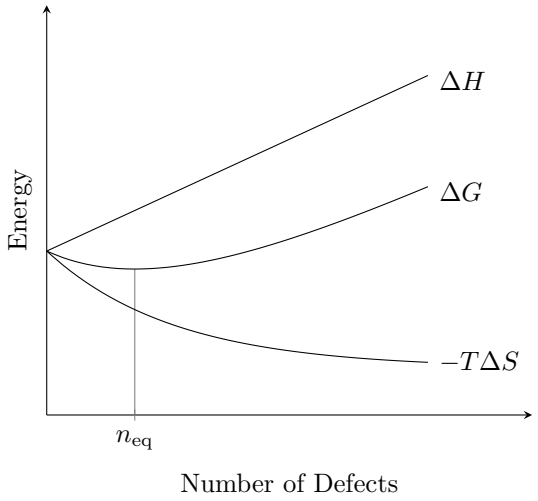

Figure A.2: Schematic illustration of the change in the Gibbs free energy ΔG and its constituent enthalpic ΔH and entropic $-T\Delta S$ components with respect to the number of defects formed within a crystal. The equilibrium number of defects present is found at n_{eq}, the minimum of ΔG.

increase its disorder. The amount of disruption to the lattice becomes smaller as each further defect is added, however, meaning that the contribution to the Gibbs free energy from the entropic term diminishes at higher defect concentrations. The result, illustrated[c] in Figure A.2, is that at any given temperature there is an optimum concentration of defects that minimises the free energy of the structure by balancing the contributions of the enthalpic and entropic terms.

A.3.2 Extrinsic Defects: Introducing Defects by Doping

The presence of impurities introduce other point defects within the crystal lattice. These defects form as necessary to compensate for the effective charge of the foreign ion. For example, the 'solution' of Sr ions into the $LaGaO_3$ perovskite can be compensated by the formation of oxide ion vacancies:

$$La_{La}^{\times} + SrO + \tfrac{1}{2}O_{O}^{\times} \longrightarrow Sr_{La}' + \tfrac{1}{2}V_{O}^{\cdot\cdot} + \tfrac{1}{2}La_2O_3. \tag{A.4}$$

The impurity may be naturally incorporated into the lattice or may be intentionally introduced during synthesis, a process which is called *doping*. Doping may be used not only to control the defect chemistry of a material, but can also affect other properties such as the phase stability or electrical conductivity.

Dopant ions with the same charge as their host site are said to be *isovalent*, whilst those that have a differing charge are said to be *aliovalent*. Aliovalent dopants that have a more positive charge than their host site are said to be *supervalent*, whilst those with a less positive charge are referred to as *subvalent*. Borrowing language

[c] Figure A.2 is an original recreation of Figure 6.1 from Mark T. Weller's Oxford Chemistry Primer *Inorganic Materials Chemistry* [237].

from semiconductor physics, supervalent and subvalent dopants can also be referred to as *donor* and *acceptor* ions respectively, because of the electrons they add to or withdraw from the system.

A.4 Migration of Defects

Fast ion migration through an otherwise-impermeable crystal membrane is central to the operation of SOFCs, and the existence and behaviour of defects within the crystal lattice are fundamental to the mechanisms that underpin this migration. Ion migration occurs when a particular type of defect in a crystal has enough energy to move sites repeatedly though the lattice in a connected manner. The energy barriers to these migration processes are high, and thus elevated temperatures (700–1000℃) are required for SOFC operation.

Ionic migration mechanisms can be classified as either vacancy-hopping or interstitial-type mechanisms. In the vacancy hopping mechanism, a lattice oxide ion neighbouring a vacant lattice site hops from its lattice position to the vacant site, resulting in a net motion of the oxide ion in one direction and the vacancy in the opposite direction, as shown in Figure 1.3. Should the geometry of the crystal be conducive to further hops happening in the same or a similar direction, long range migration of oxide ions can occur. Current-generation SOFC materials, based on Y/ZrO_2, conduct oxide ions via the vacancy-hopping mechanism.

Interstitial-type mechanisms involve either the migration of one interstitial species through the crystal lattice [16, 17] or the exchange of an interstitial ion with a lattice ion, which is displaced onto a neighbouring lattice site [18, 19]. The latter of these two mechanisms is often referred to as an interstitialcy-type mechanism, and is illustrated in Figure 1.4. Materials with interstitial-type conduction mechanisms present exciting new opportunities in the field of ion conductors, and are being researched extensively as alternative SOFC materials.

Appendix B

Program Details and Performance Considerations

B.1 Program Details

The computational chemistry packages used in this work were introduced at the beginning of Chapter 2. For the sake of completeness and reproducibility, it is noted that GULP versions 3.4.5 and 3.5.2, DL_POLY version 2.20, VASP version 4.6.36 and CASTEP version 5.0 were used in this work. Each of these packages implements a different set of computational chemistry techniques and is thus only applicable to certain research questions. The next section highlights some areas where these packages differ and briefly introduces some performance-related issues.

B.2 Performance Considerations

Measuring the performance of a computer program is a complex task, and in general a balance must be struck by program authors between fast, approximate simulations and lengthy, accurate ones. More subtly, the amount of computation required for a given problem (the computational 'cost' or 'expense') can be reduced by clever implementation of the appropriate techniques, which often requires platform-specific knowledge and careful analysis of the relative performance of various program components.

B.2.1 Parallelism

A computational task can be performed more quickly by breaking the task into chunks that can be processed in parallel. Unfortunately, this adds complexity to the

implementation and can lead to heavily reduced gains in performance once the inter-process communications overhead starts to outweigh the computational load. This non-linear relationship between increased parallelism and time means that careful benchmarking is required to optimise the computational efficiency of a program for a given problem.

In this work, we used 256 processors for our VASP calculations of the 4×4 supercell of $SrFeO_2$, 128 processors for our MD simulations of $8 \times 8 \times 8$ supercells of $SrFeO_2$ and 256 processors for our MD simulations of $6 \times 6 \times 2$ supercells of Nd_2NiO_4.

B.2.2 The Cost of Mathematical Operations

Different algorithms and mathematical operations (such as matrix inversion, for example) scale differently with simulation size or complexity. Each code is designed with a particular range of target applications in mind, and thus parts of that code are designed to optimise calculation for those particular applications. This must be considered as part of a modelling study.

A particular case in point is the selection of minimisation algorithm. For static-lattice minimisations GULP (by default) uses the second-derivative-based Newton–Raphson minimisation algorithm, because analytical second derivatives are very easy to calculate in a potential-based simulation. Using Newton–Raphson reduces the number of steps, and hence computational time, required to achieve convergence.

In contrast, it is impossible to use analytical second-derivatives in electronic structure codes such as VASP, and numerical values are very costly to compute. This cost negates any computational benefit from using the second-derivative method, and thus electronic structure codes are limited to using the first-order conjugate gradients minimisation technique.

Similarly, matrix inversion itself is a computationally expensive operation, typically of the order N^3 in complexity. Thus, for large simulations, it could be advantageous to use the conjugate gradients algorithm that takes more cheap steps, than taking fewer expensive ones. These examples are presented merely to highlight the types of issues that program authors and advanced users consider, and are entire fields of research in themselves.

Appendix C

Additional Methodology

The following sections present some additional methodology that is considered instructive to the context of this work, but did not fit neatly with the narrative presented in Chapter 2.

C.1 The Equivalence of the Verlet and Velocity Verlet Numerical Integration Algorithms

Section 2.3.1 detailed the Verlet algorithm for computing the trajectories of atoms within a molecular dynamics simulation. We then introduced velocity Verlet integrator and made the assertion that these two methods produce identical trajectories. For the curious or sceptical reader, we present below the link between the two methods.

First, we shall restate the main equations. The original Verlet algorithm is

$$\mathbf{r}_{n+1} = 2\mathbf{r}_n - \mathbf{r}_{n-1} + \mathbf{a}_n \Delta t^2, \tag{C.1}$$

and the velocities, which are not obtained directly using the Verlet method, are defined as

$$\mathbf{v}_n = (\mathbf{r}_{n+1} - \mathbf{r}_{n-1})/2\Delta t. \tag{C.2}$$

The velocity Verlet algorithm is stated as

$$\mathbf{r}_{n+1} = \mathbf{r}_n + \mathbf{v}_n \Delta t + \tfrac{1}{2}\mathbf{a}_n \Delta t^2 \tag{C.3}$$

$$\mathbf{v}_{n+1} = \mathbf{v}_n + \tfrac{1}{2}\left(\mathbf{a}_{n+1} + \mathbf{a}_n\right)\Delta t \tag{C.4}$$

Replacing the $\mathbf{v}_n$ term in Equation C.3 with Equation C.2 yields

$$\mathbf{r}_{n+1} = \mathbf{r}_n + \tfrac{1}{2}(\mathbf{r}_{n+1} - \mathbf{r}_{n-1}) + \tfrac{1}{2}\mathbf{a}_n \Delta t^2,$$

which can simply be multiplied by two and the terms cancelled as appropriate, giving the original Verlet equation (C.1).

The relationship between Equation C.4 and Equation C.2 is slightly less straightforward. Firstly, rearranging the original Verlet equation (C.1) gives

$$\mathbf{a}_n = (\mathbf{r}_{n+1} - 2\mathbf{r}_n + \mathbf{r}_{n-1})/\Delta t^2$$

and, incrementing the timestep,

$$\mathbf{a}_{n+1} = (\mathbf{r}_{n+2} - 2\mathbf{r}_{n+1} + \mathbf{r}_n)/\Delta t^2.$$

Now substituting these terms into Equation C.4, we find

$$\mathbf{v}_{n+1} = \mathbf{v}_n + (\mathbf{r}_{n+2} - \mathbf{r}_{n+1} - \mathbf{r}_n + \mathbf{r}_{n-1})/2\Delta t,$$

which can be rearranged into

$$\mathbf{v}_{n+1} = \mathbf{v}_n - (\mathbf{r}_{n+1} - \mathbf{r}_{n-1})/2\Delta t + (\mathbf{r}_{n+2} - \mathbf{r}_n)/2\Delta t.$$

The first two terms of this expression cancel by Equation C.2, leaving

$$\mathbf{v}_{n+1} = (\mathbf{r}_{n+2} - \mathbf{r}_n)/2\Delta t,$$

which is clearly equivalent to Equation C.2 if the timestep is decremented.

C.2 Eigenvectors, Eigenvalues and Eigendecomposition

Eigenvectors and their corresponding eigenvalues are important mathematical objects that are very useful in understanding and manipulating matrices. An *eigenvector* of a matrix A is a non-zero vector $\mathbf{v}$ that does not undergo rotation when transformed by that matrix:

$$A\mathbf{v} = \lambda\mathbf{v}, \tag{C.5}$$

where the scalar constant λ corresponding to $\mathbf{v}$, is called an *eigenvalue* of H. From the above, it is evident that any multiple of an eigenvector is still an eigenvector, however these multiples are not considered as eigenvectors in their own right.

Eigenvectors and eigenvalues play an important role in the construction and analysis of techniques such as conjugate gradient minimisation [74]. They are also fundamentally important in the determination and analysis of vibrational modes, because the vibrational frequencies of a system of atoms are the eigenvalues of the Hessian matrix, and corresponding eigenvectors represent the vibrational modes.

The eigenvalues and eigenvectors of a matrix can be found as follows: Equation C.5 can be rearranged as $(A - \lambda I)\mathbf{v} = 0$, and since $\mathbf{v}$ cannot be zero by definition, the

columns of the matrix $A-\lambda I$ must show linear dependence[a], and hence $A-\lambda I$ must be singular (have no inverse):

$$\det\left|A-\lambda I\right|=0. \tag{C.6}$$

Multiplying out this determinant yields an n degree polynomial in λ, where n is the dimension of the Hessian matrix. This polynomial is called the *characteristic polynomial* of A, and its roots are the eigenvalues of A. The eigenvectors of A can then be found by substituting the eigenvalues back into Equation C.5 [238]. This method is very computationally inefficient, however, and a better method is required for practical applications.

Eigendecomposition, also known as *diagonalisation*, is the process of factorising a matrix A into separate eigenvector and eigenvalue components:[b]

$$A=Q\Lambda Q^{\mathrm{T}}, \tag{C.7}$$

where Q is a matrix of the eigenvectors of A:

$$Q=\begin{bmatrix}\mathbf{v}_1 & \mathbf{v}_2 & \cdots & \mathbf{v}_n\end{bmatrix},$$

which is by definition orthogonal,[c] and Λ is a diagonal matrix of the eigenvalues of A:

$$\Lambda=\begin{bmatrix}\lambda_1 & 0 & \cdots & 0\\ 0 & \lambda_2 & & 0\\ \vdots & & \ddots & \vdots\\ 0 & 0 & \cdots & \lambda_n\end{bmatrix}.$$

If A is real and symmetric, its eigenvectors are real and orthonormal, meaning that Q is orthogonal.

At first glance this method does not appear to be any more useful than finding the characteristic polynomial of A because prior knowledge of either the eigenvalues or eigenvectors of A seems to be required. The key to the practical use of the method, however, is that eigendecomposition can be achieved by iteratively applying transforms to the matrix until it becomes diagonal [239]:

$$\begin{aligned}A_0 &\rightarrow P_1^{\mathrm{T}}\cdot A_1\cdot P_1\\ &\rightarrow P_2^{\mathrm{T}}\cdot P_1^{\mathrm{T}}\cdot A_2\cdot P_1\cdot P_2\\ &\quad\vdots\\ &\rightarrow P_n^{\mathrm{T}}\ldots P_2^{\mathrm{T}}P_1^{\mathrm{T}}A_nP_1\,P_2\,\ldots P_n=Q^{\mathrm{T}}A_nQ=\Lambda\end{aligned}$$

[a] If the columns of $A-\lambda I$ were linearly independent, then the product of that matrix with $\mathbf{v}$ would yield a vector of non-zero magnitude

[b] To see why this factorisation is possible, it may be useful to note that:
$AQ=A\begin{bmatrix}\mathbf{v}_1 & \mathbf{v}_2 & \cdots & \mathbf{v}_n\end{bmatrix}=\begin{bmatrix}A\mathbf{v}_1 & A\mathbf{v}_2 & \cdots & A\mathbf{v}_n\end{bmatrix}=\begin{bmatrix}\lambda_1\mathbf{v}_1 & \lambda_2\mathbf{v}_2 & \cdots & \lambda_n\mathbf{v}_n\end{bmatrix}=Q\Lambda$

[c] Matrix A is said to be *orthogonal* if its transpose is equal to its inverse: $AA^{\mathrm{T}}=A^{\mathrm{T}}A=I$. In an orthogonal matrix, the dot product of any two different rows or columns is zero.

C.3 Mapping Migration Points onto a Migration Coordinate

When investigating a migration process, it is very useful to have a single scalar measure of how complete the process is for a given set of input coordinates. For example, an oxide ion moving between two sites $\mathbf{O_{(1)}}$ and $\mathbf{O_{(2)}}$ can be said to have a progress of zero when it is still sitting at its starting position $\mathbf{O_{(1)}}$, and a progress of one when it has reached its final position $\mathbf{O_{(2)}}$. When it is equidistant from both points, it can be said to be at 0.5 on this migration coordinate.

This transformation is facile if the ion's migration is linear — the migration progress η is simply the displacement of the ion along the migration path l divided by the length of the path $|\mathbf{a}|$:

$$\eta = \frac{l}{|\mathbf{a}|}, \tag{C.8}$$

where $\mathbf{a}$ is the vector between the two sites, and l is the displacement of the migrating ion along that vector. Within crystals of lower symmetry, however, it is unlikely that the migration path will be linear, and a more complex, curved path such as that shown in Figure 1.8 will probably be observed. In this case, the question of how one measures the distance along the migration path arises.

The simplest way to do this is to project the location of an ion onto the vector between the two migration sites. This is shown schematically in Figure C.1. The migration vector $\mathbf{a}$ is defined by the initial and final positions of the migrating ion ($\mathbf{O_{(1)}}$ and $\mathbf{O_{(2)}}$ respectively). The vector $\mathbf{b}$ is defined by the initial position of the ion $\mathbf{O_{(1)}}$ and its current position $\mathbf{x}$. We would like to find $\mathbf{x}_\mathrm{p}$, the point on $\mathbf{a}$ from which we can project a perpendicular line to $\mathbf{x}$, and the corresponding scalar l, the length along $\mathbf{a}$ where $\mathbf{x}_\mathrm{p}$ is found.

The angle α between the two vectors can be found using the dot product[d] identity:

$$\cos\alpha = \frac{\mathbf{a}\cdot\mathbf{b}}{|\mathbf{a}||\mathbf{b}|}, \tag{C.9}$$

and so, because $\mathbf{O_{(1)}}$, $\mathbf{x}$ and $\mathbf{x}_\mathrm{p}$ form a right-angled triangle,

$$\begin{aligned} l &= |\mathbf{b}|\cos\alpha \\ &= \frac{\mathbf{a}\cdot\mathbf{b}}{|\mathbf{a}|}. \end{aligned} \tag{C.10}$$

Similarly, the perpendicular deviation of the migrating ion from the linear path d can be found using

$$d = |\mathbf{b}|\sin\alpha. \tag{C.11}$$

This technique is useful because is provides an analytical mapping from any coordinate in the Cartesian space of the model onto the linear migration coordinate, which

[d] The dot product $\mathbf{c}\cdot\mathbf{d}$ of two vectors $\mathbf{c}$ and $\mathbf{d}$, each with n components, is $\mathbf{c}^T\mathbf{d} = \sum_{i=1}^{n} c_i d_i$

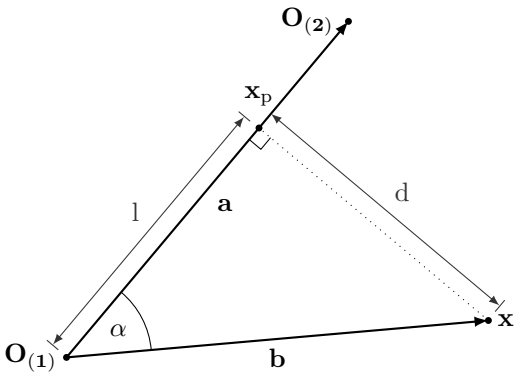

Figure C.1: Projecting an arbitrary point onto an arbitrary vector: An ion at point $\mathbf{x}$ is migrating between two sites $\mathbf{O_{(1)}}$ and $\mathbf{O_{(2)}}$. The vector between these sites is labelled $\mathbf{a}$ and a line perpendicular to $\mathbf{a}$ is constructed from point $\mathbf{x}_\mathrm{p}$, which lies on $\mathbf{a}$, to point $\mathbf{x}$. The distance l along $\mathbf{a}$ at which this line must be drawn is taken to be the coordinate of $\mathbf{x}$ in the direction of $\mathbf{a}$. The distance d of point $\mathbf{x}$ from the linear path can also be found.

is especially useful for comparison with the linear migration, and for observing how far a migration has deviated from linear geometry.

C.4 Issues Surrounding the Calculation of Oxidation Energy

As outlined previously (see Sections 3.2.3 and 4.2.3), the oxidation of the solid state materials examined in this work proceeds via

$$\tfrac{1}{2}\mathrm{O}_2 \rightleftharpoons \mathrm{O}_\mathrm{i}'' + 2\,\mathrm{h}^{\bullet}. \tag{C.12}$$

The energy of this process is calculated using contributions from various known or simulated processes.

The energy of the hole term $\mathrm{h}^{\bullet}$ consists of a contribution from the oxidised ion on the lattice site (for example, the energy of Ni^{3+} on Ni^{2+}) and the ionisation energy required to create that ion (for example, the energy of $\mathrm{Ni}^{2+} \longrightarrow \mathrm{Ni}^{3+}$). Whilst the former of these quantities is readily calculated using atomistic methods, an experimental value is used for the ionisation energy.

Likewise, whilst the energy of the oxide ion interstitial is readily calculated using atomistic methodology, the formation energy of an isolated oxide ion ($\frac{1}{2}\mathrm{O}_2 \longrightarrow \mathrm{O}^{2-}$) must be obtained by other means. The dissociation energy of diatomic oxygen and the first electron affinity of an individual oxygen atom are well-established experimentally-determined quantities. The second electron affinity of oxygen, however, is less easily defined and obtained.

It is not possible to measure the electron affinity of O^- directly by experiment

because the energy of an isolated free O^- ion and an electron is less than that of an isolated free O^{2-} ion. Therefore, any such value must be calculated via an indirect process (i.e., using a Born–Harbor cycle). Even when a value for the second electron affinity of oxygen is obtained, it is unclear as to whether this value pertains to producing a free O^{2-} ion, or an O^{2-} ion with the electron cloud distribution that occurs in the relevant crystal structure [240]. Further information can be found from Minervini et al. [137].

Both the issue of mixing experimentally and theoretically determined quantities, and that of the second electron affinity of oxygen must be considered when examining the oxidation energy. These cautionary notes notwithstanding, this methodology has proven useful in a wide range of studies [137, 173].

Appendix D

Supplementary Material Regarding Nd_2NiO_4

D.1 Crystal Structures and Trial Potentials

The first step in modelling Nd_2NiO_4 was to select an experimental structure and find a set of interatomic potentials that reproduce this structure in a satisfactory manner. A number of crystal structures for various (purportedly) stoichiometric phases of Nd_2NiO_4 are available in the literature; These structures are listed in Table D.1.

We tested the experimental structures in conjunction with a comprehensive range of Nd···O, Ni···O and O···O potentials from the literature. These potentials are listed in Table D.2. The accuracy and stability with which sets of these potentials reproduced the experimental structures was used to determine their viability for further modelling studies.

Table D.1: Experimental crystal structures for Nd_2NiO_4.

Space Group		Crystal System	Stable Temp. /K	Ref.
$I4/mmm$	(139)	Tetragonal	-	[157]
$P4_2/ncm$	(138)	Tetragonal	< 130	[156]
$Bmab$	(64)	Orthorhombic	> 130	[156]
$Bmab$	(64)	Orthorhombic	> 130	[156]
$Bmab$	(64)	Orthorhombic	> 130	[155]
$Abma$	(64)	Orthorhombic	> 130	[154]
$I4/mmm$	(139)	Tetragonal	> 874	[153]

Table D.2: List of candidate potentials and their literature references, where appropriate, for the modelling study of Nd_2NiO_4.

Ion, M	A /eV	ρ /Å	C /eV·Å^6	Y_M /|e|	k_M /eV·A^{-2}	Ref.
Nd^{3+}	1379.9	0.3601	0.0	-	-	[161]
	2638.19	0.3279	23.59	-	-	[137]
	1995.20	0.3430	22.59	-	-	[162]
	2148.14	0.3227	22.59	-	-	-
	1379.90	0.36072	22.59	-	-	[241]
	1545.21	0.35900	0.0	-	-	[36]
	13084.217	0.2550	0.0	1.322	302.35	[163]
Ni^{2+}	641.20	0.3372	0.0	-	-	[160]
	905.40	0.3145	0.0	-	-	[137]
	683.5	0.3332	0.0	2.00	8.77	[160]
Ni^{3+}	1279.23	0.2932	0.0	-	-	[137]
O^{2-}	22764.30	0.1490	43.0	-2.239	42.00	[36]
	9547.96	0.2072	32.0	-2.04	6.30	[137]
	9547.96	0.2192	32.0	-2.04	6.30	[242]
	35686.18	0.2010	32.0	-	-	-
O^{-}	35671.37	0.1376	13.72	-	-	[137]

All the structures were assessed, with the exception of that from Tamura [153]. We found that the majority of the orthorhombic structures were unstable with any combination of potentials from the literature. Refinement of the potential parameters did not produce significant improvement. Despite successful optimisation of the structure from Lehmann and Mueller-Buschbaum [154] and the low-temperature tetragonal structure from Rodríguez-Carvajal et al. [156], the validity and applicability of the (oxygen excess) structure of Nishijima et al. [157] made it the most appropriate to carry forward into the modelling work, as detailed in Section 3.2.1.

D.2 Defect Chemistry

This section provides some further information related to the the discussion of intrinsic defect chemistry in Section 3.2.2. Firstly, it is noted that the energies of all isolated point defects were calculated using the Mott–Littleton two-region approach, with radii of 12 and 24 Å for regions 1 and 2a respectively.

Secondly, although we find a 1.66 eV difference in energy between the 8g and 4d sites, the position of the interstitial is the same in both cases (i.e., for the 8g site $z = 0.25$). The difference in energy between the two sites is attributed to differing local relaxation between the two systems. In general, we found that the system was particularly sensitive to both starting configuration and the Mott-Littleton region parameters, which can perhaps be attributed to the artificially low oxygen content

Figure D.1: Configurations of cation stoichiometric supercells for the static-lattice NEB assessment of oxide ion migration in Nd_2NiO_4. The × symbol denotes interstitial oxygen at $c = \frac{3}{4}$, the + symbol denotes interstitial oxygen initially at $c = \frac{1}{4}$ and the open circle denotes the apical O2 lattice oxide ion, initially at $c = 0.18$.

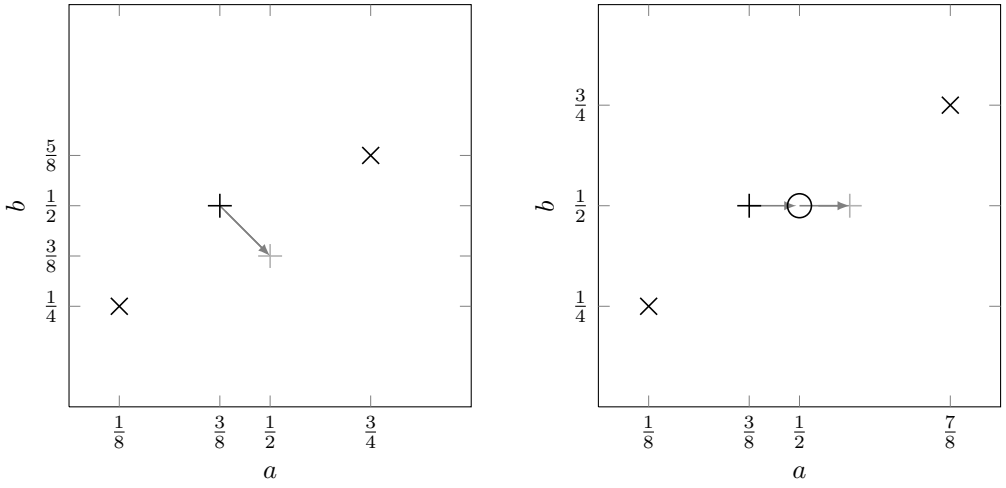

(a) Direct **(b)** Interstitialcy

of the system. Importantly, the Mott–Littleton parameters employed were selected based o the oxide Frenkel and oxidation energies they produce.

D.3 Oxide Ion Migration

D.3.1 NEB Calculations

Nudged elastic band calculations were performed to investigate the geometric and energetic factors of oxide ion migration in Nd_2NiO_4, as discussed briefly in Section 3.2.4. Further details are presented here.

A $4 \times 4 \times 1$ supercell of the high-temperature tetragonal phase of Nd_2NiO_4 was constructed. Three interstitial oxide ions were inserted into the cell giving rise to a composition of $Nd_2NiO_{4.09}$. The ions were arranged in the centre of the cell, as shown in Figure D.1, such as to make the initial and final configurations symmetrically equivalent and thus equal in energy,. Nineteen replicas were generated and simultaneously energy-minimised between these each pair of configurations, generating energy profiles for the migrations.

A similar approach was taken for the Nd deficient cells. Various Nd^{3+} ions were removed adjacent to the migrating oxide ions in an attempt to perturb the migration, whilst maintaining the symmetry of the migration process. Whilst some configurations exhibited energetic changes, no migration path was found to be more

Table D.3: Diffusion coefficients for oxide ion transport in Nd_2NiO_4 at a range of temperatures.

Temp. /K	D /cm^2 s^{-1}
873	3.44×10^{-9}
973	1.40×10^{-9}
1073	7.13×10^{-9}
1173	5.28×10^{-8}
1273	5.30×10^{-8}
1473	1.75×10^{-7}

favourable than that for interstitialcy migration in the cation stoichiometric cell. These simulations showed that the interstitial oxide ion defect is unstable next to the Nd vacancy, as in each instance the interstitial ion displaced a neighbouring apical O2 ion onto an adjacent interstitial site.

The Nd stoichiometric and Nd deficient calculations were performed both with compensating charge for the interstitial oxide ions smeared across all Ni sites and with explicit Ni^{3+} ions.

D.3.2 Molecular Dynamics

Nd Stoichiometric

Molecular dynamics simulations were performed on $6 \times 6 \times 2$ supercells of the Nd_2NiO_4 material. Sixteen oxide ions were randomly distributed onto the interstitial sites in the cell, producing a composition of $Nd_2NiO_{4.11}$. The charge of these oxide ions was compensated by altering the charge of the Ni^{3+} slightly. This 'smeared' charge model is justified because the electronic re-arrangements that can occur in the material happen on a much faster time scale than the ion motion. It is noted that the 'zero Kelvin ensemble' simulation (energy minimisation) of this cell seemed to exhibit a tilting of the NiO_6 octahedra in both the a and b directions, just as in the low-temperature tetragonal structure of Rodríguez-Carvajal et al. [156], shown in Figure 3.5c.

Section 3.2.4 detailed the change in diffusion with temperature in the form of an Arrhenius plot, shown in Figure 3.16. For completeness, Figure D.2 shows the weighted mean MSD data for O2 and the interstitial ions from which this plot was derived. Table D.3 lists the diffusion coefficients derived from this plot. The difference in calculated activation energy between the static-lattice and molecular dynamics techniques may possibly be due to concentration effects or the correlated motion of the ions in the MD simulation (see Figure 3.10).

The anisotropy of oxide ion diffusion with Nd_2NiO_4 was analysed using a modified

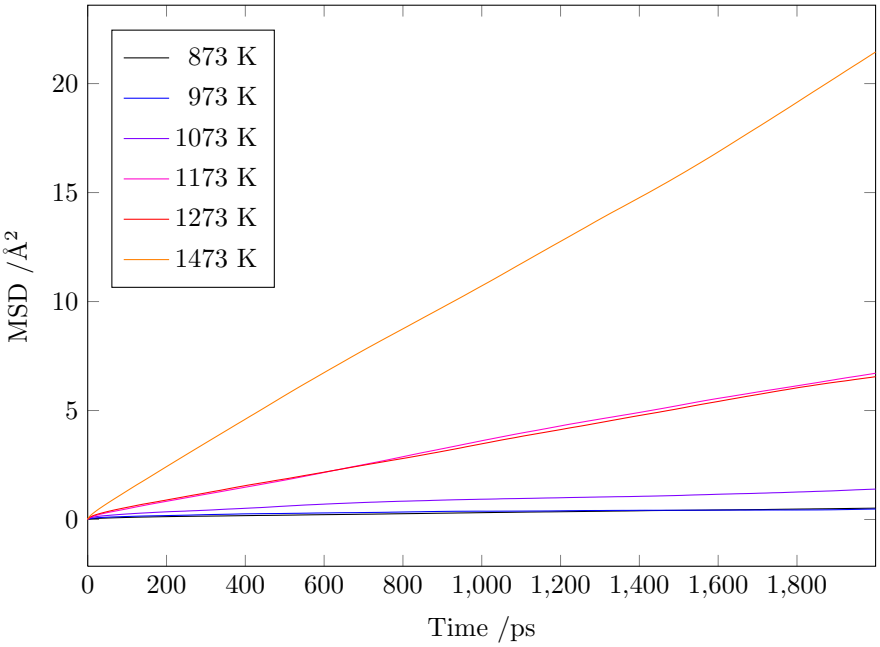

Figure D.2: Weighted mean MSD plots for O2 and O_i migration within Nd_2NiO_4 at a range of temperatures.

version of the `msdprg` program that is distributed as part of DL_POLY. We modified the program to track the displacement of ions in only one of the x, y or z Cartesian axes at a time. Figure D.3 shows the marked difference between migration in the z/c direction and migration in the xy/ab plane.

D.3.3 Nd Deficient

In addition to the stoichiometric supercells, we performed MD simulations of Nd deficient supercells of Nd_2NiO_4. These supercells contained the same levels of interstitial oxygen as the cation-stoichiometric cells, but included 13 Nd vacancies that were charge-compensated with a further additional positive charge spread across all the Ni^{3+} ions.

The Ni···Ni and Nd···Nd RDFs form these simulations are shown in Figures D.4 and D.5 respectively. These figures reveal that there is little difference between the cation sublattice of the cation-stoichiometric and Nd-deficient materials, aside from a slight reduction of around 1% in each of the unit cell parameters in the latter.

There is also little change in the cation–O1 and cation–O2 RDFs upon removal of Nd (see Figure D.6). The cation–O3 RDFs, however, appear not have reached such a well-exchanged, and thus indistinguishable, state in the Nd-deficient simulation due to the reduced oxide ion diffusivity.

Just as for the stoichiometric supercell, MSD data was calculated at each simulation

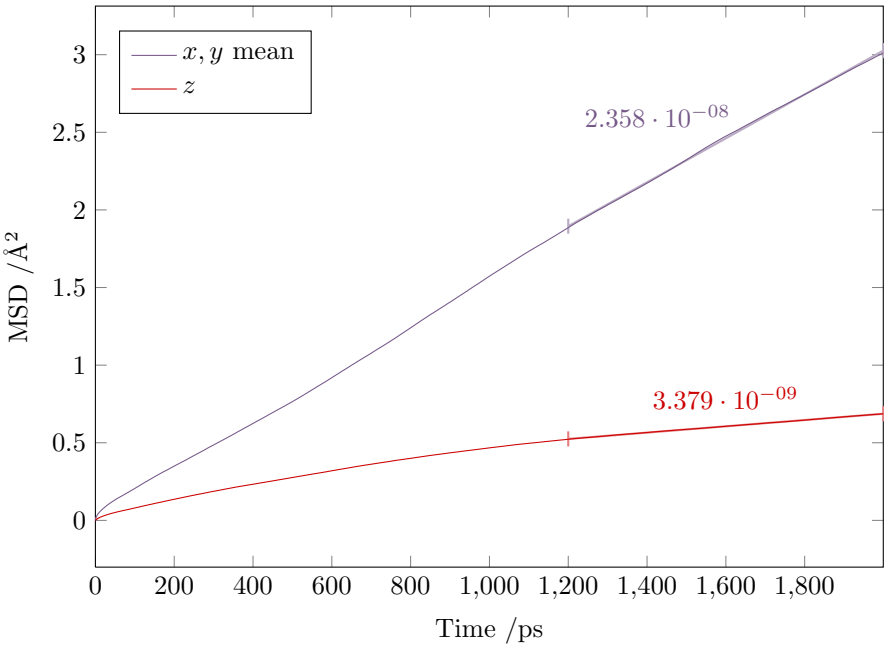

Figure D.3: Weighted mean MSD plot for O2 and O_i at 1173 K decomposed into migration in the z direction and within the x, y plane. A clear anisotropy in the migration is observed. Calculated diffusion coefficients from least squares regression are shown for each plot in units of cm^2 s^{-1}.

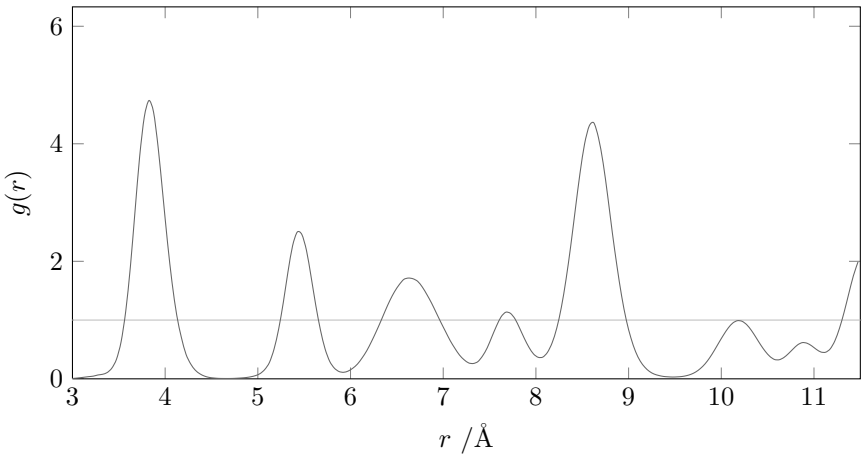

Figure D.4: Ni···Ni radial distribution function of Nd-deficient Nd_2NiO_4 at 1073 K.

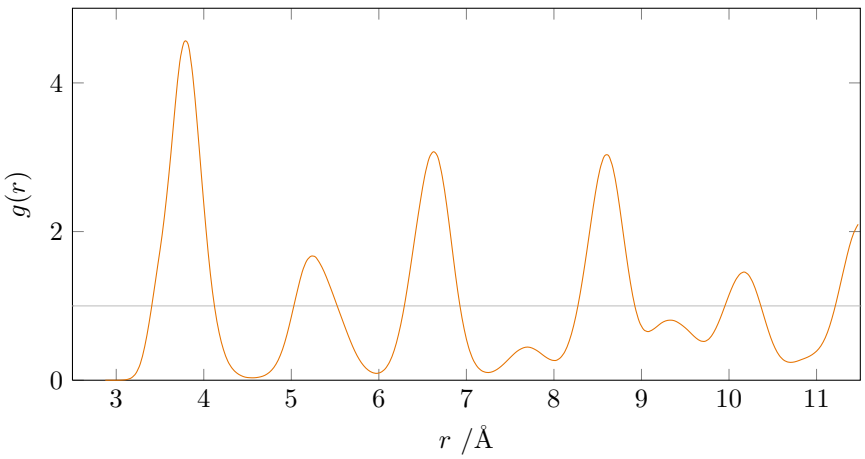

Figure D.5: Nd···Nd radial distribution function of Nd-deficient Nd_2NiO_4 at 1073 K.

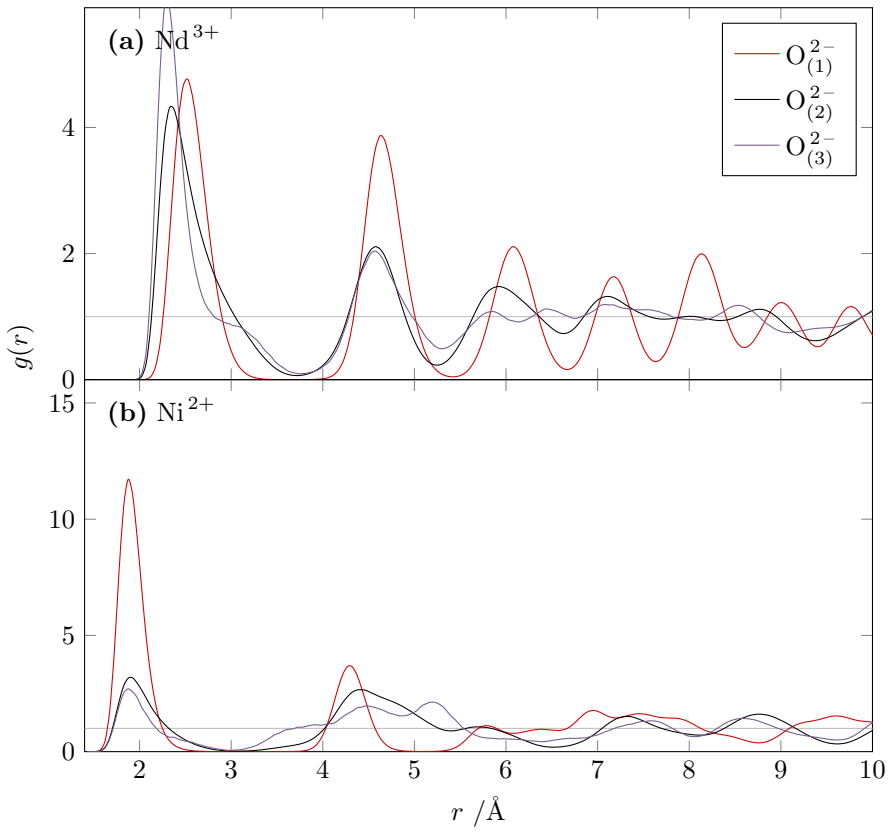

Figure D.6: Cation–oxide-ion radial distribution functions of Nd-deficient Nd_2NiO_4 at 1073 K. (a) Nd···O; (b) Ni···O; O1 ions are equatorial, whilst O2 and O3 are initially apical and interstitial respectively.

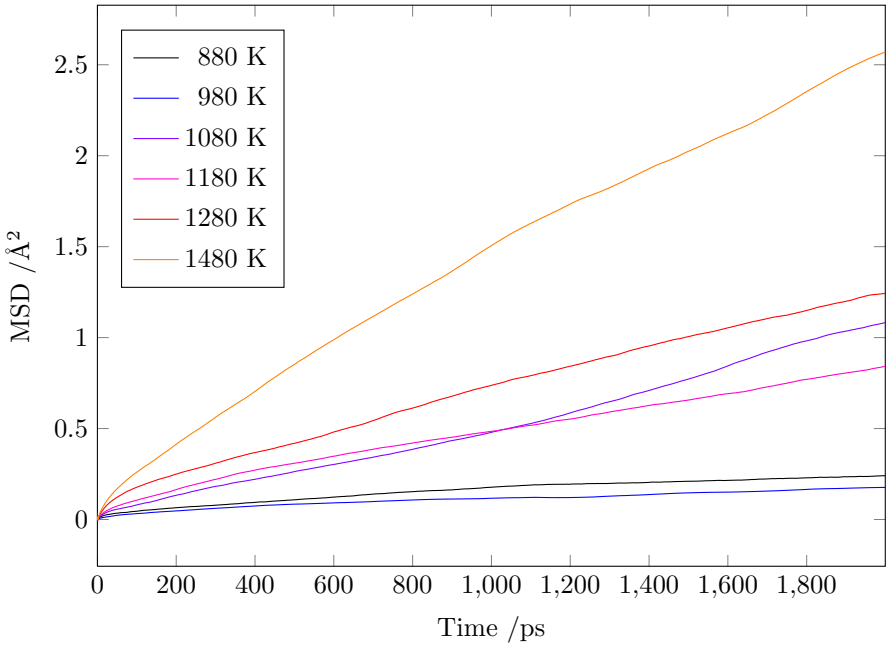

Figure D.7: Weighted mean MSD plots for O2 and O_i migration within Nd_2NiO_4 at a range of temperatures.

Table D.4: Diffusion coefficients for oxide ion transport in Nd deficient Nd_2NiO_4 at a range of temperatures.

Temp. /K	D /cm^2 s^{-1}
873	1.77×10^{-9}
973	8.35×10^{-10}
1073	7.55×10^{-9}
1173	6.65×10^{-9}
1273	1.24×10^{-8}
1473	1.34×10^{-8}

temperature in order to generate an Arrhenius plot. For completeness, Figure D.7 shows the MSD data from which the plot was derived, and Table D.4 lists the diffusion coefficients derived from the plot.

Appendix E

Supplementary Material Regarding $SrFeO_2$

E.1 Developmental Work

The production of an atomistic model of $SrFeO_2$ was a non-trivial task. As discussed in Section 4.2.1, a comprehensive range of potentials from the literature were assessed for their suitability. These potentials are listed in Table E.1. No combinations of these potentials, or any refinements of the parameters, succeeded in producing a stable potential model for the $SrFeO_2$ material, including those potentials used by Fisher et al. [173] to model the closely-related brownmillerite phase.

We employed a number of strategies to develop an improved potential model. Mean-field calculations were used to alter oxygen occupancy and location between the $SrFeO_2$ and $SrFeO_3$ compositions, and strongly indicated that the square-planar coordination of the Fe ion was the problematic feature. We attempted to produce a potential model in which the in-plane O···O interactions were distinct from the inter-plane O···O interactions, but this model did not produce a stable structure.

Our successful model was determined by systematically sampling the potential parameter space to find a new, stable starting point for the refinement of the parameters. We started with Sr···O and Fe···O potentials from Lewis and Catlow [160] and O···O from Khan et al. [36], which are very similar to those used by Fisher and Islam [173]. We systematically altered six of the parameters: Sr A, ρ and C; Fe A and ρ; and O C; and analysed the resulting structures, whilst the remaining parameters were fixed. We took the best of these models and refined it using relaxed fitting, which produced an excellent structural fit with no imaginary vibrational frequencies.

Table E.1: List of candidate potentials for the modelling study of $SrFeO_2$ and their literature references.

Ion, M	A /eV	ρ /Å	C /eV·Å^6	Y_M /|e|	k_M /eV·A^{-2}	Ref.
Sr^{2+}	992.049	0.35	0.0	-	-	[173]
	1400.0	0.3500	0.0	1.33	21.53	[160]
	959.1	0.3721	0.0	3.251	71.7	[139]
Fe^{2+}	1199.25	0.3299	0.0	-	-	[173]
	1105.2409	0.3106	0.0	2.997	19.26	[184]
Fe^{3+}	1156.36	0.3299	0.0	4.97	304.7	[243]
	1199.25	0.3299	0.0	-	-	[173]
	1102.4	0.3299	0.0	-	-	[160]
O^{2-}	22764.30	0.1490	21.0	-2.21	27.29	[173]
	22764.30	0.1490	43.0	-2.239	42.00	[36]
	22764.3	0.1490	96.9	-2.389	42.00	[139]
	9547.96	0.2192	32.	-2.04	6.3	[185]
	12420.5	0.2215	29.07	-2.8	31	[186]

E.2 Oxide Ion Migration

Section 4.2.4 detailed the findings of our investigation of oxide ion migration within the $SrFeO_2$ lattice. This sections provides further details of our static-lattice calculations and MD simulations. Firstly, a space-filling model of the material, including an interstitial oxide ion at the favourable 1b site (see Figure 4.4), is shown in Figure E.1. This figure illustrates that there is less free volume in the structure for direct migration between the lattice sites as may be implied by traditional ball-and-stick representations. Trying to force an oxide ion directly in between the two like-charged lattice oxide ions leads an unstable configuration.

We performed a carefully-constructed energy-minimisation calculation to determine whether there existed a transition state for cooperative migration in the [0 0 1] direction. We use the symmetry of the cell, as described in Figure E.2, to constrain the minimisation into finding either the saddle point for a concerted migration or the intermediate species for the step-wise process if no saddle point exists. The minimisation proceeded directly to the intermediate species, which supports the conclusion of our NEB calculations that cooperative migration will not occur in $SrFeO_2$.

An $8 \times 8 \times 8$ supercell of the material was used for our MD calculation, which were performed with DL_POLY. We used the same potential model as employed in the static-lattice calculations, with the exception that the shell model was removed. In order to simulate a partially oxidised material, we randomly inserted 32 addition oxide ions onto any of the available interstitial sites, resulting in an overall composition of $SrFeO_{2.06}$. To compensate for the charge of these interstitial ions, 64 random Fe^{3+} ions were randomly distributed over the Fe sites.

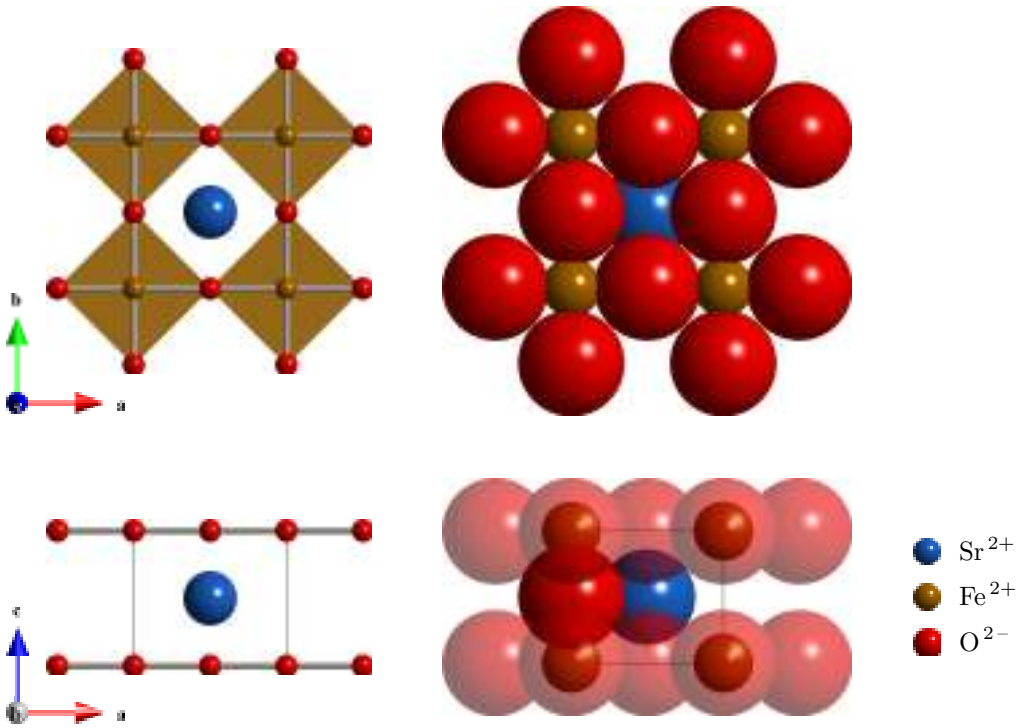

(a) Schematic Radii **(b)** Ionic Radii

Figure E.1: The $SrFeO_2$ unit cell represented as both (a) a convenient ball-and-stick schematic, and (b) a space-filling model in which ions are shown to scale in terms of their ionic radii. Figure (b) includes an additional oxide interstitial in the view down b to illustrate the large overlap between the interstitial and lattice ions.

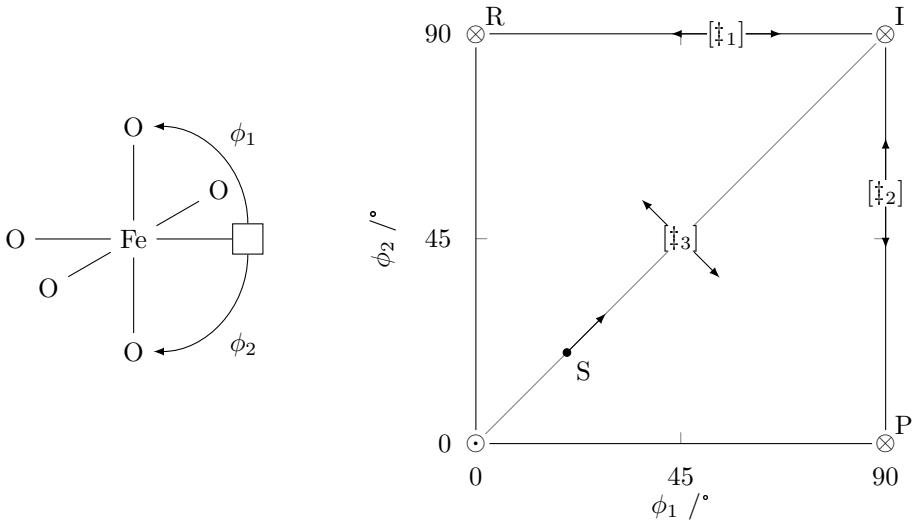

(a) Definition of the angles ϕ_1 and ϕ_2.

(b) Potential energy surface related to rotations of two oxide ions out of the FeO plane.

Figure E.2: Schematic illustration of a minimisation technique to determine whether oxide ion migration in the c direction can occur in a concerted manner, or whether such migration is step-wise. If ϕ_1 and ϕ_2 are the angles of rotation of two oxide ions out of the FeO plane, then the potential energy surface shown will be symmetrical about the grey line. The $\odot$ symbol represents a high-energy surface feature coming out of the page (where the two oxide ions are in very close proximity), and the three $\otimes$ symbols represent 'reactant' (R), 'product' (P) and intermediate (I) species in potential wells. Since our model predicts that I is in a potential well, we can characterise the two (identical) transition states $\ddagger_1$ and $\ddagger_2$ for a step-wise process R $\rightleftharpoons$ I $\rightleftharpoons$ P. If the reaction can progress in a concerted manner, then there must be a stationary point $\ddagger_3$ along the mirror plane (grey line) that corresponds to the transition state for that process. If it exists, this point can be found using conventional Newton-Raphson energy minimisation by starting at a point S already on the mirror plane.

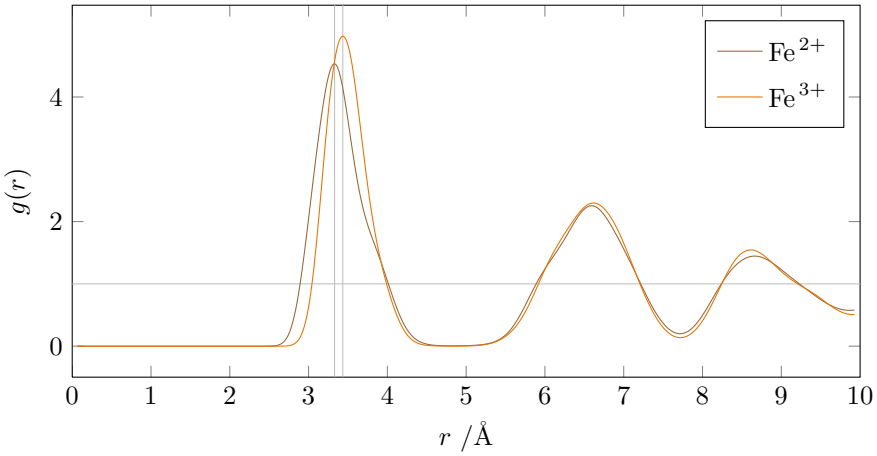

Figure E.3: Plot of the radial distribution function between Fe^{n+} ($n = 2, 3$) and Sr^{2+} in $SrFeO_2$ at 1073 K from trajectory data sampled every 500 fs over 1917 ps. The horizontal line at $g(r) = 1$ indicates a probability of finding an ion equal to that from a uniform continuum. The vertical lines have been included to highlight nearest-neighbour distances measured from the plot.

Simulations of the stoichiometric and oxidised materials at 298 K confirm that the potential model retains the structure of the material well. A plot of the Sr···Fe RDF (Figure E.3) shows that the cation sublattice stays well ordered during our high temperature simulations. Visual inspection of the trajectory data appears to show that ion motion consists mostly of isolated ion hops. Sample videos are included in the electronic supplementary information (see Appendix H).

Analysis of MSD data from simulations at a range of temperatures reveals that the change in diffusivity with respect to temperature does not follow a satisfactory trend, therefore preventing the derivation of an activation energy. This may be due in part to the disruption of the square-planar units at high temperatures, and illustrates just how challenging $SrFeO_2$ is to model.

E.3 Dopant Potentials and Solution Energies

Section 4.2.5 detailed the findings of our study of dopant ions in $SrFeO_2$. Table E.2 lists the interatomic potentials used for each dopant species, along with literature references. The table also contains references to the binary oxides used to generate the requisite lattice energies, and the defect and solution energies on both the Sr and Fe sites. These solution energies are the data plotten in Figures 4.15–4.17.

Table E.2: Buckingham potential and shell model parameters used for modelling dopant ions within the $SrFeO_2$ lattice, alongside calculated lattice energies of the corresponding binary oxide of each dopant ion, and the resulting defect and solution energies. Note: the Buckingham parameters apply to the interaction $M\cdots O^{2-}$, whilst the shell model parameters just apply to the ion M itself.

Ion, M	A /eV	ρ /Å	C /eV·Å^6	Y_M /|e|	k_M /eV·A^{-2}	Pot. Ref.	$U_{\text{latt}}(M)$	Struct. Ref.	Defect Energy /eV M^n_{Sr}	Defect Energy /eV M^n_{Fe}	Solution Energy /eV M^n_{Sr}	Solution Energy /eV M^n_{Fe}
Li^+	292.3	0.3472	0.0	-	-	[193]	-29.01	[196]	13.11	17.56	3.35	0.99
Na^+	611.1	0.3535	0.0	-	-	[193]	-24.87	[197]	14.44	19.94	2.61	1.31
K^+	902.8	0.3698	0.0	-	-	[193]	-22.21	[198]	16.59	23.00	3.43	3.03
Rb^+	1010.8	0.3793	0.0	-	-	[193]	-21.22	[199]	17.89	24.63	4.23	4.16
Mg^{2+}	821.6	0.3242	0.0	-	-	[160]	-40.36	[200]	-3.59	0.76	2.18	-0.27
Ca^{2+}	1228.9	0.3372	0.0	1.26	34.00	[160]	-35.96	[201]	-1.01	5.51	0.37	0.08
Ba^{2+}	931.7	0.3949	0.0	1.46	14.78	[160]	-31.29	[202]	4.38	11.99	1.09	1.88
Mn^{2+}	715.8	0.3464	0.0	3.00	81.20	[160]	-38.25	[203]	-2.41	2.67	1.25	-0.48
Co^{2+}	696.3	0.3362	0.0	2.00	10.74	[160]	-39.84	[203]	-3.26	1.16	1.99	-0.39
Ni^{2+}	683.5	0.3332	0.0	2.00	8.77	[160]	-40.41	[165]	-3.52	0.65	2.31	-0.33
Cu^{2+}	3799.3	0.2427	0.0	-	42.00	[194]	-44.44	[204]	-5.60	-2.25	4.25	0.79
Al^{3+}	1114.9	0.3118	0.0	-	-	[160]	-159.87	[205]	-31.36	-28.56	5.87	1.86
Sc^{3+}	1299.4	0.3312	0.0	-	-	[161]	-144.70	[206]	-27.10	-20.63	2.54	2.20
Ga^{3+}	2901.12	0.2742	0.0	-	-	[36]	-157.04	[207]	-31.62	-26.17	4.19	2.84
Y^{3+}	1345.1	0.3491	0.0	-	-	[161]	-135.03	[208]	-23.41	-15.38	1.40	2.62
In^{3+}	1495.6	0.3310	4.325	-6.1	1680.0	[195]	-141.66	[209]	-26.14	-18.88	1.98	2.44
La^{3+}	1545.21	0.3590	0.0	-	-	[36]	-127.44	[210]	-19.87	-10.72	1.14	3.49
Gd^{3+}	1336.8	0.3551	0.0	-	-	[161]	-132.47	[211]	-22.26	-13.93	1.26	4.79

Appendix F

Supplementary Material Regarding the $La_{9.33}(GeO_4)_6O_2$ Apatite Material

F.1 Defect Chemistry

The dopant chemistry of the $La_{9.33}(GeO_4)_6O_2$ Apatite Material has been discussed in detail in Chapter 5. In addition to this work, we performed a full set of intrinsic defect calculations on the material. The formation of intrinsic defects in both the $La_{9.33}$ silicate and germanate materials has been previously examined using atomistic modelling techniques [16, 219], thus our calculations, presented here, provide a good benchmarking test.

We examined the formation of full- and partial-Schottky, and Frenkel disorder within the $La_{9.33}(GeO_4)_6O_2$ lattice. The equations for these defect processes are listed in equations F.1–F.6 below. The energies for these defect formation processes are calculated from the energies of their constituent point defects, and lattice energies where required.

Table F.1: Energies of isolated point defects within the perfect $La_{9.33}(GeO_4)_6O_2$ apatite lattice.

Type of Defect	Symbol	Energy /eV
$La^{3+}(1)$ Vacancy	$V'''_{La(1)}$	44.23
$La^{3+}(2)$ Vacancy	$V'''_{La(2)}$	43.41
Ge^{4+} Vacancy	$V^{4\prime}_{Ge}$	95.69
$O^{2-}(5)$ Vacancy	$V^{\cdot\cdot}_{O(5)}$	17.90
La^{3+} Interstitial	$La_i^{\cdot\cdot\cdot}$	-41.29
Ge^{4+} Interstitial	$G_i^{4\cdot}$	-82.72
O^{2-} Interstitial	O_i''	-15.96

Full Schottky:
$$9.33\,La_{La}^{\times} + 6\,Ge_{Ge}^{\times} + 26\,O_O^{\times} \longrightarrow 9.33\,V'''_{La} + 6\,V^{4\prime}_{Ge} + 26\,V^{\cdot\cdot}_{O} + La_{9.33}(GeO_4)_6O_2 \quad \text{(F.1)}$$

La_2O_3 Schottky:
$$2\,La_{La}^{\times} + 3\,O_O^{\times} \longrightarrow 2\,V'''_{La} + 3\,V^{\cdot\cdot}_{O} + La_2O_3 \quad \text{(F.2)}$$

GeO_2 Schottky:
$$Ge_{Ge}^{\times} + 2\,O_O^{\times} \longrightarrow V^{4\prime}_{Ge} + 2\,V^{\cdot\cdot}_{O} + GeO_2 \quad \text{(F.3)}$$

La Frenkel:
$$La_{La}^{\times} \longrightarrow V'''_{La} + La_i^{\cdot\cdot\cdot} \quad \text{(F.4)}$$

Ge Frenkel:
$$Ge_{Ge}^{\times} \longrightarrow V^{4\prime}_{Ge} + G_i^{4\cdot} \quad \text{(F.5)}$$

O Frenkel:
$$O_O^{\times} \longrightarrow V^{\cdot\cdot}_{O} + O_i'' \quad \text{(F.6)}$$

Calculated energies for the individual point defects are reported in Table F.1. Interstitial oxide ions were examined in sites neighbouring the GeO_4 tetrahedra which correspond to those found experimentally by León-Reina et al. [217]. The energy of the interstitial defect at each unique site was calculated, and the most favourable of these is reported in Table F.1. Cation interstitials were incorporated on the vacant La2 sites.

The energies for the defect formation processes shown in Equations F.1–F.6 are listed in Table F.2. Oxide ion Frenkel disorder is found to be the most favourable, which is consistent with experiment. As discussed in Section 5.1.2, Frenkel disorder has been determined to be the source of interstitial oxygen, and hence the cause of oxide-ion conductivity, in the oxygen stoichiometric $La_{9.33}(SiO_4)_6O_2$ material. The low energy of La Frenkel disorder is also apparent. This suggests that there is not a high degree of ordering of the La vacancies that are inherent in the $La_{9.33}(GeO_4)_6O_2$ lattice.

The higher energies of Schottky disorder are consistent with our finding, detailed in Section 5.2.2, that the material tends to display a preference for interstitial disorder over vacancy disorder. The high energy of Ge Frenkel disorder highlights the importance and stability of the GeO_4 units in this material.

Table F.2: Formation energies for intrinsic defects in the $La_{9.33}(GeO_4)_6O_2$ apatite material.

Defect	Equation	Total Formation Energy /eV	Formation Energy /eV defect^{-1}
Full Schottky[a]	F.1	100.25	2.43
La_2O_3 partial Schottky[b]	F.2	10.23	2.05
GeO_2 partial Schottky[b]	F.3	9.94	3.31
La Frenkel	F.4	2.12	1.06
Ge Frenkel	F.5	12.97	6.48
O Frenkel	F.6	1.93	0.97

[a] A lattice energy of -1344.33 eV was calculated for for $La_{9.33}(GeO_4)_6O_2$.

[b] The lattice energies for La_2O_3 and GeO_2 were found to be -130.28 and -121.55 eV respectively, and were calculated using structures from [210] and [244].

F.2 Dopant Potentials and Solution Energies

Section 5.2.2 details our study of the dopant chemistry of the $La_{9.33}(GeO_4)_6O_2$ apatite material. This section contains further data which is complementary to the results. The potentials for each dopant ion inserted into apatite structure are listed in Table F.3, along with literature references. The table also contains a reference to the structure of the binary oxide, used to generate the requisite lattice energy, and the defect and solution energies on both the La and Ge sites. These solution energies are the data plotted in Figures 5.4–5.7.

Table F.3: Buckingham potential and shell model parameters used for modelling dopant ions within the $La_{9.33}(GeO_4)_6O_2$ lattice, alongside calculated lattice energies of the corresponding binary oxide of each dopant ion, and the resulting defect and solution energies. Note: the Buckingham parameters apply to the interaction $M\cdots O^{2-}$, whilst the shell model parameters just apply to the ion M itself. This table is continued overleaf.

Ion, M	A /eV	ρ /Å	C /eV·Å^6	Y_M /|e|	k_M /eV·A^{-2}	Pot. Ref.	$U_{\text{latt}}(M)$	Struct. Ref.	Defect Energy /eV M^n_{La}	Defect Energy /eV M^n_{Ge}	Solution Energy /eV M^n_{La}	Solution Energy /eV M^n_{Ge}
Li^+	292.3	0.3472	0.0	-	-	[193]	-29.07	[196]	34.97	87.59	0.09	4.42
Na^+	611.1	0.3535	0.0	-	-	[193]	-24.89	[197]	36.23	90.27	-0.74	5.01
K^+	902.8	0.3698	0.0	-	-	[193]	-22.22	[198]	37.94	90.43	-0.37	3.84
Rb^+	1010.8	0.3793	0.0	-	-	[193]	-21.22	[199]	38.93	91.24	0.12	4.16
Mg^{2+}	1428.5	0.2945	0.0	1.585	361.6	-	-41.28	[200]	17.43	68.21	1.53	3.80
Ca^{2+}	1090.4	0.3437	0.0	3.135	110.5	-	-35.94	[201]	20.95	74.11	-0.30	4.35
Sr^{2+}	959.1	0.3721	0.0	3.251	71.7	-	-33.43	[187]	23.21	77.15	-0.54	4.89
Ba^{2+}	905.7	0.3976	0.0	9.203	459.2	-	-31.22	[202]	25.72	78.18	-0.24	3.71
Mn^{2+}	1007.4	0.3262	0.0	3.420	95.0	-	-38.77	[203]	18.97	70.54	0.55	3.61
Fe^{2+}	1207.6	0.3084	0.0	2.997	62.9	-	-40.19	[203]	18.06	69.32	1.06	3.81
Co^{2+}	1491.7	0.2951	0.0	3.503	110.5	-	-40.89	[203]	17.59	68.41	1.29	3.60
Ni^{2+}	683.5	0.3332	0.0	2.00	8.77	[160]	-40.57	[165]	17.98	68.30	1.37	3.18
Cu^{2+}	3799.3	0.2427	0.0	-	-	[194]	-44.66	[204]	15.37	65.10	2.84	3.18
Zn^{2+}	499.6	0.3595	0.0	2.05	10.28	-	-39.64	[245]	18.91	69.35	1.37	3.30
Cd^{2+}	1725.99	0.3497	13.91	8.10	840.0	-	-32.99	[246]	23.50	77.08	-0.70	4.37

Table F.3: (Continued) Buckingham potential and shell model parameters used for modelling dopant ions within the $La_{9.33}(GeO_4)_6O_2$ lattice, alongside calculated lattice energies of the corresponding binary oxide of each dopant ion, and the resulting defect and solution energies. Note: the Buckingham parameters apply to the interaction $M\cdots O^{2-}$, whilst the shell model parameters just apply to the ion M itself.

Ion, M	A /eV	ρ /Å	C /eV·Å^6	Y_M /|e|	k_M /eV·A^{-2}	Pot. Ref.	$U_{\text{latt}}(M)$	Struct. Ref.	Defect Energy /eV M^n_{La}	Defect Energy /eV M^n_{Ge}	Solution Energy /eV M^n_{La}	Solution Energy /eV M^n_{Ge}
Al^{3+}	1114.9	0.3118	0.0	-	-	[160]	-160.82	[205]	-13.23	34.13	2.04	0.95
Ga^{3+}	2901.12	0.2742	0.0	-	-	[36]	-157.75	[207]	-10.28	37.67	3.45	2.96
In^{3+}	1495.6	0.3310	4.325	-6.1	1680.0	[195]	-141.52	[209]	-4.10	46.15	1.52	3.33
Sc^{3+}	1299.4	0.3312	0.0	-	-	[161]	-145.18	[206]	-5.39	43.77	2.07	2.78
Fe^{3+}	1102.4	0.3299	0.0	4.97	304.7	[160]	-150.25	[247]	-7.50	40.15	2.49	1.70
Co^{3+}	1329.82	0.3087	0.0	2.04	196.3	-	-157.16	[203]	-9.71	36.61	3.73	1.60
Y^{3+}	1345.1	0.3491	0.0	-	-	[161]	-135.34	[208]	-1.61	49.75	0.93	3.84
Gd^{3+}	1336.8	0.3551	0.0	-	-	[161]	-132.74	[211]	-0.56	51.31	0.68	4.10
Nd^{3+}	1379.9	0.3601	0.0	-	-	[36]	-128.95	[164]	0.65	53.14	-0.01	4.03
Ti^{4+}	754.2	0.3879	0.0	-	-	[160]	-112.13	[248]	-37.78	8.60	1.53	-0.51
Mn^{4+}	1396.4	0.3440	0.0	-	-	-	-113.94	[249]	-38.39	9.98	2.42	2.37
Zr^{4+}	985.87	0.3670	0.0	1.35	169.62	-	-113.32	[250]	-	9.12	-	0.90
Sn^{4+}	1056.8	0.3683	0.0	1.58	2037.8	-	-111.08	[251]	-35.89	12.15	2.06	1.68
Pb^{4+}	2168.4	0.3489	0.0	-	-	-	-102.88	[252]	-28.60	23.99	1.16	5.32
Ce^{4+}	1986.8	0.3511	0.0	-	-	-	-104.23	[253]	-29.34	22.83	1.77	5.52

Appendix G

Data Processing Scripts/Programs

During the course of this work, a number of original computer programs/scripts were written to facilitate the processing of simulation data. The following sections detail three of these scripts, providing brief description and usage details, as displayed by the programs' `--help` options. These scripts, and several others, can be found in the electronic supplementary material accompanying this thesis, as detailed in Appendix H.

G.1 `volumise_HISTORY.py`: A Script to Produce Time-averaged Density Data

This Python script is based on the concept of Steve Parker's `run3dbin` script. The script processes one or more HISTORY files from DL_POLY and produces a VASP CORCAR file that represents the 'time-density' of the run. The unit cell is broken up into a three-dimensional array of volume elements, each of which stores a count of how many times an ion matching a specific search pattern has been found there. Consequently, density is higher the more time and ion spends inside a particular volume element. The CORCAR file can be loaded by any molecular viewer that supports that VASP format, and overlaid on top of the structure to provide a useful pictorial view of ion migration.

The script lets you specify a target resolution (a size to attempt to make approximately square volume elements), or lets you specify your grid manually. It will concatenate multiple history files automatically, and will automatically check that they have the same cell parameters. By default it will output the CORCAR file directly to standard out, but you may override this by specifying an output file.

```
Usage: improved_volumise_HISTORY.py [options] HISTORY [HISTORY2
  [HISTORY3...]]

Options:
  --version             show program's version number and exit
  -h, --help            show this help message and exit
  -f OUTPUT_FILE, --output-file=OUTPUT_FILE
                        specify the output file to write to. If none
                        is specified, the program will write to
                        standard out
  -g GRID_DIMENSIONS, --grid=GRID_DIMENSIONS
                        explicitly specify a voxel grid of integer
                        dimensions a, b and c. Can be specified as a
                        comma, 'x' or '*' separated list, e.g.,
                        '10,20,30', '10x20x30' or '10*20*30'
  -l lines, --progress=lines
                        the script indicates how many lines of
                        HISTORY have been read by printing a
                        character every LINES lines. The default
                        value of LINES is 100000, but feel free to
                        change it if your machine is ripping through
                        the data at lightning speed ;-)
  -n NEGATIVE_ATOMs, --negative=NEGATIVE_ATOMs
                        specify a comma separated list of atom labels
                        to count towards the negative density
  -p POSITIVE_ATOMs, --positive=POSITIVE_ATOMs
                        specify a comma separated list of atom labels
                        to count towards the positive density
  -r RESOLUTION, --resolution=RESOLUTION
                        attempt to make voxels of approximate
                        dimension RESOLUTION in Angstroms. Default
                        value is 0.3 A
  -R GRID_DIMENSIONS    equivalent to -g
  -v, --verbose         be verbose about what the script is doing.
                        The default behaviour is to remain quiet
```

G.2 `doscrunch.py`: A Script to Process DOSCAR Files from VASP

The density of states output from VASP (the DOSCAR file) is rather hard to extract information from directly as it contains individual data tables for the total DOS and the DOS for each atom in the system. While this wealth of information is very useful, it must be manipulated into a more suitable form before it can be visualised.

This Python script processes the information in a DOSCAR file generated by VASP

and puts it into a more useful form for plotting. In addition to the DOSCAR, the script tries to grab some information from the INCAR, POSCAR and POTCAR files to make life easier.

The script basically extracts the relevant columns from the correct data tables in the DOSCAR file, and then sums them as required. The explicit collective DOS is the most powerful feature of the script, enabling the user to create a data file containing the summed DOS from explicit atoms from the simulation.

```
Options:
 -h, --help           Display this help message and quit
 -r, --noheaders      Don't print any headers in the output files
 -c, --colldos        Output collective DOS files for multiple
                      species
 -o, --projected      Output individual site projected DOS for each
                      atom
 -f, --force          Force overwrite of existing output files
 -m, --manual         Manually input all required data (atom labels
                      etc...)
 -d filename, --doscar=filename, --DOSCAR=filename
                      Specifies an alternative DOSCAR input file to
                      ./DOSCAR
 -i filename, --incar=filename, --INCAR=filename
                      Specifies an alternative INCAR input file to
                      ./INCAR
 -p filename, --poscar=filename, --POSCAR=filename
                      Specifies an alternative POSCAR input file to
                      ./POSCAR
 -P filename, --potcar=filename, --POTCAR=filename
                      Specifies an alternative POTCAR input file to
                      ./POTCAR
 -x list, --xcolldos=list
                      Output eXplicit collective DOS files for
                      multiple species where 'list' is a comma
                      separated list of species' numbers or number
                      ranges (x-y) as listed in the POTCAR
 -v, --verbose        Be verbose about what the script is doing
```

G.3 `bsplineconnect`: A Program to Smooth Data using B-Splines

When a data set is sampled from a rapidly varying or oscillating function, it is sometimes necessary to interpolate between the data points to achieve a satisfactory plot

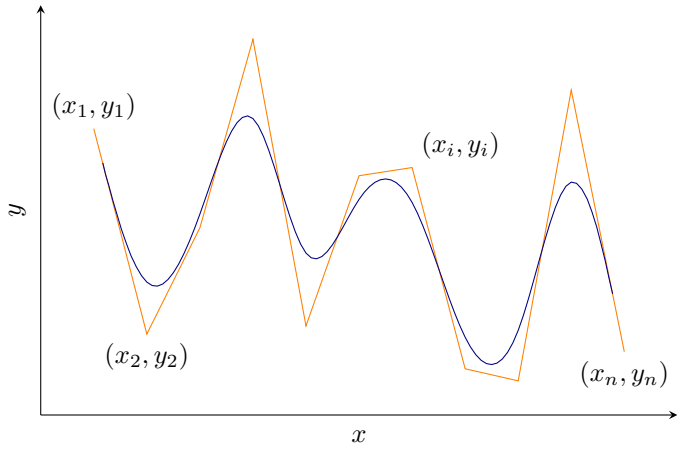

Figure G.1: Example of B-spline smoothing. The original data set (orange) is rapidly varying and has been sampled at a low frequency. The interpolated function (blue) produces a smooth curve that is defined by the original data points.

(Figure G.1). This type of functionality is included in many software packages, but no useful interpolation schemes could be employed with the particular combination of software used in this work. We therefore wrote a small script that would implement cubic B-spline data smoothing, and also perform data table manipulation as a useful additional function.

Details of the cubic B-spline connection algorithm are taken from the manual to the data processing and graph plotting software "Origin" [254]. To generate a cubic B-spline curve from a set of data points (x_i, y_i), $i = 1, 2, \ldots, n$ a set of parametric equations is used:

$$\begin{aligned} x_i(t) = {}^1\!/\!_6 \big\{ &(-t^3 + 3t^2 - 3t + 1)x_{i-1} + (3t^3 - 6t^2 + 4)x_i + \\ &(-3t^3 + 3t^2 + 3t + 1)x_{i+1} + t^3 x_{i+2} \big\}, \\ y_i(t) = {}^1\!/\!_6 \big\{ &(-t^3 + 3t^2 - 3t + 1)y_{i-1} + (3t^3 - 6t^2 + 4)y_i + \\ &(-3t^3 + 3t^2 + 3t + 1)y_{i+1} + t^3 y_{i+2} \big\}. \end{aligned} \tag{G.1}$$

The curve is calculated by iterating over the original data points using i in the range $2 \leq i \leq n - 2$. Each new data point is then generated by varying t at fixed values between 0 and 1. The resulting cubic B-splines is continuous up to the second order derivative, and winds around the original data points without passing through them. The major advantage of this smoothing algorithm is that it places no requirements at all on the input data (such as that it must be monotonic).

The script takes a series of coordinate pairs from a csv file and converts them into a larger set of output coordinate pairs that lie on the B-spline curve. Input files can have more than one dependent (y) column but only one independent (x) column, and it is assumed that, aside from a possible header line, the data are on continuous lines until the end of the file. Output can be to a file or to stdout.

```
Options:
  --version             show program's version number and exit
  -h, --help            show this help message and exit
  -d DELIMITER, --delimiter=DELIMITER
                        Single delimiter character for column
                        separation in csv input. Default is a comma.
  -e NUMERRSTR, --numbererrorstring=NUMERRSTR
                        String to use as output when no number can be
                        generated for an output field (for example,
                        if text is present at a strange point in the
                        numerical input). Default is NAN.
  -n, --nosmooth        Prevents the program from performing any
                        actual smoothing. This means that you can use
                        the table parsing features to reformat your
                        data, removing, duplicating or rearranging
                        columns using --ycols.
  -o OUTPUTFILENAME, --output=OUTPUTFILENAME
                        Output file name. If no output file is
                        specified, stdout will be used.
  -s STEPS, --segments=STEPS
                        This specifies the number of steps overwhich
                        the parametric b-spline function is
                        calculated for each set of four points.
                        Default = 10.
  -t, --titles          Specifies that the input file contains a
                        title line which is to treated separately
                        whilst parsing the file.
  -v, --verbose         Be verbose about what the script is doing.
                        The default behaviour is to remain quiet.
  -x XCOL, --xcol=XCOL  Column within the input datafile from which
                        to take data for the x coordinates. Column
                        numbering starts at 1, default x column is 1.
  -y YCOLS, --ycols=YCOLS
                        Column or comma-separated list of columns
                        within the input datafile from which to take
                        data for the y coordinates. Column numbering
                        starts at 1, default is to use all y columns
                        ('2-').
```

Appendix H

Guide to the Contents of the Accompanying DVD

Electronic supplementary material, archived data and other useful information is included with the printed copy of this thesis on a 4.7 GB DVD-R. A short summary of the directory structure of the DVD is presented in Figure H.1 to provide an overview of the disc. Archived data has been archived with `tar` and compressed using `gzip`, which are a freely available open-source utilities.

In addition to the scripts presented in Appendix G, a number of other scripts are archived, which may be of use to anyone undertaking work similar to that presented here. The latex source files from which this thesis is compiled are also included, as are source files for all of the figures. If you use this material please include an appropriate citation in your work.

```
/
   supplementary/
      Nd2NiO4/
         video/
            Nd2NiO4.11_Nd_deficient_1073K_down_c.mpg
            Nd2NiO4.11_Nd_stoichiometric_1073K_down_b.mpg
            Nd2NiO4.11_Nd_stoichiometric_1073K_down_c.mpg
      SrFeO2/
         video/
            SrFeO2.06_whole_down_c.mpg
            SrFeO2.06_whole_down_b.mpg
            possible_cooperative_mechanism_down_b.avi
   data/
      Nd2NiO4/
         71137-icsd/
            static_lattice.tar.gz
            md.tar.gz
      SrFeO2/
         static_lattice.tar.gz
         md.tar.gz
         dft.tar.gz
      La9.33Ge6O26/
         static_lattice.tar.gz
   latex/
        thesis/
        references2.bib
   scripts/
      bsplineconnect.py
      doscrunch.py
      listLatticeE.awk
      listPhonons.awk
      listStructComp.awk
      listTotalDefectE.awk
      make_history_labels_unique.awk
      nebgout2arc.awk
      subscript
      volumise_HISTORY.py
```

Figure H.1: Partial directory listing of the accompanying DVD.